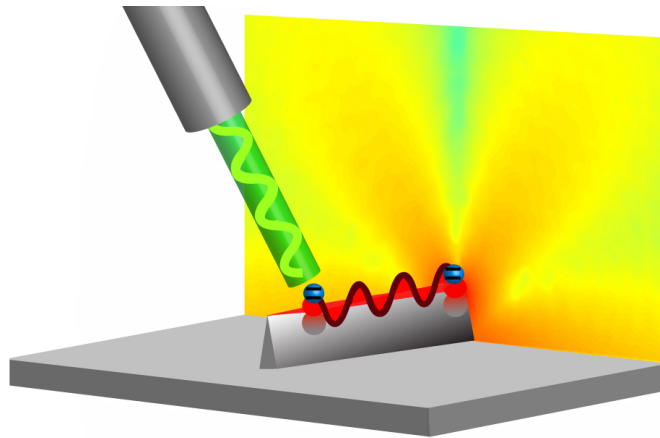Universidad Autónoma de Madrid

Departamento de Física Teórica de la Materia Condensada

PLASMONIC WAVEGUIDES: CLASSICAL APPLICATIONS AND QUANTUM PHENOMENA

Memoria de la tesis presentada por
Diego Martín Cano
para optar al grado de Doctor en Ciencias Físicas

Directores:
Esteban Moreno Soriano y Francisco José García Vidal

Madrid, Enero de 2013

Agradecimientos

Quién pensaría que llegaría el momento de escribir estos agradecimientos. No tanto por todo lo que supone, sino por todos obstáculos que ha habido por el camino... Cuántas horas pensando problemas de física (y de 'no' física) cuántas vueltas a qué escribir y cómo expresarlo... Y es que a mi modo de ver, si la fortuna te acompaña, uno de los mayores problemas que tiene aquel que hace una tesis, es enfrentarse a uno mismo. Afortunadamente en este respecto, he podido contar con la ayuda de muchas personas que me han hecho ese 'camino' más llevadero en muchos sentidos.

Primeramente, quería agradecer enormemente a mis tutores Esteban y FJ, por el gran apoyo que me han dado durante estos años, incluyendo la revisión profunda de la tesis, y por ofrecerme toda su compresión en los buenos y en los no tan buenos momentos. En especial quiero agradecerles por haberme desvelado las pautas para hacer buena investigación (hacer una escritura precisa, ser honesto con los resultados obtenidos, los valiosos consejos para presentaciones y posters, y un largo etc.).

Aunque de esto haya pasado mucho tiempo ya, recuerdo como el primer día todos los buenos consejos de Antonio (en física, cluster, origin, etc.) de los cuales he hecho buen uso durante el doctorado, ¡muchas gracias!. En especial quería agradecer a Maxim por desvelarme los secretos de COMSOL y el diseño de figuras aunque todavía me quede mucho para superar al maestro. También quiero agradecer todo el apoyo científico, y no sólo científico, recibido por parte del resto del grupo de Nanofotónica de la UAM y Zaragoza: Paloma, Felix, Pu, Juan Antonio, Jorge, Ricardo, Johan, Óscar, Roberto, Johannes, Carlos, Javier, Solete, Luis, Alexey, los Fernando, Sergio... Es díficil cuantificar el gran apoyo, las discusiones físicas interesantes, las risas y la amistad que también provienen de nuestro departamento: Milica (gracias por todas las correcciones y por proponernos tantos eventos divertidos), Pau, Enrique, Floren, Linda, Alex, Delia, Emiliano, Teresa, Héctor, Pablo Pou, Yannick, Nacho, Stefan, Dani, Guilherme, Andrei, Pablo, Lucía, Blanca, Ferdinand, Shirley, Jesper, Krzysztof... Tampoco olvido mi estancia en San Diego: David y Gina (gracias infinitas), Bobby y Chelsey, Janelle, Qing, Olesya, Felipe, Joe, Mercedeh, Matthew, Boris... La vida en el doctorado sin vosotros hubiera sido tremendamente difícil e insulsa.

Los amigos de toda la vida han sido de vital importancia para poder finalizar el doctorado y no caer en la depresión: Nuur, Huergas, Trompas, Miguelas, Javi, los amigos del barrio...

Contents

Contents

List of Figures

Abstract

English

The purpose of the present thesis is to study the interactions between quantum emitters mediated by surface electromagnetic modes that are bound to complex metallic waveguides. The motivation for this research is the strong confinement of surface electromagnetic fields. Such localization can enhance the quantum-emitter interactions and allows them to serve as basic components for ultra-compact circuits based on one-dimensional surface plasmons. Towards this aim, we present a theoretical formalism based on the quantization of the macroscopic Maxwell's equations and the Green's electromagnetic tensor. We treat the quantum character of the atomic-systems in the two-level approximation, whereas the optical properties of the macroscopic metallic waveguides are characterized by means of dielectric constants. Due to the complexity of the waveguides considered in this thesis, we develop accurate numerical models based on the finite element method to calculate the electromagnetic fields bound to the waveguides. We apply the electric dipole approximation to compute the electromagnetic Green's tensor from these numerical models. Next, we explicitly extract the contribution of the surface guided modes to the above-mentioned tensor in order to analyze its role in mediating the interactions between the emitters. The classical values of the Green's tensor are required to compute the evolution of the density matrix associated with the quantum emitters and the plasmonic waveguides, and the resulting master equation is numerically solved.

We perform a broad research of waveguide candidates that support surface electromagnetic modes, in order to construct a suitable framework to investigate the above-mentioned interaction phenomena. This analysis is started in the optical regime, inspired by the properties of surface plasmon polaritons at flat metallic surfaces. The subwavelength confinement of surface plasmons allows to boost the electromagnetic interactions with quantum emitters in planar interfaces. With the aim of further increasing the degree of confinement of such bound modes, we study the electromagnetic properties of one-dimensional plasmonic waveguides. To this purpose, we consider several of the most promising plasmonic waveguides, and characterize their relevant range of geometrical parameters for achieving deep subwavelength confinement. In order to transfer those confinement properties from the op-

Abstract

tical to other possible regimes of emission at longer wavelengths, we make use of periodical corrugations in the metals. We show how such corrugations allow us to increase the degree of confinement in the telecom and the terahertz regimes. The extension to these regimes of high technological interest enable us to identify new waveguide schemes. In particular, we propose a novel waveguide, based on periodical chains of metallic particles on top of metallic substrates, with good guiding properties for subwavelength circuitry. We describe its main propagation properties and we develope a set of passive devices using this structure.

The high spatial confinement of one-dimensional plasmonic waveguides in the optical regime, together with the availability of single-photon sources at optical wavelengths, motivates the research of electromagnetic interactions between the two. In particular, we analyze the spontaneous emission from two-level atomic-systems induced by one-dimensional plasmonic waveguides in several spatial and orientational configurations. The resulting high efficiency of single-plasmon generation leads us to explore the ability of those guided plasmons to act as interaction carriers between two separated emitters. In particular, we demonstrate their capacity to enhance the resonance energy transfer from one emitter to an accepting atomic-system, and also to generate super and subradiance phenomena which arise from mutual couplings mediated by the one-dimensional plasmonic waveguides.

The super and subradiant collective decay rates indicate the potential capability of guided plasmons to generate entanglement among two atomic-systems. To further investigate this ability, we quantify the generation of entanglement between a pair of separated two-level emitters for different waveguide-emitter configurations. First, we consider the generation of entanglement in the absence of external sources, which leads to a transitory formation of entanglement. Secondly, we introduce the presence of a laser source, which allows to achieve stationary entanglement. In both scenarios, the main physical mechanisms that generate the entanglement are explained by means of the guided plasmon properties.

Español

El objetivo de esta tesis es investigar las interacciones entre emisores cuánticos mediadas por modos electromagnéticos de superficie que existen en guías de onda metálicas complejas. La motivación para el estudio de este tipo de interacciones proviene del alto confinamiento de los campos electromagnéticos de superficie, que permite incrementar dichas interacciones. Para analizar dichos acoplamientos, se presenta un formalismo teórico basado en la cuantización de las ecuaciones macroscópicas de Maxwell y el tensor de Green electromagnético. En este formalismo, las propiedades ópticas de los materiales que forman las guías de ondas se caracterizan por constantes dieléctricas. Por otro lado, el carácter cuántico de los sistemas atómicos se trata dentro de la aproximación de dos niveles, con su correspondiente momento dipolar asociado. Debido a la complejidad de las guías de onda estudiadas en esta tesis, hemos desarrollado modelos numéricos precisos, basados en el método de elementos finitos, para calcular los campos electromagnéticos asociados a estas estructuras. En particular, usando la aproximación dipolar eléctrica, hemos extraído el tensor de Green de los modelos numéricos. Con el fin de enfatizar la relevancia de los modos de superficie guiados en las interacciones con los emisores, hemos extraído explícitamente la contribución de los modos guiados a dicho tensor. Los valores calculados del tensor de Green son utilizados para evaluar los coeficientes de la ecuación maestra que describe la interacción de los emisores y las guías plasmónicas, y que gobierna la evolución de la matriz de densidad en dichos sistemas.

Para establecer un marco adecuado en el que poder investigar los fenómenos de interacción mencionados anteriormente, se realiza una amplia investigación de guías de onda que soportan modos electromagnéticos de superficie. Comenzamos esa investigación en el régimen óptico, tomando como inspiración las propiedades de los plasmones polaritones de superficie en interfaces metálicas planas. El confinamiento de los plasmones de superficie, que se produce en tamaños más pequeños que la longitud de onda, permite aumentar las interacciones electromagnéticas de emisores cuánticos. Con el fin de incrementar el grado de localización de tales modos ligados, se estudian las propiedades electromagnéticas de guías de ondas plasmónicas unidimensionales. En este estudio consideramos varias de las guías de ondas plasmónicas más prometedoras, y caracterizamos un rango de parámetros geométricos que proporcionan un alto confinamiento. Para transferir dichas propiedades de localización del régimen óptico a otros posibles a longitudes de onda mayores (concretamente al infrarrojo cercano y al terahercio), hacemos uso de ondulaciones periódicas en la superficie de los metales. La extensión a tales regímenes de alto interés tecnológico nos ha permitido identificar nuevos sistemas de guías de ondas. En particular, se estudia una guía de ondas novedosa basada en cadenas periódicas de partículas metálicas, las cuales son colo-

Abstract

cadas encima de substratos metálicos. Estas guías de ondas muestran notables propiedades de propagación para circuitos pequeños comparados con la longitud de onda. Dichas características de guiado son estudiadas frente a cambios geométricos de las partículas, y un conjunto de dispositivos pasivos, basados en la guía de ondas mencionada, es presentado.

El alto confinamiento espacial de los modos plasmónicas unidimensionales en el régimen óptico, junto con la disponibilidad de fuentes de fotones individuales en dicho rango, motivan la investigación de las interacciones electromagnéticas entre ambos. En particular, analizamos las propiedades de emisión espontánea de sistemas atómicos de dos niveles en presencia de guías de ondas plasmónicas. Para ese estudio se han considerando amplios cambios de la configuración del sistema (posiciones y orientaciones del emisor, geometría de las guías y longitud de emisión). Las altas eficiencias resultantes para la generación de plasmones individuales, nos llevan a estudiar la posibilidad de usar los plasmones guiados como portadores de la interacción entre dos emisores separados. La capacidad para aumentar la transferencia de energía en resonancia, desde una fuente de emisión hasta un sistema atómico aceptor, es demostrada. Además la formación de fenómenos colectivos super y subradiantes mediados por la guía plasmónica es estudiada.

Finalmente investigamos la habilidad de los plasmones guiados para generar entrelazamiento cuántico entre dos sistemas atómicos separados, lo cual es debido principalmente a la aparición de estados sub y superradiantes. Dicha generación es cuantificada para diferentes guías plasmónicas, y para distintas posiciones y orientaciones de los emisores respecto a éstas. En primer lugar, se considera la generación de enredo cuántico en ausencia de fuentes externas, lo que conduce a una formación transitoria de entrelazamiento, y en segundo lugar, se introduce la presencia de una fuente láser, que permite lograr un entrelazamiento cuántico estacionario. En ambos escenarios, el principal mecanismo físico que genera el enredo se explica a través de las propiedades de los plasmones guiados.

List of acronyms

This is a list of the acronyms used in the text:

- **1D** One-dimensional

- **2D** Bi-dimensional

- **3D** Three-dimensional

- **CPWs** Channel plasmonic waveguides

- **CYPWs** Cylindrical plasmonic waveguides

- **DPPs** Domino plasmon polaritons

- **DSPs** Domino spoof plasmons

- **EM** Electromagnetic

- **FEM** Finite element method

- **GHz** Gigahertz

- **MMP** Multiple Multipole method

- **PEC** Perfect electric conductor

- **PMC** Perfect magnetic conductor

- **PMLs** Perfectly matched layers

- **PWs** Plasmonic waveguides

- **QDs** Quantum dots

- **Qubit** Quantum bit

- **RET** Resonance energy transfer

- **SIBCs** Surface impedance boundary conditions

List of acronyms

- **SPOOFSPs** Spoof surface plasmons

- **SPPs** Surface plasmon polaritons

- **THz** Terahertz

- **TE** Transverse electric

- **TEM** Transverse electromagnetic

- **TM** Transverse magnetic

- **WPWs** Wedge plasmonic waveguides

Throughout this thesis, the SI system of electromagnetic units is used, unless otherwise indicated.

1 General introduction

The progress in the physics of surface electromagnetic (EM) modes has been outstanding since the end of the 20th century due to the development of devices based on surface plasmon polaritons (SPPs) [1]. SPPs are quasi-particles supported at the surface of a conductor material, usually a metal. The origin of this quasi-particle nature is the interaction of light waves with the free electrons of the metal. Such resonant response of the electrons turns into collective oscillations, which trap the light at the metal surface. The charge density oscillations, together with the light field, constitute the SPPs and they give rise to their interesting properties. The first experimental evidence of SPPs was observed in flat metallic slabs with electron scattering experiments. Their existence was revealed through the appearance of resonances in the spectrum of the reflectance or transmittance arising from the electrons that impinged on the metallic sample [2]. The peaks of the resonances were displaced at lower energies respect to the energy of the incident electrons and this difference was attributed to the excitation of SPPs.

The aim of those early days in plasmonic research is far from the actual goal of developing SPP-based devices. Recent progresses in material fabrication have allowed to build metallic nanostructures in order to control the propagation of SPPs for designing novel applications. Some examples of these applications, which are currently under research [1], are surface enhanced Raman scattering for biomolecular detection [3, 4], near-field microscopies [5], and all-optical processing in circuits [6]. Interestingly, some of these advances in all-optical circuit processing have been recently encouraged by quantum optical devices that exploit the discrete character of SPPs. For both classical and quantum optical research, one of the most remarkable properties of SPPs is the ability to concentrate light at subwavelength scales [1, 6]. In order to place the work involved in this thesis within both research contexts, we firstly introduce some state-of-the-art devices in 'classical' research on plasmonic circuitry, including different spectral regimes and their limitations, and secondly, we detail some of the most relevant quantum developments with SPPs.

Most of the motivation for a classical information processing of SPPs on a chip comes from the possibility to fabricate photonic circuits at subwavelength sizes, in contrast to dielectric waveguide approaches [6] that are diffraction limited. Let us explain this limitation in more detail. In the case of translational-invariant all-dielectric waveguides, the light can

be confined in a finite 2D domain characterized by a cross-section, for instance a circular one. The inner core of the waveguide domain is a high refractive-index material that is surrounded by a dielectric of lower refractive-index, and consequently, the main principle that explains the light confinement in all-dielectric waveguides is the phenomenon of total internal reflection. If we decrease indefinitely the diameter of the waveguide, the guiding mechanism will become weaker since the guided EM mode will start to be increasingly unconfined [7], a fact that reduces the local intensity carried by such modes. Such diffraction limit is basically general for any kind of dielectric waveguide, including photonic crystals [8], and it represents a fundamental limitation for miniaturizing waveguides at a particular wavelength. On the other hand, surface plasmons on flat interfaces are based on the intrinsic properties of the metals [2], in particular, on the negative value of the metallic dielectric constant which allows to overcome the limit imposed by the diffraction.

The possibility to go beyond the diffraction limit has driven different research efforts to reduce the confining volume of the SPPs respect to the one in a flat surface. In particular, a one-dimensional geometrical structuring of the flat interface has allowed to produce plasmonic waveguides (PWs) with subwavelength confinement in the transverse plane, perpendicular to the direction of propagation. Such research is motivated by the possibility to fabricate highly compact chips that can process different amounts of information with a full optical approach [1]. Some examples of the routing schemes for achieving extreme localization in the optical regime, which have been experimentally fabricated, are displayed in Figure 1.1. For instance, panel (a) displays the electron microscope images of several metallic wedge PWs in one sample (see an sketch in the inset of panel (b)). These metallic wedges allow the propagation of a surface plasmon confined at the tip of the structure, which can be fabricated by sputtering metallic atoms over a dielectric wedge that is patterned with photolithographic techniques [9]. A small defect at the beginning of the waveguides can be used to evanescently excite the SPPs supported by the wedge waveguide in combination with a focused laser impinging on it at optical frequencies. The near-field intensity of the generated SPPs is spatially measured close to the surface of the sample as displayed in Figure 1.1(b), and it reflects two important characteristics. Firstly, it can be observed the sudden drop of the intensity in the lateral direction (z-direction in the sketch) that is associated to the subwavelength lateral confinement of the mode. Additionally, it can be clearly seen the intensity decay along the propagation direction, which limits the SPP propagation for a distance of $\sim 1.5\,\mu\text{m}$. Both properties show the large potential of PWs for the fabrication of subwavelength circuitry, and also their main limitation, namely, their relatively small propagation lengths ($\sim 2.3\lambda$) that arise from the losses in the metal (interband absorption, electron scattering losses, electron-hole excitations) [10]. A possible way to reduce such propagation losses is to prepare smooth crystalline structures which dimin-
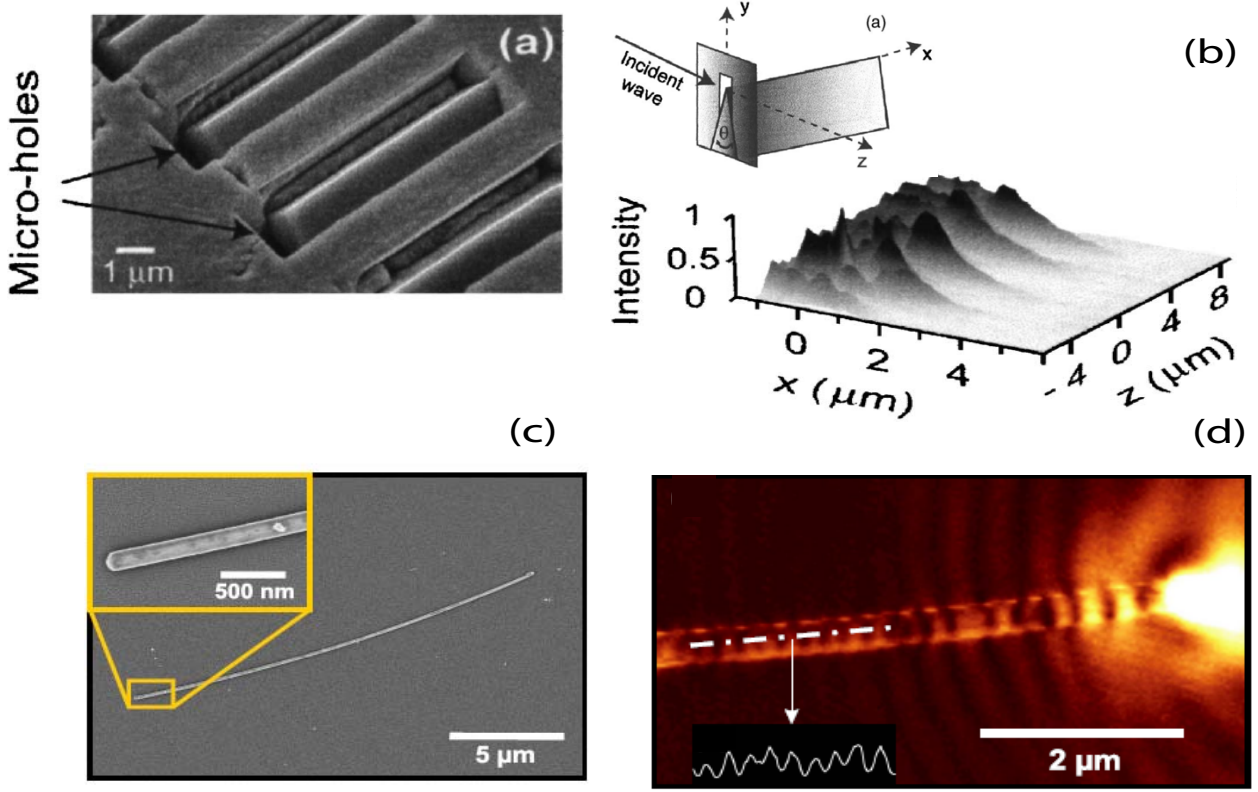
Figure 1.1: (a) Electron microscope images of finite wedge plasmonic waveguides from reference [9]. (b) Near-field intensity scan measurement corresponding to the structures in panel (a) at optical frequencies ($\lambda \sim 600$ nm). (c) Electron microscope images of a crystalline cylindrical plasmonic waveguide of radius $60\,\text{nm}$ and a finite total length of $18.6\,\mu\text{m}$ from reference [11]. (d) Direct near-field imaging of the surface plasmon field along the nanowire.

ish the surface roughness and impurities at the interfaces of the metal. One example of a crystalline PW with a smooth surface is displayed in Figure 1.1 (c) for a finite cylindrical metallic nanowire [11] that results from a chemical reduction of silver ions embedded in an aqueous electrolyte solution. A consequence of the increase of the propagating lengths with such fabrication technique is the observation of first order spatial coherence of the SPP, which can be appreciated in the near field measurement displayed in panel (d). In particular, it can be appreciated the intensity pattern, which oscillations are remarked in the measurement along a line close to the nanowire (see the inset). The physical origin of the oscillations arises from the stationary standing wave that is formed by the SPPs confined in the finite nanowire, which acts as a resonator due to the increase of the propagation lengths.

The confinement properties of PWs in the optical regime have attracted an important
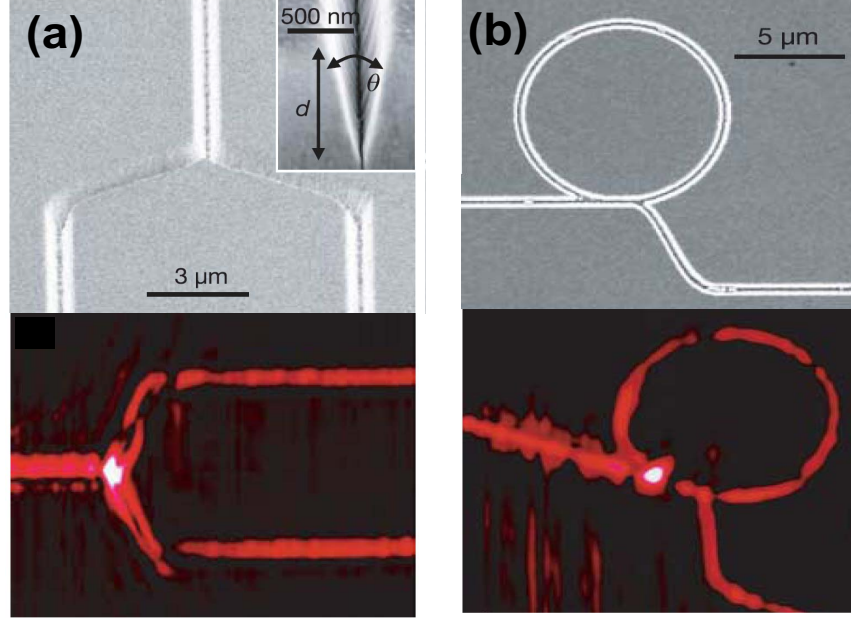
Figure 1.2: (a) Scanning electron microscope images of a channel Y-splitter (top), and its corresponding scanning SNOM images at $\lambda = 1.6\,\mu$m (down). (b) Scanning electron microscope images of a channel waveguide-ring resonator (top), and its corresponding SNOM images at $\lambda = 1.53\,\mu$m (down). Both images in this figure have been extracted from reference [12].

experimental and theoretical effort to export them to longer wavelength regimes. Such research is motivated by the technological interest of the different spectral regimes, which would also benefit from a full on-chip optical processing of EM signals. The main problem for extending the SPP properties to those wavelengths is the departure from the SPP resonance wavelength, which lies at ultraviolet frequencies. Therefore, at longer wavelengths, the metallic dielectric constant becomes more negative, the penetration of the electromagnetic fields in the metal diminishes and the subwavelength transverse confinement is gradually lost.

An example of those interesting regimes of longer wavelengths is the near-infrared, which is the closest respect to the optical spectrum. One of the main motivations for extending the optical plasmonic circuits to the near-infrared is its vital role in long distance telecommunications nowadays, from $\lambda = 1.26\,\mu$m to $1.67\,\mu$m, in which the diffraction-limited dielectric fibers are the main approach [13]. Due to the proximity in frequency of the near-infrared

with respect to the optical regime, most of the PWs have been simply re-scaled to larger sizes to support the corresponding SPPs at telecom wavelengths. For instance, one of the most successful examples extending PWs to the telecom regime is the channel PW [14–18]. Figure 1.2 (a) and (b) display two examples of channel-based passive devices [17], together with the typical cross-section of the waveguide (see the inset in (a)), that permit the modulation of incoming SPP signals. The large bandwidth associated to the channel allows to operate with 1D guided SPPs in the full spectrum of the telecom regime. This operation at a broad interval of wavelengths clearly shows the usefulness of spatial and spectral modulating devices, like those shown in the figure. The near-field measurement of both devices performance, shown in the lower images, reflects the long propagation lengths achieved in the channel PWs ($\sim 100\,\mu$m) at telecom wavelengths. However, such scales are achieved at the expense of loosing the subwavelength confinement, whose particular extension is estimated to be [19] roughly twice the operating wavelength ($\sim 2.5\,\mu$m). Consequently, the degree of delocalization of the SPP at the telecom and longer wavelength regimes increases, and other approaches are needed to recover the very deep subwavelength character of conventional PWs in the optical regime.

A different interesting regime at longer wavelengths is the terahertz (THz), that ranges from 100 GHz to 50 THz [23]. The large multidisciplinary scope and unexplored capabilities of this regime have motivated the creation of previously nonexistent THz sources and detectors [24, 25, 23]. As a consequence, some important THz applications have been developed such as imaging techniques for security and medicine purposes [25–27], food and pharmacy processes monitoring [28], astronomical observation [29], and wireless communications [30]. In particular, the design of circuitry and waveguides may have a critical role in the intercommunication between different components [30]. Due to such development interest, there is a large effort for extending the subwavelength confining properties of SPPs from the optical to the THz regime, since they are potentially beneficial for designing ultra-compact circuits in different devices, $e.g.$, on-board of satellites [23, 30]. A possible way to extend the SPP properties to the THz is by making use of the spoof plasmon concept [31], which is based on the periodic patterning of metallic structures. The corrugations or indentations milled in the metal surface allow to create surface electromagnetic modes, whose dispersion relations and modal confinement resemble to those for SPPs at optical frequencies [20, 32, 22, 33–35]. Figure 1.3 displays two interesting examples showing the capabilities of spoof plasmonic waveguides for fabricating 1D subwavelength circuitry, and for enhancing the EM fields in the THz regime. In particular, panel (a) displays a theoretical proposal consisting of a 1D corrugated cylindrical wire that can be used to achieve full-transverse subwavelength confinement [20]. Moreover, it can be appreciated in the left image the spatial extension of the electric field, which is on the order of the external radius ($\sim 0.25\lambda$), thus showing the
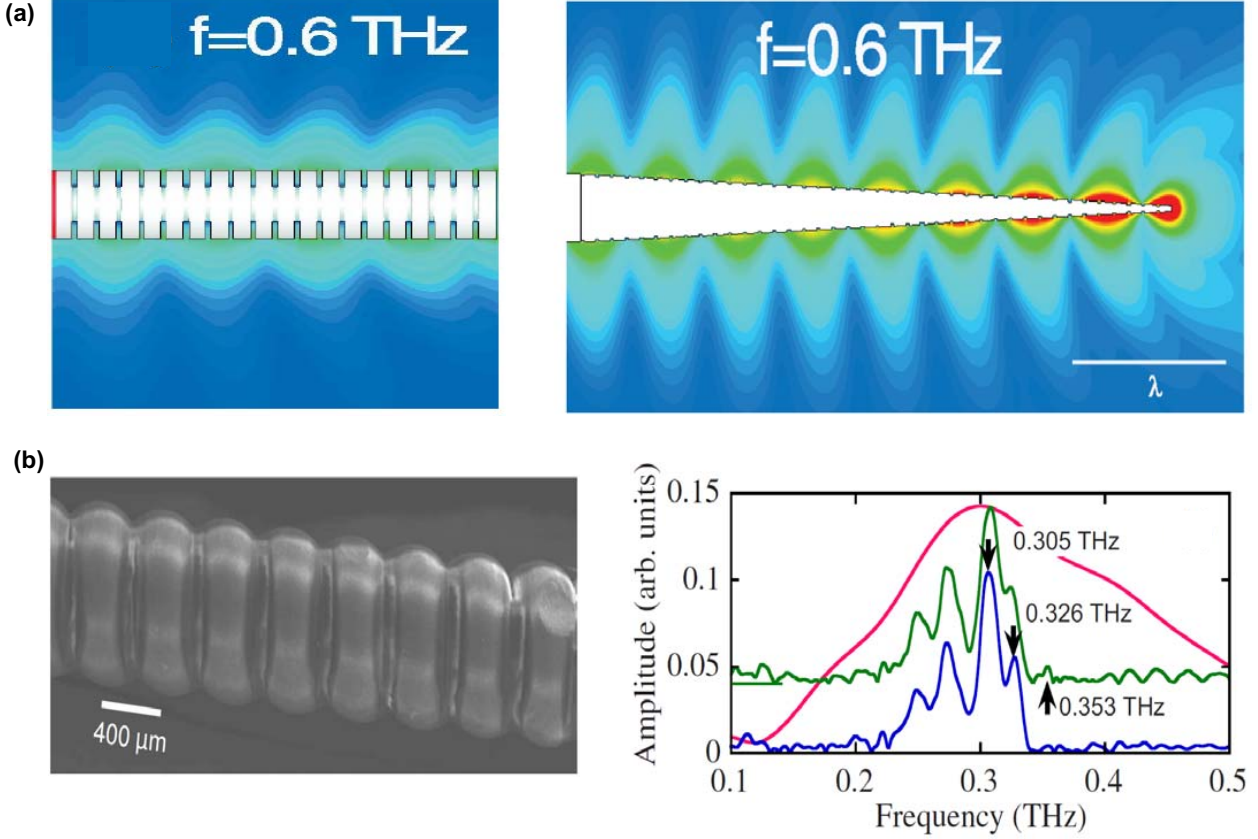
Figure 1.3: (a) (left) Near field of the electric field amplitude on a corrugated wire with periodicity $d = 50\,\mu$m, aperture $a = 10\,\mu$m, external radius $R = 100\,\mu$m and internal radius $r = 50\,\mu$m for f=0.6THz and (right) a conic taper on a corrugated cone extracted from reference [20]. (b) (left) Electron microscope image of the helical corrugated wire from reference [21]. (right) Transmitted spectrum through the helical wire from reference [22], corresponding to the same experiment as in the left image.

above-mentioned subwavelength confining properties. Interestingly, an adiabatic reduction of both structural radii allows the focusing of the surface EM modes supported by the wire, as shown in the right image of panel (a). This EM concentration can be important for the enhancement of typical low intensity signals at THz frequencies [35]. Moreover, an experimental proposal of a 1D spoof waveguide is displayed in panel (b) which corresponds to an helically grooved wire [22]. In this case, the EM field enhancement associated to the subwavelength transverse confinement is reflected in the transmitted spectra which displays intensity maxima due to the presence of highly localized surface EM modes (right image, green and blue lines). These waveguides and most of the considered spoof PWs in the literature [20, 22, 33–35] imply some fabrication and implementation challenges due to the

non-planar symmetry or their lack of 2D transverse confinement [32, 31]. One possibility to solve such complexity is by means of dielectric waveguides [36, 37], in spite of their restriction to the diffraction-limit, which prevents to achieve higher degrees of confinement for a certain dielectric material. A part of the work in this thesis is devoted to research new 1D corrugated metallic waveguides that present simpler and planar approaches in addition with deep subwavelength confinement [38, 39]. Moreover, inspired by the spoof plasmon concept, we introduce the benefits of corrugations in conventional plasmonic waveguides for telecom wavelengths [40] in order to recover the lost subwavelength confinement properties of optical frequencies that we commented above.

In all previous PWs in which deeply tight surface EM modes are supported, the most limiting factor is the finite propagation lengths arising from the metal absorption. Such energy loss is particularly accentuated for the optical regime in which the SPP propagation lengths are on the order of microns or even less [6]. The small scales involved in the propagation and confinement of SPPs, at optical wavelengths, make the fabrication of PWs circuits to be a challenging objective. One possible way to manage such small lengths is by means of using quantum optical emitters, which allow to study a vast non-linear and linear phenomena on the scales of very few nanometers. These quantum effects, together with the small sizes of the emitters, provide the necessary ingredients to integrate such atomic systems on a chip and perform a full quantum processing with SPPs. The benefits of using quantum optics with surface plasmons have started to be explored during the beginning of this century and different scientific works have started to consolidate a new branch of research with the name of quantum plasmonics. This research field explicitly exploits the subwavelength quantum character of SPPs and emitters for future quantum optical applications and in the following we detail some of those works.

The broad number of non-linear phenomena associated with quantum emitters allows quantum optics to be a framework to perform the excitation, detection and switching of confined guided plasmons at subwavelength scales, *i.e.* the basic characteristics for on-chip quantum processing with SPPs. Moreover, the quantization of plasmonic systems opens the possibility to approach the power of quantum computation processing [42] to plasmonics. In particular, several experimental groups [41, 43, 44] have successfully corroborated the most elementary process that quantum optics needs to exploit the discrete nature of plasmons, *i.e.*, the excitation of a single SPP quasiparticle or single-plasmon [45]. One of the pioneering experiments which showed such single particle nature of plasmons [41] is shown in Figure 1.4. In particular, panel (a) sketches the basic idea behind the experiment, which is the coupling of a quantum dot (QD) to a cylindrical silver nanowire of similar characteristics to that commented above in Figure 1.1. The main purpose of the experiment was to use the QD as a single-photon source, in which a laser-induced excitation of the emitter mainly decays as a
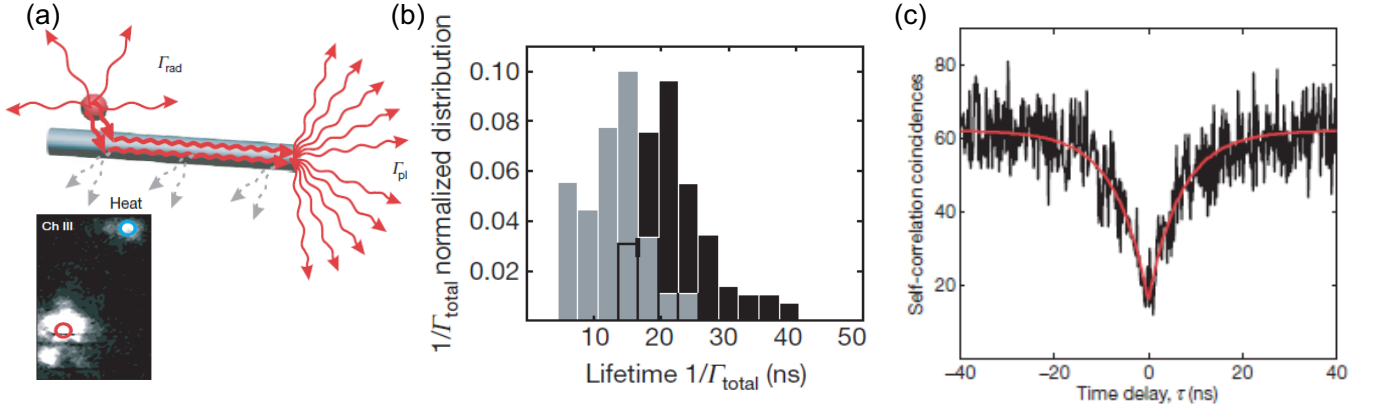
Figure 1.4: (a) (top image) Sketch of the different decay channels of an exciton in a QD due to spontaneous emission in a nanowire. (lower image) Experimental fluorescence image from the sytem. The red circle illustrate light directly emitted from the QD whereas the blue circle displays the end of the nanowire that were used for the photon cross-correlation measurements. (b) Normalized histograms of the quantum dot lifetimes distributions, for uncoupled QDs (black bars), and for coupled QDs and wires (grey bars). (c) Experimental second-order cross-correlation (black line) as a function of the time delay between the count coincidences. All the images in the different panel have been extracted from reference [41].

consequence of the EM coupling induced by the SPPs bound to the nanowire. Importantly, such predominant decay is basically due to the subwavelength transverse confinement of the guided plasmons, which enhances the density of EM states available to the emitter. Consequently, as sketched on panel (a), a small part of the spontaneously emitted photons are directly scattered from the QDs to free space, whereas most of them are mainly coupled to SPPs that travel along the wire, and finally they are partially scattered to free-space at the ends of the nanowire. The fluorescence emitted directly from the QD and from the wire ends (see a resulting experimental image in the lower figure in (a)) is then collected with an optical setup that ends in two different photodetectors. Finally, such detectors individual counts can be mutually correlated with the help of a computer and a photon counting board, in order to test the photon statistics of the system. One of the important results in this experiment is the modification of the radiative decay rates of the exciton (or equivalently its inverse, the lifetime) due to the plasmon EM coupling, which has been also corroborated by other experimental works [5, 43, 44]. Such is a general process for any single emitter coupled to a general EM reservoir and is commonly known as the Purcell effect [47].
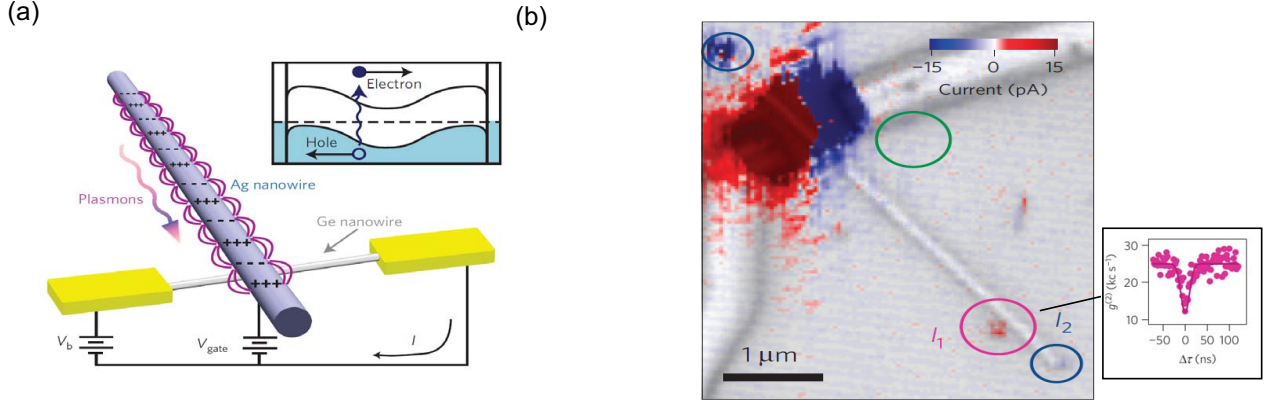
Figure 1.5: (a) Sketch of the electrical detection of SPPs in silver nanowires perpendicularly coupled to Ge nanowires. (b) Detected intensity I as a function of the laser focusing position, with a superposed reflection image of a device. Both panels were extracted from reference [46].

Remarkably, the weight of the lifetime distributions for QDs coupled to nanowires, shown in the histogram of panel (c) (grey bars), is largely reduced compared to uncoupled dots (black bars), evidencing the Purcell effect due to the EM coupling with the SPPs supported by the wire. A more restrictive proof of the excitation of single-plasmons is the measurement of the normalized second-order time cross-correlation function $g^{(2)}(\tau)$, which is defined as

$$g^{(2)}(\tau) = \frac{\langle I_1(t) I_2(t+\tau) \rangle}{\langle I_1(t) \rangle \langle I_2(t+\tau) \rangle}, \qquad (1.1)$$

where I_1 and I_2, are the total intensities of the signals that are detected in two different photodetectors, respectively, and τ is the delay time between both intensity detections. If a single photon is emitted from the source then the detected photons in both detectors show ideally no coincidences at zero delay τ, since only one photon can be observed. Experimentally, the indication for such antibunching event is a value $g^{(2)}(\tau = 0)$ higher than zero, due to the non-ideal behaviour of the photodetectors, but smaller than 0.5 to preclude the excitation of a larger number of photons [48]. The second order cross-correlation function was measured by analyzing the time correlations between the detected signals from the light collected spatially from the quantum dot area (red circle, lower image in (a)) and from the wire end (blue circle), which involves the propagation of SPPs along the nanowire. The resulting cross-correlated function from both channel measurements is represented in panel (c) versus the time delay between the detectors. It can be seen the antibunch dip at zero delay, with a depth ratio between the counting values at $\tau = 0$ and at $\tau \gg 0$ values smaller than 0.5, therefore indicating the emission of single plasmons.

The detection of single plasmons in the above experiment is indirect since it relies on the

9

out-coupling of SPPs to free-space at the nanowire ends. Nevertheless, several groups have also advanced in the implementation of on-chip single plasmon detectors. In Figure 1.5 (a) it is displayed one of those experimental setups with indications of near-field detection of single plasmons. Panel (a) displays a silver crystalline wire that is coupled perpendicularly to a germanium semiconductor cable, which is bound with gold electrodes to a conducting substrate. When an SPP supported in the nanowire approaches the Ag-Ge junction, it generates electron-holes pairs which induce a current in the Ge wire that can be measured through the electrodes. An example of those detected currents are displayed in panel (b), in which an impinging laser at $\lambda = 530$ nm scans the sample of the Ag-Ge wire system, containing QDs that are randomly deposited (similar to Figure 1.4(a)). As a consequence, a current is detected when the laser impinges on a QD close to wire (red circle) or on the ends of the Ag-wire (blue circles) and, in contrast, no signal is detected for QDs far from the silver nanowire (green circle). Additionally, similarly to the image shown in Figure 1.4(c), a second-order correlation antibunch dip was detected at the far-field (see the inset), suggesting that near-field detected currents were probably produced by single SPPs. A different experimental setup is considered in reference [49], in which the excitation of SPPs supported in a rectangular gold waveguide is detected by a NbN superconducting wire that is perpendicularly aligned to the PW. The resulting second-order cross-correlation function using both a free-space and a SPP signal, detected in the superconducting wire, clearly shows a photon antibunch dip, whose normalized depth could be improved with the use of better single sources [49]. Importantly, the authors claim that due to the near field counting rate dependence, which is linear with the exciting laser intensity, this may correspond to the first on-chip detector of single-plasmons.

The above experiments demonstrate how SPPs fulfill the elementary requirements of quantum optics as information carriers, and show that the basic experimental tools to generate and detect single guided plasmons are present. With this experimental background, there is a large number of quantum non-linearities that can be envisioned for designing quantum plasmonic processing devices. An interesting example, proposed in reference [50], corresponds to the design of a single-plasmon transistor which is detailed in the following. The basic working principle of such switch can be understood by the mirror properties of a two-level energy emitter coupled to a PW [see the sketch in Figure 1.6(a)]. In Figure 1.6(b) is represented the reflectance (black line), corresponding to an incoming guided plasmon imping on the emitter, versus the energy detuning δ_k between the SPP and the emitter. On resonance ($\delta_k = 0$), it is clearly seen how the emitter in the ground state behaves nearly like a perfect mirror, as appreciated in the large values of the reflectance that are close to 1. Such good mirror properties are a consequence of the subwavelength transverse confinement of the SPPs, which allows a predominant coupling of the emitter
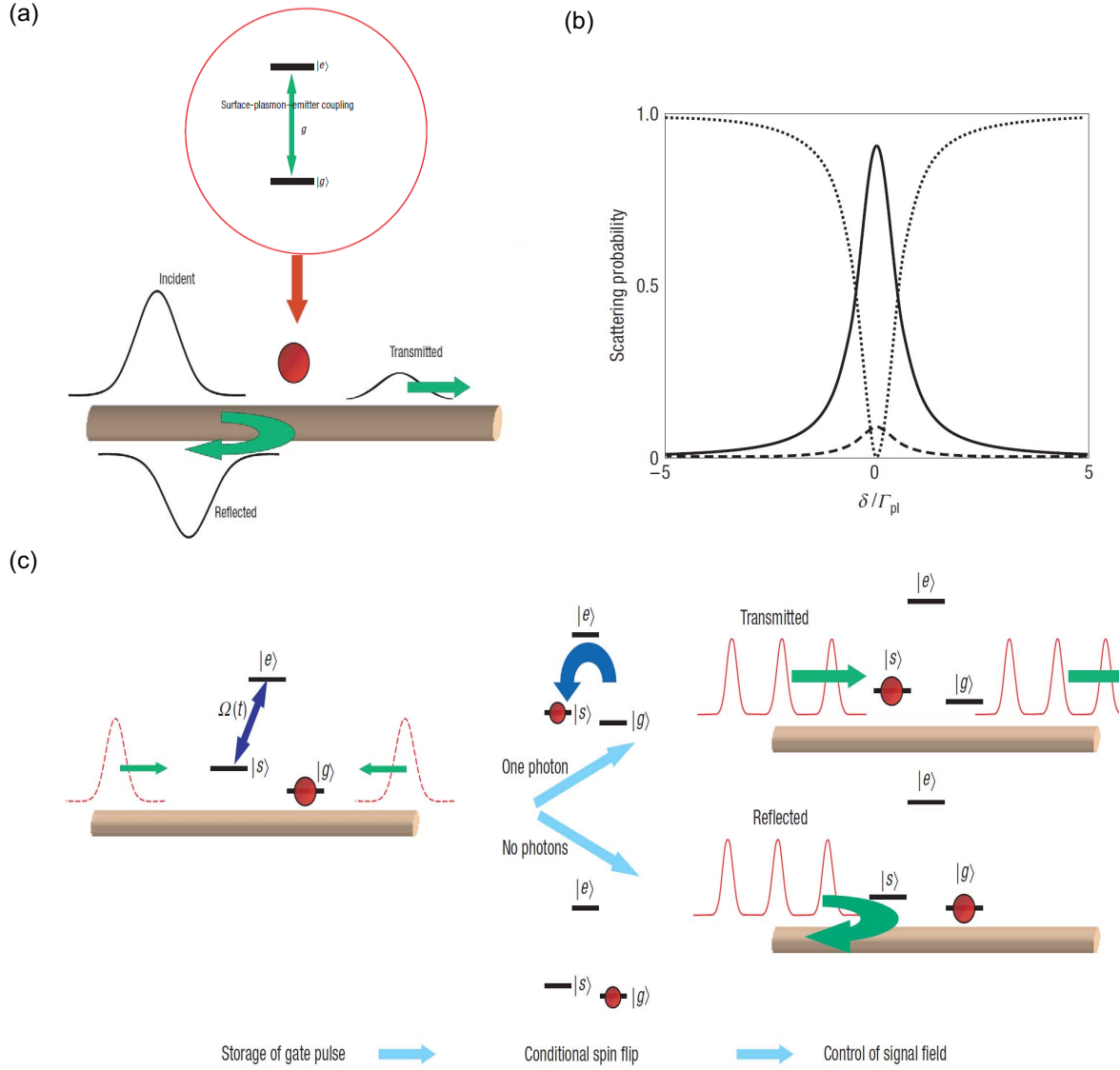
Figure 1.6: (a) Sketch of a two-level emitter with excited ($|e\rangle$) and ground states ($|g\rangle$) coupled to a cylindrical PW. Additionally, it is illustrated the nearly resonant scattering process of a left incident single plasmon and the emitter. (b) Reflectance, R, as a function of detuning, together with the transmittance (T, dotted line), and the probability of losing a photon into other decay channels ($1 - R - T$). The coupling efficiency of the emitter to the SPP is 95%. (c) Illustration of a three level emitter coupled to a cylindrical wire which can act as a single plasmon transistor. All the figures have been extracted from reference [50].

excitation with the plasmonic EM mode. The single-plasmon reflectance can be exploited to be the basis of a transistor when combined with an extra metastable state $|s\rangle$ that is coupled by means of a classical field (with Rabi frequency $\Omega(t)$) to the excited state of the emitter $|e\rangle$ (see an illustration in the left image of Figure 1.6(c)). Importantly, this $|s\rangle$-$|e\rangle$ transition has no direct coupling to the SPP and that conditions the mirror characteristics of the three-level emitter coupled to the PW. The switch operation is the following (see an sketch in Figure 1.6(c)). Starting the emitter in the ground state $|g\rangle$, we can apply a time dependent control field ($\Omega(t)$) simultaneously synchronized with the arrival of an incoming single SPP, that acts like a gate-signal in the transistor. This pulse $\Omega(t)$ allows to store the single-plasmon in the metastable state $|s\rangle$, which makes the system to become completely transparent for incoming SPPs, due to the fact that the $|s\rangle$-$|e\rangle$ transition is decoupled from the guided plasmon. If no SPP gate signal impinges on the emitter when the classical field is applied, the pulse $\Omega(t)$ has no effect on the emitter excitation which remains in $|g\rangle$ for the entire process, and the system behaves like a good mirror for incoming SPPs. Therefore, the transistor mechanism is to store different 'gate' single plasmons that conditionally changes the internal state of the emitter, and this storage protocol is used to control the passage of outgoing SPPs.

In addition to the previous logic process, further research works are exploring the capabilities of subwavelength PWs in quantum plasmonic phenomena with two quantum emitters. One of the main motivations for studying these bipartite systems is the possibility to use them as gates [51] for quantum computations. Importantly, it has been theoretically demonstrated that a minimum requirement of such gates to be universal for quantum computing, *i.e.*, for performing all necessary non-classical calculations, is the availability of entanglement between two different parties [52]. Moreover, other quantum applications such as quantum teleportation and quantum cryptography are also based on the existence of entanglement in bipartite systems. The entanglement preserving characteristics of SPPs, has been demonstrated in metallic hole arrays [53–55] for free-propagating photons that pass through those systems. Inspired by such properties, a part of the work in this thesis is to study the possibility to generate entanglement between a pair of separated two-level emitters mediated by PWs [56, 57]. In particular, it is demonstrated the importance of the subwavelength properties of SPPs for generating the entanglement due to the appearance of collective states of the emitters, whose decay rates are subradiant and superradiant [58], *i.e.*, smaller or larger than the single emitter decay rate, respectively.

Another example of a quantum process that can benefit from the subwavelength confinement properties of SPPs in PWs is the study of energy transfer between fluorescent molecules, a process known as Resonance Energy Transfer (RET). The relevance of RET is manifest in different nature processes like the photosynthesis occurring in plant cells

and bacteria at optical wavelengths [47]. In this mechanism certain proteins inside the cell, acting like antennas, carry the energy to the reaction center in order to perform metabolic processes. Though this physical transport can be explained classically to certain extent [47], it is important to remark that the quantum character of such process has been experimentally revealed [59, 60]. There are different regimes of operation for RET depending on the separation between the molecules. Such phenomenon typically takes place in nature for small distances in vacuum ($< 10\,\mathrm{nm}$), in which non-radiative energy transfer occurs. This non-radiative process is very sensitive to the separation between the molecules, and it has been used as an indicator of structural changes in large proteins that have fluorophores attached to them [61]. The working principle of these sensing schemes is the drastic reduction of the energy transfer rate with the increase of the separation between the molecules. Several researchers have explored the possibility to extend such phenomenon to longer separations assisted by different intermediary structures. In particular, it has been demonstrated that a metallic slab between the fluorophores enhances the radiative energy transfer rate at distances on the order of hundred nanometers [62]. The reason for the increase of these lengths is due to the coupling through SPPs, whose subwavelength confinement enhances the RET process as compared to vacuum at the same distances. A different plasmonic approach has considered boosting this radiative transfer at longer distances by coupling separated chromophores along very wide metallic waveguides [63], which almost resemble a flat metallic surface. In this thesis we have researched the increase of SPP mediated energy transfer between separated molecules along conventional 1D PWs that show deep subwavelength transverse confinement [58].

Structure of the thesis

Once we have put into context the research in which our theoretical work has been conducted, we outline the rest of the content of this thesis:

In Chapter 2, we present a theoretical framework that allows us to study the EM phenomena related to the plasmonic waveguides researched in this thesis. We study a numerical formalism based on the inhomogeneous Green's tensor that is obtained from the macroscopic Maxwell equations and the finite element numerical approach. Importantly, we demonstrate how to obtain an analytical formula that extracts the particular contribution of the PW modes to the Green's tensor. The basis of the finite element method is presented and the particular models for obtaining the EM modes, from which we extract the Green's tensor, are discussed. From the quantization of the macroscopic Maxwell's equations, we derive the master equation governing the dynamics of N-qubits in inhomogeneous absorbing materials for two situations: in the absence of free-evolving external fields and also including the presence of a resonant coherent laser. With the EM calculations of the Green's tensor, we can evaluate the resulting coefficients of interaction in the master equation for realist PWs, and we can also include the specific contribution of the guided SPPs with the derived analytical formula.

Chapter 3 is intended for studying a broad framework of plasmonic guiding approaches to build subwavelength circuitry from the optical to the terahertz regime. We study some of the most promising PWs in the optical regime, in order to apply them for single-plasmon emission and plasmon mediated coupling between emitters. Additionally, inspired by the spoof plasmon concept, we show how to obtain subwavelength confinement in conventional PWs for the telecom regime, making use of designed corrugations in the metal surface. In particular, we identify a new PW consisting of a 1D periodic chain of metallic particles on top of a metallic substrate, which shows good properties in comparison with other standard PWs. We extend such approach to the terahertz in order to create novel subwavelength circuitry and, based on their band insensitivity to the waveguide width, we show its robustness and simplicity for building several passive devices.

In Chapter 4, we study the interaction of quantum emitters mediated by different PWs at optical wavelengths. We show how 1D standard PWs can enhance and control the single photon emission in the optical regime with high efficiencies. Additionally, the coupling of two separated quantum emitters mediated by 1D PWs is demonstrated, and the coefficients arising from the master equation are calculated for several PWs. Next, we apply the 1D plasmonic enhanced coupling between two emitters to analyze resonance energy transfer and super and subradiance phenomena.

Chapter 5 is devoted to study the entanglement generation between two separated qubits

mediated by PWs. We demonstrate that PWs allow the transitory generation of entanglement in the absence of external sources, explaining the main mechanisms that generates it, and considering different possible system configurations. Next, we show how a resonant coherent laser that impinges on the emitters, allows to create stationary entanglement between separated emitters in realistic PWs. For such study, we consider different initial state conditions and we explain the main physical reasons that form it. Several issues related to the experimental implementation, like the influence of the laser intensity, the effect of pure dephasing, and the waveguide efficiency, are studied. Additionally, the second order cross-correlation at zero delay is also analyzed, and its characteristics are pointed as a possible entanglement witness.

Finally, in Chapter 6 we present a brief summary of the main results of this thesis and future outlook.

2 Theoretical methods

2.1 Introduction

For researching the physical phenomena introduced in chapter 1, we need to obtain mathematical tools both for classical and quantum calculations. In this chapter we present the theoretical framework which has allowed us to study such physical processes for metallic waveguides. In the first two sections, we deal with the phenomenological macroscopic Maxwell equations governing classical electromagnetic problems, in which all the microscopic problem is incorporated in the dielectric constant. Specifically in section 2.2, we write down the classical macroscopic Maxwell equations in the presence of arbitrary inhomogeneous materials with local spatial response and noise electromagnetic sources. In subsection 2.2.2, we analyze the formal solution of Maxwell equations in terms of the electromagnetic Green's tensor in presence of inhomogeneous media. In particular, in subsection 2.2.3, we derive the explicit contribution from waveguide modes to the total Green's tensor. Next, in section 2.3, we revisit the resolution of the classical electromagnetic problems in terms of the finite element numerical approach. The general properties of the finite element method and its Galerkin's approach is described in subsection 2.3.2, whereas in subsection 2.3.3 we deal with the particular models that have been considered for the electromagnetic waveguides studied in this thesis. Finally, in section 2.4, we depart from the previous classical description and consider the quantum mechanical character of emitters and electromagnetic fields. In section 2.4.1, the classical Maxwell's equations from section 2.2 are quantized and the matter-field Hamiltonian in presence of absorbing matter is obtained. Next in subsection 2.4.2, we focus on the interaction of quantum emitters with quantized electromagnetic fields within the minimal coupling scheme, which is described in terms of their associated electric charges and potentials. In the following, we show how we can transform such description into a more convenient one expressed in terms of the electromagnetic fields, *i.e* the multipolar-coupling Hamiltonian. Finally in subsection 2.4.3, we derive the master equation governing the dynamics of N-qubits in inhomogeneous materials, first focusing in the absence of free-evolving external fields and then including the action of a resonant coherent laser.

2.2 Classical electromagnetism

2.2.1 Macroscopic Maxwell's Equations

The main problems presented in the following chapters requires, as a first starting point, the resolution of the macroscopic Maxwell's equations with the appropriate boundary conditions for each considered waveguide structure. The macroscopic Maxwell equations governing the temporal evolution of electromagnetic fields in the presence of inhomogeneous dielectric bodies, and without additional charge or current densities are [47, 64]:

$$\nabla \times \mathbf{E}(\mathbf{r}, t) = -\frac{\partial \mathbf{B}(\mathbf{r}, t)}{\partial t}, \tag{2.1}$$

$$\nabla \times \mathbf{H}(\mathbf{r}, t) = \frac{\partial \mathbf{D}(\mathbf{r}, t)}{\partial t}, \tag{2.2}$$

$$\nabla \cdot \mathbf{D}(\mathbf{r}, t) = 0, \tag{2.3}$$

$$\nabla \cdot \mathbf{B}(\mathbf{r}, t) = 0. \tag{2.4}$$

In such system of equations, $\mathbf{E}$ is the electric vector field, $\mathbf{H}$ the magnetic field, $\mathbf{B}$ the magnetic induction, wheras $\mathbf{r}$ and t are the usual spatial and temporal coordinates, respectively. Additionally, $\mathbf{D}$ represents the displacement field vector, which is related to the polarization field $\mathbf{P}$ according to the constitutive relation

$$\mathbf{D}(\mathbf{r}, t) = \varepsilon_0 \mathbf{E}(\mathbf{r}, t) + \mathbf{P}(\mathbf{r}, t). \tag{2.5}$$

For non-magnetic matter, it can also be assumed that

$$\mathbf{B}(\mathbf{r}, t) = \mu_0 \mathbf{H}(\mathbf{r}, t), \tag{2.6}$$

where ε_0 and μ_0 are the vacuum permittivity and permeability, respectively. Let us consider arbitrarily inhomogeneous isotropic materials and assume that the polarization responds linearly and locally in space to the electric field. In this case, following closely reference [64], the most general local relation in space between the polarization and the electric field, which is in agreement with the causality principle and the dissipation-fluctuation theorem (linear to external perturbation), is

$$\mathbf{P}(\mathbf{r}, t) = \varepsilon_0 \int_0^\infty \mathrm{d}\tau \, \chi(\mathbf{r}, \tau) \mathbf{E}(\mathbf{r}, t - \tau) + \mathbf{P}_N(\mathbf{r}, t), \tag{2.7}$$

where $\chi(\mathbf{r}, t)$ is the local dielectric susceptibility response as a function of space and time, and $\mathbf{P}_N(\mathbf{r}, t)$ is the (noise) polarization associated with absorption. It is particularly important to realize that, by the Fourier theorem, any time dependent real (observable) field can be treated as an integral of monochromatic fields, *e.g.*, such representation for the electric field is

$$\mathbf{E}(\mathbf{r}, t) = \int_{-\infty}^\infty \mathbf{E}(\mathbf{r}, \omega) e^{-i\omega t} \, \mathrm{d}\omega, \tag{2.8}$$

where ω refers to the monochromatic angular frequency and $\mathbf{E}(\mathbf{r}, \omega)$ is the electric field Fourier transform which is complex-valued in general.

Therefore, we can treat any transitory solution as a sum of stationary solutions that follows the Fourier transform of equations (2.1)-(2.4):

$$\nabla \times \mathbf{E}(\mathbf{r}, \omega) = i\omega \mathbf{B}(\mathbf{r}, \omega), \tag{2.9}$$

$$\nabla \times \mathbf{B}(\mathbf{r}, \omega) = -i\frac{\omega}{c^2}\varepsilon(\mathbf{r}, \omega)\mathbf{E}(\mathbf{r}, \omega) + \mu_0 \mathbf{J}_N(\mathbf{r}, \omega), \tag{2.10}$$

$$\nabla \cdot \varepsilon_0 \varepsilon(\mathbf{r}, \omega)\mathbf{E}(\mathbf{r}, \omega) = \rho_N(\mathbf{r}, \omega), \tag{2.11}$$

$$\nabla \cdot \mathbf{B}(\mathbf{r}, \omega) = 0, \tag{2.12}$$

where we have introduced the noise charge density

$$\rho_N(\mathbf{r}, \omega) = -\nabla \mathbf{P}_N(\mathbf{r}, \omega), \tag{2.13}$$

and the noise current density

$$\mathbf{J}_N(\mathbf{r}, \omega) = -i\omega \mathbf{P}_N(\mathbf{r}, \omega), \tag{2.14}$$

which follow the charge-current conservation

$$\nabla \mathbf{J}_N(\mathbf{r}, \omega) - i\omega \rho_N(\mathbf{r}, \omega) = 0. \tag{2.15}$$

In order to derive (2.9)-(2.12), we have made use of the Fourier transform of equations (2.5) and (2.6) with the local spatial response (2.7), *i.e.*,

$$\mathbf{D}(\mathbf{r}, \omega) = \varepsilon_0 \varepsilon(\mathbf{r}, \omega)\mathbf{E}(\mathbf{r}, \omega) + \mathbf{P}_N(\mathbf{r}, \omega), \tag{2.16}$$

$$\mathbf{B}(\mathbf{r}, \omega) = \mu_0 \mathbf{H}(\mathbf{r}, \omega), \tag{2.17}$$

and

$$\mathbf{P}(\mathbf{r}, \omega) = \varepsilon_0[\varepsilon - 1]\mathbf{E}(\mathbf{r}, \omega) + \mathbf{P}_N(\mathbf{r}, \omega), \tag{2.18}$$

$$\tag{2.19}$$

where ε is the complex relative permittivity constant

$$\varepsilon(\mathbf{r}, \omega) = 1 + \int_0^\infty d\tau \, \chi(\mathbf{r}, \tau)e^{i\omega\tau}. \tag{2.20}$$

For solving either formally or numerically the system of equations (2.9)-(2.12), it is useful to transform them into wave equations which can be solved for a single EM field. With the help of equations (2.16)-(2.17), we can easily obtain:

$$\nabla \times \nabla \times \mathbf{E}(\mathbf{r}, \omega) - \frac{\omega^2}{c^2}\varepsilon(\mathbf{r}, \omega)\mathbf{E}(\mathbf{r}, \omega) = i\omega\mu_0 \mathbf{J}_N(\mathbf{r}, \omega), \tag{2.21}$$

$$\nabla \times \varepsilon^{-1}\nabla \times \mathbf{H}(\mathbf{r}, \omega) - \frac{\omega^2}{c^2}\mathbf{H}(\mathbf{r}, \omega) = \nabla \times \varepsilon^{-1}\mathbf{J}_N(\mathbf{r}, \omega), \tag{2.22}$$

which can be solved separately for the electric and magnetic field, respectively.

2.2.2 Total Green's tensor

The wave equations can be formally solved in terms of the Green's tensor approach. The calculation of the Green's tensor is specially interesting because it permits to evaluate non-classical properties of interacting quantum emitters as it will be shown in section 2.4. In particular, the electric field in the wave equation (2.21) can be calculated from the total Green's tensor, which is defined as the solution corresponding to an infinitesimal unit current dyad:

$$\nabla \times \nabla \times \mathbf{G}(\mathbf{r}, \mathbf{r}', \omega) - \frac{\omega^2}{c^2} \varepsilon(\mathbf{r}, \omega) \mathbf{G}(\mathbf{r}, \mathbf{r}', \omega) = \mathbb{I} \delta(\mathbf{r} - \mathbf{r}'), \quad (2.23)$$

where $\mathbf{G}$ represents the Green's tensor, $\mathbb{I}$ is the unit dyad and $\delta(\mathbf{r} - \mathbf{r}')$ is the spatial-delta function. As a consequence of the linearity of equation (2.21), we can write its solution like an infinitesimal sum of its generating linear current densities $\mathbf{J}_N$ as

$$\mathbf{E}(\mathbf{r}, \omega) = \mathbf{E}_0(\mathbf{r}, \omega) + i\omega\mu_0 \int_V \mathbf{G}(\mathbf{r}, \mathbf{r}', \omega) \mathbf{J}_N(\mathbf{r}', \omega) \, \mathrm{d}^3\mathbf{r}', \quad (2.24)$$

where $\mathbf{E}_0$ represents an additional homogeneous solution and $\mathbf{J}_N$ is confined in a volume V. We can clearly see the physical interpretation of the Green's tensor as an electric response function in the sense that it carries the interaction from the spatial point $\mathbf{r}'$ generated by the current density $\mathbf{J}_N$ to the spatial point $\mathbf{r}$. In the case of an infinitesimal harmonic current density located at $\mathbf{r}_0$ with an induced dipole moment $\mathbf{d}$, $\mathbf{J}_N(\mathbf{r}', \omega) = -i\omega\mathbf{d}\delta(\mathbf{r}' - \mathbf{r}_0)$, the resulting electric field in such point dipole approximation is:

$$\mathbf{E}(\mathbf{r}, \omega) = \omega^2 \mu_0 \mathbf{G}(\mathbf{r}, \mathbf{r}_0, \omega) \mathbf{d}, \quad (2.25)$$

where we have assumed that all the field is generated by the dipolar current, *i.e.* $\mathbf{E}_0 = 0$.

2.2.3 Guided Green's tensor

We are specially interested in the interaction of quantum emitters with plasmonic guided modes and therefore, we need to discriminate its contribution from the total Green's tensor contained in equation (2.25). For such purpose, we deduce the general guided Green's tensor for an inhomogeneous z-translational invariant waveguide. We make the derivation for a step-index waveguide, *i.e.*, constituted by different piecewise domains which are characterized by complex dielectric constants. In particular, we will concentrate on the results for a single-mode plasmonic waveguide with small absorption, which is the case of interest in this thesis.

An arbitrary guided field in a waveguide can be represented as an infinite series of forward and backward propagating normal modes, which are solutions of the free-source ($\mathbf{J}_N = 0$)

equations (2.21)-(2.22) [65, 7]. The nth guided mode propagating forward in the z-direction can be represented as:

$$\mathbf{E}_n^+(\mathbf{r}, \omega) = (\mathbf{e}_n + \mathbf{e}_{zn})e^{ikz}, \tag{2.26}$$

$$\mathbf{H}_n^+(\mathbf{r}, \omega) = (\mathbf{h}_n + \mathbf{h}_{zn})e^{ikz}, \tag{2.27}$$

where $\mathbf{e}_n$, and $\mathbf{e}_{zn}$ represent the transversal and longitudinal electric modal field, respectively, whereas $\mathbf{h}_n$ and $\mathbf{h}_{zn}$ represent the corresponding magnetic fields. Additionally, $\mathbf{r}$ is the spatial position and k is the complex propagation constant. Notice that the values of those EM modal fields are also dependent on the transverse coordinates of the waveguide. In a similar fashion, the corresponding nth guided mode propagating backwards in the z-direction is represented as

$$\mathbf{E}_n^-(\mathbf{r}, \omega) = (\mathbf{e}_n - \mathbf{e}_{zn})e^{-ikz}, \tag{2.28}$$

$$\mathbf{H}_n^-(\mathbf{r}, \omega) = (-\mathbf{h}_n + \mathbf{h}_{zn})e^{-ikz}. \tag{2.29}$$

For absorbing waveguides like the plasmonic waveguides, the sign of the imaginary part of the propagation constant k is chosen appropriately in order to have an evanescent decaying wave in the propagation direction that satisfies causality. The expansion of the fields in terms of the forward and backward propagating modes reads as

$$\mathbf{E}(\mathbf{r}, \omega) = \sum_n \{a_n \mathbf{E}_n^+(\mathbf{r}, \omega) + a_{-n} \mathbf{E}_n^-(\mathbf{r}, \omega)\}, \tag{2.30}$$

$$\mathbf{H}(\mathbf{r}, \omega) = \sum_n \{a_n \mathbf{H}_n^+(\mathbf{r}, \omega) + a_{-n} \mathbf{H}_n^-(\mathbf{r}, \omega)\}, \tag{2.31}$$

here $\mathbf{E}$, $\mathbf{H}$ are the generated electric and magnetic fields, whereas a_n and a_{-n} are modal amplitudes constants, which are zero for backward ($z < 0$) and forward ($z > 0$) propagation directions, respectively. With the help of the Lorentz reciprocity theorem and the use of a density current source $\mathbf{J}(\mathbf{r})$, the different modal amplitudes a_n and a_{-n} can be calculated. Let us remark that a_n and a_{-n} depend on the position and orientation of $\mathbf{J}(\mathbf{r})$ respect to the waveguide. Such current density can be generated by a source that is externally driven, like a classical dipole or a quantum emitter. $\mathbf{E}$ and $\mathbf{H}$ are solutions of the curl Maxwell's equations, and therefore, for a position of the source, they satisfy:

$$\nabla \times \mathbf{E} = i\omega\mu_0 \mathbf{H}, \tag{2.32}$$

$$\nabla \times \mathbf{H} = -i\omega\varepsilon_0\varepsilon\mathbf{E} + \mathbf{J}. \tag{2.33}$$

Now let us consider the following relation between the source-free fields [equations (2.26)-(2.29)] and the fields in presence of a source [equations (2.32) and (2.33)]:

$$\nabla \cdot (\mathbf{E}_n^{\pm} \times \mathbf{H} - \mathbf{E} \times \mathbf{H}_n^{\pm}) = \mathbf{H} \cdot \nabla \times \mathbf{E}_n^{\pm}$$
$$-\mathbf{E}_n^{\pm} \cdot \nabla \times \mathbf{H} - \mathbf{H}_n^{\pm} \cdot \nabla \times \mathbf{E} + \mathbf{E} \cdot \nabla \times \mathbf{H}_n^{\pm} = -\mathbf{J} \cdot \mathbf{E}_n^{\pm} \tag{2.34}$$

where we have made use of the vectorial relation $(\nabla \cdot (\mathbf{a} \times \mathbf{b}) = \mathbf{a} \cdot (\nabla \times \mathbf{b}) - \mathbf{b} \cdot (\nabla \times \mathbf{a}))$. Integrating equation (2.34) over a volume bounded by a surface S, and transforming the volume integral of the divergence to a surface integral by means of Stokes theorem, we arrive to the desired form of Lorentz reciprocity theorem:

$$\oint_S (\mathbf{E}_n^{\pm} \times \mathbf{H} - \mathbf{E} \times \mathbf{H}_n^{\pm}) \cdot \mathbf{n} dS = -\int\int\int_V \mathbf{J} \cdot \mathbf{E}_n^{\pm} \, \mathrm{d}V, \tag{2.35}$$

where $\mathbf{n}$ is the outward normal vector to the surface S. Let us choose the integration volume to be formed by two facets S1 ($z = z1$) and S2 ($z = z2$) parallel to the propagation direction and a surrounding S3 area matching S1 and S2 (see Figure 2.1). There is no contribution from the surface S3 because the mode is confined in the transverse directions at the frequency ω, and we suppose that the transverse area is large enough to make the contributions from the normal guided modes, $\mathbf{E}_n^{\pm}$ and $\mathbf{H}_n^{\pm}$, negligible. For the forward propagating normal modes $\mathbf{E}_n^+$ and $\mathbf{H}_n^+$, equation (2.35) takes the values

$$\int_{S1} (\mathbf{E}_n^+ \times \mathbf{H} - \mathbf{E} \times \mathbf{H}_n^+) \cdot \mathbf{n} \, \mathrm{d}S = 2a_{-n}N_n \tag{2.36}$$

$$\int_{S2} (\mathbf{E}_n^+ \times \mathbf{H} - \mathbf{E} \times \mathbf{H}_n^+) \cdot \mathbf{n} \, \mathrm{d}S = -a_n e^{2ikz_2} + a_n e^{2ikz_2} = 0 \tag{2.37}$$

where $N_n = \int_{S1}(\mathbf{e}_n \times \mathbf{h}_n) \cdot \mathbf{z} \, \mathrm{d}S$ is the normalization of the nth mode, and we have made use of the expansions (2.32)-(2.33) and the Heaviside dependence of a_n and a_{-n} on the propagation direction z. Additionally, in order to derive equations (2.36)-(2.37), we have made use of the most general orthogonality relation $\int_{S1}(\mathbf{e}_n \times \mathbf{h}_m) \cdot \hat{z} \, \mathrm{d}S = 0, (n \neq m)$, which is valid for degenerate and lossy modes, so this derivation so far is valid for absorbing waveguides. For frequencies in which the imaginary propagation constant, $\mathrm{Im}(k)$, is much smaller than the real propagation constant ($\mathrm{Im}(k) << \mathrm{Re}(k)$), the conventional power orthogonality, $\int_{S1}(\mathbf{e}_n \times \mathbf{h}_m^*) \cdot \hat{z} \, \mathrm{d}S \simeq 0, (n \neq m)$, is approximately correct [7] due to the real character of the transverse EM fields. Therefore, the normalization coefficient becomes the
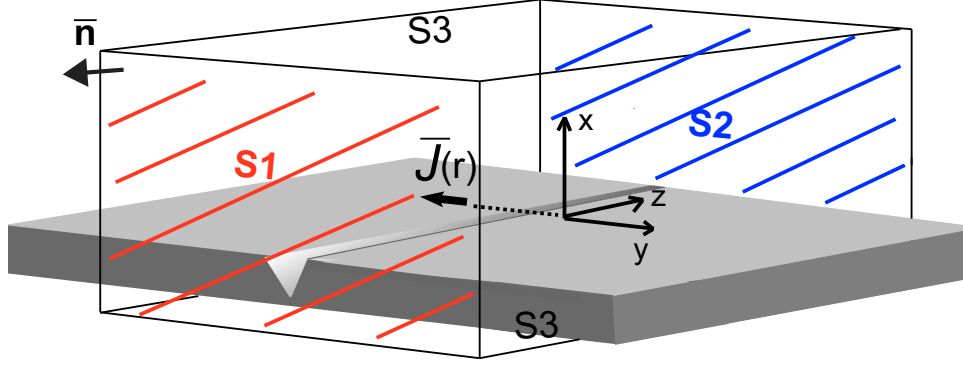
Figure 2.1: S1 (red) backward-propagation surface, S2 (blue) forward-propagation surface, S3 surrounding surface, $\mathbf{J}(\mathbf{r})$ linear current indicated by a black arrow.

Poynting vector integral over the whole transversal area, $N_n \simeq \int_{S1} (\mathbf{e}_n \times \mathbf{h}_n^*) \cdot \mathbf{z} \, dS$. Since the cases $(\text{Im}(k) << \text{Re}(k))$ are the most interesting for using plasmonic waveguides at optical frequencies as mediators of interactions between emitters for separation distances on the order of the wavelength, we will make use of the just mentioned normalization. In addition, if the emitter current density $\mathbf{J}$ is concentrated in an infinitely small filament at $\mathbf{r} = \mathbf{r}_0$, combining (2.36) and (2.35), we obtain

$$a_{-n} = \frac{-\mathbf{J} \cdot \mathbf{E}_n^+}{2N_n}. \tag{2.38}$$

Repeating the analogous steps that were taken from equation (2.36) to (2.38) for the modes $\mathbf{E}_n^-$ and $\mathbf{H}_n^-$, we find:

$$a_n = \frac{-\mathbf{J} \cdot \mathbf{E}_n^-}{2N_n}. \tag{2.39}$$

Once the dependence of a_n and a_{-n} with the source has been deduced, we can calculate the guided Green's tensor, which is defined as the operator which gives the electric field when the contraction $i\omega\mu_0 \mathbf{G}_{guided}(\mathbf{r}, \mathbf{r}', \omega)\mathbf{J}(\mathbf{r}')$ is formed. From the expansion (2.30) and

the coefficients (2.38)-(2.39), we deduce the guided Green's tensor:

$$\mathbf{G}_{guided}(\mathbf{r}, \mathbf{r}', \omega) = -\sum_{n=1}^{\infty} \frac{\mathbf{E}_n(\mathbf{r})\mathbf{E}_n(\mathbf{r}')}{i\omega\mu_0 2N_n}, \mathbf{r} \neq \mathbf{r}' \tag{2.40}$$

where

$$\mathbf{E}_n(\mathbf{r}) = \left\{ \begin{array}{ll} \mathbf{E}_n^+(\mathbf{r}), & z > z' \\ \mathbf{E}_n^-(\mathbf{r}), & z < z' \end{array} \right\} \tag{2.41}$$

and

$$\mathbf{E}_n(\mathbf{r}') = \left\{ \begin{array}{ll} \mathbf{E}_n^+(\mathbf{r}'), & z' > z \\ \mathbf{E}_n^-(\mathbf{r}'), & z' < z \end{array} \right\} \tag{2.42}$$

This modal expansion is valid outside the source region. If the field inside the source region need to be evaluated the term [65]

$$-\frac{\hat{z}\hat{z}}{k_0}\delta(\mathbf{r} - \mathbf{r}'), \tag{2.43}$$

should be added. Since the transverse fields amplitudes are larger than longitudinal ones for the considered waveguides, we will focus on transverse alignments of the sources and consequently this last term does not contribute. If we focus at distances $z > z'$, for a slightly absorbing single plasmonic mode and evaluate the guided Green's tensor (2.40) with (2.26) and (2.28) for transverse source alignments, we obtain:

$$\mathbf{G}_{guided}(\mathbf{r}, \mathbf{r}', \omega) = -\frac{\mathbf{e}_n\mathbf{e}_n e^{ik(z-z')}}{i\omega\mu_0 2N_n}, \tag{2.44}$$

where $N_n = \int_{S1}(\mathbf{e}_n \times \mathbf{h}_n^*) \cdot \hat{z}\, \mathrm{d}S$ as we commented above.

This deduced Green's tensor contribution of the guided modes will be very important to evaluate guided plasmon mediated models for the interaction coefficients in the master equations and resonance energy transfer as we will see in chapter 4. In order to calculate the guided modes $(\mathbf{E}_n(\mathbf{r}, \omega), \mathbf{H}_n(\mathbf{r}, \omega))$, we solve Maxwell's wave equations [either (2.21) or (2.22)] in each domain and impose the appropriate boundary conditions, which turn into an eigenvalue calculation [7]. In general, except for very simple cross-sections, geometrically-complex waveguides support hybrid-modes whose eigenvalue equations are difficult to be solved analytically, if not impossible, and a numerical solving method is required. In order to obtain any waveguide mode, we have made use of numerical methods as we explain in the next subsection in further detail.

2.3 Electromagnetic computational modelling: Finite element method

Before we start describing the finite element method (FEM), in order to set a proper theoretical framework, let us recall some of the standard concepts of mathematical physics

applied to electromagnetism.

2.3.1 Basic aspects of the formulation of boundary-values problems

Certain boundary-value problems in mathematical physics can be expressed by a differential equation defined in a spatial domain, Ω, like

$$\mathcal{L}\phi = f, \tag{2.45}$$

together with the appropriate boundary conditions in the surface S that encloses the domain Ω. In equation (2.45), $\mathcal{L}$ is a general differential operator, f is the forcing term and ϕ the solution of the physical equation. The wave equations (2.21) and (2.22) constitute one of these boundary-value problems, which can provide the solutions of an arbitrary z-translational invariant waveguide or a periodic waveguide applying the suitable boundary conditions, with or without the presence of arbitrary current density sources. In particular for the wave equation (2.21), the operator $\mathcal{L}$ equals $\nabla \times \nabla \times -\frac{\omega^2}{c^2}\varepsilon$, the forcing term is $f = i\omega\mu_0\mathbf{J}_N(\mathbf{r}, t)$, and ϕ is the corresponding electric ($\mathbf{E}$) or magnetic ($\mathbf{H}$) vector field solution. In the following, we make a brief survey of the different boundary conditions that allow to solve such electromagnetic problems [66]:

- **Continuity**
  The continuity of the electric $\mathbf{E}$ and magnetic field $\mathbf{H}$ arise from the curl equations in Maxwell's equations (2.1)-(2.2) in the absence of boundary sources

$$\mathbf{n} \times (\mathbf{E_1} - \mathbf{E_2}) = \mathbf{0}, \mathbf{n} \times (\mathbf{H_1} - \mathbf{H_2}) = \mathbf{0}. \tag{2.46}$$

  These conditions are fulfilled for the tangential components in the boundary between any medium 1 and 2 (with normal vector $\mathbf{n}$).

- **Perfect electric and magnetic conductor**
  The perfect electric conductor (PEC) and the perfect magnetic conductor (PMC) boundaries fulfill

$$\mathbf{n} \times \mathbf{E} = \mathbf{0}, \tag{2.47}$$

  and

$$\mathbf{n} \times \mathbf{H} = \mathbf{0}, \tag{2.48}$$

  respectively. These conditions impose a null value of the EM-field tangential components in the boundary. For example, PEC is fulfilled approximately at low-frequencies in metals [67] whereas PMC in some metamaterials [68].

- **Surface impedance boundary condition**

  The surface impedance boundary condition

  $$\sqrt{\frac{\varepsilon_c}{\varepsilon_1}}\mathbf{n} \times \mathbf{H} + \mathbf{n} \times (\mathbf{n} \times \mathbf{E}) = 0, \tag{2.49}$$

  is used for conductors in which the EM fields are known to penetrate only a short distance in the conductor [67], where ε_c and ε_1 are the complex dielectric functions of the conductor and surrounding materials, respectively. A requirement for this boundary condition to be a valid approximation is that the magnitude of the complex dielectric function of the conductor, ε_c. is much greater than that of the surrounding material, ε_1.

- **Radiative scattering condition**

  The open or free-space boundary condition can be specified [66] by

  $$\lim_{r\to\infty} r\{(\nabla \times \mathbf{E}) + i\frac{\omega}{c}\varepsilon\hat{\mathbf{r}} \times \mathbf{E} = 0\}, \lim_{r\to\infty} r\{(\nabla \times \mathbf{H}) + i\frac{\omega}{c}\varepsilon\hat{\mathbf{r}} \times \mathbf{H} = 0\}, \tag{2.50}$$

  where $r = \sqrt{x^2 + y^2 + z^2}$ refers to the distance from the boundary to the origin, and it has been assumed that the whole system is confined at a finite distance from this latter. Such conditions reflect the fact that free-space propagating electromagnetic fields decay as $1/r$ [66].

- **Port-boundary condition**

  The port boundary condition can be used for terminating an infinite waveguide. Though they do not represent strictly a physical boundary [66], they allow to make the boundary totally non-reflecting for an EM eigenmode solution of the waveguide with propagation constant, k. Additionally, it permits to include such eigenmode as an input electromagnetic source. When E is the dependent variable the matched boundary condition reads

  $$(\nabla \times \mathbf{E}) - ik(\mathbf{E} - (\mathbf{n} \cdot \mathbf{E})\mathbf{n}) = -i2k(\mathbf{E}_0 - (\mathbf{n} \cdot \mathbf{E}_0)\mathbf{n}), \tag{2.51}$$

  where $\mathbf{E}_0$ refers to the electric field of the eigenmode wave source. The correspondent equation when H is the dependent variable has the same form as equation (2.51) but exchanging the roles of $\mathbf{E} \leftrightarrow \mathbf{H}$ for both the source and total fields.

In principle we can deal with any electromagnetic problem with the above boundary conditions. However, it is very convenient to use an additional artificial bulk material which largely improves the free-radiation conditions of unbounded and bounded modes. Such materials have been introduced in 1994 by Berenger [69] with the name of *perfectly matched*

layers or simply PML, and the basic idea of such materials is to make them absorbing and totally non-reflecting for any incident EM mode. The PML can be understood as absorbing uniaxial materials or metamaterials, whose properties can be deduced through a conformal mapping from complex coordinates $\mathbf{r}'$ to real coordinates $\mathbf{r}$ by means of the following transformation

$$\tilde{x} = \int_0^x s_x(x') \, \mathrm{d}x', \tag{2.52}$$

$$\tilde{y} = \int_0^y s_y(y') \, \mathrm{d}y', \tag{2.53}$$

$$\tilde{z} = \int_0^z s_z(z') \, \mathrm{d}z'. \tag{2.54}$$

Using such mapping, we obtain the following transformation of the differentials

$$\frac{\partial}{\partial \tilde{x}} = \frac{1}{s_x(x)} \frac{\partial}{\partial x}, \tag{2.55}$$

$$\frac{\partial}{\partial \tilde{y}} = \frac{1}{s_y(y)} \frac{\partial}{\partial y}, \tag{2.56}$$

$$\frac{\partial}{\partial \tilde{z}} = \frac{1}{s_z(z)} \frac{\partial}{\partial z}, \tag{2.57}$$

which transform Maxwell's equations in complex coordinates, for a homogeneous material, and in the absence of sources, to

$$\nabla_s \times \mathbf{E} = i\omega\mu \cdot \mathbf{H}, \tag{2.58}$$

$$\nabla_s \times \mathbf{H} = -i\omega\varepsilon \cdot \mathbf{E}, \tag{2.59}$$

$$\nabla_s \cdot (\varepsilon \cdot \mathbf{E}) = 0, \tag{2.60}$$

$$\nabla_s \cdot (\mu \cdot \mathbf{H}) = 0, \tag{2.61}$$

where $\nabla_s = \frac{1}{s_x(x)} \frac{\partial}{\partial x} + \frac{1}{s_y(y)} \frac{\partial}{\partial y} + \frac{1}{s_z(z)} \frac{\partial}{\partial z}$. Due to the resemblance of equations (2.58)-(2.61) with those for an uniaxial material [66], the above-mentioned coordinate transformation can be associated to a dielectric and permeability tensor by comparison between both system of equations. For an uniaxial material, those Maxwell equations are identical by exchanging ∇_s by ∇, and exchanging the regular values of ε and μ in (2.58)-(2.61) with tensors $\tilde{\varepsilon}$ and $\tilde{\mu}$, respectively and adding some new constitutive relations. Performing such equivalency, we can find that such tensors have the form [66]

$$\tilde{\varepsilon} = \varepsilon\Lambda, \tag{2.62}$$

$$\tilde{\mu} = \mu\Lambda, \tag{2.63}$$

in which

$$\Lambda = \bar{x}\bar{x}\left(\frac{s_y s_z}{s_x}\right) + \bar{y}\bar{y}\left(\frac{s_z s_x}{s_y}\right) + \bar{z}\bar{z}\left(\frac{s_x s_y}{s_z}\right), \tag{2.64}$$

Moreover, the constitutive relations $E_j^u = s_j E_j^s, j = x, y, z$ and $H_j^u = s_j H_j^s, j = x, y, z$ are applied, in which the magnitudes with upper index s fulfil equations (2.58)-(2.61) and those with the index u fulfil the equations for the uniaxial material. The importance of the transformations (2.55)-(2.57) is that any plane wave coming from a homogeneous medium, reflecting in the boundary of the PML, has its reflection coefficients equal to zero for an arbitrary angle of incidence (respect to the boundary normal vector) [66]. This condition is fulfilled for any frequency. In addition, for complex values of the values s_x, s_y and s_z, the wave propagating in the PML is evanescent and therefore we can truncate the domain of simulation with the boundary conditions (2.50) or (2.47) for large enough domains of PML's. The PML behaviour is in contrast to the scattering boundary conditions (2.50) since their performance to arbitrary wave-fronts is largely better [66], and the artificial reflections can be made negligible for any wavelength without the restrictive condition $\lim_{r \to \infty}$ in (2.50).

2.3.2 General steps of the finite element method

In contrast to waveguides with simple geometries, the electromagnetic solutions for arbitrary cross-sections waveguides is a non-trivial analytical task. Such is typically the case for most of the plasmonic or periodic waveguides considered in this thesis. Therefore, in order to calculate those solutions, we need to make use of computational methods which allow us to obtain a precise numerical solution. In particular, we have focused on the use of the FEM, which is a well-developed numerical approach for solving electromagnetic problems [66]. The idea behind the method is to convert the resolution of a continuous partial differential equation (2.45) into a problem that has a finite number of unknown variables, *i.e.*, a discretization of the original problem. The main basic steps for the method can be listed in the following manner:

- Discretization or subdivision of the domain

- Selection of the interpolation functions

- Formulation of the system of equations

- Solution of the system of equations

In the following we explain in more detail the basics of those general steps, based on reference [66], and the particular approaches adopted through the use of the commercial software COMSOL Multiphysics. Finally, in subsection 2.3.3, we comment about the particular models and details for the computations of the electromagnetic simulations considered in this thesis.

Discretization or subdivision of the domain

The discretization of the domain Ω is the first and one of the most important steps in the FEM, due to the fact that it affects the computer storage requirements, computational time, and the accuracy of the numerical results. In this step, the full domain Ω is divided (or meshed) in small domains $\Omega^e(e = 1, ..., M)$, which are referred as *elements* and they are labeled by the subscript e, where M is the total number of them. For two dimensional domains we have made use of triangles, whereas for three dimensional domains we have generated tetrahedra (see Figure 2.2), since both of them are the most suited for irregular domains. The element election is also connected to the expansion of the solutions and the formulation of the problem, which are done in terms of its nodes or segments. For implementation purposes, each segment or node in an element is described by its coordinate values, local and global number. The local number indicates its position in the element, whereas its global number describes its position in the entire domain. Logically, there is a linear transformation which transfer from local and global number.

The stage of meshing is a preprocessing step since it must be generated before the system of equations can be set up. In order to generate accurate meshes, there are basic tips based on the discrete spatial Fourier theory, which are shared by other similar computational methods [70] and that quantify the minimum number of discrete elements to describe the main physics. The mesh details for the particular electromagnetic models considered in this thesis are explained at the end of this section, in subsection 2.3.3.
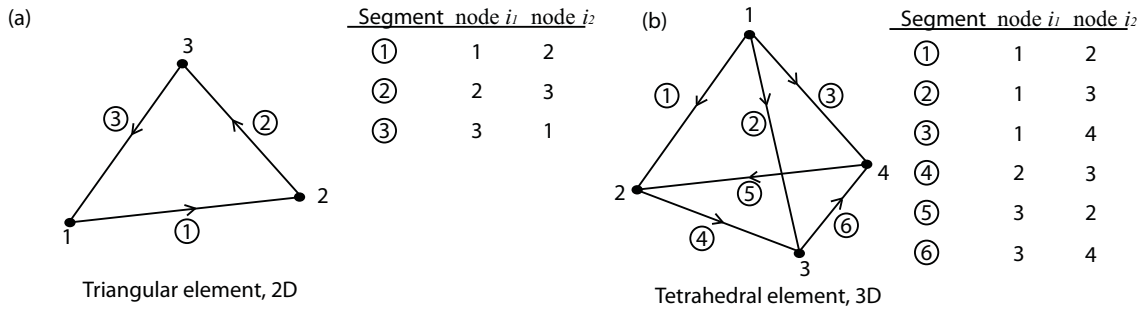
Figure 2.2: Triangular element [panel(a)] and tetrahedral element [panel(b)] with their nodes and segments labeling.

Selection of the interpolation functions

The next step in the FEM is the selection of an interpolation function that provides an approximation of the unknown solution within an element. Typically higher-order polynomial can be used and in particular we have made use of the second-order approximation (quadratic), which showed accurate-enough solutions for the quantities considered in this

thesis. In most of the FEM approaches, the unknown solution is expanded in terms of interpolating functions at the nodes associated with the elements generated in the previous meshing stage (see Figure 2.2), *e.g.*, in the case of using Lagrange elements [66]. Such elements impose continuity of the functions in the whole domain of simulation Ω. However, for electromagnetic problems like the one involved in equations (2.21) and (2.22), it is wiser to formulate the problem in terms of the segments of the triangles and the tetrahedra instead of doing it at the nodes [66]. Such approach known as *vector elements* or *Nedelec elements*. Compared to node-based elements approaches, there are significant improvements with the use of the vector elements [66], such as: the elimination of spurious solutions from the automatic imposition of the divergence equations (equations (2.3) and (2.4)), the convenience to impose boundary conditions at material interfaces, and the easiness to treat field singularities at material corners and edges. These advantages come from the formulation of the expansion in vector elements and their associated properties as we detail next. We particularize to the expansion of the electric field in the vector element approach, though the expression for the magnetic field is analogous.

In general, the approximate expression for the unknown electric vector field solution $\tilde{\mathbf{E}}$ in an element, labeled e, is written as:

$$\tilde{\mathbf{E}}^e = \sum_{j=1}^{n} \mathbf{N}_j^e \tilde{E}_j^e = \{\mathbf{N}^e\}^T \{\tilde{E}^e\} = \{\tilde{E}^e\}^T \{\mathbf{N}^e\}, \tag{2.65}$$

where n is the number of segments (or nodes in Lagrange elements) in an element, $\tilde{E}_j^e$ is the tangential value of the solution $\tilde{\mathbf{E}}^e$ at the j segment, and $\mathbf{N}_j^e$ is the interpolation function at segment j, which is also known as the expansion or basis function. The symbol $\{\}$ denotes a column vector, whereas the superscript T denotes the transpose of the vector. We first focus on the first-order expansion which has a more intuitive introduction and we briefly discuss the extension to the second-order at the end of this subsection.

For first-order approximation, a triangle has a number of segments $n = 3$, whereas for the tetrahedra $n = 6$, as displayed in Figure 2.2. In the vector element approach the basis function $\mathbf{N}_j^e$ at first order, in both triangles and tetrahedra, are chosen such that:

$$\mathbf{N}_j^e = \mathbf{W}_{j_1, j_2} \ell_j^e = \{L_{j_1}^e \nabla L_{j_2}^e - L_{j_2}^e \nabla L_{j_1}^e\} \ell_j^e, \tag{2.66}$$

where $L_{j_1}^e$ is a linear interpolation function that equals 1 at the initial node j_1, and 0 at the final node j_2 of the segment j, where both j_1 and j_2 values are defined as shown in Figure 2.2. The scalar term ℓ_j^e is simply the length of the j segment. The properties of the linear

vector functions $\mathbf{W}_{j_1,j_2}$ are the key point of the definition (2.66), since [66]:

$$\nabla \mathbf{W}_{j_1,j_2} = 0, \tag{2.67}$$

$$\nabla \times \mathbf{W}_{j_1,j_2} = 2\nabla L_{j_1}^e \times \nabla L_{j_2}^e, \tag{2.68}$$

$$\mathbf{e}_j \cdot \mathbf{W}_{j_1,j_2} = \frac{1}{\ell_j^e}, \tag{2.69}$$

where $\mathbf{e}_j$ is the vector along the j edge direction. We can observe from the property (2.69) together with equation (2.66) the constant value of the j tangential electric field component, which guarantees the tangential continuity along the edge j in triangles or also along the faces that contains an edge on a tetrahedra. Consequently, the vector element permits to characterize easily any boundary material condition since the tangential components of the electromagnetic fields are always continuous with this basis. Moreover, the tangential character of the fields with this expansion eliminates the problem of the singularities, since these are associated to the normal component of the fields, which are zero in the segments (or the facets in 3D). We can also observe from the property (2.67) that the zero divergence of the fields [equations (2.3)-(2.4)] is naturally imposed. Therefore, such property eliminates the appearance of spurious solutions of the EM modes associated to the failure of the divergence condition [66].

The vector elements commented so far in both two and three dimensions are complete to first-order. These elements have a rather poor convergence, *i.e.*, their solution approaches the exact one slowly as the mesh is refined. In order to have better convergence, we have made use of second-order vector elements. We briefly comment below the extension to this higher order approximation in order to obtain the fundamental idea and differences with the first order expansion. To extend the previous basis to second-order, either in 2D or 3D, the first-order basis (2.66) has to be multiplied basically by an interpolation function of second-order [66]. A consequence of the second-order basis, is that the polynomial has evaluation points at the interior of the element. For example, for 2D, in addition to the points in the edges, there are points in the inner part of the triangle area. For 3D, such evaluation points also appears inside the volume of the tetrahedra. Due to the definitions of the second-order basis from the linear basis (2.66), the points evaluated at the surface keep imposing naturally the continuity of the tangential vector fields along different subdomains. For the points inside the tetrahedron volume, the points have tangential and normal-to-surface components, which permit the satisfaction of the boundary conditions for different material subdomains, *i.e.*, discontinuity of normal components at the interface.

Formulation of the system of equations

Once the mesh has been generated and the interpolation functions have been chosen, we need to formulate the full system of equations to solve it in terms of the previous discrete expansion. The method that we have made use is based on the Galerkin's method that we detail below [66].

Galerkin's method belongs to the family of weighted residual methods, which, as the name indicates, seek the solution by weighting the residual of the differential equation. Assume that $\tilde{\phi}$ is an approximate solution to general differential equation (2.45). The substitution of $\tilde{\phi}$ for ϕ in (2.45) would then result in a nonzero residual

$$r = \mathcal{L}\tilde{\phi} - f \neq 0, \tag{2.70}$$

and the best approximation for $\tilde{\phi}$ will be the one that reduces the residual r to the minimum value at all i points of the domain Ω. Within this idea, weighted residual methods enforce the condition

$$R_i = \int_\Omega w_i r \, d\Omega = 0, \tag{2.71}$$

where R_i denote the weighted residual integral and w_i are the chosen weighting functions.

In Galerkin's method, the weighting functions are selected to be the same as those used for expansion of the approximate solution. This usually leads to the most accurate solution and is therefore a popular approach in developing finite element equations. Therefore, applied to the FEM, such weighting functions corresponds to the element linear basis (2.66) in first-order approximation (or additionally for second-order, multiplied with the additional interpolation function as commented in the previous subsection). For equation (2.45), the weighted residual for the eth element is

$$R_i^e = \int_{\Omega^e} \mathbf{N}_i^e (\mathcal{L}\tilde{\mathbf{E}}^e - f) \, d\Omega = 0, \quad i = 1, 2, 3, ...n. \tag{2.72}$$

where n refers to the number of nodes and/or segments in the element. Substituting (2.65) into (2.72) yields

$$R_i^e = \int_{\Omega^e} \mathbf{N}_i^e \mathcal{L} \{\mathbf{N}^e\}^T \{\tilde{E}^e\} \, d\Omega - \int_{\Omega^e} \mathbf{N}_i^e f \, d\Omega = 0, \quad i = 1, 2, 3, ...n. \tag{2.73}$$

which can be written in matrix form as

$$\{R^e\} = [K^e]\{\tilde{E}^e\} - \{b^e\}. \tag{2.74}$$

Here $\{R^e\} = [R_1^e, R_2^e, ..., R_n^e]^T$ is the residual vector for the element e. $[K^e]$ and $\{b^e\}$ are a $n \times n$ matrix and a $n \times 1$ vector, respectively, which elements are given by

$$K_{ij}^e = \int_{\Omega^e} \mathbf{N}_i^e \mathcal{L} \mathbf{N}_j^e \, d\Omega, \tag{2.75}$$

$$b_i^e = \int_{\Omega^e} \mathbf{N}_i^e f \, d\Omega. \tag{2.76}$$

Since the expansion, and therefore the weighting function associated with the ith segment (or node in Lagrange elements), includes all the other elements directly connected to i, the weighted residual R_i associated with the ith segment (or node) is a summation over the elements directly connected to it. Therefore we may expand (2.74) using the linear transformation between local and global numbers, and then sum for each element like

$$\{R\} = \sum_{e=1}^{M} \{\overline{R}^e\} = \sum_{e=1}^{M} ([\overline{\overline{K}}^e]\{\tilde{\overline{E}}^e\} - \{\overline{b}^e\}), \tag{2.77}$$

where M is the total number of elements in the whole domain Ω. The overline refers to the fact that the previous matrix and vectors have been expanded or augmented. To be specific, $[\overline{\overline{K}}^e]$ has been expanded or augmented (by zero filling) from $[K^e]$ to a $N \times N$ matrix using the relation between local and global numbers, where N is the total number of unknowns or segments. Analogously, $\{\overline{b}^e\}$ is expanded from $\{b^e\}$ to a $N \times 1$ vector. Such summation over all the elements is commonly known as assembly. The full system of equations can then be obtained by setting (2.77) to zero resulting in

$$\sum_{e=1}^{M} ([\overline{\overline{K}}^e]\{\tilde{\overline{E}}^e\} - \{\overline{b}^e\}) = \{0\}, \tag{2.78}$$

which can be written in a matrix form as

$$[K]\{\tilde{\mathbf{E}}\} = \{b\}. \tag{2.79}$$

Before (2.79) can be solved for a specific problem, we need to apply the required boundary conditions at the surface S of the whole domain Ω, *e.g.*, any of the conditions displayed from (2.46) to (2.51).

Solution of the system of equations

Solving the system of equations (2.79) is the final step in a finite element analysis. The resulting system has one of the following forms:

$$[K]\{\tilde{\mathbf{E}}\} = \{b\}, \tag{2.80}$$

or

$$[A]\{\tilde{\tilde{\mathbf{E}}}\} = \lambda[B]\{\tilde{\tilde{\mathbf{E}}}\}. \tag{2.81}$$

Equation (2.80) is of deterministic type, resulting from either a force-term in a differential equation or a port boundary conditions or both. In electromagnetics, deterministic systems are usually associated with scattering, radiation and other problems where it exists

a source of excitation. On the contrary (2.81) is of eigenvalue type, resulting from a homogeneous governing differential equation and homogeneous boundary conditions. This case corresponds to wave propagation in waveguides and resonances in cavities. In this case, the known vector $\{b\}$ vanishes and the matrix $[K]$ can be written as $[A] - \lambda[B]$, where λ is an eigenvalue that is complex in general.

Once we have solved the system of equations for the electric $\{\tilde{\mathbf{E}}\}$ (or equivalently for the magnetic field $\{\tilde{\mathbf{H}}\}$), we can compute all the desired parameters, such as complex propagation constants, scattering or radiation patterns, energy flow, etc. Then we can display them in the form of plots or contour plots which are more meaningful and interpretable. This final stage, often referred to as postprocessing, can also be separated from the previous steps.

All the previous steps have being performed using the commercial program COMSOL Multiphysics. The details of this implementation can be further read in reference [71].

2.3.3 Specific waveguide modelings

In this subsection we describe the methodology to construct the models used with the FEM for the simulation of EM fields in the structures considered in this thesis. The emphasis is made on the modeling aspects while the analysis of the corresponding physics will be described in the following chapters.

Translational invariant waveguide mode calculations

In order to calculate the modes of a z-translational invariant plasmonic waveguide, we have made 2D simulations with the FEM, solving equation (2.21) in the absence of sources (or alternatively (2.22)) and for a certain wavelength λ. Such problem correspond to an eigenvalue problem as the one discussed in equation (2.81), where the eigenvalue represent the propagation constant, k, of a specific EM mode supported by the waveguide. Due to the z-translational invariance of the waveguides, the program solves the electric and magnetic fields using the modal decompositions used in (2.26) and (2.27), which allow the simulations to be done in a 2D domain. The full domain of the structure was divided in small subdomains, including the cross-section of the waveguide, and each one is described with the dielectric constant of the simulated materials from appropriate databases [72–74]. One example of the typical domains and subdomains used for the simulations is displayed in Figure 2.3. The size of the simulation domain was of the order of several free-space wavelengths, for avoiding the interaction of the outer boundaries of the domain with the natural modes of the waveguide. Consequently, the choice of either perfect conductor (2.47) or scattering boundary condition (2.50) boundary conditions turned into negligible differences, *i.e.*
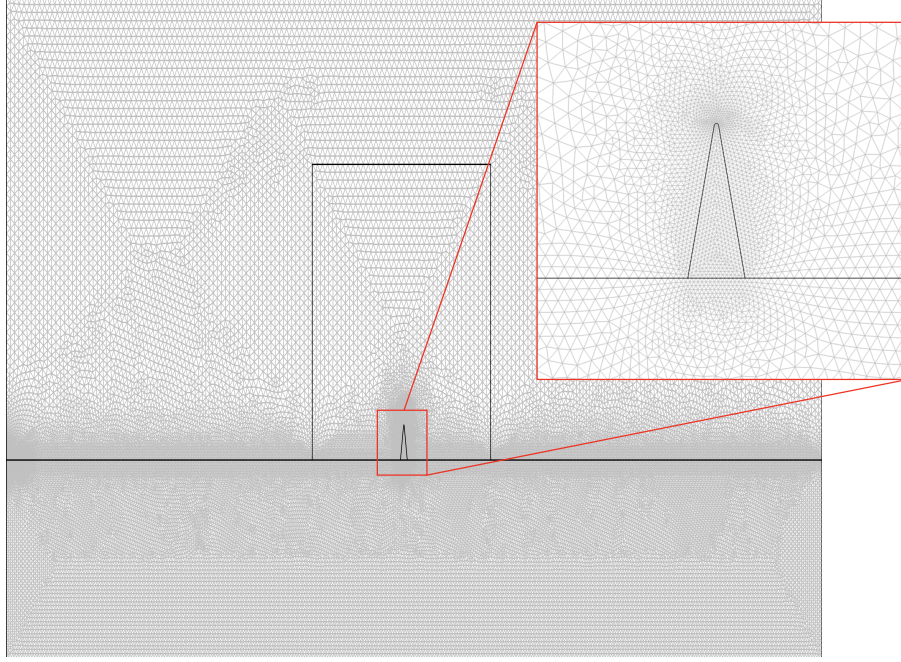
Figure 2.3: Bidimensional domain of the simulation with the cross-sections of the waveguide and the generated mesh. Inset: Zoom of the waveguide close to the surface.

below 1% in the propagation constant.

In order to assemble the system of equations, non-uniform meshes were generated as shown in Figure 2.3. The diversity of the element sizes were chosen to account for the physics of the waveguide modes. For a proper characterization of the EM field close to the metal, the typical maximum element size was of the order of $\lambda/100$ close to the metallic boundary (see the inset of Figure 2.3). Such element size allows to account for the large spatial EM field variations inside the metal (skin depth) and close out of it. Additionally, since the waveguide electromagnetic fields are concentrated at a bounded region of the order of the wavelength, the variation and relevance of these fields are smaller at distances outside that region. Therefore the maximum element size was enlarged gradually to $\lambda/10$ for far distances ($\gtrsim \lambda$) which allows describing the EM field variations without sacrificing computational time and accuracy. The generated meshes with the above prescriptions provided a precision below 1% for the calculated propagation constant, and they involved on the order of one million degrees of freedom.

In order to compare the typical results obtained within this type of models, we compare the results with another well-established numerical tool like the Multiple Multipole method [75]. This method is based on the expansion of the electromagnetic solutions in terms of multipolar functions and it is considered to be semi-analytic. In particular, we compare the
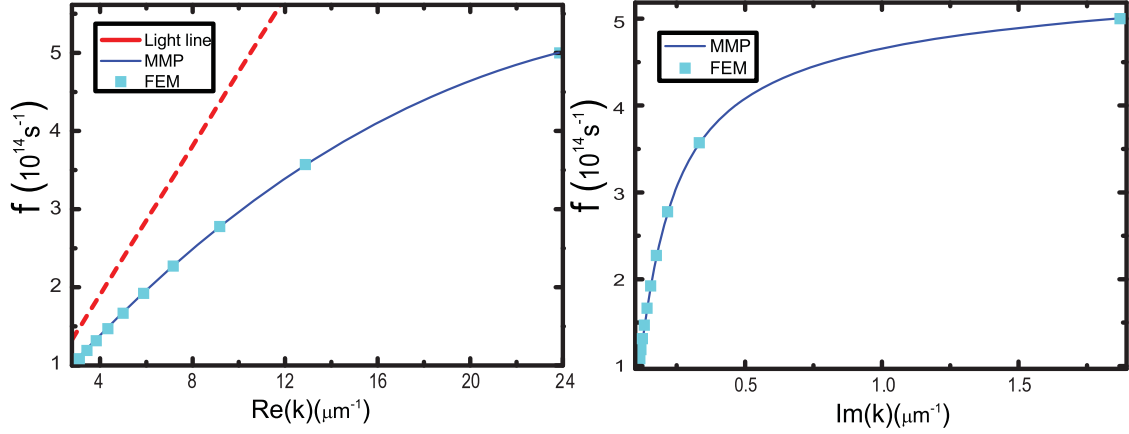
Figure 2.4: Panel (a), Frequency versus real part of the complex propagation constant K of a cylindrical plasmonic waveguide obtained from a FEM calculation (cyan points), and the MMP calculation (blue line). Panel (b), represents the frequency versus the imaginary part of K with the same legend parameters and structure as in panel (a).

results of the complex propagation constant k obtained from both methods, for a cylindrical waveguide of radius 20 nm and characterized by the same gold dielectric constant [74]. This permits to perform a consistent comparison between both methods and a exigent test, since the propagation constant completely characterizes the eigenmode solution, *i.e*, the modal confinement and the EM fields penetration in the metal. In Figure 2.4 it is represented the frequency versus both, the real [panel (a)] and the imaginary part [panel (b)] of the propagation constant at optical and telecom wavelengths. We can observe how their values differ less than 1% between both methods and for all dispersion points. The resulting accuracy in both figures is representative of the well characterization of the cylindrical mode. This conclusion is reasonable to be extensible to all the modes considered in this thesis, in which the above-mentioned convergence criteria with the mesh refinement is followed.

Periodic waveguide mode calculation and harmonic propagation in periodic devices

In our analysis of periodic waveguides, two kind of simulations have been performed. For the computation of band structures, an eigenfrequency problem of the kind (2.81) is studied in a single 3D unit cell, with Bloch boundary conditions in the propagation direction and scattering boundary conditions in the transverse boundaries. The Bloch boundaries imposes a phasor e^{ikd}, where k is the propagation wavenumber which is specified, d is the periodicity set by the cell size in the propagation direction, and the resulting eigenvalue is

a frequency with a complex value, in general. By energy conservation, the imaginary part of the frequency can be translated linearly into a more intuitive imaginary propagation constant through the group velocity [2].

For device modeling (tapers, beam-splitters, etc..), the excitation of the corresponding scattering problem is provided by Port boundary conditions, the ports being fed by the solutions of the corresponding eigenvalue problem. Open space is mimicked with PML [66] or/and scattering boundary conditions whereas the end of the devices were terminated in PML.

In both kind of simulations, the waveguide material properties were assigned in 3D domains with the materials from appropriate databases [72–74]. In addition, the transversal lengths of the whole domain (perpendicular to the periodicity direction) were several wavelengths in size in order to avoid the influence of the external boundaries in the guided modal properties.

Due to the various length scales involved in the physical problem, highly non-uniform meshes are used. In order to ensure an adequate representation of the electromagnetic fields, the size of the elements is a fraction of the skin depth inside the metallic parallelepipeds, a fraction of the characteristic geometric dimension (*e.g.*, a, see the insets of Figure 2.5) in the neighborhood of the structure, and a fraction of the operating wavelength at the boundaries of the simulation domain. The final mesh is different for each simulation, but typical values of the tetrahedra sizes in different regions of the simulation domain are of the order of $1/5$ of the skin depth or characteristic geometric dimension, and $1/10$ of the wavelength. The mesh size is refined until the results are stable with an accuracy of 1%. For instance, in the case of band structure computations, the convergence criterium is based on the value of both the real and imaginary parts of the frequency.

For periodic spoof-plasmonic modes with PEC conditions, we can compare the FEM dispersion results with the semi-analytical results from a modal expansion technique [76]. The modal expansion basically expresses the electromagnetic solutions as a sum of incident plane waves in the different regions of the periodic structure. In Figure 2.5(a) we compare the results between both methods for a groove periodic structure with periodicity d, depth $h = 1.7d$ and aperture $a = 0.1d$, using the formula from reference [76]. In spite of the very different approach of the methods we can see that the qualitative behaviour is good for the lowest order approximation in the modal expansion and quantitatively very good if we take into account a higher order approximation.

In order to check the consistency of the calculated propagation losses, we compare the FEM results obtained through an eigenmode calculation in a Bloch cell, and through a scattering problem as the one used for device modeling. The metal losses are taken into account with surface impedance boundary conditions for the dielectric constant of aluminium [73]. In
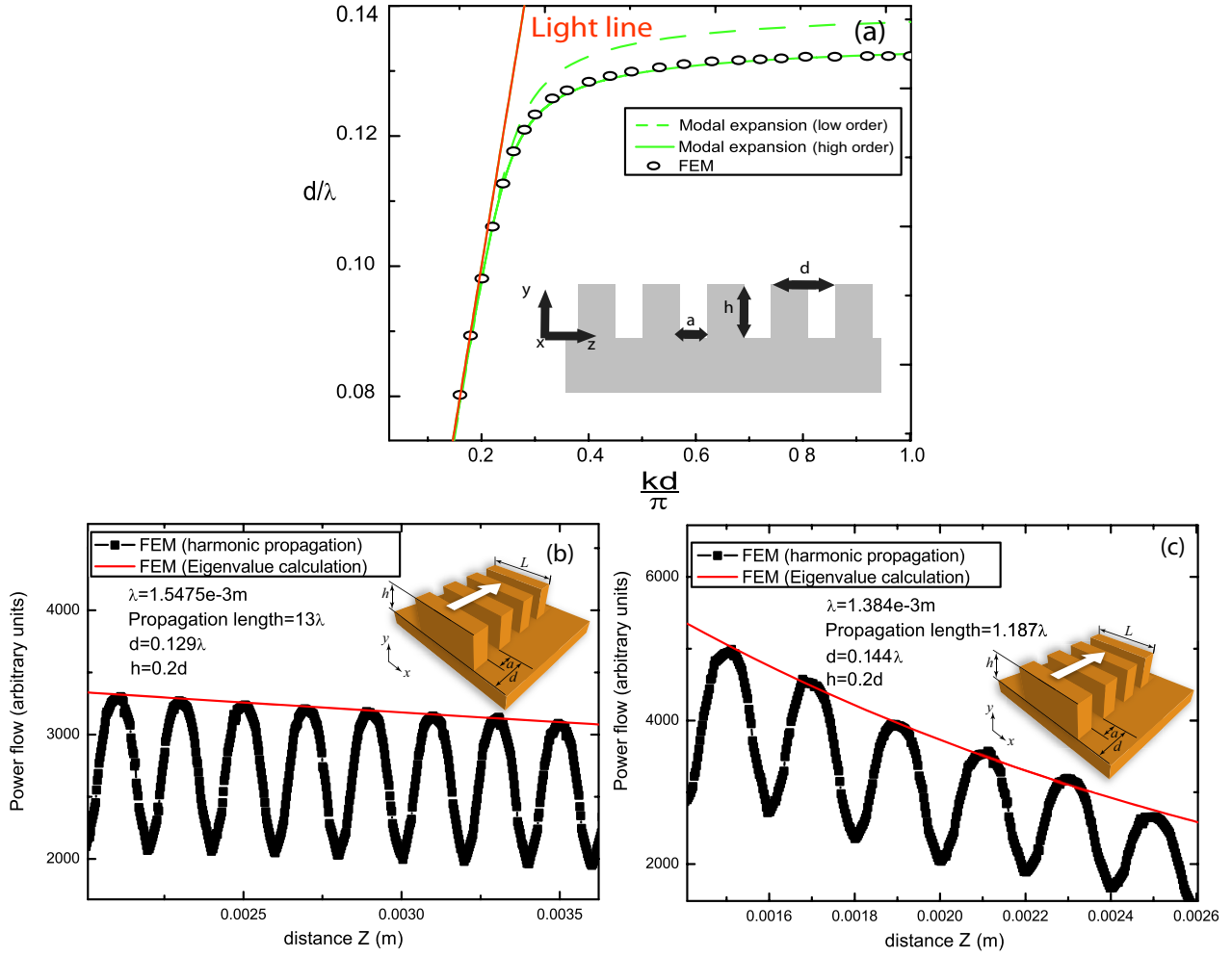
Figure 2.5: Panel (a) Frequency versus the propagation constant k of a groove structure obtained from a FEM calculation (black square points), and a modal expansion calculation for low diffraction orders (dashed green line) using the height resonating in the groove, h, in the formula of reference [76], and using the height effectively resonating in the groove, $h + a/2$, due to the finite size of the hole (green line). Inset: Cross-section of the grooves array along the propagation direction. Panel (b) and (c) represents the Poynting vector norm (interconnected black squares) along a straight section for a domino chain with periodicity $d = 200\,\mu$m, $L = a = 0.5d$ and $h = 1.5d$ (see the inset for a sketch with the defining parameters). The line crosses along the propagation Z-direction and the reflection symmetry plane, and it lies above above the teeth for a distance $h = 0.1d$. The red line represents an exponential decaying function with the decay constant obtained from a Bloch-cell eigenvalue with the same structural parameters.

particular, we compare the power flow decay in a periodic array of metallic parallelepipeds, with period $d = 200\,\mu$m, waveguide width $L = 0.5d$ and $a = 0.5d$ (see Figure 2.5 panels (b) and (c)). Since different wavelengths have different regimes of confinement, we have focused on two particular wavelengths, one in which the propagation length is long (13λ, panel (b)) and the other one in which is small ($\sim 1\lambda$, panel (c)). In both panels, we have represented the Poynting vector norm (black square-dots line) along a line in the periodicity direction and slightly above the parallelepipeds obtained from a scattering problem. Additionally, we have represented an exponential (red line) with its decay constant extracted from the eigenvalue calculation, and its amplitude fitted to the amplitude maximum of the scattering problem. Apart from tiny deviations arising from the reflections in the PML, it can be observed that the decay of the amplitude is very similar between the two kind of calculations in both panels. This agreement shows that the consistency between these two different calculations is very good.

Electric-point dipole emission in 3D domains

The emission of an electric point dipole, with dipolar moment $\mathbf{d}$ in the point $\mathbf{r}_0$, corresponds to the solution of the wave equation (2.21) with a linear harmonic current $\mathbf{J}_N(\mathbf{r}, \omega) = -i\omega\mathbf{d}\delta(\mathbf{r} - \mathbf{r}_0)$ [47]. In order to compute the electromagnetic fields excited by such dipolar source with the FEM, a point dipole is modeled as an element of length l, with a current intensity I_0, and orientation given by the unit vector $\mathbf{n}$. The associated dipole moment for such linear current is [77] $\mathbf{d} = (iI_0l/\omega)\mathbf{n}$ and the length l is kept very short in comparison with the emission wavelength ($l \sim \lambda/330$) to satisfy the dipole approximation. For simulating the different materials, the subdomains are specified by the corresponding dielectric constants and, in order to simulate infinitely long plasmonic waveguides, the spatial domain of interest is properly terminated with PML [66]. The size of the simulation domain is of the order of $30\lambda^3$ (approximately with similar dimensions in each direction), which permits to avoid the interaction of the transversal boundaries with the propagation of the plasmonic modes. A non-uniform mesh is employed where the typical element sizes are chosen to satisfy the following criteria: $\sim \lambda/300$ in the dipole neighborhood, $\sim \lambda/40$ at the waveguide metal interfaces, $\sim \lambda/12$ at the planar metal interface surrounding the channel, and $\sim \lambda/4$ in vacuum away from the source. This kind of generated meshes typically involve on the order of one million degrees of freedom. In order to check the accuracy of the results, the mesh element sizes has been refined until the extracted electric field is stable with an accuracy of 1%.

Let us compare the explained tools for modeling an electric-dipole in the point approximation with a semi-analytical normal mode expansion, expressed in terms of the reflection
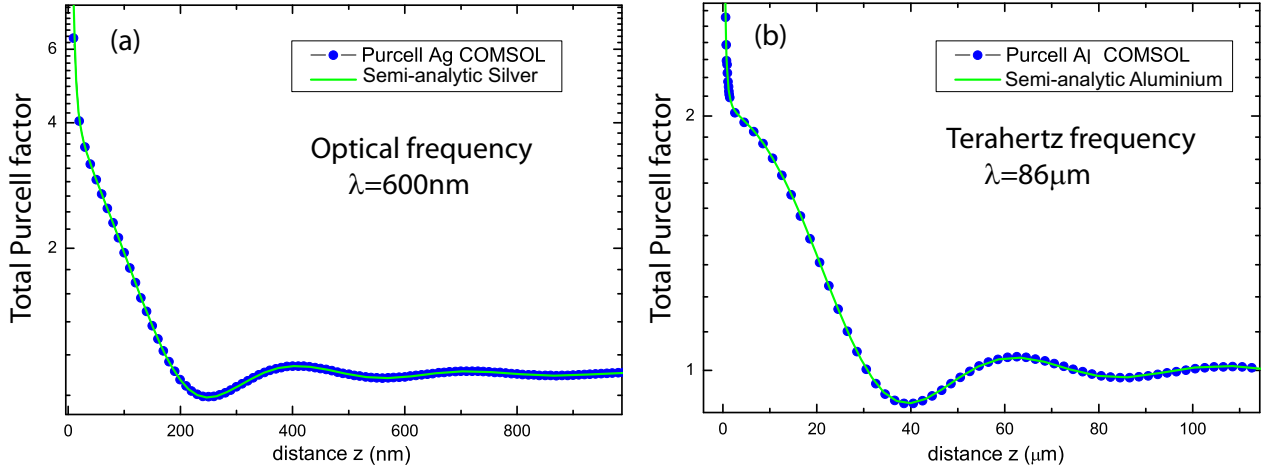
Figure 2.6: Panel (a) and (b) Purcell factor for an emitter placed above a semi-infinite metallic region versus the emitter-to-surface separations, obtained from a FEM calculation (blue dots), and a semi-analytical calculation (green line). In panel (a) the silver properties from reference [72] are used, whereas in panel (b) the aluminium properties from reference [73] are taken.

coefficients [10, 78], for a flat metallic surface. In particular, we compare the total Purcell factor, *i.e.*, the total power dissipated by the dipole in the presence of the inhomogeneous medium (metallic-air surface) divided by the one in the homogeneous hosting medium (air). In order to check the accuracy, we present the Purcell factor for different dipole-to-surface distances, and two different wavelengths of emission: an optical wavelength [$\lambda = 600\,\mathrm{nm}$, panel (a)] and a terahertz one [$\lambda = 86\,\mu\mathrm{m}$ panel (b)]. As explained with further details in chapter 4, the election of these two frequencies are relevant since the surface plasmons at a flat metallic surface are only highly confined at optical wavelengths. Therefore both frequencies are a strong test for the different emitting channels, *i.e.* free-space radiation, surface plasmon radiation, and non-radiative excitations originating from the imaginary part of the metal [10]. Any artificial reflection from the perfect matching layers terminating the simulation box, or a bad characterization of the mesh, would turn into large variations of the Purcell effect, specially for the predominant emitting channel. We can observe that the differences between both methods for any distance and both regimes are less than 1% and therefore the agreement is excellent.

2.4 Macroscopic Quantum Electrodynamics

2.4.1 Field quantization. Electromagnetic Hamiltonian

In this section we depart from the pure classical description of the electromagnetism and we start describing the quantum electrodynamical effects. In order to quantize the macroscopic Maxwell equations, we make use of the quantization of the sources and fields, following reference [64]. The continuous set of complex fields $\mathbf{J}_N(\mathbf{r}, \omega)$ or equivalently $\mathbf{P}_N(\mathbf{r}, \omega)$ in equation (2.21) can be regarded as playing the role of a set of dynamical variables of the overall system, which is composed of the electromagnetic field and the medium (including the dissipative system). It is convenient to write such dynamical variable in the following form

$$\mathbf{P}_N(\mathbf{r}, \omega) = i\sqrt{\frac{\hbar \varepsilon_0 \varepsilon''}{\pi}} \mathbf{f}(\mathbf{r}, \omega), \tag{2.82}$$

where $\mathbf{f}(\mathbf{r}, \omega)$ is the fundamental dynamic variable and ε'' is the imaginary part of the dielectric constant (2.20). The transition from classical to quantum theory consists in the replacement of the classical fields $\mathbf{f}(\mathbf{r}, \omega)$ and $\mathbf{f}^*(\mathbf{r}, \omega)$ by the operator-valued bosonic fields $\hat{\mathbf{f}}$ and $\hat{\mathbf{f}}^\dagger$, respectively. Such operators are associated with the elementary excitations of the composed system within the framework of linear light-matter interaction. Thus the commutation relations for the components of the dynamical variables are

$$[\hat{f}_k(\mathbf{r}, \omega), \hat{f}_{k'}^\dagger(\mathbf{r}', \omega')] = \delta_{kk'} \delta(\mathbf{r} - \mathbf{r}') \delta(\omega - \omega') \quad , \tag{2.83}$$

$$[\hat{f}_k(\mathbf{r}, \omega), \hat{f}_{k'}(\mathbf{r}', \omega')] = 0 \qquad , \tag{2.84}$$

and the Hamiltonian of the composed system is

$$\hat{H} = \int \mathrm{d}^3\mathbf{r} \int_0^\infty \mathrm{d}\omega \, \hbar\omega \hat{\mathbf{f}}^\dagger(\mathbf{r}, \omega) \hat{\mathbf{f}}(\mathbf{r}, \omega). \tag{2.85}$$

The replacement of the electric field $\mathbf{E}$ [equation (2.24)], of the magnetic field $\mathbf{B}$ [equation (2.9)], and the displacement vector $\mathbf{D}$ [equations (2.16), (2.14) and (2.21)] by the quantum mechanical operators, lead us (recalling equations (2.82) and (2.14)) to

$$\hat{\mathbf{E}}(\mathbf{r}, \omega) = i\sqrt{\frac{\hbar}{\pi\varepsilon_0}} \frac{\omega^2}{c^2} \int \mathrm{d}^3\mathbf{r}' \sqrt{\varepsilon''(\mathbf{r}', \omega)} \mathbf{G}(\mathbf{r}, \mathbf{r}', \omega) \hat{\mathbf{f}}(\mathbf{r}', \omega), \tag{2.86}$$

$$\hat{\mathbf{B}}(\mathbf{r}, \omega) = (i\omega)^{-1} \nabla \times \hat{\mathbf{E}}(\mathbf{r}, \omega), \tag{2.87}$$

and

$$\hat{\mathbf{D}}(\mathbf{r}, \omega) = \varepsilon_0 \varepsilon(\mathbf{r}, \omega) \hat{\mathbf{E}}(\mathbf{r}, \omega) + \hat{\mathbf{P}}_\mathbf{N}(\mathbf{r}, \omega) = (\mu_0 \omega^2)^{-1} \nabla \times \nabla \times \hat{\mathbf{E}}(\mathbf{r}, \omega), \tag{2.88}$$

from which the electromagnetic field operators in the Schrödinger picture are obtained by integration over ω:

$$\hat{\mathbf{E}}(\mathbf{r}) = \int_0^\infty d\omega\, \hat{\mathbf{E}}(\mathbf{r}, \omega) + \int_0^\infty d\omega\, \hat{\mathbf{E}}^\dagger(\mathbf{r}, \omega), \tag{2.89}$$

$$\hat{\mathbf{B}}(\mathbf{r}) = \int_0^\infty d\omega\, \hat{\mathbf{B}}(\mathbf{r}, \omega) + \int_0^\infty d\omega\, \hat{\mathbf{B}}^\dagger(\mathbf{r}, \omega), \tag{2.90}$$

and [1]

$$\hat{\mathbf{D}}(\mathbf{r}) = \hat{\mathbf{D}}^\perp(\mathbf{r}) = \int_0^\infty d\omega\, \hat{\mathbf{D}}(\mathbf{r}, \omega) + \int_0^\infty d\omega\, \hat{\mathbf{D}}^\dagger(\mathbf{r}, \omega). \tag{2.91}$$

With this formalism, the electromagnetic field is expressed in terms of the classical Green's tensor $\mathbf{G}(\mathbf{r}, \mathbf{r}', \omega)$ satisfying the generalized wave equation (2.23) and the continuum of the fundamental bosonic variables $\mathbf{f}(\mathbf{r}, \omega)$ and $\mathbf{f}^\dagger(\mathbf{r}, \omega)$ fulfilling the bosonic commutation relations (2.83-2.84). All the information about the dielectric matter (dependence in space and frequency, and absorptive properties) is included in the permittivity $\varepsilon(\mathbf{r}, \omega)$ of the classical problem.

The previous quantization scheme meets all the basic requirements of quantum electrodynamics. Therefore, it can be shown by using very general properties of the permittivity and the Green's tensor that the electric and magnetic fields satisfy the correct commutation relations at equal times [64].

$$[\hat{E}_k(\mathbf{r}), \hat{E}_l(\mathbf{r}')] = [\hat{B}_k(\mathbf{r}), \hat{B}_l(\mathbf{r}')] = 0, \tag{2.92}$$

$$[\varepsilon_0 \hat{E}_k(\mathbf{r}), \hat{B}_l(\mathbf{r}')] = -i\hbar \epsilon_{klm} \partial_m^r \delta(\mathbf{r} - \mathbf{r}'). \tag{2.93}$$

ϵ_{klm} represents the Levi-Civita tensor and $\partial_m^r = \frac{\partial}{\partial x_m}$ is the partial derivative over the spatial coordinates $x_1 = x, x_2 = y, x_3 = z$. Additionally, the electromagnetic field operators in the Heisemberg picture satisfy the Maxwell equations (2.1)-(2.4), with the time derivative of any operator $\hat{\mathbf{Q}}$ being given by

$$\dot{\hat{\mathbf{Q}}} = (i\hbar)^{-1}[\hat{\mathbf{Q}}, \hat{\mathbf{H}}], \tag{2.94}$$

where $\hat{\mathbf{H}}$ is the Hamiltonian (2.85) including the EM fields and dielectric medium interactions.

Regarding to the (zero-temperature) statistical implications of the quantization scheme, the vacuum expectation of $\hat{\mathbf{E}}$ is obviously zero whereas the fluctuation is not. From equations

---

[1]From here on, the longitudinal ($\hat{\mathbf{F}}^\parallel(\mathbf{r})$) and transversal ($\hat{\mathbf{F}}^\perp(\mathbf{r})$) components of an arbitrary vector operator ($\hat{\mathbf{F}}(\mathbf{r})$) are defined by $\hat{\mathbf{F}}^{(\parallel)\perp}(\mathbf{r}) = \int d^3\mathbf{r}\, \delta^{(\parallel)\perp}(\mathbf{r} - \mathbf{r}')\hat{\mathbf{F}}^\parallel(\mathbf{r})$, with $\delta^\parallel(\mathbf{r} - \mathbf{r}')$ and $\delta^\perp(\mathbf{r} - \mathbf{r}')$ being defined as the longitudinal and transversal tensor-value delta function, *i.e* $\delta^\parallel(\mathbf{r}) = -\nabla \otimes \nabla \frac{1}{4\pi|\mathbf{r}|}$ and $\delta^\perp(\mathbf{r}) = \delta(\mathbf{r}) - \delta^\parallel(\mathbf{r})$, respectively.

(2.83), (2.84) and (2.86) we obtain, with the help of the general relation of the complex Green's tensor [64]

$$\frac{\omega^2}{c^2} \int \mathrm{d}^3\mathbf{s}\, \varepsilon''(\mathbf{s}, \omega) \mathbf{G}_{ik}(\mathbf{r}, \mathbf{s}, \omega) \mathbf{G}^*_{\ jk}(\mathbf{r}', \mathbf{s}, \omega) = \mathrm{Im} G_{ij}(\mathbf{r}, \mathbf{r}', \omega), \tag{2.95}$$

the following equation

$$\langle 0 | \hat{E}_k(\mathbf{r}, \omega) \hat{E}^\dagger_l(\mathbf{r}', \omega') | 0 \rangle = \frac{\hbar \omega^2}{\pi \varepsilon_0 c^2} \mathrm{Im} G_{kl}(\mathbf{r}, \mathbf{r}', \omega) \delta(\omega - \omega'). \tag{2.96}$$

This equation shows that the fluctuation of the electromagnetic field is determined by the imaginary part of the Green's tensor, which is consistent with the dissipation-fluctuation theorem [47]. Therefore the quantization scheme respects both the basic requirements of quantum theory in terms of the correct commutation relations (2.92)-(2.93) and statistical physics (*i.e.*, the dissipation-fluctuation theorem).

2.4.2 Emitter-field interaction

The interaction of the quantized electromagnetic field with quantum emitters placed inside a dielectric-matter configuration or near dielectric bodies can be strongly influenced by this absorbing medium. A typical example in this thesis is the dependence of the spontaneous emission rate of an excited two-level emitter on the presence of a plasmonic waveguide. In order to study such related phenomena, the Hamiltonian (2.85) must be supplemented with the Hamiltonian describing the interaction of charged particles with the medium-assisted electromagnetic field. Probably one of the first historical atom-field Hamiltonians dates from Dirac's work [79], and it is known as the minimal coupling since it raises from the 'minimal' change of the particles momentum $\mathbf{p}$ by the new momentum $\mathbf{p} - q\mathbf{A}$, due to the reaction of the atom charge q to a radiation vector potential $\mathbf{A}$. Let us start describing such Hamiltonian for a general system with charged particles.

Minimal-coupling Hamiltonian

In order to describe the interaction with matter in the minimal-coupling scheme, it is necessary to express both the scalar potential $\hat{\varphi}$ and vector potential $\hat{\mathbf{A}}$ in terms of the fundamental bosonic fields $\hat{\mathbf{f}}(\mathbf{r}, \omega)$ and $\hat{\mathbf{f}}^\dagger(\mathbf{r}, \omega)$. The potentials in the Coulomb gauge are defined by

$$\nabla \hat{\varphi} = -\hat{\mathbf{E}}^\parallel(\mathbf{r}), \tag{2.97}$$

$$\hat{\mathbf{A}}(\mathbf{r}) = \int_0^\infty \mathrm{d}\omega\, \frac{\hat{\mathbf{E}}^\perp(\mathbf{r}, \omega)}{i\omega} + \mathrm{H.c.}, \tag{2.98}$$

and the canonically conjugated momentum field respect to $\hat{\mathbf{A}}(\mathbf{r})$ is

$$\hat{\mathbf{\Pi}}(\mathbf{r}) = -i\varepsilon_0 \int_0^\infty \mathrm{d}\omega\,\omega\hat{\mathbf{A}}^\perp(\mathbf{r},\omega) + \text{H.c.}, \tag{2.99}$$

where H.c. denotes Hermite conjugate. Applying the minimal-coupling scheme, we can write the total Hamiltonian for a system of charges in the form [64]

$$\begin{aligned}
\hat{H} = \int \mathrm{d}^3\mathbf{r} \int_0^\infty \mathrm{d}\omega\,\hbar\omega\hat{\mathbf{f}}^\dagger(\mathbf{r},\omega)\hat{\mathbf{f}}(\mathbf{r},\omega) + \sum_\alpha \frac{1}{2m_\alpha}[\hat{\mathbf{p}}_\alpha - q_\alpha\hat{\mathbf{A}}(\hat{\mathbf{r}}_\alpha)]^2 \\
+ \frac{1}{2}\int \mathrm{d}^3\mathbf{r}\,\hat{\rho}_{At}(\mathbf{r})\hat{\varphi}_{At}(\mathbf{r}) + \int \mathrm{d}^3\mathbf{r}\,\hat{\rho}_{At}(\mathbf{r})\hat{\varphi}_M(\mathbf{r}),
\end{aligned} \tag{2.100}$$

where $\hat{\mathbf{r}}_\alpha$ is the position operator and $\hat{\mathbf{p}}_\alpha$ is the canonical momentum operator of the αth non-relativistic particle of charge q_α and mass m_α, whose sum constitute an atomic system (emitter) or ensemble of them. Additionally, the subindexes At and M refers to atomic and medium-assisted quantities. Let us briefly explain the four terms arising from the Hamiltonian (2.100). The first term is the energy of the electromagnetic field in the presence of dielectric including absorption, *i.e.* imaginary part of ε. The second term is the kinetic energy of the charged particles (with the vector potential defined by eq. [2.98]) and the third term is their Coulomb energy, where the corresponding scalar potential $\hat{\varphi}_{At}$ is given by

$$\hat{\varphi}_{At}(\mathbf{r}) = \int \mathrm{d}^3\mathbf{r}'\,\frac{\hat{\rho}_{At}(\mathbf{r}')}{4\pi\varepsilon_0|\mathbf{r} - \mathbf{r}'|}, \tag{2.101}$$

with

$$\hat{\rho}_{At}(\mathbf{r}') = \sum_\alpha q_\alpha\delta(\mathbf{r} - \hat{\mathbf{r}}_\alpha), \tag{2.102}$$

being the charge density of the particles. The last term is the Coulomb energy of interaction of the particles with the medium, where φ_M is defined by equation (2.97). The evolution of the corresponding $\hat{\mathbf{D}}$ and $\hat{\mathbf{B}}$ field operators, together with their definitions [equations (2.90) and (2.91) respectively], with the Hamiltonian (2.100) satisfy [64] the operators-valued Maxwell equations

$$\begin{aligned}
\nabla\hat{\mathbf{B}}(\mathbf{r}) &= 0, \tag{2.103} \\
\nabla\times\hat{\mathbf{E}}(\mathbf{r}) + \dot{\hat{\mathbf{B}}}(\mathbf{r}) &= 0, \tag{2.104} \\
\nabla\hat{\mathbf{D}}(\mathbf{r}) &= \hat{\rho}_{At}(\mathbf{r}), \tag{2.105} \\
\nabla\times\hat{\mathbf{H}}(\mathbf{r}) - \dot{\hat{\mathbf{D}}}(\mathbf{r}) &= \hat{\mathbf{j}}_{At}(\mathbf{r}), \tag{2.106}
\end{aligned}$$

where

$$\hat{\mathbf{j}}_{At}(\mathbf{r}) = \frac{1}{2}\sum_\alpha q_\alpha[\dot{\hat{\mathbf{r}}}_\alpha\delta(\mathbf{r} - \hat{\mathbf{r}}_\alpha) + \delta(\mathbf{r} - \hat{\mathbf{r}}_\alpha)\dot{\hat{\mathbf{r}}}_\alpha]. \tag{2.107}$$

In equations (2.103)-(2.106), the longitudinal component of the electric field and the displacement field [compared to (2.86) and (2.88)] now contain additional longitudinal components that result from the charge distribution $\hat{\rho}_{At}(\mathbf{r})$, *i.e.*,

$$\hat{\mathbf{E}}(\mathbf{r}) = \hat{\mathbf{E}}_M(\mathbf{r}) - \nabla\hat{\varphi}_{At}(\mathbf{r}), \tag{2.108}$$

$$\hat{\mathbf{D}}(\mathbf{r}) = \hat{\mathbf{D}}_M(\mathbf{r}) - \varepsilon_0\nabla\hat{\varphi}_{At}(\mathbf{r}), \tag{2.109}$$

where $\hat{\mathbf{E}}_M(\mathbf{r})$ and $\hat{\mathbf{D}}_M(\mathbf{r})$ are defined according to equations [(2.86),(2.89)] and [(2.88),(2.91)], respectively.

Multipolar-coupling Hamiltonian

Up to now we have considered the minimal-coupling Hamiltonian for several charges which can be the constituents of a single or several emitters. In order to consider the interaction of several emitters, is more convenient to do it in a multipolar-coupling formalism [64, 80]. The multipolar-coupling Hamiltonian describes the interaction in terms of field strengths, atomic polarizations and magnetizations, instead of doing it by means of potentials like in (2.100). Let us consider several atomic systems (atoms, molecules, quantum-dots, NV-centers, etc..) at different atomic positions $\mathbf{r}_i$ and introduce the atomic polarization for the ith atomic system

$$\hat{\mathbf{P}}_i(\mathbf{r}) = \sum_{\alpha_i} q_{\alpha_i}(\hat{\mathbf{r}}_{\alpha_i} - \mathbf{r}_i) \int_0^1 \mathrm{d}\lambda\,\delta[\mathbf{r} - \mathbf{r}_i - \lambda(\hat{\mathbf{r}}_{\alpha_i} - \hat{\mathbf{r}}_i)], \tag{2.110}$$

and then the total charge density (2.102) of non-overlapping systems can be rewritten as

$$\hat{\rho}_{At}(\mathbf{r}) = \sum_i \left\{ q_i\delta(\mathbf{r} - \hat{\mathbf{r}}_i) - \nabla\hat{\mathbf{P}}_i(\mathbf{r}) \right\}, \tag{2.111}$$

with

$$q_i = \sum_{\alpha_i} q_{\alpha_i}, \tag{2.112}$$

being the total charge of the ith atomic system. In order to perform the transition from the minimal-coupling scheme to the multipolar one we apply an unitary transformation, known as the Power-Zienau-Woolley transformation [64, 80], which is

$$\hat{\mathcal{H}} = \hat{U}^\dagger H\hat{U}, \tag{2.113}$$

where the unitary operator is given by

$$\hat{U} = \exp\left[\sum_i \frac{i}{\hbar} \int \mathrm{d}^3\mathbf{r}\,\hat{\mathbf{P}}_i(\mathbf{r})\hat{\mathbf{A}}(\mathbf{r})\right]. \tag{2.114}$$

The resulting multipolar Hamiltonian from the transformation (2.113) for neutral atomic systems (*i.e.* $q_i = 0$) that are not non-overlapping, is [80]

$$
\hat{\mathcal{H}} = \int \mathrm{d}^3\mathbf{r} \int_0^\infty \mathrm{d}\omega\, \hbar\omega \hat{\mathbf{f}}^\dagger(\mathbf{r},\omega)\hat{\mathbf{f}}(\mathbf{r},\omega)
$$
$$
+ \sum_i \sum_{\alpha_i} \frac{1}{2m_{\alpha_i}} \left\{ \hat{\mathbf{p}}_{\alpha_i} + q_{\alpha_i} \int_0^1 \mathrm{d}\lambda\, \lambda(\hat{\mathbf{r}}_{\alpha_i} - \mathbf{r}_i) \times \hat{\mathbf{B}}[\mathbf{r}_i + \lambda(\hat{\mathbf{r}}_{\alpha_i} - \mathbf{r}_i)] \right\}^2 \qquad (2.115)
$$
$$
+ \sum_i \frac{1}{2\varepsilon_0} \int \mathrm{d}^3\mathbf{r}\, \hat{\mathbf{P}}_i(\mathbf{r})\hat{\mathbf{P}}_i(\mathbf{r}) - \sum_i \int \mathrm{d}^3\,\mathbf{r}\hat{\mathbf{P}}_i^\perp(\mathbf{r})\hat{\mathbf{E}}(\mathbf{r}),
$$

where $\hat{\mathbf{B}} = \nabla \times \hat{\mathbf{A}}$ [with $\hat{\mathbf{A}}$ defined in (2.98)] and $\hat{\mathbf{E}}$ is defined according to (2.89).

From equation (2.115), it is seen that the atomic systems interact only through the inhomogeneous medium-assisted electromagnetic field. In particular, in the electric small dipole approximation we can ignore the term involving $\hat{\mathbf{B}}(\mathbf{r})$, and the displacement field $\hat{\mathbf{E}}(\mathbf{r})$ does not vary significantly over the region ith polarization $\hat{\mathbf{P}}_i(\mathbf{r})$, so we can obtain:

$$
\hat{\mathcal{H}} = \int \mathrm{d}^3\mathbf{r} \int_0^\infty \mathrm{d}\omega\, \hbar\omega \hat{\mathbf{f}}^\dagger(\mathbf{r},\omega)\hat{\mathbf{f}}(\mathbf{r},\omega) + \sum_i \left\{ \sum_{\alpha_i} \frac{1}{2m_{\alpha_i}} \{\hat{\mathbf{p}}_{\alpha_i}\}^2 + \frac{1}{2\varepsilon_0} \int \mathrm{d}^3\mathbf{r}\, \hat{\mathbf{P}}_i(\mathbf{r})\hat{\mathbf{P}}_i(\mathbf{r}) \right\}
$$
$$
- \sum_i \hat{\mathbf{d}}_i \hat{\mathbf{E}}(\mathbf{r}_i),
$$

$$(2.116)$$

where $\hat{\mathbf{d}}_i = \sum_{\alpha_i} q_{\alpha_i}(\hat{\mathbf{r}}_{\alpha_i} - \mathbf{r}_i)$ is the ith dipolar operator. We can observe that the first term corresponds to the EM field-matter Hamiltonian (2.85), the second term in brackets correspond to the sum of each atomic Hamiltonian $\hat{\mathcal{H}}_i$ and the last term correspond to the displacement interaction term. Restricting our attention to two-level atomic systems and using the usual raising and lowering operators anticommutation relations $\{\hat{\sigma}_i, \hat{\sigma}_j^\dagger\} = \frac{1}{2}$, we can write the ith atomic Hamiltonian as:

$$
\hat{\mathcal{H}}_i = \hbar\omega_{e,i} \left|e_i\right\rangle \left\langle e_i\right| + \hbar\omega_{g,i} \left|g_i\right\rangle \left\langle g_i\right| = \hbar\omega_i \hat{\sigma}_i^\dagger \hat{\sigma}_i + constant, \qquad (2.117)
$$

in which the ith dipolar operator becomes

$$
\hat{\mathbf{d}}_i = \mathbf{d}_i \hat{\sigma}_i + \mathbf{d}_i^* \hat{\sigma}_i^\dagger. \qquad (2.118)
$$

and $\mathbf{d}_i = \left\langle e_i\right| \hat{\mathbf{d}} \left|g_i\right\rangle$ is the two-level (qubit) transition dipole matrix from the ith atomic system excited level e_i to the ground level g_i. In addition, $\hat{\sigma}_i^\dagger$ ($\hat{\sigma}_i$) is the i-qubit raising (lowering) operators, and $\omega_i = \omega_{e,i} - \omega_{g,i}$ is the ith qubit transition frequency.

2.4.3 Dynamics of two-level systems: Master equation

In this subsection we review the tools required to determine the evolution of arbitrary quantum states formed by a pair of two-level emitting systems, *i.e.* two qubits emitters.

Specifically, we derive the master equation governing N-qubit emitters that later we will apply in chapter 5 for the case of two qubits (N=2). The main steps in the derivation, following very closely reference [81], are the next: we write down the multipolar Hamiltonian, perform the evolution of an arbitrary system operator $\hat{O}$, and finally apply it to the system density matrix operator ρ. We split the derivation of the master equation in two parts regarding to the application of basic approximations to the off-resonant evolution and to the on-resonant one, respectively. As an application to the dynamics in the presence of PWs, we obtain the formulas of the master equation coefficients for such systems. Finally, we consider how to add the effect of a free-evolving resonant laser in the master equation.

Evolution of the system operator with the Multipolar Hamiltonian

The multipolar Hamiltonian in the electric dipole approximation for a system of N-qubits in the presence of dispersive and absorbing materials reads [using (2.116), (2.117) and (2.118)] as:

$$
\begin{aligned}
\hat{H} = & \int \mathrm{d}^3\mathbf{r} \int_0^\infty \mathrm{d}\omega\, \hbar\omega \hat{\mathbf{f}}^\dagger(\mathbf{r},\omega)\hat{\mathbf{f}}(\mathbf{r},\omega) + \sum_{i=1}^N \hbar\omega_i \hat{\sigma}_i^\dagger \hat{\sigma}_i \\
& - \sum_{i=1}^N \int_0^\infty \mathrm{d}\omega\, [\hat{\mathbf{d}}_i \hat{\mathbf{E}}(\mathbf{r}_i,\omega) + \text{H.c.}],
\end{aligned}
\tag{2.119}
$$

where $\hat{\mathbf{d}}_i$ is the dipole moment operator of the ith two-level atom [equation (2.118)] and $\hat{\mathbf{E}}(\mathbf{r},\omega)$ is the electromagnetic field operator (2.86). We recall that the bosonic operators $\hat{\mathbf{f}}$ and $\hat{\mathbf{f}}^\dagger$ represent the previously explained dynamical variables of the electromagnetic field and the medium [see equation (2.82)], including the reservoir associated with the losses in the medium. In addition, $\mathbf{G}(\mathbf{r},\mathbf{r}',\omega)$ is the classical Green's tensor in the presence of an arbitrary absorbing medium characterized by the inhomogeneous complex dielectric function $\varepsilon = \varepsilon' + i\varepsilon''$, satisfying equation (2.23).

For the interaction of the qubit emitters and the electromagnetic field, it is convenient to split the frequency integrals of the field (2.86) into on-resonant ($\int_0^{'\infty}$) and off-resonant ($\int_0^{''\infty}$) terms respect to the qubit transition. Let us now derive the time evolution of an arbitrary system operator $\hat{O}$ with the qubit emitters. We expect that the on-resonant part of the electromagnetic field Hamiltonian (2.85) gives rise to the most important contribution to the evolution of the system operators. Considering such contribution and notation, we can write the equation of motion of $\hat{O}$ in the Heisenberg picture as:

$$
\begin{aligned}
\dot{\hat{O}} = & -\frac{i}{\hbar}[\hat{O},\hat{H}_{\text{res}}] + \frac{i}{\hbar}\sum_{i=1}^N \int_0^{''\infty} \mathrm{d}\omega\, \{[\hat{O},\hat{\mathbf{d}}_i]\hat{\mathbf{E}}(\mathbf{r}_i,\omega) \\
& + \hat{\mathbf{E}}^\dagger(\mathbf{r}_i,\omega)[\hat{O},\hat{\mathbf{d}}_i]\},
\end{aligned}
\tag{2.120}
$$

where

$$\hat{H}_{\mathrm{res}} = \int \mathrm{d}^3\mathbf{r} \int_0^{'\infty} \mathrm{d}\omega\, \hbar\omega \hat{\mathbf{f}}^\dagger(\mathbf{r},\omega)\hat{\mathbf{f}}(\mathbf{r},\omega) + \sum_{i=1}^N \hbar\omega_i \hat{\sigma}_i^\dagger \hat{\sigma}_i$$
$$- \sum_{i=1}^N \int_0^{'\infty} \mathrm{d}\omega\, [\hat{\mathbf{d}}_i \hat{\mathbf{E}}(\mathbf{r}_i,\omega) + \mathrm{H.c.}]. \tag{2.121}$$

Note that in equation (2.120) normal ordering is adopted, such that $\hat{\mathbf{E}}(\mathbf{r}_i,\omega)$ is on the right-hand side and $\hat{\mathbf{E}}^\dagger(\mathbf{r}_i,\omega)$ on the left-hand side of the operators, which is appropriate when taking expectation values (using the vacuum state) of the creation and annihilation operators. First, let us calculate the second term (off-resonant) in equation (2.120) under some approximations and then proceed with the first term (on-resonant term). The operators $\hat{\mathbf{E}}(\mathbf{r}_i,\omega)$ and $\hat{\mathbf{E}}^\dagger(\mathbf{r}_i,\omega)$ are expressed in terms of the dynamical variables $\hat{\mathbf{f}}$ regarding to equation (2.86). In order to calculate the second term, we formally integrate the equation of motion for the operators $\hat{\mathbf{f}}(\mathbf{r},\omega)$ and $\hat{\mathbf{f}}^\dagger(\mathbf{r},\omega)$. Recalling the bosonic commutation relations (2.83)-(2.84), we can easily see that $\hat{\mathbf{f}}$ fulfill the following Heisenberg equation of motion

$$\dot{\hat{\mathbf{f}}}(\mathbf{r},\omega) = \frac{1}{i\hbar}[\hat{\mathbf{f}}(\mathbf{r},\omega),\hat{H}] = -i\omega\hat{\mathbf{f}}(\mathbf{r},\omega) + \frac{\omega^2}{c^2}\sqrt{\frac{\varepsilon''(\mathbf{r},\omega)}{\hbar\pi\varepsilon_0}}\sum_{i=1}^N \hat{\mathbf{d}}_i \mathbf{G}^*(\mathbf{r}_i,\mathbf{r},\omega). \tag{2.122}$$

We can formally integrate equation (2.122) and obtain

$$\hat{\mathbf{f}}(\mathbf{r},\omega,t) = \hat{\mathbf{f}}_{\mathrm{free}}(\mathbf{r},\omega,t) + \frac{\omega^2}{c^2}\sqrt{\frac{\varepsilon''(\mathbf{r},\omega)}{\hbar\pi\varepsilon_0}}\sum_{i=1}^N \int_0^t \mathrm{d}t'\, \hat{\mathbf{d}}_i(t')\mathbf{G}^*(\mathbf{r}_i,\mathbf{r},\omega)e^{-i\omega(t-t')}, \tag{2.123}$$

where $\hat{\mathbf{f}}_{\mathrm{free}}(\mathbf{r},\omega,t)$ evolves freely. If we insert (2.123) in (2.86), and we make use of the relation (2.95), we finally obtain

$$\hat{\mathbf{E}}(\mathbf{r},\omega,t) = \hat{\mathbf{E}}_{\mathrm{free}}(\mathbf{r},\omega,t) + \frac{\omega^2}{c^2}\frac{i}{\pi\varepsilon_0}\sum_{i=1}^N \int_0^t \mathrm{d}t'\, e^{-i\omega(t-t')}\mathrm{Im}\mathbf{G}(\mathbf{r},\mathbf{r}_i,\omega)\hat{\mathbf{d}}_i(t'), \tag{2.124}$$

where $\hat{\mathbf{E}}_{\mathrm{free}}(\mathbf{r},\omega,t)$ is defined inserting $\hat{\mathbf{f}}_{\mathrm{free}}(\mathbf{r},\omega)$ in equation (2.86).

In anticipation of the expected atomic energy-level shifts caused by the plasmonic waveguide environment, we introduce for mathematical convenience a modified atomic transition frequency $\tilde{\omega}_i$, which allows to write the slowly varying atomic operator as

$$\hat{\tilde{\sigma}}_i(t) = \hat{\sigma}_i(t)e^{i\tilde{\omega}_i t}, \tag{2.125}$$

so that equation (2.118) becomes

$$\hat{\mathbf{d}}_i(t) = \mathbf{d}_i\hat{\tilde{\sigma}}_i(t)e^{-i\tilde{\omega}_i t} + \mathbf{d}_i^*\hat{\tilde{\sigma}}_i^\dagger(t)e^{i\tilde{\omega}_i t}. \tag{2.126}$$

Master equation derivation: basic approximations to the off-resonant term

Let us continue evaluating the second term of the equation of motion (2.120) in terms of the Green's tensor and the transition atomic operators. Now we insert equation (2.124) in the second term of equation (2.120) and we obtain

$$\hat{F}''(t) = \hat{F}''_{\text{free}}(t) + \sum_{i,j} \hat{F}''_{ij}(t), \tag{2.127}$$

where

$$\hat{F}''_{\text{free}}(t) = \frac{i}{\hbar} \sum_i \int_0^{''\infty} d\omega \, \{[\hat{O}(t), \hat{\mathbf{d}}_i(t)]\hat{\mathbf{E}}_{\text{free}}(\mathbf{r}_i, \omega, t) + \hat{\mathbf{E}}^\dagger_{\text{free}}(\mathbf{r}_i, \omega, t)[\hat{O}(t), \hat{\mathbf{d}}_i(t)]\}, \tag{2.128}$$

and

$$
\begin{aligned}
\hat{F}''_{ij}(t) = -\frac{1}{\hbar\pi\varepsilon_0} \int_0^t dt' \int_0^{''\infty} d\omega \, \frac{\omega^2}{c^2} \{ & [\hat{O}(t), \hat{\mathbf{d}}_i(t)] \cdot \text{Im}\mathbf{G}(\mathbf{r}_i, \mathbf{r}_j, \omega) \\
& \cdot [\mathbf{d}_j \hat{\tilde{\sigma}}_j(t') e^{-i(\omega-\tilde{\omega}_j)(t-t')} e^{-i\tilde{\omega}_j t} + \mathbf{d}_j^* \hat{\tilde{\sigma}}_j^\dagger(t') e^{-i(\omega+\tilde{\omega}_j)(t-t')} e^{i\tilde{\omega}_j t}] \\
& - \text{Im}\mathbf{G}(\mathbf{r}_j, \mathbf{r}_i, \omega) \cdot [\mathbf{d}_j \hat{\tilde{\sigma}}_j(t') e^{i(\omega+\tilde{\omega}_j)(t-t')} e^{-i\tilde{\omega}_j t} \\
& + \mathbf{d}_j^* \hat{\tilde{\sigma}}_j^\dagger(t') e^{i(\omega-\tilde{\omega}_j)(t-t')} e^{i\tilde{\omega}_j t}] \cdot [\hat{O}(t), \hat{\mathbf{d}}_i(t)]\}.
\end{aligned} \tag{2.129}
$$

The time integrals contain the solution to $\hat{\tilde{\sigma}}_i(t')$ which is itself unknown, and therefore we need to approximate it. We may assume that the time integrals run over a small correlation time τ_c [64, 82]. Such correlation time is larger than the inverse of the atomic system resonance frequency $\tilde{\omega}_i$, which at optical frequencies is on the order of $\tilde{\omega}_i^{-1} \sim 10^{-15}$s. Additionally, this correlation time is typically small compared to the time scale on which the atomic system is changed owing to the coupling to the medium-assisted electromagnetic field. One can estimate this time scale to be within the range $1/(100\gamma_0)$-$1/(10\gamma_0)$ [56], where $1/(\gamma_0)$ is the typical decay time of the slowly varying operators in homogeneous environments, which is on the order of $1/\gamma_0 \sim 10^{-9}$s for optical emitters [41, 44, 47]. If we restrict ourselves to resolving times $(t - t')$ within both assumptions, we can consider a Markovian approximation and substitute $\hat{\tilde{\sigma}}_i(t')$ by $\hat{\tilde{\sigma}}_i(t)$ [2]. In addition, for frequencies outside the range $-100\gamma_0 \leq (\omega - \tilde{\omega}_i) \leq 100\gamma_0$, the rapidly varying exponentials average the time integrals to zero. In the spirit of such coarse-grained time averaging method, we may make the replacement

$$\int_0^t dt' \, e^{-i(\omega-\tilde{\omega}_i)(t-t')} \to \zeta(\omega - \tilde{\omega}_i), \tag{2.130}$$

---

[2]It is important to notice this approximation neglects any long time correlation effects and therefore we restrict to distances $\mathbf{r}_i - \mathbf{r}_j$ between the emitters that fulfill $t \gg \frac{(\mathbf{r}_i - \mathbf{r}_j)}{v_g}$, where v_g is the group velocity of the medium-assisted electromagnetic fields.

where

$$\zeta(x) = \pi\delta(x) + i\mathcal{P}(1/x). \tag{2.131}$$

We can also suppress the terms containing both $\hat{\tilde{\sigma}}_i(t')$ $(\hat{\tilde{\sigma}}_i^\dagger(t'))$ and $\hat{\tilde{\sigma}}_i(t')$ $(\hat{\tilde{\sigma}}_i^\dagger(t'))$ operators, since they imply earlier resolving times $1/(2\tilde{\omega}_i)$ which can not be appreciated in the coarse-grained time averaging method. In this way we derive

$$\begin{aligned}
\hat{F}''_{ij}(t) \simeq -\frac{1}{\hbar\pi\varepsilon_0} \int_0^{''\infty} \mathrm{d}\omega \frac{\omega^2}{c^2} \{ &\mathbf{d}_i \mathrm{Im}\mathbf{G}(\mathbf{r}_i,\mathbf{r}_j,\omega)\mathbf{d}_j^* \zeta(-(\omega+\tilde{\omega}_j))[\hat{O}(t),\hat{\sigma}_i(t)]\hat{\sigma}_j^\dagger(t) \\
&+ \mathbf{d}_i^* \mathrm{Im}\mathbf{G}(\mathbf{r}_i,\mathbf{r}_j,\omega)\mathbf{d}_j \zeta(\tilde{\omega}_j-\omega)[\hat{O}(t),\hat{\sigma}_i^\dagger(t)]\hat{\sigma}_j(t) \\
&- \mathbf{d}_i^* \mathrm{Im}\mathbf{G}(\mathbf{r}_i,\mathbf{r}_j,\omega)\mathbf{d}_j \zeta(\tilde{\omega}_j+\omega)\hat{\sigma}_j(t)[\hat{O}(t),\hat{\sigma}_i^\dagger(t)] \\
&- \mathbf{d}_i \mathrm{Im}\mathbf{G}(\mathbf{r}_i,\mathbf{r}_j,\omega)\mathbf{d}_j^* \zeta(\omega-\tilde{\omega}_j)\hat{\sigma}_j^\dagger(t)[\hat{O}(t),\hat{\sigma}_i(t)] \}.
\end{aligned} \tag{2.132}$$

Taking into account that the frequencies are off-resonant in equation (2.132), then $\omega\pm\tilde{\omega}_i$ is different from zero and the δ-function does not contribute to the frequency integrals. Therefore we can approximate

$$\zeta(\omega\pm\tilde{\omega}_i) \to i\mathcal{P}(1/(\omega\pm\tilde{\omega}_i)) \tag{2.133}$$

an insert the resulting expression for $\hat{F}''_{ij}(t)$ into equation (2.127). Now we can combine the resulting equation (2.127) with (2.120) and obtain the evolution

$$\dot{\hat{O}} = -\frac{i}{\hbar}[\hat{O},\hat{\tilde{H}}_{\mathrm{res}}] + \hat{F}''_{\mathrm{free}} + i\sum_{\substack{i,j=1 \\ i\neq j}}^{N} \{g_{i^*j}^-[\hat{O},\hat{\sigma}_i^\dagger]\hat{\sigma}_j + g_{ij^*}^+[\hat{O},\hat{\sigma}_i]\hat{\sigma}_j^\dagger + g_{ij^*}^-\hat{\sigma}_j^\dagger[\hat{O},\hat{\sigma}_i] + g_{i^*j}^+\hat{\sigma}_j[\hat{O},\hat{\sigma}_i^\dagger]\}, \tag{2.134}$$

where the coherent coefficients $g_{ij}^{-(+)}$ are defined as

$$g_{ij}^{-(+)} = \frac{P}{\pi\hbar\varepsilon_0} \int_0^\infty \mathrm{d}\omega \frac{\omega^2}{c^2} \frac{\mathbf{d}_i \mathrm{Im}\mathbf{G}(\mathbf{r}_i,\mathbf{r}_j,\omega)\mathbf{d}_j}{\omega - (+)\tilde{\omega}_j}. \tag{2.135}$$

The notation $i^*(j^*)$ refers to substitute $\mathbf{d}_i(\mathbf{d}_j)$ by its complex conjugate $\mathbf{d}_i^*(\mathbf{d}_j^*)$. In particular, it is illustrative to identify $\hat{O}$ with the atomic raising operator $\hat{\sigma}_i$ in order to see the influence of dipole-dipole medium-assisted coupling induced by the presence of other emitters. The average of equation (2.134) in this case yields

$$\langle\dot{\hat{\sigma}}_i\rangle = -\frac{i}{\hbar}\langle[\hat{\sigma}_i,\hat{\tilde{H}}_{\mathrm{res}}]\rangle - i\frac{i}{\hbar}\sum_{i\neq j,j=1}^{N} g_{i^*j}\langle\hat{\sigma}_i\hat{\sigma}_j\rangle, \tag{2.136}$$

where g_{i^*j} is the resonant interatomic coupling coefficient, defined as

$$g_{i^*j} = g_{i^*j}^+ + g_{i^*j}^-. \tag{2.137}$$

The sum in equation (2.134) contains terms for different indexes, whereas the equal indexes have being included in the resonant Hamiltonian $\hat{\tilde{H}}_{\text{res}}$ (denoted by the tilde symbol, $\sim$, on $\hat{H}_{\text{res}}$), which is defined according with formula (2.121) but substituting the atomic transition frequency ω_i by the medium-modified atomic transition frequency:

$$\tilde{\omega}_i = \omega_i - g_{i*i}, \tag{2.138}$$

where the medium-induced frequency shift g_{i*i} is defined as

$$g_{i*i} = g_{i*i}^+ - g_{i*i}^-. \tag{2.139}$$

Due to the $\tilde{\omega}_i$ dependence of g_{i*i}, equation (2.138) is a self-consistent transcendental equation, so we need to approximate its evaluation. Applying Kramers-Kronnig relations to the Green's tensor, from equation (2.135) we find the approximate expression [81, 83]

$$g_{ij}^- = \frac{\tilde{\omega}_j^2}{\hbar\varepsilon_0 c^2}\mathbf{d}_i\text{Re}\mathbf{G}(\mathbf{r}_i, \mathbf{r}_j, \tilde{\omega}_j)\mathbf{d}_j - g_{ij}^+. \tag{2.140}$$

Then from equations (2.140) and (2.137) we obtain the approximate resonant atomic coupling

$$g_{i*j} = \frac{\tilde{\omega}_j^2}{\hbar\varepsilon_0 c^2}\mathbf{d}_i^*\text{Re}\mathbf{G}(\mathbf{r}_i, \mathbf{r}_j, \tilde{\omega})\mathbf{d}_j, \tag{2.141}$$

and additionally from (2.138), we obtain the frequency shift of each atom

$$g_{i*i} = \frac{\tilde{\omega}_i^2}{\hbar\varepsilon_0 c^2}\mathbf{d}_i^*\text{Re}\mathbf{G}(\mathbf{r}_i, \mathbf{r}_i, \tilde{\omega})\mathbf{d}_i - 2g_{i*i}^+, \tag{2.142}$$

where the last part can safely be neglected if the frequency shift is caused by the presence of macroscopic objects [81, 83], *i.e.* the reflection part of the Green's tensor. Since the atoms can be assumed to be localized in some small free-space region, the Green's tensor at the positions of the atom can be always be written as a sum of the homogeneous vacuum Green's tensor $\mathbf{G}_{\text{homo}}$ and the reflected scatter field $\mathbf{G}_{\text{scatter}}$ [81, 47]. Due to the singularity of $\text{Re}\mathbf{G}_{\text{homo}}$ at equal spatial points [84], equation (2.142) actually applies to the reflection part $\mathbf{G}_{\text{scatter}}$ only. The homogeneous divergence is an artifact of quantum theory in free-space for the Markovian approximation and it can be remedied by mass renormalization, which give rise to the vacuum-induced Lamb-shift $\delta\omega_i^{homo}$ [84–86]. The vacuum interaction can never be switch-off and therefore the only observable quantity is $\omega_i + \delta\omega_i^{homo}$. Since our interest is to study the dynamical process due to plasmonic interaction from quantum emitters, we consider that such free-space Lamb shift has been already included in ω_i. Both the medium-induced (2.138) and the vacuum-induced Lamb shifts can also shift the values of the Green's tensor. However the effect of the Lamb-shift for optical frequencies is small ($\omega_i \sim 10^{15}\text{Hz}$ and $\delta\omega_i^{homo} \sim 10^9\text{Hz}$, $\delta\omega_i \sim \delta\omega_i^{homo}$).

It is interesting to notice from equation (2.140) that the resonant dipole-dipole interaction is not symmetric respect to i and j due to the dependence in $\tilde{\omega}_j$. This asymmetry could be important with the appearance of sharp resonances in the Green's tensor, when this tensor value at $\tilde{\omega}_i$ and $\tilde{\omega}_j$ could be very different. Only if the difference $|\tilde{\omega}_i - \tilde{\omega}_j|$ is small compared with the frequency scale variation of the Green's tensor, such asymmetry can be disregarded, and the use of an average frequency $\frac{\tilde{\omega}_i + \tilde{\omega}_j}{2}$ is a very good approximation. For identical or closely identical emitters such assumption means that the Green's tensor varies smoothly with frequency. That is the case for broadband plasmonic waveguides for frequencies far from the surface plasmon resonance, which are the frequencies of interest in this thesis due to their longer propagation lengths, and it will be shown with further detail in chapters 3 and 4.

Recalling our main motivation, we are particularly interested in the evolution of the qubit system and therefore in applying the evolution (2.134) to the reduced density matrix of the system, $\hat{\rho}$. Using the relationship

$$\langle \hat{O}(t) \rangle = \text{Tr}[\hat{\varrho}(0)\hat{O}(t)] = \text{Tr}[\hat{\varrho}(t)\hat{O}(0)] = \text{Tr}[\hat{\rho}(t)\hat{O}(0)] \tag{2.143}$$

where O is an arbitrary system operator, Tr denotes the trace, ϱ is the total density operator of the overall system, and using the cyclic properties of the trace, we can write from equation (2.134) the following equation of motion for the expectation value of $\hat{O}$:

$$\langle \dot{\hat{O}} \rangle = \text{Tr}\left[-\frac{i}{\hbar}[\hat{\tilde{H}}_{\text{res}}, \hat{\rho}]\hat{O}\right] + i \sum_{\substack{i,j=1 \\ i \neq j}}^{N} \text{Tr}\left[\left\{[g_{i^*j}^-(\hat{\sigma}_i^\dagger\hat{\sigma}_j\hat{\rho} - \hat{\sigma}_j\hat{\rho}\hat{\sigma}_i^\dagger) + g_{ij^*}^+(\hat{\sigma}_i\hat{\sigma}_j^\dagger\hat{\rho} - \hat{\sigma}_j^\dagger\hat{\rho}\hat{\sigma}_i)]\right.\right.$$
$$\left.\left. + [g_{ij^*}^-(\hat{\sigma}_i\hat{\rho}\hat{\sigma}_j^\dagger - \hat{\rho}\hat{\sigma}_j^\dagger\hat{\sigma}_i) + g_{i^*j}^+(\hat{\sigma}_i^\dagger\hat{\rho}\hat{\sigma}_j - \hat{\rho}\hat{\sigma}_j\hat{\sigma}_i^\dagger)]\right\}\hat{O}\right]. \tag{2.144}$$

In such derivation we have assumed that the initial off-resonant free field is in the vacuum state and then

$$\langle \hat{F}''_{\text{free}} \rangle = 0. \tag{2.145}$$

Equation (2.143) implies that $\text{Tr}\left[\frac{d\hat{\rho}(t)}{dt}\hat{O}(0)\right] = \text{Tr}\left[\hat{\rho}(0)\frac{d\hat{O}(t)}{dt}\right]$ and since $\hat{O}$ is an arbitrary system operator, we can deduce from equation (2.144) the following equation of motion for $\hat{\rho}$ in the Schrödinger picture:

$$\dot{\hat{\rho}} = -\frac{i}{\hbar}[\hat{\tilde{H}}_{\text{res}}, \hat{\rho}] + \left\{i \sum_{\substack{i,j=1 \\ i \neq j}}^{N} \{[g_{i^*j}^-(\hat{\sigma}_i^\dagger\hat{\sigma}_j\hat{\rho} - \hat{\sigma}_j\hat{\rho}\hat{\sigma}_i^\dagger) + g_{ij^*}^+(\hat{\sigma}_i\hat{\sigma}_j^\dagger\hat{\rho} - \hat{\sigma}_j^\dagger\hat{\rho}\hat{\sigma}_i)] + \text{H.c.}\}\right\}. \tag{2.146}$$

In this master equation, the resonant dipole-dipole interaction and the resonant atom-field interaction are taken into account without any restriction on the strength of the latter

one. Therefore, equation (2.146) is suitable to study strong-coupling phenomena, which are typically associated to the appearance of high peaks of the Green's tensor at a narrow frequency interval, *e.g.*, in cavity resonances.

Master equation derivation: basic approximations to the on-resonant term

Due to the lossy character of plasmonic waveguides [58], which are the structures of interest in this thesis, and the typical small transition dipole moment of optical emitters ($\tilde{\omega}_i >> \gamma$) [41, 44, 47], we can consider that the atomic-field interaction is weak. Therefore, the on-resonant term from the equation of motion (2.120)

$$\hat{F}'(t) = \hat{F}'_{\text{free}}(t) + \frac{i}{\hbar} \sum_i \int_0^{''\infty} \mathrm{d}\omega \left\{ [\hat{O}(t), \hat{\mathbf{d}}_i(t)] \hat{\mathbf{E}}(\mathbf{r}_i, \omega, t) + \hat{\mathbf{E}}^\dagger(\mathbf{r}_i, \omega, t) [\hat{O}(t), \hat{\mathbf{d}}_i(t)] \right\}, \quad (2.147)$$

can be treated within the approximation scheme taken previously for the off-resonant terms, *i.e.*, coarse-grain time averaging and Markovian approximation. Repeating the analogous steps that led us from equation (2.127) to equation (2.132) for the resonant terms, we obtain the same equation as in (2.132) but substituting the off-resonant integrals ($\int^{''\infty}$) by the on-resonant integrals ($\int^{'\infty}$). Since the frequency integral now run over the resonance region, we may approximate the ζ function by the δ function

$$\zeta(\omega \pm \tilde{\omega}_i) \rightarrow \pi\delta(\omega \pm \tilde{\omega}_i). \quad (2.148)$$

Then, inserting equations (2.147) and (2.148) into the first term at the right-hand side of equation (2.134), we can the derive the following equation of motion

$$\dot{\hat{O}} = -i \sum_{i=1}^N \tilde{\omega}_i [\hat{O}, \hat{\sigma}_i^\dagger \hat{\sigma}_i] + \hat{F}_{\text{free}} - \frac{1}{2} \sum_{i,j=1}^N \{\gamma_{i^*j}[\hat{O}, \hat{\sigma}_i^\dagger]\hat{\sigma}_j + \gamma_{ij^*}\hat{\sigma}_j^\dagger[\hat{O}, \hat{\sigma}_i]\}$$
$$+ i \sum_{\substack{i,j=1 \\ i \neq j}}^N \{g_{i^*j}^-[\hat{O}, \hat{\sigma}_i^\dagger]\hat{\sigma}_j + g_{ij^*}^+[\hat{O}, \hat{\sigma}_i]\hat{\sigma}_j^\dagger + g_{ij^*}^-\hat{\sigma}_j^\dagger[\hat{O}, \hat{\sigma}_i] + g_{i^*j}^+\hat{\sigma}_j[\hat{O}, \hat{\sigma}_i^\dagger]\}, \quad (2.149)$$

where

$$\gamma_{ij} = \frac{2\tilde{\omega}_j^2}{\hbar\varepsilon_0 c^2} \mathbf{d}_i \mathrm{Im}\mathbf{G}(\mathbf{r}_i, \mathbf{r}_j, \tilde{\omega}_j)\mathbf{d}_j, \quad (2.150)$$

are related with the spontaneous emission coefficients, *i.e.*, dissipative coefficients, of each atom due their local-field ($i = j$) and the ones due to medium-assisted interaction with the other atoms ($i \neq j$). Additionally, we have the term

$$\hat{F}_{\text{free}} = \hat{F}'_{\text{free}} + \hat{F}''_{\text{free}}, \quad (2.151)$$

which in the absence of medium-assisted excitations, the free-field is in the vacuum state, and thus

$$\langle \hat{F}_{\text{free}} \rangle = 0. \tag{2.152}$$

Tracing out the on-resonant and off-resonant field variables and recalling the steps that we took from equation (2.134) to (2.146), we can derive the following equation for the reduced density operator

$$\dot{\hat{\rho}} = -i \sum_{i=1}^{N} \tilde{\omega}_i [\hat{\sigma}_i^\dagger \hat{\sigma}_i, \hat{\rho}] - \frac{1}{2} \sum_{i,j=1}^{N} \{ \gamma_{i^*j} (\hat{\sigma}_i^\dagger \hat{\sigma}_j \hat{\rho} - \hat{\sigma}_j \hat{\rho} \hat{\sigma}_i^\dagger) + \text{H.c.} \}$$
$$+ i \sum_{\substack{i,j=1 \\ i \neq j}}^{N} \{ g_{i^*j}^- [\hat{\rho}, \hat{\sigma}_i^\dagger] \hat{\sigma}_j + g_{ij^*}^+ [\hat{\rho}, \hat{\sigma}_i] \hat{\sigma}_j^\dagger + g_{ij^*}^- \hat{\sigma}_j^\dagger [\hat{\rho}, \hat{\sigma}_i] + g_{i^*j}^+ \hat{\sigma}_j [\hat{\rho}, \hat{\sigma}_i^\dagger] \}. \tag{2.153}$$

We can simplify equation (2.153) even more if we take into account that the frequency scale variation of the Green's tensor is slow in comparison with the atomic frequency differences, as in the case of broadband PWs. In these cases, the coefficients are approximately reciprocal

$$g_{i^*j}^\pm \simeq g_{ji^*}^\pm, \tag{2.154}$$

$$\gamma_{i^*j} \simeq \gamma_{ji^*} \tag{2.155}$$

and then equation (2.153) becomes

$$\dot{\hat{\rho}} = -i \sum_{i=1}^{N} \tilde{\omega}_i [\hat{\sigma}_i^\dagger \hat{\sigma}_i, \hat{\rho}] + i \sum_{\substack{i,j=1 \\ i \neq j}}^{N} g_{i^*j} [\hat{\sigma}_i^\dagger \hat{\sigma}_j, \hat{\rho}]$$
$$- \frac{1}{2} \sum_{i,j=1}^{N} (\gamma_{i^*j} (\hat{\sigma}_i^\dagger \hat{\sigma}_j \hat{\rho} - 2 \hat{\sigma}_j \hat{\rho} \hat{\sigma}_i^\dagger + \hat{\rho} \hat{\sigma}_i^\dagger \hat{\sigma}_j)). \tag{2.156}$$

This master equation contains the information about the dynamics of N two-level emitters in the presence of an arbitrary absorbing medium, fulfilling the weak atom-field condition, and in the absence of free-evolving fields.

Plasmonic waveguide master equation coefficients

In order to apply the master equation (2.156) for plasmonic waveguides, we need to perform the calculation of the Green's tensor for evaluating the coupling coefficients (2.150) and (2.141). By means of using the numerical method described in subsection (2.3.3) and the electric-dipole formula (2.25), the total Green's tensor (2.40) is numerically calculated. In particular, we are interested in the contribution of the guided plasmons to the total Green's

tensor, for quantifying their roles in the dynamics of the system. For this analysis, we can use the general formula (2.40) in order to evaluate the guided Green's tensor. Nevertheless, due to the larger values of the transverse EM fields, we will focus on transverse alignments of the emitter dipole moment and therefore formula (2.44) is valid for such purpose. This equation can be calculated by performing numerical calculations with the computational model described in subsection (2.3.3). After substituting the classical EM fields in (2.44), we can insert this guided Green's tensor in equation (2.150) in order to obtain the plasmonic spontaneous emission coefficient, $\gamma_{ij,\,\mathrm{pl}}$,

$$\gamma_{ij,\,\mathrm{pl}} = \frac{\tilde{\omega}_j \, [\mathbf{d}_i \mathbf{e}_n] \, [\mathbf{d}_j \mathbf{e}_n]}{\hbar \int_{S1} (\mathbf{e}_n \times \mathbf{h}_n^*) \cdot \hat{z} \, \mathrm{d}S} e^{-\mathrm{Im}k(z-z')} \cos[\mathrm{Re}k(z-z')], \qquad (2.157)$$

which for $i = j$, becomes the contribution of plasmons to the ith emitter decay rate, γ_{pl}. Analogously, if we substitute equation (2.44) in the dipole-dipole coefficient (2.141) we obtain

$$g_{ij,\,\mathrm{pl}} = -\frac{\tilde{\omega}_j \, [\mathbf{d}_i \mathbf{e}_n] \, [\mathbf{d}_j \mathbf{e}_n]}{2\hbar \int_{S1} (\mathbf{e}_n \times \mathbf{h}_n^*) \cdot \hat{z} \, \mathrm{d}S} e^{-\mathrm{Im}k(z-z')} \sin[\mathrm{Re}k(z-z')]. \qquad (2.158)$$

For emitters positions close to the waveguide surface, these semi-analytical formulas give an excellent approximation to the crossed ($i \neq j$) coupling coefficients terms [(2.141) and (2.150)], as it will be shown in chapter (4), and this fact emphasizes the relevance of the surface plasmons in the dynamics. Additionally, this approximation facilitates the calculation of the coupling coefficients since it involves a 2D simulation instead of a 3D one, which avoids the computation of large domains and therefore it saves important computational time and resources.

Coherent influence on the evolution due to the presence of a resonant laser

So far in order to derive equation (2.156) we have assumed that the free field of the system starts in the vacuum state and then $\langle \hat{F}_{\mathrm{free}} \rangle = 0$. The dissipation associated to the presence of a plasmonic environment will finally make the system excitation to decay on time. Since in nanophotonics the use of lasers is customary, it is attractive to consider its pumping effect on the system to avoid the decay of the excitations. A full quantum-mechanical description of the laser is certainly very interesting but, as a first approach to this problem, it is convenient to do some simplifications. Specifically, we are going to assume that the medium-assisted electromagnetic free-field is described by a nearly monochromatic coherent laser (with angular frequency ω_{laser}), with a spectrum much narrower than the spectral width of the atoms, γ_{ii}. In such case the laser dynamics is barely affected by the presence of the the atomic systems and we can substitute the laser operator $\hat{\mathbf{E}}_{\mathrm{free}}$ by its c-number $\langle \hat{\mathbf{E}}_{\mathrm{free}} \rangle$. Within such approximations, the laser contributes only to the coherent dynamic of

the system and we may include the following additional terms in the Hamiltonian (2.119) as in resonance-fluorescence problems [87, 88, 51, 82, 89–91]

$$H_{\text{laser}} \simeq \hbar\omega_{\text{laser}}\hat{\mathbf{f}}^{\dagger}_{\text{free}}\hat{\mathbf{f}}_{\text{free}} - \sum_i [\hbar\Omega_i\,\hat{\sigma}^{\dagger}_i e^{i\omega_{\text{laser}}t} + \text{H.c.}], \qquad (2.159)$$

where the weak atom-field strength and the phase of the laser are characterized by the Rabi frequencies $\Omega_i = \mathbf{d}_i\mathbf{E}_{\text{L}}\,e^{i\mathbf{k}_{\text{L}}\mathbf{r}_i}/\hbar$, where $\mathbf{E}_{\text{L}}$ and $\mathbf{k}_{\text{L}}$ are the amplitude and wavevector of the driving laser field, respectively. With the additional term (2.159), the total Hamiltonian (2.119) will be time-dependent but we can perform the time-dependent unitary transformation $\hat{U} = e^{-i\omega_{\text{laser}}(\hat{\mathbf{f}}^{\dagger}_{\text{free}}\hat{\mathbf{f}}_{\text{free}}-\sum_i \hat{\sigma}^{\dagger}_i\hat{\sigma}_i)t}$, such that we obtain a time independent Hamiltonian $\hat{H}_{\text{rotated}} = \hat{U}\hat{H}\hat{U}^{\dagger} + i\hat{U}\partial_t\hat{U}^{\dagger}$ [88, 82]. The physical interpretation of such transformation corresponds to a frequency shift to the laser frame and the resulting Hamiltonian is [51, 82]

$$\hat{H}_{\text{rotated}} = \int \mathrm{d}^3\mathbf{r} \int_0^{\infty} \mathrm{d}\omega\, \hbar\omega\hat{\mathbf{f}}^{\dagger}(\mathbf{r},\omega)\hat{\mathbf{f}}(\mathbf{r},\omega) + \sum_{i=1}^{N} \hbar(\omega_i - \omega_{\text{laser}})\hat{\sigma}^{\dagger}_i\hat{\sigma}_i$$
$$-\sum_{i=1}^{N} \int_0^{\infty} \mathrm{d}\omega\,[\hat{\mathbf{d}}_i\hat{\mathbf{E}}(\mathbf{r}_i,\omega) + \text{H.c.}] - \sum_i [\hbar\Omega_i\,\hat{\sigma}^{\dagger}_i + \text{H.c.}], \qquad (2.160)$$

where the frequencies of the emitters have been shifted by the laser frequency.

Repeating the arguments and steps taken to derive equation (2.156), we may derive the following master equation

$$\dot{\hat{\rho}} = -i\sum_{i=1}^{N}(\tilde{\omega}_i - \omega_{\text{laser}})[\hat{\sigma}^{\dagger}_i\hat{\sigma}_i, \hat{\rho}] + i\sum_{i=1}^{N}[\hbar\Omega_i\,\hat{\sigma}^{\dagger}_i + \text{H.c.}, \hat{\rho}]$$
$$+ i\sum_{\substack{i,j=1 \\ i\neq j}}^{N} g_{i*j}[\hat{\sigma}^{\dagger}_i\hat{\sigma}_j, \hat{\rho}] - \frac{1}{2}\sum_{i,j=1}^{N}(\gamma_{i*j}(\hat{\sigma}^{\dagger}_i\hat{\sigma}_j\hat{\rho} - 2\hat{\sigma}_j\hat{\rho}\hat{\sigma}^{\dagger}_i + \hat{\rho}\hat{\sigma}^{\dagger}_i\hat{\sigma}_j)), \qquad (2.161)$$

where the coefficients γ_{i*j} and g_{i*j} are defined according to formulas (2.150) and (2.141), respectively. In chapter 5, we will make use of this master equation to study the generation of stationary entanglement between two qubits. In order to solve both equations (2.156) and (2.161) we have made use of the Matlab quantum numerical toolbox [92], which solves the evolution of the density operator. In the absence of laser we have compared with the analytical data [93] and both methods provide numerically identical results, whereas in the presence of laser we have checked with Mathematica numerical calculations as in references [57, 56], and the differences were below 0.01%.

2.5 Conclusions

In this chapter we have derived the theoretical framework for studying both classical and quantum phenomena involving plasmonic waveguides.

Specifically, in section 2.1, the classical phenomenological Maxwell equations have been presented for an arbitrary absorbing environment, which optical properties are described by means of a response function that is local in spatial coordinates and non-local in time. After introducing the constitutive relations, including a noise polarization in them, we have shown the Maxwell's equations in the Fourier frequency space with the presence of noise sources. Next, the wave equations form of those equations have been presented which permit us to give a formal solution of the electromagnetic fields in terms of the Green's tensor for inhomogeneous mediums. Importantly, the explicit contribution from plasmonic waveguide modes to this tensor has been derived.

Since a large number of interesting electromagnetic problems in plasmonic waveguides have a cumbersome analytical resolution, we have made use of the finite element method to obtain a computational solution in these systems. In particular, we have described the general structure of this numerical method in its Galerkin's approach, and we have specified the main steps to solve realistic electromagnetic models: translational invariant and periodical waveguides mode calculations, harmonic propagation in periodical devices, and electric dipole excitation of waveguides.

Finally in section 2.4, we have presented a quantum mechanical formalism to study the interaction of emitters and electromagnetic fields. As a result of the quantization of the classical Maxwell's equations, we have shown the electromagnetic field-matter Hamiltonian that represents the energy of the elementary light-matter excitations. In addition, the minimal-coupling Hamiltonian that accounts for the interaction of electric charge distributions from quantum emitters with the quantized medium-assisted potentials has been presented. After performing a Power-Zienau-Woolley unitary transformation, this interaction Hamiltonian has been transformed to the multipolar Hamiltonian that is expressed in terms of the electromagnetic field operators. Finally, within the electric-dipole approximation and considering two-level emitters, we have derived the master equation governing the dynamics of N-qubits in the presence of plasmonic waveguides for the weak coupling regime. Both the absence and presence of a resonant coherent laser have been considered in this equation.

3 Plasmonic waveguides: from the optical to the terahertz regime

3.1 Introduction

Surface plasmon polaritons (SPPs) have a great potential for telecommunications as circuit interconnections [1] and key elements for subwavelength circuitry [6]. The potential of SPPs is based on the subwavelength nature of their electromagnetic (EM) modes, which allows a strong localization of their EM fields and the building up of ultra-small SPP-based circuits [94]. In addition, such localization of the SPP implies high energy densities which enhance the emission and the efficiency of EM sources coupled to the SPP [47]. Whereas most of the studied applications have exploited the classical aspects of SPPs, encouraging and exciting applications have started to exploit their quantum character [41, 45, 50, 95], as it will be commented with further details in chapters 4 and 5.

Importantly, the SPP properties have been extended from the optical [6, 96, 97] to the terahertz regime [32], thanks to the geometrical tailoring of their dispersion relations [31]. Such geometrical tailoring consists in the design of corrugations in the metal surface which allows the creation of deeply confined SPP-like modes, or spoof plasmons [32, 34, 33]. These corrugations are crucial in order to achieve subwavelength confinement in open metallic waveguides for frequencies ranging from the telecom to the terahertz regime, since non-corrugated plasmonic waveguides are highly delocalized [19, 98]. For both classical and quantum applications exploiting the deep localization of SPPs, it is interesting to research SPP waveguides with higher degree of subwavelength confinement. In addition, it is also highly desirable to find new, simpler and more robust SPP waveguides for longer wavelengths, in which SPPs get largely localized.

In this chapter we describe some of the most suitable plasmonic waveguiding approaches to built subwavelength circuitry from the optical to the terahertz regime. In subsection 3.2.1 we introduce the concept of SPP in flat surfaces, which naturally arises from the optical properties of metals on interfaces. In order to confine and control the SPPs into one dimension, we study some of the most promising plasmonic waveguides [6] in the optical regime. In subsections 3.2.3-3.2.4, we show how to obtain subwavelength confinement in plasmonic

waveguides for the telecom regime making use of corrugations in the metal. In particular, in subsection 3.2.4, we pay special attention to a new corrugated waveguide mode that we call *domino plasmon*. Finally, in subsections 3.3.1-3.3.4, we exploit the domino approach in order to create subwavelength confined electromagnetic (EM) modes for designing robust circuitry in the terahertz regime.

3.2 Optical and telecom plasmonic waveguides

3.2.1 Surface plasmon on a flat surface

In this subsection, we describe briefly the main features of flat surface plasmon polaritons (SPPs) which have the properties that mainly inspired the present work. SPPs are collective interactions between photons and electrons at metal-dielectric interfaces. These collective modes can be described macroscopically as solutions of Maxwell equations, in which the materials are described by their respective macroscopic dielectric functions [2]. The dielectric function of the dielectric domain ε_{die} is taken as a positive real constant for frequencies far from material resonances, *e.g.*, optical phonons [99]. However, the dielectric function for the metal varies strongly with the frequency due to the presence of free electrons, and it has a complex value because of the energy loss mechanisms of the electron. Such function can be described by a damped-Drude model [100]

$$\varepsilon_{\text{metal}} = 1 - \frac{\omega_{\text{p}}^2}{\omega^2 + i\gamma\omega}, \tag{3.1}$$

where ω_{p} is the plasma frequency, ω the EM field angular frequency and γ is the damping rate of the electrons due to scattering processes in the metallic lattice. In Figure 3.1, we can see the dispersion from the real part of the dielectric function for silver ($\omega_{\text{p}} = 9\text{eV}$ and $\gamma = 0.07\text{eV}$). Notice that such dependence is qualitatively the same for several metals [100, 73], and therefore also their properties for supporting SPPs. From Figure 3.1 we can observe two main characteristics of the metallic dielectric constant. Firstly, it is increasingly negative for frequencies smaller than the SPP resonance frequency $\frac{\omega_{\text{p}}}{\sqrt{2}}$ (or equivalently $\lambda > 195\text{nm}$). Secondly, we can observe that at the surface plasmon resonance wavelength $\lambda = 195\text{nm}$, $\varepsilon_{\text{metal}}$ is very close to -1. Such condition can be deduced by inserting $\omega = \frac{\omega_{\text{p}}}{\sqrt{2}}$ in equation (3.1), if we neglect the small imaginary part of $\varepsilon_{\text{metal}}$ which is one order of magnitude smaller than the real part (see the inset of Figure 3.1). The negative values and the condition $\varepsilon_{\text{metal}} \to -1$ are crucial for the confinement of the SPPs as it will be clarified below.

The SPP solutions are surface EM waves confined in the metallic surface with a characteristic TM (or equivalently P) polarization, *i.e.*, no-magnetic vector components along
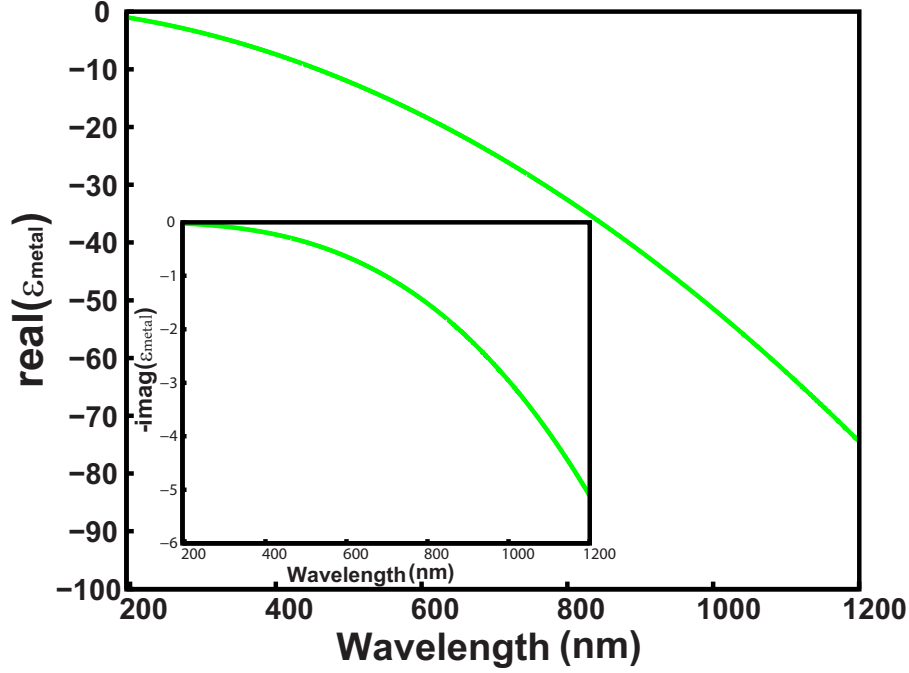
Figure 3.1: Real part of the damped-Drude dielectric function for silver versus the EM wavelength. The parameters of the silver model are ($\omega_{\mathrm{p}} = 9\mathrm{eV}$ and $\gamma = 0.07\mathrm{eV}$). Inset: Imaginary part of the silver dielectric function versus the EM wavelength. The damped-Drude model for silver have the same parameters as in the main figure.

the propagation direction. We can see an example of such solution in figures 3.2(a) and (b), which show the electric field norm for a SPP propagating in the z-direction for an air-silver interface. It can be seen in both figures that the electric field arrows are mainly aligned vertically, but it also has a small z component of the electric field (see Figure 3.2(a)). Such quasi-orthogonal polarization respect to the metallic surface is general for PWs and is a consequence of the realistic metallic boundary. We can also appreciate the change of sign in the y-component of the arrows along the propagation direction due to the spatial phase of the SPP field, which is modulated by the SPP spatial wavelength $\lambda_{\mathrm{plasmon}}$. Also we can observe how the electric field fades away from the surface, thus showing its confined nature. Importantly, the higher confinement implies a magnification of the SPP electric fields, because of the Poynting's energy conservation.

Let us study the SPP properties with further details, including the reasoning of the mechanisms that generate the confinement of the SPP on the surface. The SPP complex
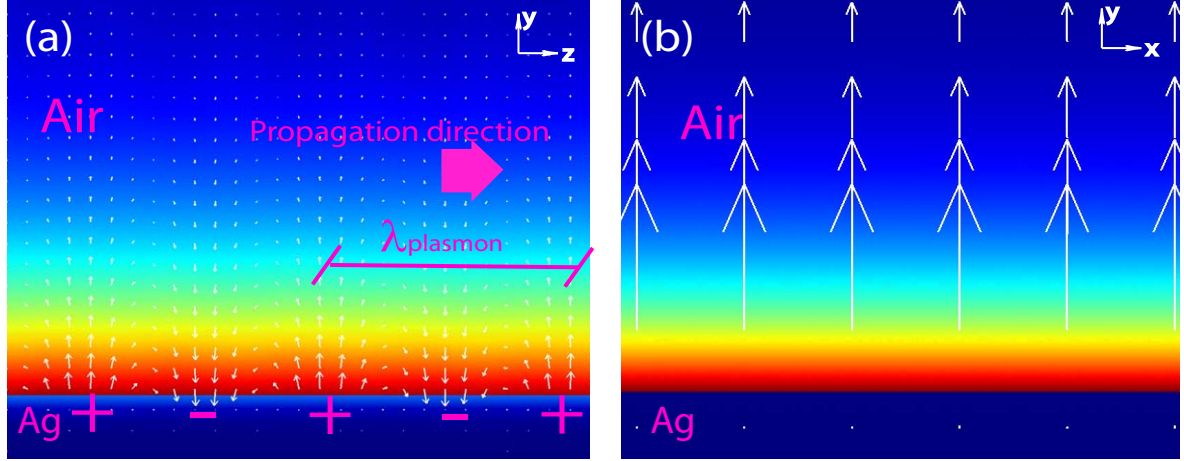
Figure 3.2: (a) Transverse y-z cut of the electric field norm of a SPP propagating in the z direction for a silver-air interface at $\lambda = 600\,\mathrm{nm}$. For both panels, the electric field magnitudes are displayed in arbitrary units. The intensity goes from red (highest) to blue (lowest). Also for both panels, the white arrows represent the electric vectorial field. (b) Corresponding transverse y-x cut of the electric field norm of the SPPs in a flat surface shown in panel (a).

wavevector k_zSPP, can be written analytically as [2]:

$$k_\mathrm{zSPP} = \frac{\omega}{c}\sqrt{\frac{\varepsilon_\mathrm{metal}\varepsilon_\mathrm{die}}{\varepsilon_\mathrm{metal} + \varepsilon_\mathrm{die}}}, \tag{3.2}$$

where c is the speed of light. This last relation has a real and an imaginary part which are related to the phase and the damping of the SPP, respectively. Because of the implicit frequency dependence of the metallic dielectric function, the SPP propagating properties depends non-linearly with the energy $\hbar\omega$.

Firstly, we discuss the phase properties of the SPPs in flat surfaces. In Figure 3.3 (a) we illustrate the typical dispersion relation of SPPs for an Ag-Vacuum interface, *i.e.*, the energy $\hbar\omega$ against the real part of equation (3.2), $\mathrm{Re}(k_\mathrm{zSPP})$. We can observe how the real part of the SPP wavevector departs from the light cone ($\omega = ck_0$), increasing its value for higher energies. Consequently, the SPP has a spatial modulation $e^{i\mathrm{Re}(k_\mathrm{zSPP})z}$ with a periodic length ($\lambda_\mathrm{SPP} = \frac{2\pi}{k_\mathrm{zSPP}}$) smaller than the one in free space ($\lambda = \frac{2\pi}{k_0}$) and the plasmon wavelength decreases for higher energies. Such reduction is specially pronounced at energies close to the SPP resonant energy, in which the dispersion relation presents an asymptote ($\hbar\frac{\omega_\mathrm{p}}{\sqrt{2}}$). Additionally, it can be deduced from equation (3.2) that the SPP band starts infinitesimally from the zero energy ($\hbar\omega = 0$) and so the SPP has no lower energy cut-off.
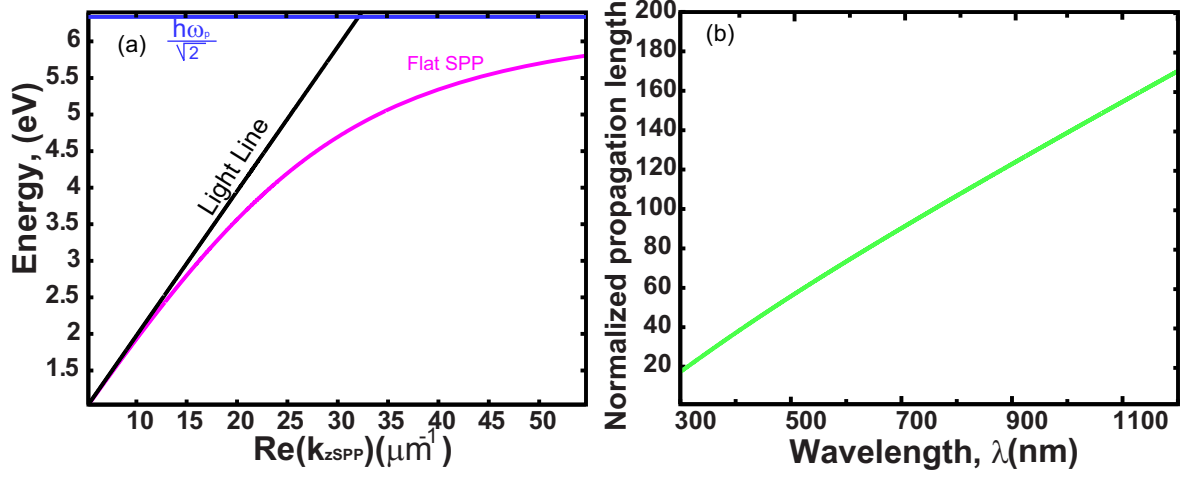
Figure 3.3: (a) Dispersion relation for the SPP fundamental band (magenta line) in a flat silver-air surface. The calculations for both panels have been done using the dielectric constant of silver for the Drude model as specified in the main text. The black line represents the light cone or equivalently the free-propagation dispersion $\omega = ck_{\text{zSPP}}$. The blue line represents the plasmon energy resonance asymptote $\hbar\frac{\omega_{\text{p}}}{\sqrt{2}}$. (b) Propagation length versus the operating wavelength for the same flat surface as in panel (a).

We can easily understand the mechanism of confinement in a SPP propagating in the z-direction. In the general SPP dispersion relation, $k_{\text{zSPP}}^2 + k_{\text{y}}^2 = (\frac{\omega}{c})^2$ [2], we can see that the transverse momentum k_{y} is imaginary mainly because $\text{Re}(k_{\text{zSPP}}) > \frac{\omega}{c}$ and therefore $k_{\text{y}}^2 < 0$. Consequently, the SPP EM fields have a factor proportional to an exponential $e^{-|\text{Im}(k_{\text{y}})|y}$ which confines the SPP to the surface [2]. Importantly, the inequality $\text{Re}k_{\text{zSPP}} > \frac{\omega}{c}$ comes from the negative value of the metallic dielectric function. Such negative value makes the denominator inside the square root in equation (3.2), $\varepsilon_{\text{metal}} + \varepsilon_{\text{die}} = -|\varepsilon_{\text{metal}} + \varepsilon_{\text{die}}|$, to be smaller, in absolute value, than the modulus of the numerator, $|\varepsilon_{\text{metal}}\varepsilon_{\text{die}}|$, and therefore the square root multiplying $\frac{\omega}{c}$ is larger than 1. Accordingly, the main mechanism for confinement is the negative value of the metallic dielectric function. For increasing energies, k_{zSPP} and $|\text{Im}(k_{\text{y}})|$ grow and the confinement increases. When the energy comes closer to the SPP energy asymptote $\frac{\omega_{\text{p}}}{\sqrt{2}}$, the denominator in equation (3.2) gets closer to zero due to the condition $\varepsilon_{\text{metal}} \to -1$ and the subwavelength confinement can be achieved. Therefore, it is the approach to the $\varepsilon_{\text{metal}} = -1$ condition, associated to the SPP resonance, what permits the SPP to achieve subwavelength confinement.

Let us turn our attention to the propagation losses of the SPP. It is intuitive that a higher mode confinement is followed by a larger damping of the SPP. This intuition comes from the higher fraction of the EM fields penetrating inside the metal, which lose their

energy due to the electrons decay mechanisms [2]. This energy loss can be seen from the complex character of the SPP wavevector, which comes from the imaginary part of the metallic dielectric function. The imaginary part of k_{zSPP} implies an exponential decay in the z-direction, $e^{-|\text{Im}k_{\text{zSPP}}|z}$. We define the propagation length as the distance along the propagation direction in which the incoming modal power has decreased to $1/e$ of its initial value, *i.e.*, $\frac{1}{2\text{Im}(k_{\text{zSPP}})}$. In Figure 3.3 (b) we plot the SPP propagation length versus the EM wavelength. We can indeed observe how the propagation length diminishes for decreasing wavelengths due to the higher confinement of the plasmon. A compromise between the degree of confinement and the losses is always present in any metallic waveguide due to the electron energy losses. Therefore, the damping of the SPP must be considered for the design of any application done with plasmonic waveguides.

We can provide some representative propagation values to identify clearly the challenges that must be tackled in order to achieve subwavelength confinement with SPPs. The asymptote of the SPP lies in the ultra-violet regime and consequently the mode confinement is poorer at smaller energies. For realistic silver [72] at an optical wavelength of 600nm, the modal size (defined as $\frac{1}{|\text{Im}(k_{\text{y}})|}$) and the propagation length are 0.55λ and 30λ, respectively. Moreover, for the same metal, those numbers are 1.68λ and 198λ for the telecom at a wavelength of 1500nm. Finally, for the terahertz at the wavelength of 100μm, the same normalized numbers are 37λ and $1.4 \cdot 10^4\lambda$, respectively. Therefore, we can see from the obtained values of the modal size, that both the telecom and terahertz SPP in flat surfaces are not subwavelength confined in contrast with optical SPPs. Therefore, the intrinsic subwavelength nature of SPPs at optical frequencies is lost at wavelengths longer than the telecom regime, and consequently, other approaches are necessary to recover the confinement at sub-λ scales.

3.2.2 Conventional plasmonic waveguides

In this subsection we give a brief review of some of the most important 1D plasmonic waveguides (PWs) which show deep transversal confinement in the optical regime. In particular, we study the dispersion and confinement characteristics of a metallic cylinder, a wedge and a channel. All these PWs share a 2D transversal confinement which is achieved confining one of the delocalized dimensions in the SPP of a flat surface (orthogonal to the propagation direction). The additional confinement is obtained by breaking the translational symmetry of such delocalized direction, which is materialized by modifying the flat metallic surface with different cross-sections. Such spatial modifications increase the effective index experienced by the new SPP, which is higher than the one for free space and that for the SPPs in flat surfaces. Accordingly, the new SPP becomes confined in the broken-symmetry di-

rection, and it can only propagate in the 1D invariant direction. The tighter confinement of the SPP in the 1D PW permits to further control the directionality of the SPP, and it increases the field-enhancement close to the PW cross-section.

Cylindrical plasmonic waveguide

One of the canonical PWs in the optical regime is the cylindrical plasmonic waveguide (CYPW). Such structure consists in an infinite metallic cylinder characterized by a radius R, as represented by its transverse cut in Figure 3.4(a). The main properties of the CYPWs are fixed by the radius R, thus showing a simple characterization of its properties. However, the lack of additional structural parameters limits a further control over the SPP propagation and field-enhancement characteristics. This structure has been extensively studied [101, 102] because of its simplicity, but also due to the possibility of fabricating nanowires even at the monocrystalline level [11]. Even though some simple devices like splitters have been tested [103], the development of circuitry seems difficult. Such difficulty resides in the chemical synthesis of the wires which spreads them randomly in the samples [41, 44, 104]. Therefore, a post-processing method is required to select the wires and fabricate the circuit, which complicates the circuitry production.

As in the case of the SPP in a flat surface, the dispersion characteristics of the CYPW fundamental mode are intimately related with its propagation properties. In Figure 3.4(b) we display the dispersion relation for the fundamental CYPWs bands for three different radius R: $R = 35$nm, $R = 50$nm and $R = 100$nm. For comparison purposes, the SPP dispersion relation in a flat surface is also displayed. In the numerical calculations, we use the permittivity values of silver [72] and vacuum claddings. The CYPWs bands lie on the right side of the light cone in the dispersion diagram, thus confirming their confined nature as in the case of the SPP in a flat surface described in subsection 3.2.1. In addition, the SPP wavevector grows at higher energies and therefore its modal confinement increases. Similarly to the SPP in a flat surface, the CYPW fundamental mode does not posses a lower energy cut-off, a fact that it is confirmed from the analytical study of CYPWs [101].

However, there are large differences between the CYPW and the SPP in flat surfaces. For example, we can see how the bands for the cylinder lie far at the right side of the SPP band in a flat surface, therefore indicating a larger surface confinement of the first in comparison to the latter. It can be also observed how the bands get more confined for smaller radii. Consistently with such radius dependence, we can observe the tendency of the CYPW bands to recover the SPP results in flat surfaces for increasing radii, which is due to the higher resemblance of the cylindrical surface with the flat interface. Another important difference with the SPP in a flat surface is the spatial confinement of the EM fields, which

Figure 3.4: (a) Scheme of the transverse cut of the CYPWs in the plane orthogonal to the propagation direction. The main structural parameters are displayed as commented in the main text. (Surface plot) Transversal electric field norm of its fundamental SPP mode for $\lambda = 600$nm in arbitrary units. The intensity goes from red (highest) to blue (lowest). The white arrows represent the vectorial electric field. (b) Dispersion relation of the CYPWs fundamental bands of different radius. For comparing purposes it is shown the SPP band in a flat surface, the second CYPW mode and the light cone as indicated in the figure. (c) Propagation length versus the operating wavelength for the CYPWs fundamental modes with the same radiuses as in (b). For all the panels the chosen metal is silver, which dielectric constant is taken from [72], and the cladding is air, $\varepsilon_{\mathrm{die}} = 1$.

are transversally concentrated at the surface of the cylinder. Such confinement is illustrated in Figure 3.4(a) for the electric field of the CYPW fundamental mode with $R = 35$ nm at a wavelength $\lambda = 600$ nm. The mechanism of confinement is equivalent to that of a SPP in a flat metallic surface that is curved into a cylindrical geometry [101]. Accordingly, the electric field vectors are radially polarized in Figure 3.4(a) and they correspond to the TM polarization of a SPP in a flat metallic interface (as shown in subsection 3.2.1) that is confined in a cylindrical surface. However, we can observe how the electric field norm of the cylindrical SPP mode has diminished importantly one radius far away from the metallic surface. In particular for a radial distance of 82 nm (0.1λ) from the surface of the cylinder, the SPP carries 70% of the total energy, clearly showing the deep subwavelength scale of its radial confinement length.

The effect of confinement for the different radii and wavelengths are also reflected in the propagation length that is displayed in Figure 3.4(c). We can observe how the propagation lengths decrease for smaller wavelengths and also for smaller radiuses due to the increase of confinement commented above. The large degree of confinement can be also observed in the smaller propagation lengths compared to the SPP in a flat surface. For example, at an operating wavelength of $\lambda = 600$nm, the propagation lengths for $R = 35$ nm, $R = 50$ nm and $R = 100$ nm are respectively 3λ, 5λ and 10λ. These propagation lengths are considerably smaller than the 30λ corresponding to the SPP in a flat surface. Such propagation lengths have to be considered for CYPWs applications and they limit their use to optical interconnections or ultra-small circuits on the order of several free-space wavelengths.

Finally, in Figure 3.4(b), we have also displayed the CYPW second mode with radius $R = 35$nm. It can be observed that the second CYPW mode for $R = 35$nm lies far at the left of the CYPW fundamental band. Therefore the second mode is much less confined than the fundamental one, a fact that is general for other PWs that support a SPP that is deeply confined in its fundamental mode [19]. Since we are interested in highly compact SPP modes, in the following structures, we focus only on their fundamental modes.

Wedge plasmonic waveguide

The wedge plasmonic waveguide (WPW) has been shown to be a good candidate for achieving large degrees of confinement and practical propagation lengths [9]. The wedge structure consist of a triangular tip, which is invariant in the propagation direction and is fused on the top of a flat metallic surface (see Figure 3.5(a) for a transverse cut of the WPW). Different WPWs cross-sections are characterized by three parameters: the height L, the taper angle θ and the radius of the tip R. In comparison with the CYPW, the wedge is structurally more complex and its larger number of parameters permits a further control
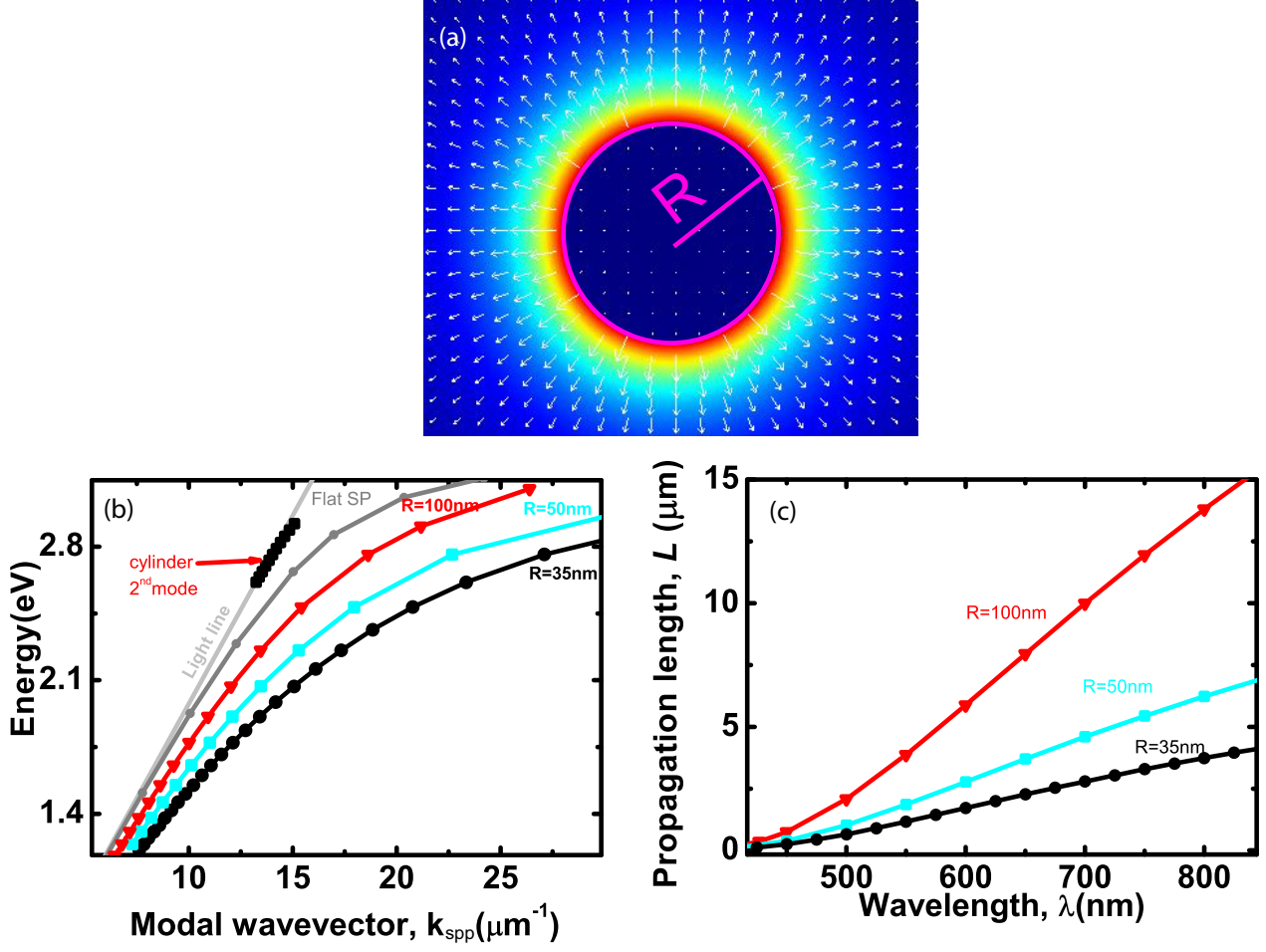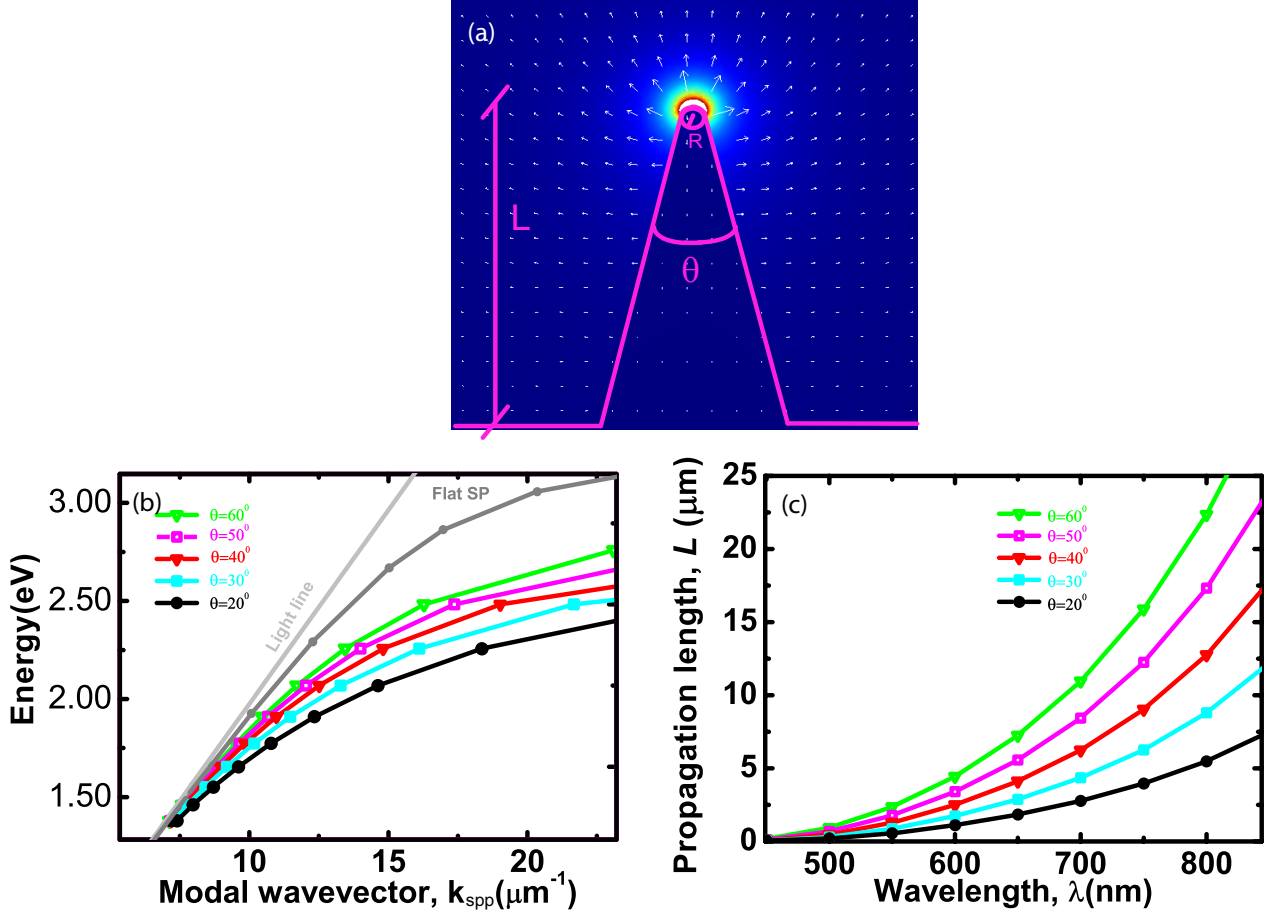
Figure 3.5: (a) Scheme of the transverse cut of the WPWs in the plane orthogonal to the propagation direction. The main structural parameters are displayed as commented in the main text. (Surface plot) Transversal electric field norm of the fundamental WPW SPP mode for $\lambda = 600$nm in arbitrary units. The intensity goes from red (highest) to blue (lowest). The white arrows represent the vectorial electric field. (b) Dispersion relation of the WPWs fundamental bands of different taper angles, with tip radiuses $R = 5$nm and height of $L = 200$nm. For comparing purposes it is shown the SPP band in a flat surface as indicated in the figure. (c) Propagation length versus the operating wavelength for the WPWs fundamental modes with the same parameters as in (b). For all the panels the chosen metal is silver, which dielectric constant is taken from [72], and the cladding is air, $\varepsilon_{\rm die} = 1$.
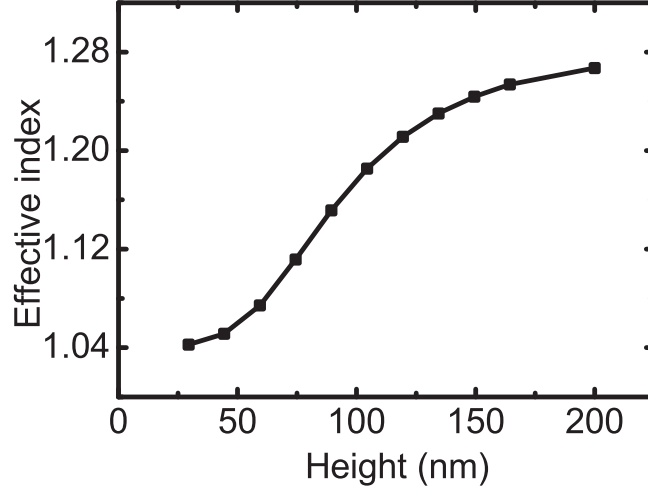
Figure 3.6: Effective mode index variation with the height L for a wedge SPP with fixed tip radius and taper angles of 5nm and 30^0 respectively. The operating wavelength is set to 600nm for these calculations. The chosen metal is silver, which dielectric constant is taken from [72] and the cladding is air $\varepsilon_{\mathrm{die}} = 1$.

on the plasmon propagation and enhancing field capabilities. Moreover, focused-ion beam [9] and high-quality photolithography-procedures [105] have been successfully used for the fabrication of WPW, though large technological improvements are necessary in order to perform complex optical circuits [106].

In Figure 3.5(b) we display the dispersion relation of the fundamental WPW band for several taper angles with heights $L = 200$nm and tip radii $R = 5$nm. The SPP dispersion relation in a flat surface is also shown for comparison purposes. In order to perform the calculations, we have used the values of silver dielectric constants [72] and air claddings. There are large differences between the WPW and the SPP propagation characteristics. We can clearly observe how the bands lie far at the right side of the SPP band in a flat surface, thus showing a higher degree of confinement than in the flat interface. It can be also observed how the modal wavevector increases for decreasing wedge angles θ and accordingly, the modal size of the wedge SPP mode diminishes for smaller angles. Consistently with such behaviour, it can be seen the tendency of the wedge bands to recover the SPP band in a flat surface for large angles, which is a consequence of the higher resemblance of the wedge with the planar interface.

Importantly, there is one difference from the bands of the SPP in a flat surface and the CYPW previously analyzed. For smaller energies the WPW bands present cross-overs with the SPP band in a flat surface due to the finite height L of the wedge. Therefore, the WPW shows a low energy cut-off at which the mode becomes delocalized at both sides of the tip

and it propagates similarly to the SPP mode in a flat surface commented in subsection 3.2.1.

Another important difference from the previous PWs, is the modal confinement of the WPW mode. As shown in Figure 3.5(a), the WPW concentrates the electric fields on the tip, which produces large field enhancements due to its small size [106]. The electric field follows the normal direction of the metallic surface and therefore, the WPW mode is predominantly polarized in radial fashion around the tip (see the arrows in Figure 3.5(a)). In particular, approximating the transversal modal size of the WPW mode to a circular shape, the equivalent modal radius is only 0.1λ, thus showing its strong sub-λ confinement. The tip confinement is well understood by means of the effective index method [94]. In that method, the boundary conditions of the wedge are seen as stacks of finite metallic films, that have different widths [94]. The effective indexes of such finite metallic films increases with smaller films widths. In addition, those effective indexes are higher than the corresponding ones for the SPP in a flat surface. Therefore, the wedge has a higher effective index nearby the tip and consequently the EM field becomes confined close to it. Logically, similar tip-shaped waveguides like ridges [107] have a similar confinement mechanism and consequently, alike propagating properties. Due to the similarity of the CYPW and WPW electric fields, one would naively think that a cylinder of radius $R = 5\,\text{nm}$ will give the same degree of confinement. However a CYPW with such radius will hardly propagate along the waveguide and the computed propagation distance is only 0.29λ. The main difference between both is the effect of the metallic substrate which pushes the SPP outside the tip, thus reducing the penetration of the electric fields. The effect of the height in the confinement will be clarified below but let us first study the influence of the radial confinement in the propagation length for the WPW.

In Figure 3.5(c) we can see the propagation length versus the wavelength for WPW modes with the same parameters displayed in (b). For decreasing wavelengths, we can observe how the propagation length diminishes due to the general trade-off between confinement and loss for SPPs. Also, we can see how for smaller wedge angles θ, the propagation length diminishes due to the larger degree of confinement commented above. In general, as a consequence of the increase of localization, the propagation length of the WPW mode is reduced respect to the one in a flat surface. For example, for wedge modes with angles $\theta = 30°$, $40°$ and $50°$ at a wavelength $\lambda = 600\,\text{nm}$, the propagation lengths are 3λ, 4λ and 6λ, respectively.

Let us finally focus on the effect of the height in the modal confinement. In Figure 3.6 it is shown the variation of the modal effective index $n = \frac{k_{\text{SPP}}}{k_0}$ as a function of the height L, where k_0 is the free-space wavevector in air. The parameters λ, θ, and R, are fixed to $600\,\text{nm}$, $30°$ and 5nm, respectively. The confinement for large heights is mainly due

to the tip as discussed above and therefore we can observe how the effective index vary slowly for heights $L > 170$nm. For smaller heights the mode on the tip feels the presence of the substrate more significantly. Consequently the substrate start expelling the mode from the tip and the modal effective index decreases. Logically, for very small heights, the WPW mode is so pushed by the flat surface that it tends to the SPP effective index in a flat surface ($n_{\text{flat SPP}} = 1.04$ for $\lambda = 600\,\text{nm}$). Similar to the effect of very large angles commented above, the modal index crosses with the one in a planar interface at a height $L = 25\,\text{nm}$ in which the mode becomes delocalized in the substrate at both sides of the tip.

Channel plasmonic waveguide

The channel plasmonic waveguide (CPW) has shown promising properties for deep confinement in PWs [6]. Such structure consists of an triangular trench carved in a metallic substrate, whose cross-section is displayed in Figure 3.7(a). The channel properties are characterized by the height L, taper angle θ and the radius of the tip R. As in the case of the wedge plasmon, these parameters allows a large range of variations in order to further control the channel mode dispersion relation and its field-enhancing abilities. The CPW properties have been shown in an extensive number of experiments mostly with focused-ion beam lithography [17, 18], but also with photo-lithographic technics [108]. In contrast with the two previous PWs, complex plasmonic circuits have been experimentally demonstrated. Such experiments include passive elements like Mach-Zehnder interferometers, ring resonators, tapers, beam splitters [17, 18, 109, 14, 15] and active devices like lasers for similar U-shape structures [110].

In order to describe their propagation properties, we start studying the dispersion relation of the CPW fundamental mode. In Figure 3.7(b) we display the bands for the fundamental modes of several CPWs with different taper angles. For those channels, the heights are $L = 139$nm and the tip radii $R = 5$nm. In order to perform realistic calculations, we have used the dielectric constant of silver, measured from optical experiments [72], and air claddings. Firstly, it can be observed how the bands reside on the right part of the light cone, thus showing their confined character. We can also see how the confinement of the channel SPP increases for higher energies, thus displaying the typical behaviour of plasmonic bands. In addition, we can observe the tendency of the bands to have larger SPP wavectors for smaller taper angles. Therefore sharper angles θ confine more the CPW mode. Such trend is due to the larger departure of the channel shape from the flat surface, since the SPP in a planar interface is less confined, *i.e.*, the SPP band lies at the left of the channel ones. Nevertheless, that higher confinement is limited in energy because the CPW bands crosses the SPP band in a flat surface, thus showing low energy cut-offs. Accordingly, for those
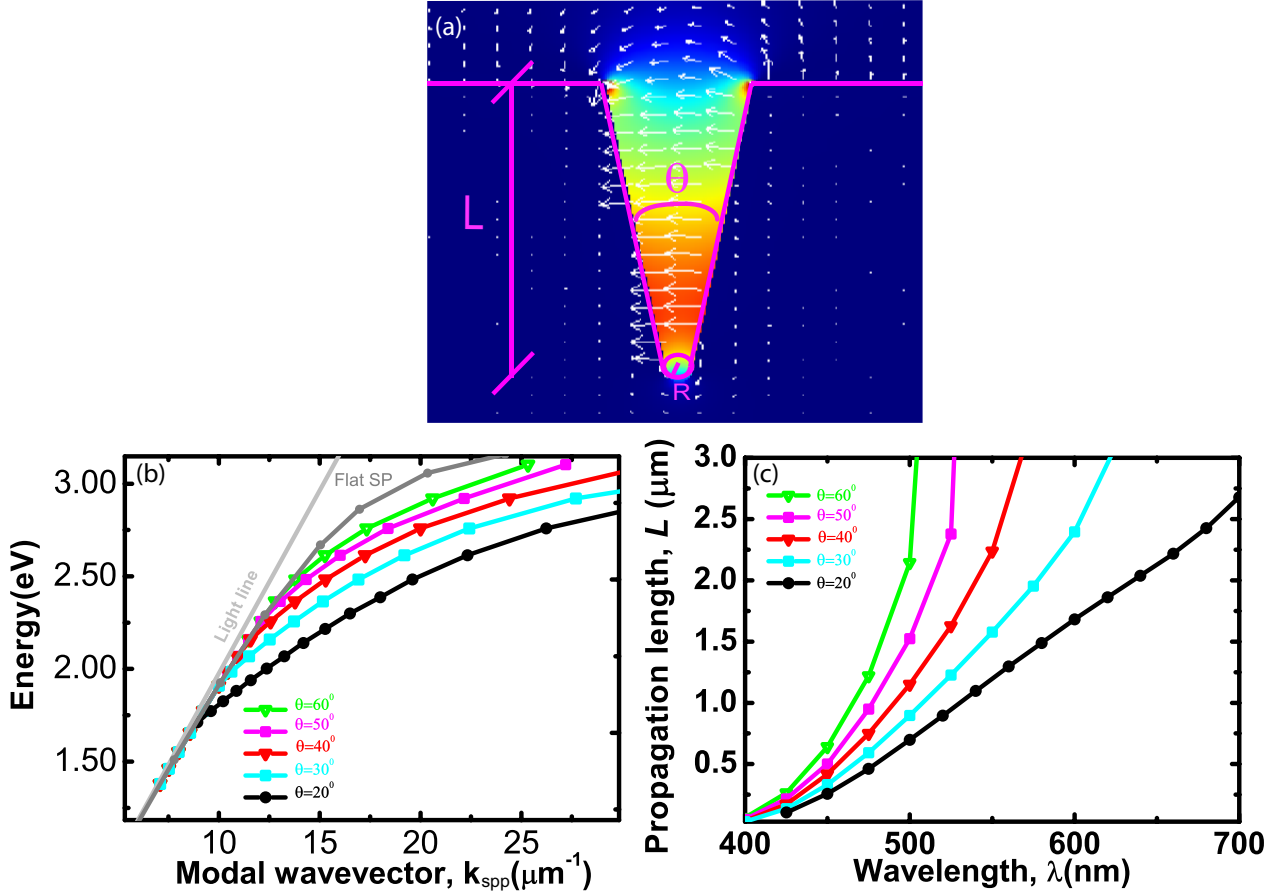
Figure 3.7: (a) Scheme of the transverse cut of the CPWs in the plane orthogonal to the propagation direction. The main structural parameters are displayed as commented in the main text. (Surface plot) Transverse electric field norm of the fundamental CPW SPP mode for $\lambda = 600$nm in arbitrary units. The intensity goes from red (highest) to blue (lowest). The white arrows represent the electric vectorial field. (b) Dispersion relation of the CPWs fundamental bands of different taper angles, with tip radiuses $R = 5$nm and height of 139nm. For comparing purposes it is shown the SPP band in a flat surface as indicated in the figure. (c) Propagation length versus the operating wavelength for the CPWs fundamental modes with the same parameters as in (b). For all the panels the chosen metal is silver, which dielectric constant is taken from [72], and the cladding is air, $\varepsilon_{\mathrm{die}} = 1$.
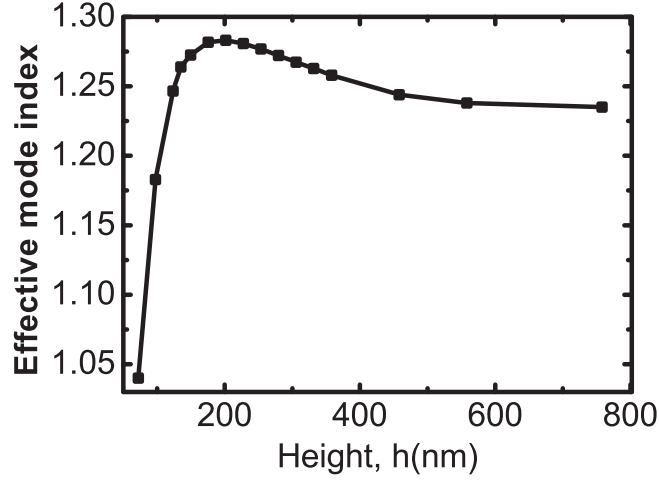
Figure 3.8: Effective mode index variation of CPW with height. The tip radius and taper angles are fixed to 5nm and 20^0, respectively. The operating wavelength is set to 600nm for these calculations. The chosen metal is silver, which dielectric constant is taken from [72] and the cladding is air $\varepsilon_{\text{die}} = 1$.

cut-off energies, the CPW becomes spread at both sides of the trench, thus losing their lateral confinement, similar to the SPP in a planar interface. Also, it can be observed how the energy values of those cut-offs decrease for sharper angles, a fact consistent with the higher confinement of channels with smaller angles. The origin of such cut-offs is intimately related to the finite height of the channels, whose effect in the confinement will be clarified at the end of this subsection.

Let us understand the confinement mechanism in the channel SPP. The EM fields of the CPW fundamental mode are confined in the gap region, as it is displayed for the electric field in Figure 3.7(a). 70% of the energy propagates within the gap which, approximating such confinement area by a rectangular shape, and averaging both vertical and horizontal transversal sizes, has an average length of 0.1λ (with 139 nm and 34 nm of vertical and horizontal confinement, respectively). The confinement mechanism provided by the gap is well understood within the effective index method [94]. In such method, the triangular trench is seen as stacks of finite metal-dielectric-metal gaps with different widths. The effective index of those gaps is larger for smaller widths and larger than the SPP effective index in a flat surface. Accordingly, the channel effective index is higher at the bottom of the channel, a fact reflected in the confinement of the electric field in the lower part as shown in Figure 3.7(a). The effect of the gap in the confinement can be also appreciated in the polarization of the electric field which is mainly horizontal, thus following the normal direction of both sides of the gap. Such gap boundary conditions are present in other PWs,

like slots or rectangular trenches and therefore they share similar confinement mechanisms and propagating properties [111].

The effect of confinement is also reflected in the propagation losses of the channels. In Figure 3.7(c) we display the propagation length versus the wavelength for the same parameters of the channels considered in panel (b). The propagation lengths diminish for larger energies and smaller angles, accordingly to the increase of confinement described above. The propagations lengths of the channel are in general much smaller than the ones for the SPP in a flat surface, due to the higher degree of confinement. For example, in comparison with the propagation length for the SPP in a planar geometry (30λ at $\lambda = 600\,\text{nm}$), the channels with angles $\theta = 20°$ and $\theta = 30°$ only propagate 3λ and 4λ, respectively. Only for larger angles, the propagation are comparable but at the expense of large lateral delocalization.

The dependence on the height L largely affects the confinement of the channel SPP. For studying such dependence, the modal effective index variation $n = \frac{k_{\text{SPP}}}{k_0}$ with the height is displayed in Figure 3.8 for a fixed wavelength ($\lambda = 600$nm), angle ($\theta = 20°$) and tip radius ($R = 5$nm). At very large heights the modal index is practically constant because the CPW mode is confined deeply in the gap, nearby the tip. Consequently, the channel mode does not feel the upper part of the metallic substrate [19]. When we decrease the height, the mode starts to be pushed outside the gap and it starts feeling the wedge borders of the channel which have a confining effect as commented in the previous subsection. Accordingly, the effective index of the channel SPP increases until it reaches a maximum at $L = 200$nm. For smaller heights than the maximum, the mode starts to be importantly expelled from the gap and the wedges. Therefore, we can observe how the effective index decreases. Finally at the height $L = 72\,\text{nm}$, the channel modal size is so delocalized that its effective index equals the one of an SPP in a flat surface ($n_{\text{flat SPP}} = 1.04$). In other words, the channel presents a cut-off for that height in which the mode is highly delocalized at both sides of the gap.

3.2.3 Effect of corrugation on conventional waveguides

In order to fulfill the potentialities of light guiding based on SPP excitation, it is convenient to search for improved ways to control and tune the propagation characteristics of SPP modes. The research is specially critical for longer wavelengths, like the telecom regime, due to the high vertical delocalization of the SPPs in a flat surface, as commented at the end of subsection 3.2.1. The use of corrugations [31, 112, 113, 20, 32, 33] has proven to be crucial in expanding the SPPs properties to the far-infrared, terahertz and microwave regimes. Such approach, also known as spoof plasmonics, permits to confine the otherwise highly delocalized SPP modes and it will be further explained in section 3.3. In this subsection we

transfer the spoof concept to conventional PWs modes in the optical and telecom regime. We demonstrate how the introduction of a subwavelength periodic modulation in a PW strongly modifies the guiding characteristics and the confinement of its SPP modes.

First we consider a SPP mode that is bound to and propagates along the channel plasmon waveguide (CPW) similar to that studied in subsection 3.2.2 (see the upper illustration in Figure 3.9). In Figure 3.10(a) we plot the dispersion relation (frequency versus parallel momentum) of the fundamental CPW mode whose geometrical parameters are taken from experiments [16]. The metal considered is gold and its frequency-dependent dielectric function is taken from [74]. Due to the finite depth of the grooves, this CPW mode presents a cutoff wavelength with the SPP in a flat surface which, for the chosen set of geometrical parameters (see caption of Figure 3.10), appears at around $1.3\,\mu$m. Grey curves in Figure 3.10(a) illustrate the modification of the CPW dispersion relation induced by a sub-λ periodic modulation in the CPW (see the lower illustration in Figure 3.9, and the inset of Figure 3.10). The depth of the grating is fixed at 30nm for all the considered periods. We can observe that the main effect of the corrugation is to shift the cutoff wavelength of the CPW mode to longer wavelengths, reaching a value of $1.6\,\mu$m for the shortest period analyzed, $d = 25$ nm. Also, as its dispersion relation departs more from the light line, the bands for the corrugated CPW becomes more localized than the smooth one. Our finding that cutoff wavelength shifts to longer wavelengths in corrugated V-grooves could explain why in the experiments exists a propagating CPW mode in the wavelength range between 1424-1640 nm [17], despite the fact that calculations for a non-corrugated V-groove with the same geometrical parameters ($\theta = 25$ degrees) predict a cutoff wavelength of 1440 nm [19]. Scanning electron microscope images reveal the presence of a weak periodic modulation in CPWs that are fabricated with focused ion beam techniques (see an example in Figure 3.11). When a shallow corrugation of 30 nm with a period $d = 25$ nm is now introduced in the V-groove, our calculations show that the cutoff wavelength moves from 1440 nm to 1750 nm, larger than the wavelength range analyzed in the experiments.

A much stronger effect associated with a longitudinal sub-λ periodic corrugation is seen for another type of SPP modes: a slot SPP mode that propagates along a gap carved between two metal plates. Here we consider a waveguide structure that is composed of a slot perforated on a thin silver film deposited on top of a glass substrate ($\varepsilon = 2.25$), see inset of Figure 3.10(b). The main geometrical parameter that controls the dispersion relation of these modes is the width of the slot, w. Figure 3.10(b) shows two different non-corrugated structures, $w_1 = 75$ nm (red line) and $w_2 = 135$ nm (grey line). The geometry of the corrugation is chosen so the distance between two widest points, W, is equal to w_2 whereas the minimal distance is equal to w_1, see inset of Figure 3.10 (b). The introduction of a periodic modulation has a drastic effect on the dispersion relation. One could naively
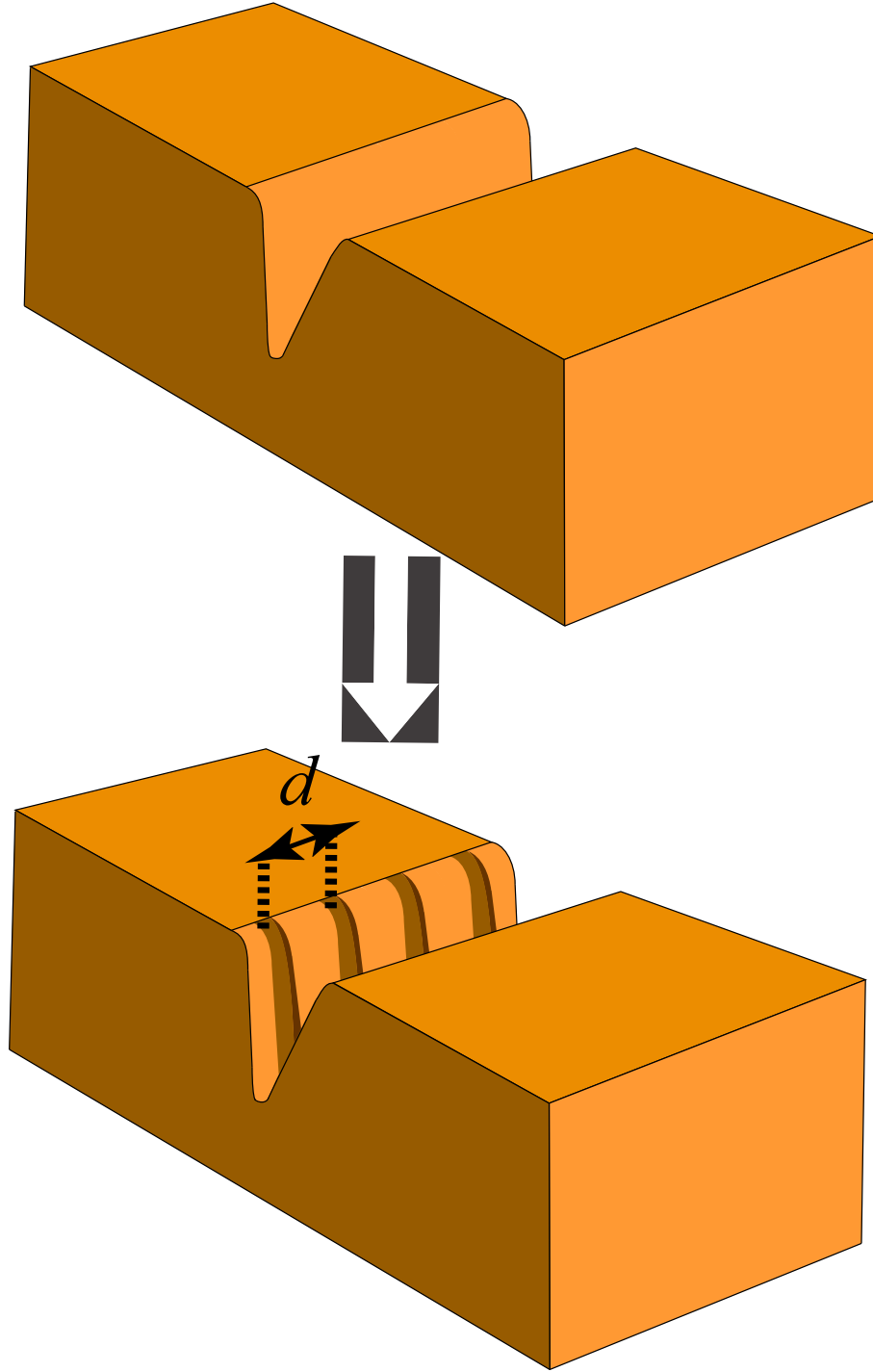
Figure 3.9: 3D illustration of a non-corrugated (upper) channel and a corrugated one (lower) with periodicity d. The rest of the defining geometrical parameters are displayed in the inset of Figure 3.10(a).
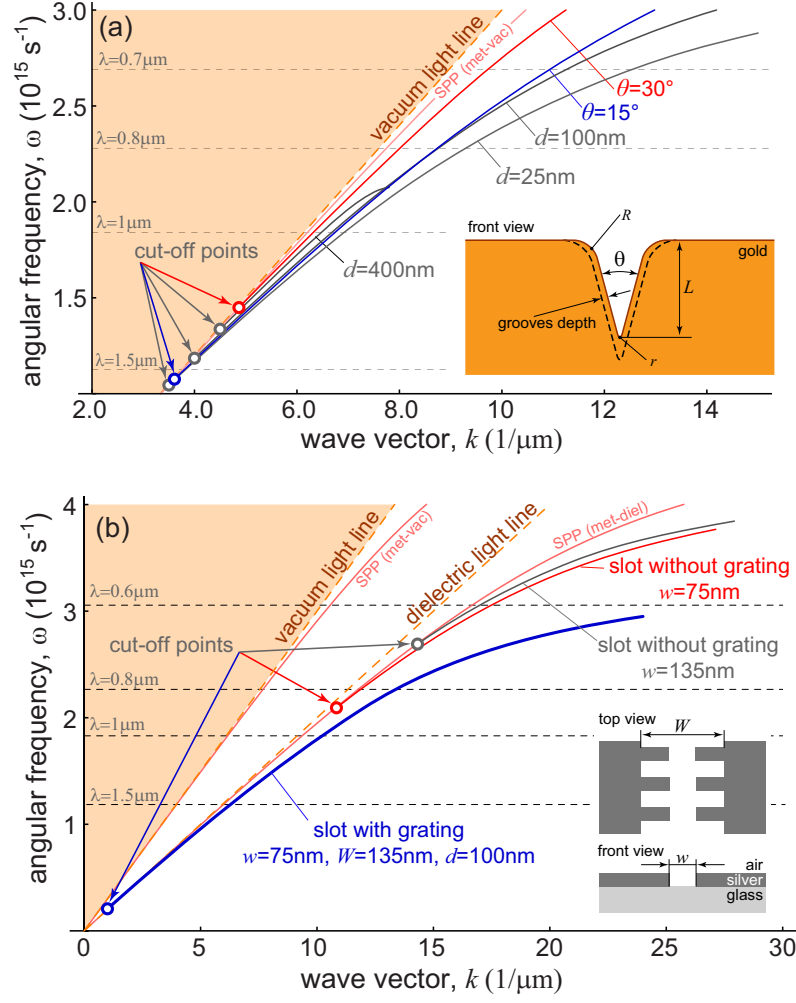
Figure 3.10: (a) Dispersion curves for CPWs. Red and blue curves represent those for a CPW mode without corrugation for two different angles, $\theta = 30^0$ and $\theta = 15^0$. The depth of the CPW is $L = 1.1\,\mu\text{m}$ and the radii of curvature at the edges are $r = 10\,\text{nm}$ and $R = 100\,\text{nm}$. Grey lines display the dispersion curves for CPW corrugated modes ($\theta = 30^0$) where the depth of the grating is fixed at $30\,\text{nm}$ and three different periods are studied: $d = 400\,\text{nm}$, $d = 100\,\text{nm}$ and $d = 25\,\text{nm}$. Inset shows the geometry. (b) Dispersion curves for slot waveguide modes. Red and grey curves are those for the slot without grating. Blue curve is the dispersion curve for a corrugated slot. The period of the grating is $d = 100\,\text{nm}$.
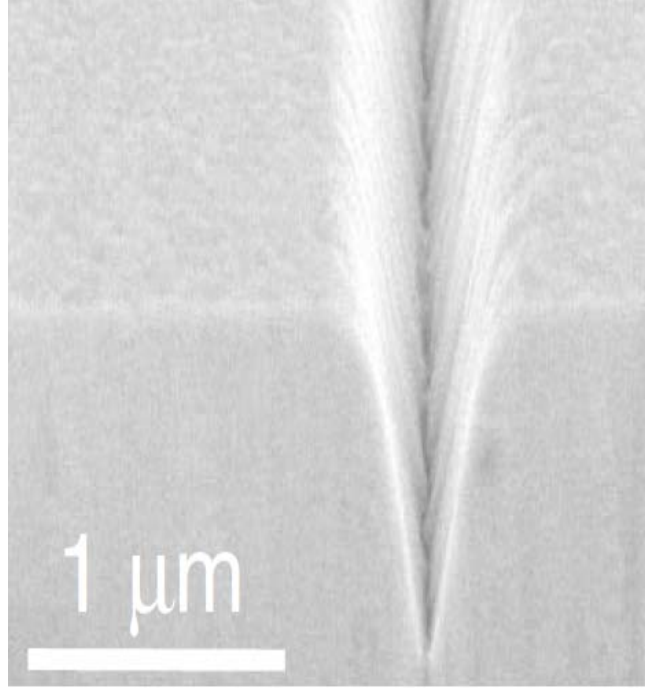
Figure 3.11: Scanning electron microscope image from the V-groove used in reference [17], where a corrugation can be observed inside the groove.

expect that the resulting dispersion curve would be located between those for the non-corrugated cases. However, the band for the corrugated slot departs strongly from those two curves, resulting in a much longer cutoff wavelength and larger confinement. Then, our results clearly show that a sub-λ periodic modulation could also be used to improve the guiding properties of slot waveguide modes.

In the following we show that a sub-λ periodic modulation could indeed create a SPP mode in structures where, without corrugation, laterally confined SPP modes are not supported. As an example we consider a metallic ridge (height h and width L) placed on top of a substrate made of the same metal (see Figure 3.12). For small enough heights the metal substrate expels the mode and there is a cutoff with the SPP in a flat surface. The cut-off origin is similar to the one appearing for the WPW discussed in subsection 3.2.2. For the parameters $h = 120\,\mathrm{nm}$ and $L = 37.5\,\mathrm{nm}$, the ridge structure does not support the propagation of SPP modes transversally localized due to such cut-off. In Figure 3.12(a) we render the dispersion relations of the geometrically-induced SPP modes that emerge when a sub-λ periodic modulation is introduced into a gold ridge. The six curves correspond to different values of the modulation depth, g. As clearly seen in the figure, even the weakest modulation ($g = 20\,\mathrm{nm}$) is able to create a laterally confined SPP mode (*i.e.*, the dispersion curve is lower than the SPP-curve for the flat metal surface). When the depth g is enlarged,
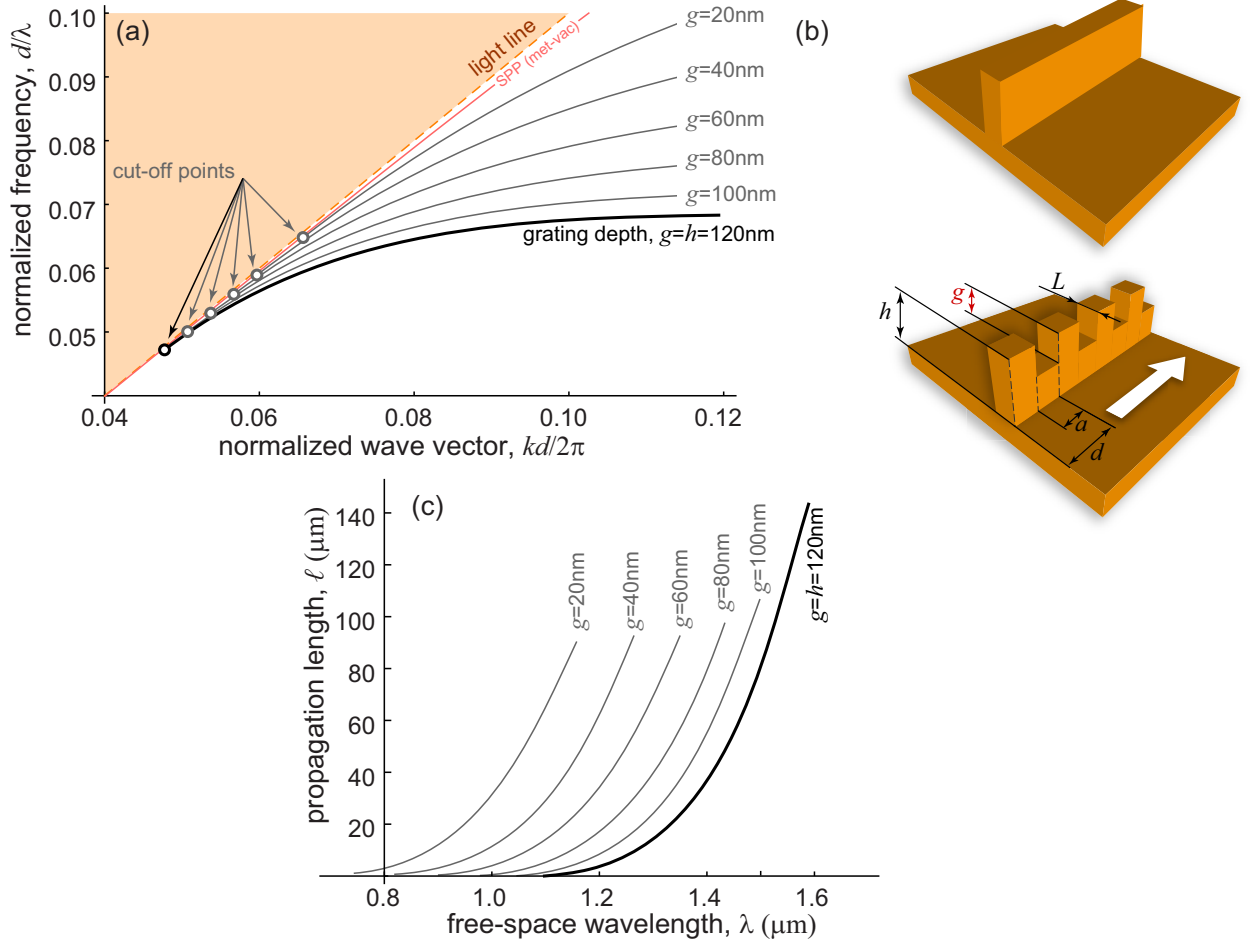
Figure 3.12: Creation of a geometrically-induced ridge SPP mode. (a) Dispersion curves for SPP modes running on a corrugated ridge with different modulation depths. (b) Geometry of the ridge structure without (upper one) and with a modulation (lower one): corrugation period $d = 75$ nm, width of the ridge $L = 37.5$ nm, height of the ridge $h = 120$ nm and the grooves width $a = d/2 = 37.5$ nm. (c) Corresponding propagation lengths for the cases analyzed in panel (a).

the dispersion relation further departs from the light line, increasing the mode localization. Accompanying this movement, the cutoff frequency shifts to lower frequencies. The increase in the mode localization also affects the propagation length of these geometrically-induced SPP modes. For a fixed wavelength, the transversally confined mode propagates less distance for larger g, as seen Figure 3.12(c). In addition, we can also observe that the propagation is strongly reduced for optical wavelengths $\lambda < 800$ nm but not so much for telecom wavelengths. For example for a telecom wavelength $\lambda = 1.31\,\mu$m, the most confined case ($g = h = 120$ nm) has a propagation length of 13λ. Therefore we can conclude that the effect of corrugation strongly modify the dispersion properties of conventional PWs and

it permits to increase deeply the SPP confinement at telecom wavelengths.

3.2.4 Domino plasmon polaritons

In this subsection we present a new waveguide inspired by the increase of confinement due to the corrugation on a ridge structure. In the case where a ridge has a grating depth equal to the height of the ridge, the geometry resembles a 1D chain of metallic box-shaped particles placed on top of a metal film (see Figure 3.13). Due to the structure resemblance with a domino chain, we call this new type of SPP as domino plasmon polariton (DPP). The properties of its guided modes are defined by the geometric parameters characterizing the dominoes as illustrated in Figure 3.13, *i.e.*, periodicity d, height h, lateral width L, and inter-domino spacing a. Importantly, the DPP, due to its planar symmetry, presents a full geometrical compatibility with lithographic technics in contrast to other suitable but complex waveguides in the telecom regime, like channels and wedges.

The DPP mode has a high electric field localization near the top part of the domino structure, see Figure 3.13. In this figure the horizontal slice renders the electric field intensity evaluated in a xz-plane that is parallel to the metal substrate and located 5 nm above the domino's top face. The intensity also presents a strong subwavelength confinement in the transverse direction. Regarding the vectorial nature of the EM-fields associated with a DPP, the electric field has mainly y and z components (see yellow lines in the vertical plane of Figure 3.13) whereas the magnetic field has predominant x and z components (see blue lines in the horizontal plane of Figure 3.13).

It is worth discussing the differences between the DPP modes described above and the plasmon modes supported by 1D arrays of metal nanoparticles placed on top of a dielectric film [114, 115]. In this last case, the near-field coupling between the localized plasmon modes of the metal nanoparticles leads to the formation of a very flat plasmon band characterized by a deep sub-λ confinement but very short propagation lengths. However, in the case of DPP modes, the presence of the metal substrate results in the emergence of a "polaritonic" part in the dispersion relation that runs close to the SPP band of the flat surface [see Figure 3.14(a)]. Accordingly, DPP modes operating within this polaritonic regime posses a very long propagation length but, as expected, are much less confined than the modes supported by a chain of metal nanoparticles. The propagation properties of a DPP mode depend on the lateral size (L) of the structure. By varying this dimension we could find optimal properties of the DPP mode, like enhanced field confinement and/or longer propagation length. Figure 3.14(a) shows the DPP dispersion curves for four different values of L. As this width is reduced from $L = \infty$ to $L = 0.5d = 37.5$ nm, the cutoff frequency increases and, for a fixed frequency, the wavevector is smaller for narrower dominoes. Accordingly,
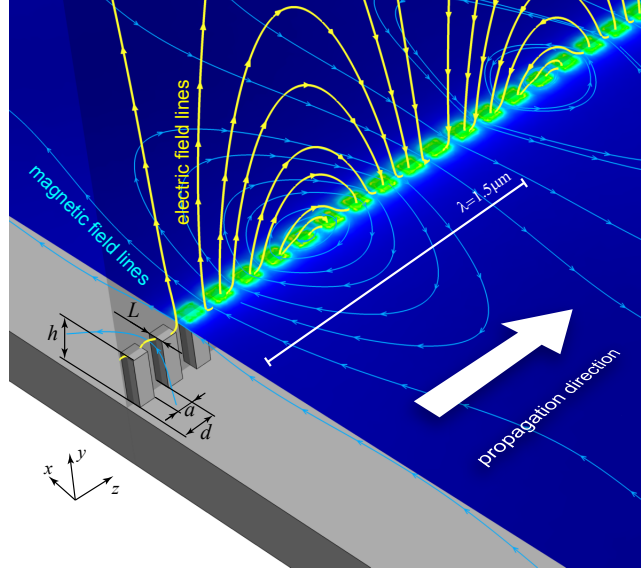
Figure 3.13: Electric and magnetic fields associated with a domino plasmon polariton mode. Yellow (blue) lines represent the electric (magnetic) vector field. Electric field intensity map is evaluated on a horizontal plane located on top of the domino structure. The geometrical parameters of the domino structure are: modulation period $d = 75$ nm, lateral width of the ridge $L = 37.5$ nm, height $h = 120$ nm and the grooves' width $a = d/2$. The operating wavelength is $\lambda = 1.5 \, \mu$m. The definition of the cartesian axes is also depicted.

the DPP propagation length for very narrow dominoes is larger than that for a wider one (see Figure 3.14(b)). Interestingly, even for a domino width of only $L = d/2 = 37.5$ nm, the propagation length at $\lambda = 1.5 \, \mu$m is around $80 \, \mu$m, a value that is larger than those predicted for other types of SPP modes that present high confinement like channels [19] or wedge plasmon polaritons [106].

Figures 3.15(a-c) render the electric field intensity distribution for three DPPs in a plane perpendicular to the propagation direction located at the center of the gap between two dominoes. The lateral sizes analyzed are $L = 0.5d$, $L = 3.5d$ and $L = 10d$ and the operating wavelength is $\lambda = 1.5 \, \mu$m. The color scale is the same for the three distributions. As expected from the dispersion curves, the DPP mode is more confined for the wider domino, $L = 10d$. When the domino width is decreased, the EM energy is carried within a bigger volume. This is illustrated in Figs. 3.15(a-c) by representing the energy isocurves for the three different dominoes. The percentage associated with each isocurve measures the amount of EM energy (with respect to the total one) carried out through the area inscribed into the curve. This is a valid way to define the modal size of a waveguide mode [116]. A closer look at the intensity distributions shows that the electric field in the case $L = 3.5d$
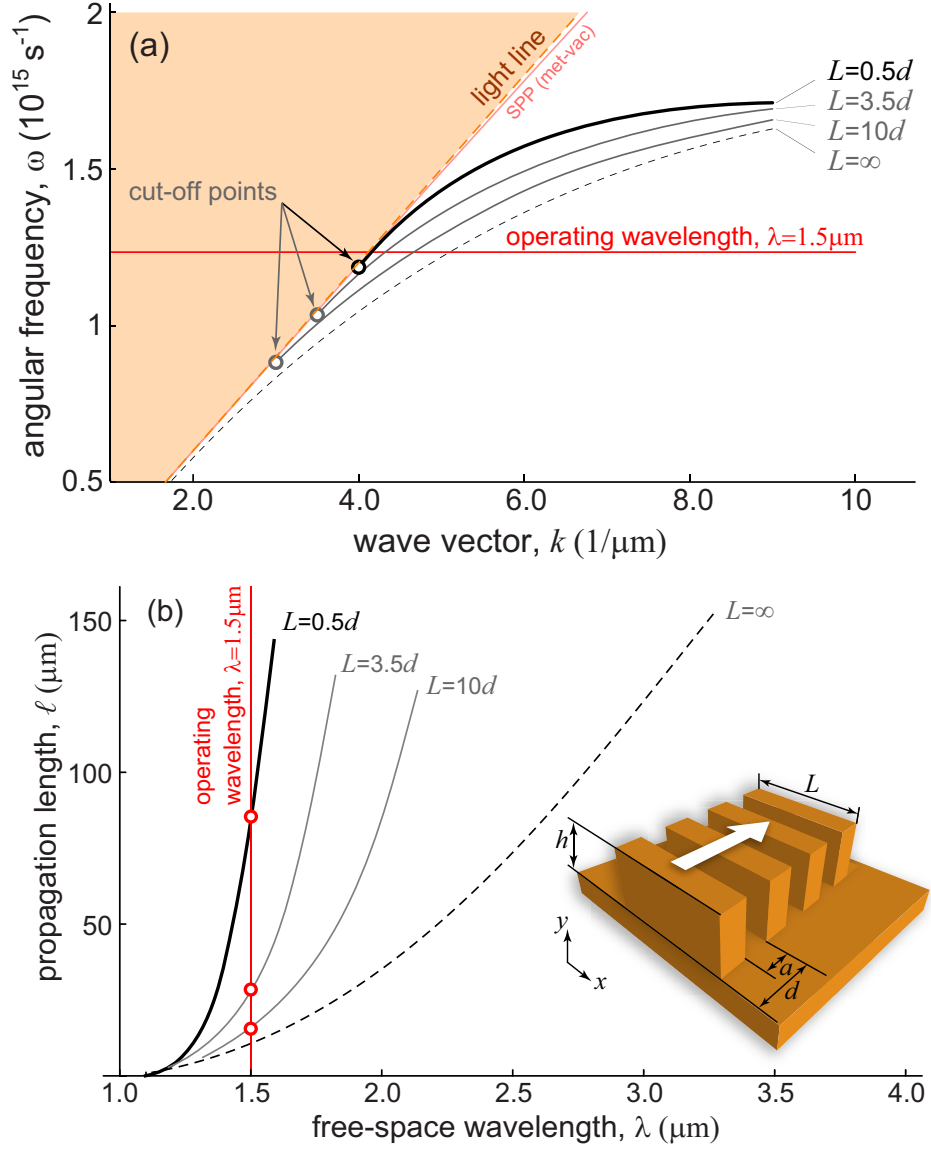
Figure 3.14: Dependence of the DPP propagation characteristics with the domino width. (a) Dispersion curves of the DPP modes for four different widths L of the structure. The geometrical parameters of the domino structure are the same as in previous figure. (b) Propagation length versus free-space wavelength for the four structures analyzed in panel (a).

presents a stronger field enhancement than $L = 10d$ or $L = 0.5d$ cases. In all cases, a comparison of electric field distributions with the operating wavelength (white bars) in Figure 3.15 illustrates the strong sub-λ transversal confinement associated with the propagation of DPP modes. These results show a superior confinement compared to conventional CPW and similar to the WPW in the telecom regime [106].
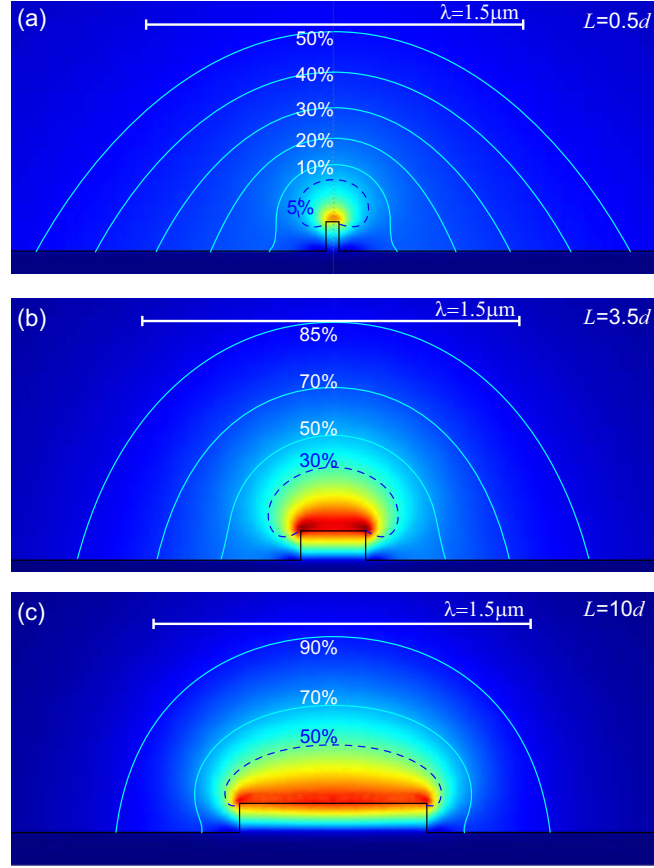
Figure 3.15: (a-c) Electric field intensity distributions evaluated at $\lambda = 1.5\,\mu$m in a plane perpendicular to the propagation direction for three different values of L. The blue lines show several energy isocurves: the percentage measures the amount of energy (with respect to total one) carried through the area bounded by the corresponding isocurve.

3.3 Terahertz plasmonic waveguides

3.3.1 Concept of spoof plasmon

The terahertz (THz) electromagnetic (EM) spectrum covers one of the most interesting and multidisciplinary research fields in science nowadays [24, 25, 23]. Such interest is due to its potential applications in astronomy [29], medicine [26], imaging [117] and information processing [118]. An important goal within the THz research is the development and integration of photonic circuits that must be efficiently coupled to THz sources and detectors [30]. Within this endeavor, several approaches for THz waveguides have been proposed recently, mainly divided in dielectric [36, 37] and conventional SPP PWs [119, 98]. In general, the miniaturization of dielectric waveguides is diffraction-limited and they are not monolithic, which make their integration more difficult for circuitry purposes. The extremely high delocalization of SPPs in the THz, as we illustrated in subsection 3.2.1, also makes conventional SPPs unpractical for THz circuitry purposes. In order to provide a solution to such high delocalization, the concept of spoof plasmons (SPOOFSPs) was introduced [31, 76]. The SPOOFSPs has proven to be a very promising route in transferring the optical SPPs properties to the design of ultra-compact THz waveguides [20, 34, 33, 120–122, 31, 76]. In this subsection we describe the concept and main characteristics of SPOOFSPs in corrugated grooves within the approximation of perfect electric conductor for the metal [67]. Such approximation is very good for the THz frequencies due to the high values of the plasma frequency of the metal ($\sim 10^3$THz).

Let us understand the main ingredients for supporting SPOOFSPs in the surface of a perfect electric conductor (PEC), with properties analogous to those of SPPs in a flat surface for the optical regime. In the PEC approximation, the electrons of the metal shield perfectly the EM fields, its conductivity gets infinite and no energy can be stored inside the metal. Since the existence of the SPPs is linked to the storage of electromagnetic energy in the surface of the metal, no surface EM modes exist in a flat PEC interface. If we want to mimic the behavior of optical SPPs in a flat surface in this limit, we can perforate tiny holes or trenches in order to store effectively the EM energy in the flat interface (see an example of a sketch in Figure 3.16(a)). The indentations, that act like open cavities, must be smaller than the wavelength in order to create modes with transversal modal sizes at sub-λ scales. In addition, the cavities need to be sufficiently close, at subwavelength distances, in order to couple to each other, a requirement that allows the propagation in such effective medium. Finally, we need some degree of symmetry in order to avoid the radiation to escape to the far-field, and therefore to have confined surface modes. This confinement can be achieved through a sub-λ periodic modulation of the indentations. The subwavelength periodicity
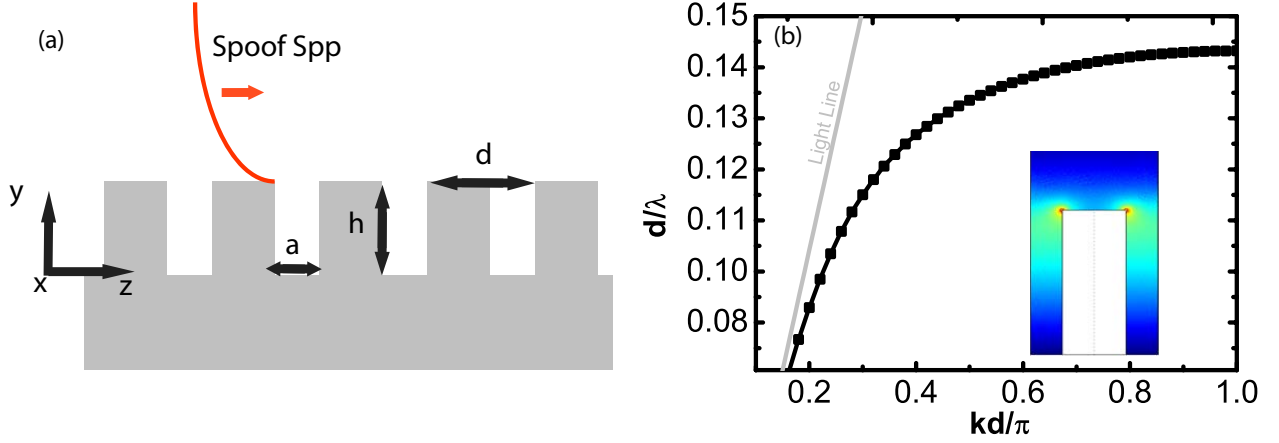
Figure 3.16: (a) Cross-section of the grooves array along the propagation direction. The parameters a, h and d characterizing the groove structure are displayed. (b) SPOOFSP dispersion relation for a groove metallic structure with parameters $a = 0.5d$ and $h = 1.5d$. The frequency and the modal wavevector are normalized by the periodicity d due to the universal scaling of PEC metals as explained in the main text. Inset: Spatial surface plot of the electric field norm, in arbitrary units, of a flat SPOOFSP at $k_z = \frac{\pi}{d}$. The intensity goes from red (highest) to blue (lowest).

makes the radiation of each periodic element to destructively interfere at the far-field due the opposite phases between the elements [123]. Therefore, with such periodic symmetry, these modes are confined and do not radiate outwards the surface. Accordingly with such sub-λ features, the perforated metal behave like an effective metallic homogeneous material or metamaterial [31, 124] which supports SPOOFSPs.

Once we have identified the main ingredients to have SPOOFSPs, let us study the geometrically-induced modes supported by an array of grooves in a PEC substrate with air cladding. The properties of the groove structure are defined by the periodicity d, groove width a and height h (see Figure 3.16(a)). Such structure supports a SPOOFSP which propagates in the z-direction and is confined in the y-direction. In Figure 3.16(b), we show the dispersion relation of the fundamental SPOOFSP for an array of grooves with structural parameters $a = 0.5d$ and $h = 1.5d$, where d is the periodicity. Once a and h are chosen proportional to d, the choice of the periodicity only scales the operating frequency. Such property is due to the scale invariance of Maxwell equations and the PEC condition in the metal, since the latter does not depend on the frequency. Therefore, for universal frequency characterization, we make use of the normalized frequency $\frac{d}{\lambda}$ and normalized propagating wavevector $\frac{kd}{\pi}$, since it permits us to characterize spoof (PEC) structures independently of the chosen d.

We can observe in Figure 3.16(b) the high similarity between the SPOOFSP dispersion

relation and that for the SPP band in a flat surface at optical frequencies (recall Figure 3.3(a)). At small frequencies, the SPOOFSP is very close to the light line and accordingly, the mode is poorly confined. For larger frequencies the modal wavevector increases and the SPOOFSP gets subwavelength confinement. Finally, for higher frequencies, we can see in Figure 3.16(b) that the band reaches an asymptote. At such limit, the group velocity is zero and therefore the mode has an upper cut-off, which coincides with the border of the first Brillouin zone ($k_z = \frac{\pi}{d}$). The physical origin of the asymptote is the Bragg's condition imposed by the periodicity, *i.e.*, a π phase difference between the periodic elements, which cancels the radiation along the propagation z-direction due to the destructive interference between the elements. Therefore, at the Braag condition, the SPOOFSP supported by the groove must resonate vertically in the y direction inside the gaps, as displayed in the inset of Figure 3.16(b).

The guided mode of a groove array is the analogous spoof version to the SPP in a flat surface, studied in subsection 3.2.1 at optical frequencies, since its confinement properties can be understood in a similar fashion. The confinement mechanism in the interface of the grooves apertures is, as in the case of the SPP in a planar interface, related to the equation $k_z^2 + k_y^2 = (\frac{\omega}{c})^2$. The condition $k_z > \frac{\omega}{c}$ force k_y to be purely imaginary and consequently, the mode gets confined in the transversal y-direction, as shown in the inset of Figure 3.16(b). Because of such analogy, the SPOOFSP supported by the groove is not localized in the transverse x-direction, which limits its use for confined THz circuits. To better understand the dispersion physics of the SPOOFSP, let us make use of a simplified model that consider a single mode inside the groove, that neglects diffraction effects, and for the condition $\lambda >> d$. The approximation for the dispersion relation in such model is [76]

$$k_z = k_0 \sqrt{1 + \left(\frac{a}{d}\right)^2 \tan^2(k_y h)}, \tag{3.3}$$

where k_z is the modal wave vector, $k_0 = 2\pi/\lambda$, and the y component of the wave vector inside the grooves, k_y, is related with the corresponding z and x components by $k_x^2 + k_y^2 + k_z^2 = k_0^2 = (\frac{\omega}{c})^2$. The EM fields inside the grooves are independent of z and x for the chosen longitudinal polarization and thus $k_z = k_x = 0$, $k_y = k_0$, which corresponds to a TEM mode. This means that equation (3.3) presents an asymptote for $k_0 h = \pi/2$ or, in other words,

$$\frac{d}{\lambda} = \frac{d}{4h}, \tag{3.4}$$

which corresponds to the resonance condition for the TEM mode inside the groove. With such resonant condition the estimated normalized frequency is 0.17 and the numerical calculation is 0.14, thus showing a reasonable agreement with the simplified model. The departure from the single mode model is due to the effect of the borders in the groove

apertures. In fact, we can certainly see at the inset of Figure 3.16(b), that the maximum of the electric field is displaced slightly outside the groove. Therefore the height h in the pure resonant condition (3.4) is effectively elongated, and the normalized frequency asymptote in the full calculation is shifted to a smaller value.

3.3.2 Domino spoof plasmons

Due to the relatively recent development of the THz technology, there is a need to design photonic circuits for the THz regime in order to develop integrated-applications [23, 30]. For such purpose, it is highly desirable to develop THz-waveguides that fulfill the requisites of easy fabrication, subwavelength confinement, low loss, and device flexibility. In this subsection, we study the domino plasmon approach, considered in section 3.3.4, as a novel SPOOFSPs waveguide [38] fulfilling all those requisites for the THz regime. Since the electrons oscillations are completely damped at THz frequencies, *i.e.*, $\omega < \gamma$ in equation (3.1), the physics of the domino structure, at THz frequencies, substantially differs between the same structure at telecom wavelengths. To remark such difference, we specifically call its supported modes as domino spoof plasmons (DSPs).

Dispersion relation

The properties of the domino spoof plasmon, are mainly controlled by the geometric parameters defining the dominoes, *i.e.*, periodicity d, height h, lateral width L, and inter-domino spacing a (see the inset of Figure 3.17(a)). In contrast with corrugated wires [20], this is a planar system and should not pose significant manufacturing problems which is much simpler than corrugated V-grooves [34] or wedges [33].

In the following we describe the dispersion properties of DSPs and to gain physical insight, we model the metal as a perfect electric conductor (PEC). Later, realistic metals will be considered, letting us discern what is the frequency regime where DSPs display the most promising behaviour. Due to the simple scaling properties of PECs, we choose the periodicity d as the unit length. We first set the inter-domino spacing to $a = 0.5d$, but this value is not critical for the properties of DSPs as it will shown below. DSP bands present a typical surface plasmonic character, *i.e.*, the bands approach the light line for low frequencies and the curve reach an horizontal frequency limit at the edge ($k_{\text{edge}} = \pi/d$) of the first Brillouin zone (see Figure 3.17(a), notice that only fundamental modes are plotted). In all cases DSP modes lie outside the light cone, a fact that explains their non-radiative character in the transverse directions. While the limit frequency of SPPs for large k is related to the plasma frequency, the corresponding value for DSPs is controlled by the geometry as in the case of the SPOOFSP supported by grooves, that were shown in the subsection above.
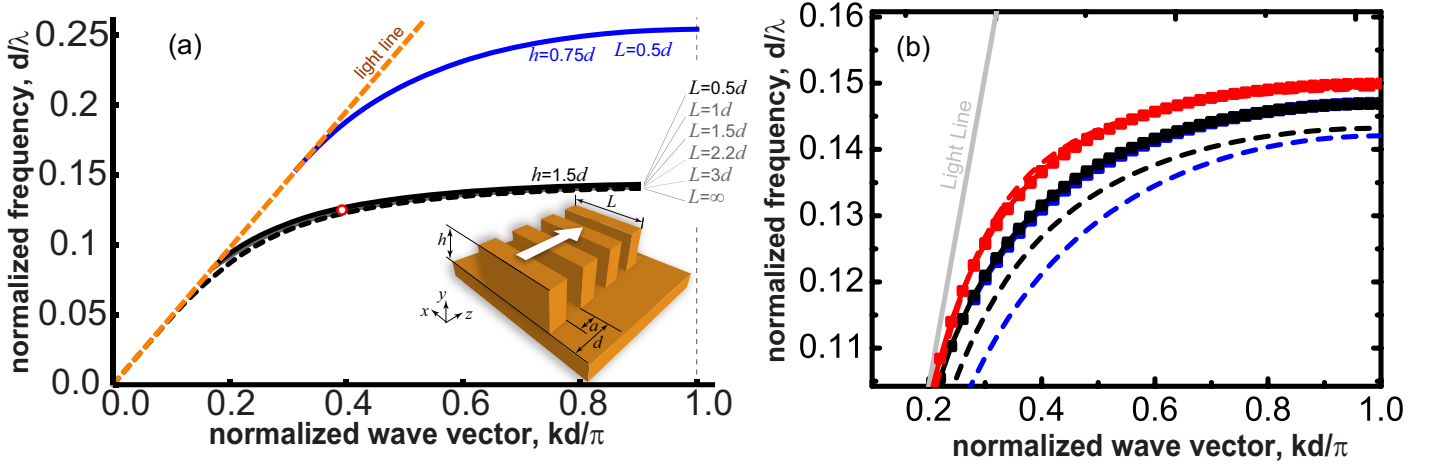
Figure 3.17: (a) Dispersion relation of DSPs for various lateral widths L. Black and grey (blue) lines correspond to height $h = 1.5d$ ($h = 0.75d$). Dashed line stands for infinitely wide dominoes ($L = \infty$). Metals are modelled as PECs. Inset: diagram of the domino structure and geometric parameters (the arrow depicts the mode propagation direction). (b) Dispersion relation of DSPs for three inter-dominoes spacings a for lateral widths $L = 0.5d$ (squares) and $L = \infty$ (dashed lines). The height is set to $h = 1.5d$. The three different a values are: $a = 0.25d$ (red), $a = 0.5d$ (black) and $a = 0.75d$ (blue). Notice that the bands corresponding to $a = 0.25d$ for both L are almost indistinguishable.

The influence of the height h in a DSP with $L = 0.5d$ is clear: the band frequency rises for short dominoes ($h = 0.75d$, blue line) as compared with that of taller ones ($h = 1.5d$, black line). In particular, the values of the normalized frequencies asymptotes are 0.25 and 0.14 for the two heights, respectively. Interestingly, the ratio between both frequencies $\frac{0.25}{0.14} \approx 2$ coincide approximately with the ratio of both heights ($\frac{1.5}{0.75} = 2$). Such behaviour would be expected for the (1D) array of grooves studied in the previous subsection, which has approximately a normalized resonant frequency equal to $\frac{d}{4h}$. In fact, the similar behavior between both structures is supported by the representation of a DSP band, with $L = \infty$ (1D groove array) and $h = 1.5d$ (see the dashed line in Figure 3.17(a)). In comparison with the corresponding band for $L = 0.5d$ (black line), the $L = \infty$ bands display similar quantitative values and almost identical qualitatively results.

Let us study the variation of the bands with the domino interspace a, fixing the height ($h = 1.5d$). In Figure 3.17(b), we display the dispersion relations for $L = 0.5d$ at three different a values: $a = 0.25d$ (red squares), $a = 0.5d$(black squares) and $a = 0.75d$ (blue squares). For comparison purposes, we have represented the case $L = \infty$ for the same values of a, which are displayed by dashed-lines with the same colors, respectively. We can observe the same qualitative SPOOFSP behavior for all the bands independently of a. The bands
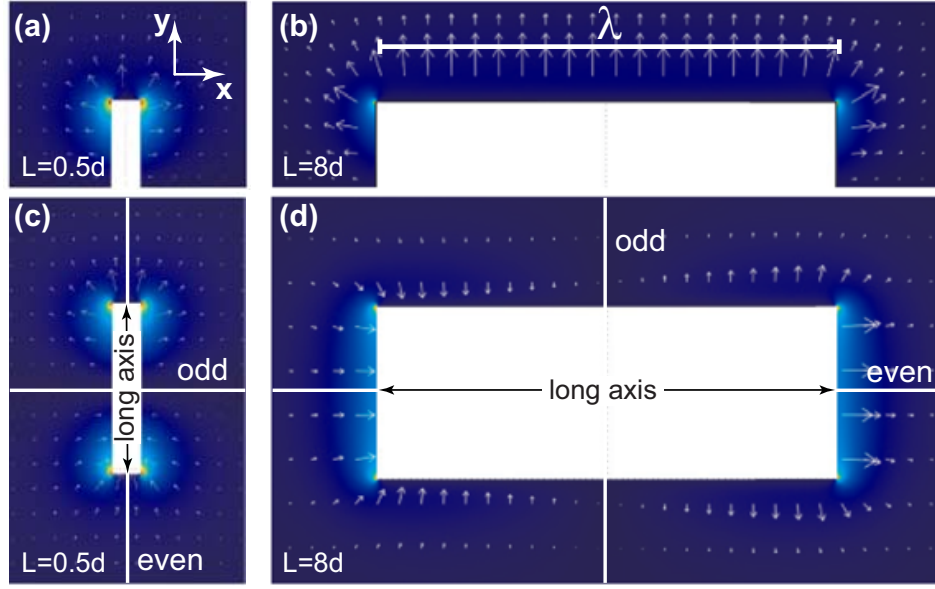
Figure 3.18: (a) and (b), Modal shape of DSPs: transverse (xy) electric field (arrows) and horizontal (xz) electric field (color shading) for DSPs of height $h = 1.5d$ and widths $L = 0.5d$ (a) and $L = 8d$ (b). (c) and (d), Same as in panels (a) and (b), but now for a 1D array of free-standing metallic rods ($h = 3d$). The designations *even* and *odd* label the symmetries of the modes with respect to the corresponding white lines. The fields in (a)-(c) are plotted for $d/\lambda = 0.125$, marked with a red open dot in fig 3.17, the white bar in (b) being the wavelength (valid for panels (a)-(c)). The field in (b) is computed for the same k as in panels (a)-(c), corresponding now to $d/\lambda = 0.056$. In panels (a)-(d) metals are modelled as PECs.

are not displaced far from the case $a = 0.5d$, thus showing that a is not as critical as the height h (recall Figure 3.17(a)). Additionally, it can be seen the tendency of the bands to get higher normalized wavevectors for larger values of a. Such qualitative behaviour coincides for both L representative cases. That characteristic is consistent with the TEM model for the 1D groove structure. The smaller values of a decrease the effects of diffraction inside the groove, since both $L = 0.5d$ and $L = \infty$ modes converge numerically to the same TEM mode. Therefore, the resonant condition (3.4) is fulfilled more accurately for both L, and the values of the normalized asymptote frequency increases to 0.15, which is closer to the 0.17 pure TEM model. In fact, in agreement with that interpretation, we can observe that in the case $a = 0.25d$, both, $L = 0.5d$ and $L = \infty$ bands, can hardly get distinguished. In the rest of the section, we set the inter-domino spacing to an intermediate value, $a = 0.5d$, which impose less demanding conditions for fabrication purposes.

Those results lead us to the most striking characteristic of DSPs, which is their behaviour when the lateral width L is changed. All bands in the range $L = 0.5d, \ldots, 3d$ lie almost on

top of each other (Figure 3.17(a), grey curves). In other words, the modal effective index, $n_{\text{eff}} = k/k_0$, is rather insensitive to the lateral width L. If we now look at the numerically computed dispersion relations of Figure 3.17(a) in the light of equation (3.3) for the grooves, it seems that the DSPs fulfill $k_y \approx k_0$ in equation (3.3) for a wide range of L. Remarkably, the bands remain almost unchanged even for $L = 0.5d$, whose modal size is well inside the subwavelength regime, as observed in the field distribution plotted in panel (a) of Figure 3.18 for $L = 0.5d$. Notice that the white bar representing λ in panel (b) is valid for panels (a)-(c), and the modal size, defined as the FWHM of the modulus of the Poynting field distribution, is $0.21\,\lambda$ for panel (a). Therefore the DSP shows a deep subwavelength traversal size, which makes it promising for sub-λ circuitry at very long-wavelengths, in which the PEC condition applies.

The insensitivity of DSPs to the lateral size L constitutes the foundation of some of the devices presented later, and can be linked in an intuitive way to the structure geometry. The key role played by the metallic substrate can be explained by comparison of DSPs and the modes of a Yagi-Uda structure, *i.e.*, a periodic array of free standing metallic rods [123, 114, 125]. For small L, the dispersion of DSPs of height h is identical to that of the fundamental mode of a Yagi-Uda structure of height $2h$. The field of the DSP is simply the upper half of the fundamental mode of a rod array of height $2h$, see Figs. 3.18(a) and (c). For large L this correspondence does not hold anymore, as demonstrated by comparison of panels (b) and (d) which display completely different symmetries. For dominoes, a mode with the same symmetry as the Yagi-Uda mode shown in panel (d) is forbidden because the horizontal electric field has to be zero at the metallic ground. This mode suppression is critical because the frequency of the fundamental mode of a Yagi-Uda structure, which is essentially controlled by the length of the long axis of the rods, is very sensitive to the lateral width L, being very different for short vertical rods and long horizontal rods.

It is also important that the air gaps between the dominoes are laterally open. Let us imagine that, instead of being open, they were laterally closed by PEC walls. Since the electric field inside the gap points longitudinally from one domino to the next one, it should then vanish at both PEC lateral walls, giving a cosine-like x dependence. It is then clear that the mode frequency should increase when the lateral size L is decreased, arriving to the conclusion that the modes of such structure have L-sensitive bands. In contrast, for DSPs, the boundary conditions at the laterally open gaps are more akin to perfect magnetic walls, and the corresponding field is approximately x-independent inside the air gaps even when $L \rightarrow 0$. For instance, Figure 3.18(a) suggests that for $L = 0.5d$ a substrate of lateral size about 2λ should be sufficient to achieve the mentioned effects.
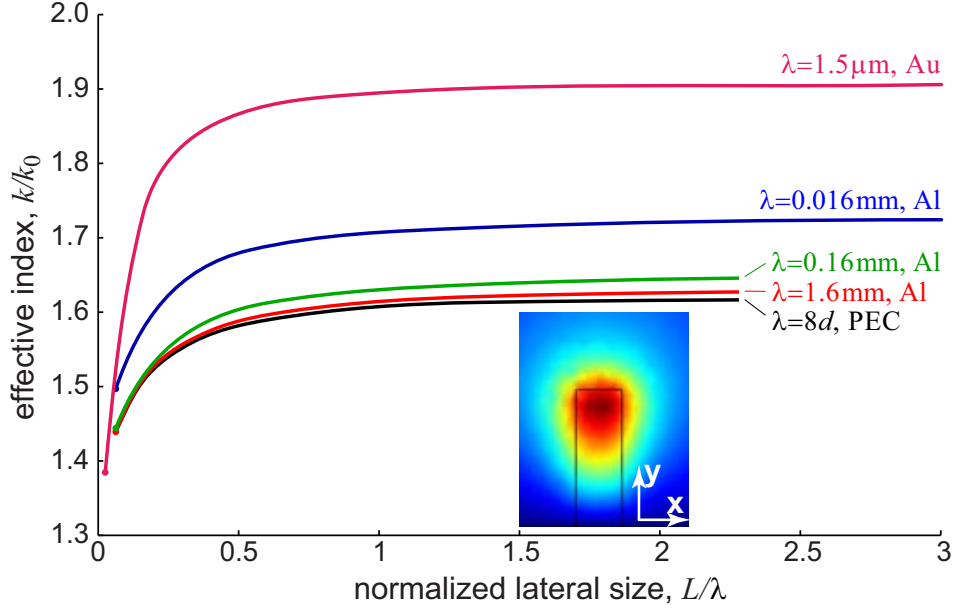
Figure 3.19: DSP modal effective index as a function of lateral dimension L in units of wavelength. Various operating frequency regimes are considered: $\lambda = 1.6\,\text{mm}$ (red), $\lambda = 0.16\,\text{mm}$ (green), $\lambda = 0.016\,\text{mm}$ (blue), and $\lambda = 1.5\,\mu\text{m}$ (magenta). To compute them, a realistic description of the metals is used. As described in the main text, the periodicity d is different for the various operating frequencies, and $h = 1.5d$, $a = 0.5d$, $L = 0.5d, \dots, 24d$. Inset: Electric vector field (modulus) distribution in the transversal plane between dominoes for $L = 0.5d$ and $\lambda = 0.16\,\text{mm}$. For appreciating the x-dependence in the gap, we have drawn with a black line the cross-section of the nearby dominoes.

The effect of realistic metals

The lateral insensitivity in the dominoes at terahertz frequencies is very different from DPPs at the optical and telecom regimes where the skin depth penetrates importantly into the metal. Therefore the PEC condition breaks and so the simplicity of the DSP physics, including the lateral insensitivity (see Figure 3.14). Such situation is general to conventional plasmonic modes in the optical and telecom regime for which sub-λ lateral confinement is not a trivial issue ([126] or see subsection 3.2.2). When the lateral size of the structure supporting such modes becomes subwavelength, either the modal size grows, or the effective index increases largely. Let us scrutinize in more detail the role played by the lateral dimension L, considering now realistic metals in DSPs in which the frequency regime can change its properties. The periodicity d is chosen to set the operating wavelength in the desired region of the EM spectrum, and L is varied in the range $L = 0.5d, \dots, 24d$, while the remaining parameters are kept constant ($a = 0.5d$, $h = 1.5d$). Aluminum is selected for low frequencies, where metals behave almost like PECs. To take into account the realistic

effect of the metal, we use surface impedance boundary conditions [67] with the dielectric permittivity of Aluminum taken from Ref. [73]. This approximation is justified in the THz regime due to the nanometer sized skin depths in real metals [127]. In order to work at $\lambda = 1.6\,\text{mm}$, providing an operating angular frequency of the order of 0.2 THz, we first consider $d = 200\,\mu\text{m}$. The evolution of the modal effective index as a function of the lateral dimension normalized to the wavelength is plotted in Figure 3.19. The curves corresponding to a PEC (black line) and aluminum at $\lambda = 1.6\,\text{mm}$ (red line) are, as expected, almost identical. We can now quantify the sensitivity of the effective index to L, its variation being only about 12% even when L goes from $L = \infty$ to $L = 0.5d = \lambda/16$, well inside the sub-λ regime. The rapid variation of n_{eff} when $L << d$ can be understood with the help of equation (3.3). In this limit the EM fields start to be x-dependent inside the air gaps, as verified by inspection of the fields (inset of Figure 3.19). Such variation is reflected in the fact that $k_x \neq 0$ and consequently $k_y < k_0$ inside the gap. Then, if we assume that equation (3.3) is still valid in this limit, it predicts that the modal effective index is reduced when $L \rightarrow 0$. To investigate the performance of DSPs at higher frequencies, the structures have been scaled down by factors $1/10$ and $1/100$. The fact that the curves corresponding to $\lambda = 0.16\,\text{mm}$ (green line) and $\lambda = 0.016\,\text{mm}$ (blue line) do not lie on top of the previous ones is a signature of the departure of aluminum from the PEC behaviour. Nevertheless, even at $\lambda = 0.016\,\text{mm}$, the variation of the effective index is still smaller than 15%, a property that can be exploited for taper design in the far infrared, albeit with slightly reduced performance as compared with the THz case. When the operating frequency moves to the telecom regime ($\lambda = 1.5\,\mu\text{m}$, magenta line) the variation of the effective index is much larger (about 38%). Let us mention in passing that, for this wavelength, we use gold due to its lower losses and so the geometric scaling had to be different (the periodicity is now $d = 0.13\,\mu\text{m}$) in order to support a domino plasmon polariton mode. The important message of Figure 3.19 is that, although a variation of n_{eff} begins to be noticeable when the lateral dimension L goes below $\lambda/2$, DSP bands are fairly insensitive to L in the range $L = 0.5d, \ldots, 24d$ when operating at low frequencies. Such property has, to our knowledge, never been reported for spoof plasmon modes in corrugated wedges, channels, or wires.

Propagation and bending losses

Now that we have identified the THz range as one of the most promising spectral regimes for the DSP, we will characterize the corresponding absorption (ohmic) and bending losses. Figure 3.20(a) displays the propagation length ($\ell = [2\text{Im}(k)]^{-1}$) of DSPs as a function of wavelength for various widths L ($d = 200\,\mu\text{m}$ for all curves). The only source of damping in the domino structure is absorption by the metal as no radiation losses occur in the straight
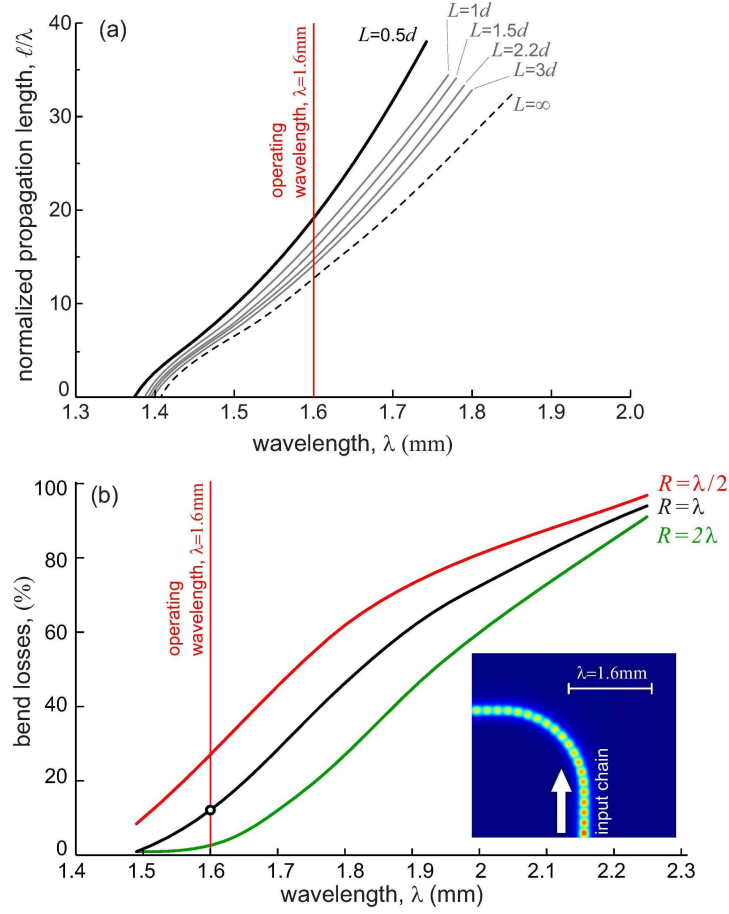
Figure 3.20: (a) Normalized propagation length of DSPs in rectilinear guides of various L as a function of λ ($h = 1.5d$, $a = 0.5d$, $d = 200\,\mu$m). (b) Bend loss of DSPs for three radii of curvature as a function of λ ($h = 1.5d$, $a = 0.5d$, $L = 0.5d$, $d = 200\,\mu$m). Inset: Poynting vector field (modulus) distribution in a horizontal plane slightly above ($30\,\mu$m) the height of the bend (top view). The chosen wavelength and radius of curvature are marked with an open black dot in panel (b). The red solid vertical lines in both panels indicate the operating wavelength used later, $\lambda = 1.6$ mm.

waveguide configuration. In order to take into account the inherent ohmic losses in the metal, we use surface impedance boundary conditions [67] with the dielectric permittivity of Aluminum taken from Ref. [73]. The propagation length is very short for small λ, when the first Brillouin zone edge is reached, but it rises at increasing wavelengths as the dispersion curve approaches the light line. Several lateral widths L are considered and it is observed that DSPs structures of smaller L travel longer distances before their modes are damped. The radiation losses occurring in a waveguide of $L = 0.5d$ with a 90° bend are analyzed in panel (b). In this case the metal is modelled as a PEC for easier evaluation of radiation

93

losses. Data for three radii of curvature of the bend, $R = \lambda/2, \lambda, 2\lambda$, are presented. In all three cases, losses are low for small λ but they grow as the wavelength is increased, *i.e.*, when the modal wave vector approaches k_0. The dependence with the radius of curvature of the bend is not surprising either, radiation losses being higher for smaller radius of curvature. Consideration of absorption and bending losses suggests that $\lambda = 1.6\,\text{mm}$ can be an appropriate operating wavelength. For $\lambda = 1.6\,\text{mm}$ and $L = 0.5d = 100\,\mu\text{m}$, the modal size is $0.34\,\text{mm}$, *i.e.*, about $\lambda/5$. The propagation length is about 20λ, much larger than the size of the devices presented later, and the bend loss for $R = \lambda$ is reasonably low, about 10%. Notice that for corrugated V-grooves, the bend loss for $R = 2\lambda$ is around 50% [34].

3.3.3 Circuitry elements based on dominoes spoof plasmons

We have characterized the main properties of domino plasmons and shown its promising propagation characteristics for applications in THz circuitry. In this subsection we design some DSPs passive devices enabling the spatial and temporal modulation of EM fields in the THz. We choose the operating wavelength to be $\lambda = 1.6\,\text{mm}$ and $d = 200\,\mu\text{m}$, which correspond to the far THz [23]. In all the next computations the metal is considered as a PEC, to easily quantify the device radiation loss.

Waveguide tapering [20, 35, 128, 33] is interesting for field concentration and amplification, both important requirements for imaging applications [129, 130] and circuit integration [131]. Tapering is expected to be easy in domino structures due to the insensitivity to lateral width L of the dispersion relation of DSPs. This hypothesis is confirmed in Figure 3.21(a), which shows a top view of the propagation of power along a tapered domino structure. The lateral widths of the waveguide are $L_{\text{in}} = 16d$ at the input port (bottom) and $L_{\text{out}} = 0.5d$ at the output port (top). The length of the taper is $16d$, *i.e.*, two wavelengths at the operating frequency, corresponding to a taper semi-angle of $\theta = 31°$. Remarkably, reflection is smaller than 2% and only 5% of the incoming power is lost as radiation due to the shrinkage of the lateral dimension along the taper. Panels (b)-(e) are cross sections at different positions along the taper, vividly showing the process of field subwavelength concentration and enhancement. A similar design does not work in the telecom regime due to the sensitivity of DSP bands to the lateral dimension L at those frequencies, as shown in subsection 3.2.4. A more adiabatic taper, with smaller change of n_{eff} per unit length, would not circumvent the problem because absorption loss can be high in the telecom regime (for instance, for $\lambda = 1.5\,\mu\text{m}$, $d = 0.13\,\mu\text{m}$, and $L = 16d$, the propagation length is $\ell = 1.2\,\mu\text{m}$).

We now discuss how to construct power dividers and directional couplers [37, 132]. Fig-
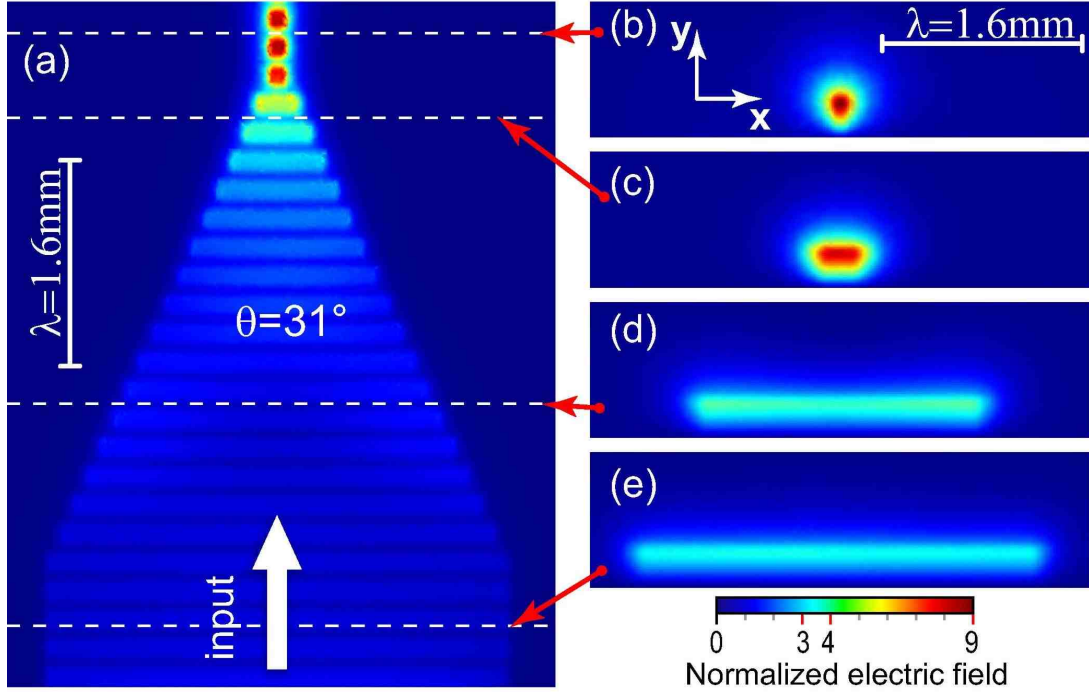
Figure 3.21: (a) Poynting vector field (modulus) distribution in a horizontal plane slightly above (30 μm) the height of the tapered domino structure (top view). The lateral width is tapered from $L_{\mathrm{in}} = 16d$ to $L_{\mathrm{out}} = 0.5d$ ($h = 1.5d$, $a = 0.5d$, $d = 200\,\mu\mathrm{m}$, $\lambda = 1.6\,\mathrm{mm}$). (b)-(e), Amplitude of electric field in transverse vertical planes (longitudinal views) at the locations shown by white dashed lines in (a). The white bar in (b) showing the operating wavelength is valid for the last four panels.

ure 3.22 plots the dispersion relation of the modes supported by one and two parallel domino chains. Black solid line corresponds to the DSP of $L = 0.5d$. For two parallel waveguides (both with $L = 0.5d$), interaction gives rise to symmetric and antisymmetric supermodes which, for a separation $s = 0.5d$, are shown by magenta curves with the solid line depicting the even supermode, whereas the dashed one represents the odd supermode. Blue dashed-dotted line corresponds to a wider structure of $L = 1.5d$ and, importantly, this band stays very close to that of the $s = 0.5d$ even supermode. Due to this good overlapping, a simple linking of a wide domino structure with $L = 1.5d$ to two parallel domino chains (widths $L = 0.5d$ and separation $s = 0.5d$) should not result in an important impedance mismatch. This is verified in Figure 3.23(a), displaying a top view of a power divider based on the previous idea. The input port ($L = 1.5d$) at the bottom feeds the wide domino which, after 5 periods, is linked to two parallel domino structures ($L = 0.5d$, $s = 0.5d$). Due to symmetry only the even supermode is excited. The lateral separation s between the individual waveguides is then increased, followed by 90° waveguide bends. Simulations show
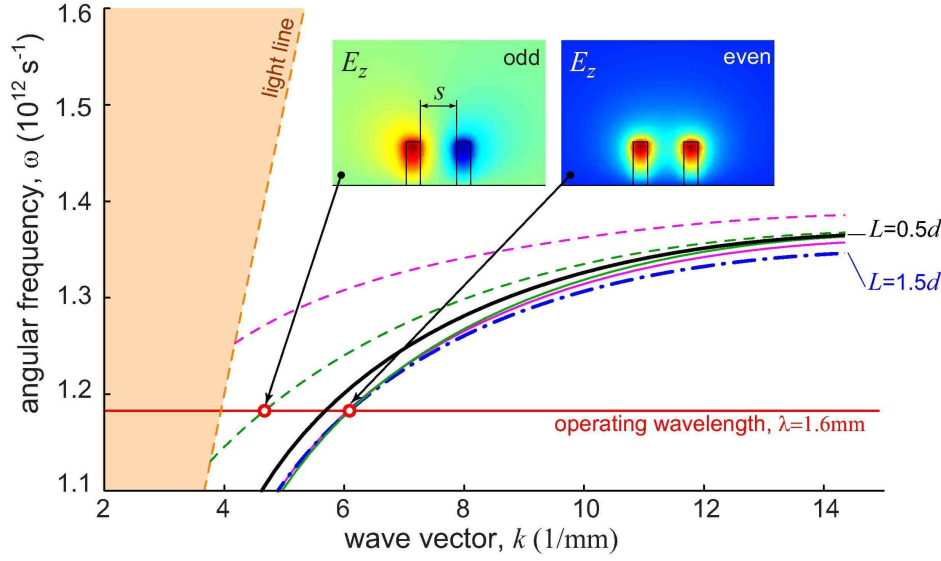
Figure 3.22: Dispersion relations corresponding to one and two parallel domino structures. Black solid (blue dashed-dotted) line is for DSP of $L = 0.5d$ ($L = 1.5d$). Magenta solid (dashed) line is for the even (odd) supermode of parallel domino structures separated a distance $s = 0.5d$, whereas green solid (dashed) line is the corresponding supermode for $s = 1.25d$. The individual dominoes in double structures have $L = 0.5d$. The red solid horizontal line indicates the operating wavelength, $\lambda = 1.6$ mm, used later. Insets: longitudinal electric field for the odd and even supermodes of two parallel domino structures separated a distance $s = 1.25d$ at the operating wavelength, and displayed in a transverse cross section lying at the center of the inter-domino gaps. For all structures $h = 1.5d$, $a = 0.5d$, $d = 200\,\mu$m.

that reflection is also negligible in this power splitter. Total radiation loss in the device is equal to that happening in the bends (previously discussed in Figure 3.20(b)), each being 5% of the incoming power, which is small taking into account that the bend radius is equal to the operating wavelength.

Coupling between parallel domino structures can also be easily understood with the help of Figure 3.22, displaying with green lines the even (solid) and odd (dashed) supermodes for parallel domino chains separated a distance $s = 1.25d$. The insets show the modal shape of both modes. A larger s is chosen in this simulation to prevent the cut-off of the odd supermode. The coupling length needed to exchange the carried power between the waveguides is estimated as $\pi/|k_{\text{even}} - k_{\text{odd}}| = 2.05$ mm. This value agrees with the result found in the simulation of a directional coupler. Figure 3.23(b) displays a top view of two parallel domino chains ($L = 0.5d$) separated a distance $s = 1.25d$. A mode is launched in the left bottom waveguide and characteristic beatings with the predicted coupling length
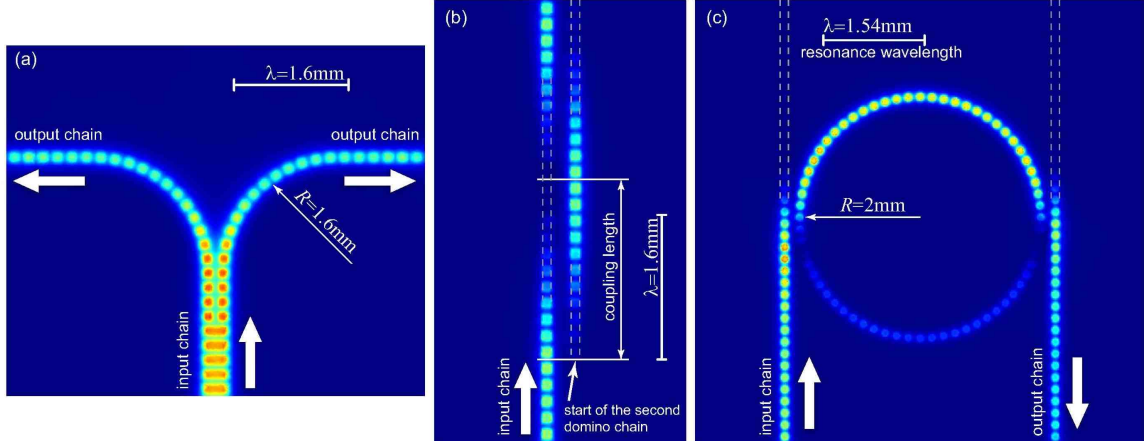
Figure 3.23: Top view of: (a) Power divider. (b) Directional coupler. (c) Waveguide ring resonator. The Poynting vector (modulus) is displayed in a horizontal plane slightly above (about $30\,\mu$m) the height of the domino structures. White bars show the operating wavelength in each panel. The various geometric parameters are described in the main text, the periodicity being $d = 200\,\mu$m in all cases.

are observed when a second waveguide is located close to it.

As a final example a waveguide ring resonator is demonstrated, able to route various frequencies to different output ports [18]. To show once more the robustness of our proposal, this device has been designed with posts of circular cross section as seen from above (radius $r = 0.28d$), instead of square cross section parallelepipeds. The top view of this device is displayed in Figure 3.23(c). For the chosen geometric parameters (ring radius $R = 2\,$mm, minimum separation in the coupling sections $s = 1.25d$), it is possible to drop a resonant wavelength $\lambda = 1.54\,$mm at the output port. Non-negligible radiation losses only occur at the bends in the waveguide ring and they are about 25% of the input power, reasonably small considering that no optimization was attempted.

All the devices described in this section have been studied with PEC condition and therefore are scalable to other regimes as it was pointed in subsection 3.3.2. Recently almost all the previous calculated domino devices and properties have been successfully tested with experiments in the GHz regime [121, 122, 133] and in the far-infrared [134]. These results encourage the realization of the domino structure for the THz regime in which there are specially distinctive and important applications.

3.3.4 A planar approach: L-shape Domino

In this subsection we present a new design for a THz waveguide, based on the concept of domino plasmons described in the previous subsections. The structure consists of a
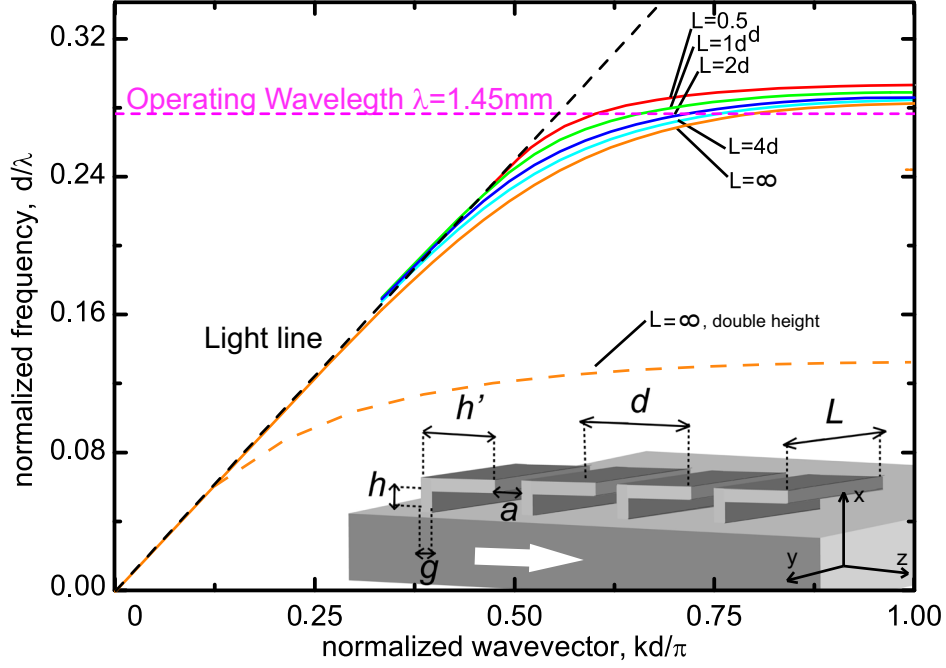
Figure 3.24: Inset: sketch of the structure under study with a description of the geometrical parameters (the arrow defines the mode propagation direction). Main panel: the bands associated with the fundamental EM modes supported by the system for $d = 400\,\mu$m, $h = 0.2d$, $h' = 0.6d$, $g = 0.06d$ and several lateral widths L: $L = 0.5d$ (red), $L = 1d$ (green), $L = 2d$ (blue), $L = 4d$ (cyan), $L = \infty$ (orange). The band for the fundamental EM mode in which $h = d$ and $h' = 0.6d$ and $L = \infty$ is also shown (dashed orange line).

periodic chain of 3D L-shaped metallic particles attached to a metallic substrate. A sketch of the structure analyzed in this work is shown in the inset of Figure 3.24. This illustration also displays the geometrical parameters of the THz waveguide: the periodicity d, particle base-width g, inter-particle spacing a, lateral width L, and the short and long sides of the letter L, h and h', respectively. Two-dimensional arrays of mushroom-shaped metal particles (similar to L-shaped) have been studied before [135, 136] mainly in the context of plasmonic metamaterial surfaces. Here we propose to reduce the dimensionality, aiming for one-dimensional (1D) THz waveguiding.

Figure 3.24 displays the bands of the fundamental surface EM modes for L-shape dominoes waveguides with different lateral sizes ($L = 0.5d, 1d, 2d, 4d, \infty$). The rest of the parameters are fixed to $h = 0.2d$, $h' = 0.6d$, $g = 0.06d$ and $a = 0.4d$. All the geometrical parameters are referred to the period of the array, d, that is chosen to be $d = 400\mu$m, in order to have an operating wavelength within the THz regime. In order to take into account the inherent ohmic losses in the metal, we use surface impedance boundary conditions [67]
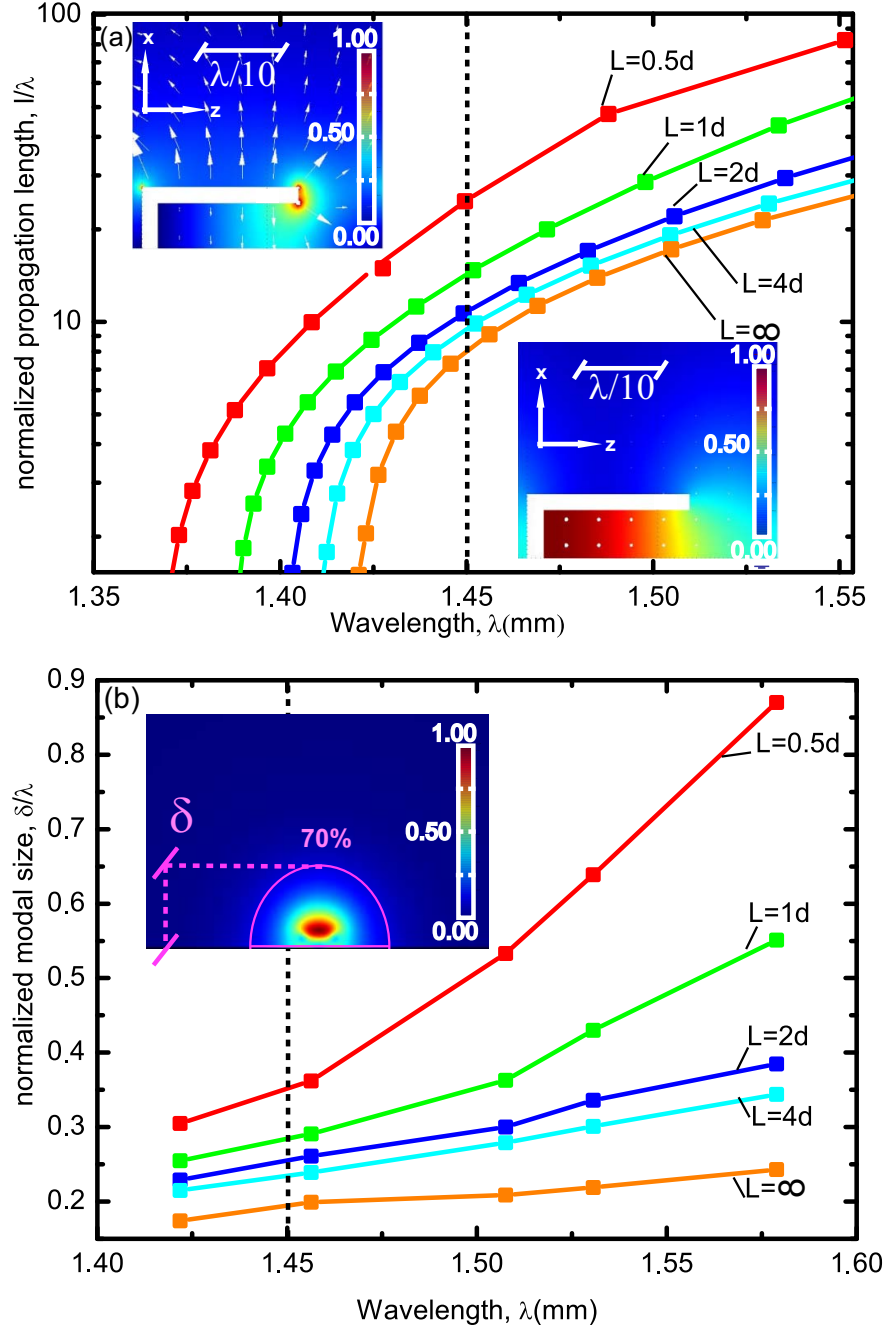
Figure 3.25: (a) Normalized propagation length of the L-shaped spoof domino for different L's as a function of λ. Upper (lower) inset: the electric (magnetic) field contour cut along a xz-plane that shows a single unit cell for $L = \infty$ and evaluated at $\lambda = 1.45$mm. (b) Normalized modal size δ (see definition in the main text) for different L's as a function of λ. Inset: Poynting vector field (modulus) distribution in a transverse xy-plane placed between the particles also evaluated at $\lambda = 1.45$mm for $L = 0.5d$. The magenta line shows the area that carries 70% of the total modal power. In both panels, the geometrical parameters are the same as those used in Figure 3.24.

with the dielectric permittivity of Aluminum taken from Ref. [73].

As observed in Figure 3.24, the surface EM modes supported by the array of L-shaped metallic particles display dispersion relations resembling those of the DSPs described in subsection 3.3.2. The bands depart progressively outside the light cone, thus corresponding to confined propagating EM modes, and they reach a frequency asymptote at the first Brillouin zone. The most remarkable property of the L-shaped dominoes is the weak dependence of the bands with the lateral size L as shown in Figure 3.24. It can be seen that relatively large lateral changes do not severely modify the bands, similar to the DSP dispersion properties shown in subsection 3.3.2. In the case of the DSPs, the asymptote frequency is mainly dictated by the height of the dominoes, whereas in the L-shape domino, such role is mainly played by the sum of the two sides of the letter L, $h + h'$. The empty space between consecutive metal particles create an effective groove whose depth is defined by $h + h'$ [137]. The resonance wavelength of this groove, $4(h + h')$, determines approximately the asymptote of the bands. From that estimation, we would obtain a normalized asymptotic wavelength, d/λ, of 0.31, close to that observed in Figure 3.24, around 0.28. Following that simple estimation, an increase by a factor of 2 on $h + h'$ results in a reduction by half of the asymptote frequency. Accordingly, such reduction is observed in Figure 3.24 (orange dashed line). The fact that the propagating properties in the L-shaped THz waveguide can be tuned by two geometrical parameters (h and h') adds more flexibility respect to the conventional domino one. Moreover, the L-shaped domino can also present a very high planar aspect ratio by making $h << h'$, which could have important implications for fabrication purposes.

For any practical implementation of the L-shape dominoes, it is important to characterize their propagation losses. Figure 3.25(a) depicts the propagation length versus wavelength for the lateral sizes L considered above. In general, it can be observed how the propagation length decreases at smaller wavelengths for all the lateral sizes. In addition, we can observe the propagation length diminishes for larger lateral sizes at a fixed wavelength. Those decreases are a consequence of the deeper confinement at higher frequencies due to the larger modal wavevectors (see Figure 3.24). Nevertheless, there is a broad wavelength bandwidth presenting long enough propagation lengths for the whole range of lateral sizes. For example, for an operating wavelength of 1.45mm, the propagation length ranges from 8λ (for $L = \infty$) to 24λ (for $L = 0.5d$).

As can be seen in the upper and lower insets of Figure 3.25(a), the electric and magnetic fields of the fundamental surface EM mode are very strongly confined to the waveguide. In order to evaluate this localization more quantitatively, we make use of the modal size δ, defined as the transverse size corresponding to the circular area that carries 70% of the modal power (see the inset of Figure 3.25(b) for an illustration). Figure 3.25(b) shows the

evolution of δ as a function of the wavelength for the lateral sizes considered above. As expected, the modal size diminishes at higher frequencies until the asymptote frequency is reached. Notice however the very deep-subwavelength confinement associated with the surface EM modes: at the operating wavelength $\lambda = 1.45$mm, the modal size ranges from 0.19λ (for $L = \infty$) to 0.36λ (for $L = 0.5d$). The insensitivity to lateral sizes L and the
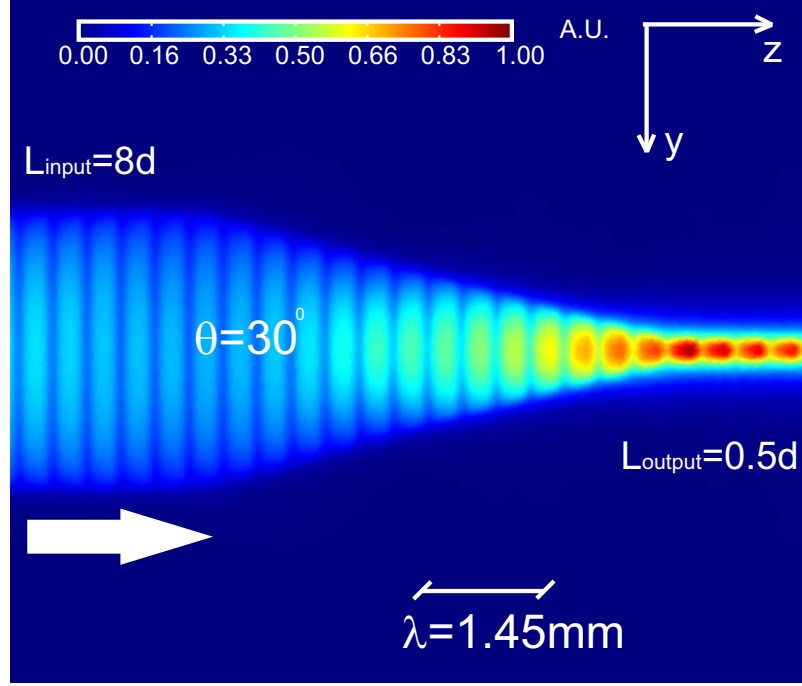
Figure 3.26: Poynting vector field (modulus) distribution in a yz-horizontal plane above ($x = 0.5d$) the tapered L-shaped dominoes. The lateral width is changed gradually from $L_{\text{in}} = 8d$ to $L_{\text{out}} = 0.5d$ with an angle $\theta = 30°$. The rest of the parameters are as in previous figures. The vector field is evaluated at $\lambda = 1.45$mm and is in arbitrary units.

long-enough propagation lengths, can be exploited to concentrate THz energy along the waveguide, by using, for instance, a tapered configuration (such as in Figure 3.26). In this structure, the lateral width of the waveguide is reduced in the direction of propagation. As the effective mode propagation constant presents a weak dependence with lateral width, it is expected that the change in L does not increase the scattering and reflection losses of the surface EM mode when it propagates along the tapered waveguide. As shown in Figure 3.26 this is indeed the case in our structure. The device performance is analyzed at an operating wavelength of 1.45mm, where the lateral width of the input waveguide is $L = 8d$ and that of the output one is $L = 0.5d$. The aperture angle of taper is chosen to be $\theta = 30^0$. By

analyzing the Poynting vector both at the input and output sides of the device and on the boundaries of the 3D simulation region, the reflection loss is calculated to be less than 7% whereas the scattering loss is 3%. Therefore, if we ignore ohmic losses, more than 90% of the input power is channeled through the narrow L-shaped domino.

3.4 Conclusions

We have analyzed extensively the propagation characteristics of promising one dimensional plasmonic waveguides in the optical regime: metallic cylinders, wedges and channels. Their propagation properties has been studied within a large range of their structural parameters and the relation of them with the modal confinement has been pointed. The additional confinement mechanism of the PWs respect to the SPP in a flat surface has been explained and the consequent higher degree of confinement and control of the PWs respect to the SPPs in planar interfaces have been emphasized.

Next, we have illustrated the abilities of geometrical corrugations to strongly tailor the SPPs dispersion relations and confinement of conventional metallic waveguides in the optical and telecom regime. In particular we have demonstrated the ability to lower the cut-off frequencies even for slightly corrugated channels, slots and ridges. We have also demonstrated how the corrugation of a ridge leads to the emergence of new transversally confined SPP modes that conventional non-corrugated ones does not support them. Importantly, we have identified a new plasmonic waveguide for the telecom regime, the so-called domino plasmon polaritons, which is fully compatible with lithographic technics. Their dispersion relations, propagation lengths and modal sizes have been studied for several lateral widths of the dominoes. Interestingly, we have found a good trade-off between transversal subwavelength confinement and propagation lengths, which can be superior to conventional telecom SPP waveguides like wedges and channels.

Finally, it has been introduced the concept and main ingredients of spoof surface plasmons which naturally arises from sub-λ indentations in the surface of perfect electric-conducting metals. It has been illustrated how a 1D groove structure permits to transfer the dispersion properties of optical SPPs to long wavelengths, like the THz regime. Then, we have extended the domino concept to the THz regime, as a novel spoof plasmon waveguide which present easy fabrication and full transverse subwavelength confinement. We have analyzed its dispersion relation for several dominoes parameters and we have pointed their relation with the 1D groove structure. Interestingly, we have found a remarkable band insensitivity with the lateral width of the domino. Their properties for realistic metals in different frequency regimes have being studied, and the suitability of the dominoes for the THz regime

has been demonstrated. In addition, an extensive study of the bending and propagation losses has shown the reasonable low losses for the application of the domino structure in integrated THz circuits. To illustrate such goal, we have analyzed the robustness of the THz domino approach presenting key passive elements for THz circuitry that work at deep subwavelength scales. Based on the lateral band insensitivity, the performance of tapers, couplers, beam splitters and waveguide-ring resonators has been demonstrated. In order to facilitate possible experimental realizations, we have presented an alternative L-shape domino structure with higher planar geometry and more controlling parameters. We have analyzed its dispersion and propagation losses properties for different parameters showing similar properties to the original dominoes. For testing its potential for THz applications, we have shown the performance of a concentrator based on the variation of its lateral width.

4 Quantum emitters coupled to surface electromagnetic modes

4.1 Introduction

Controlling the radiation of atoms, molecules, or quantum dots is a hot topic in the current nanophotonics agenda. It is well known [138] that the spontaneous decay rate of a single emitter can be enhanced or suppressed by careful modification of the photonic density of states accessible to the oscillating dipole. Optical nanoantennas are one example of structures providing such command [139]. When several sources are present, the emitted radiation can be exchanged among them. Depending on the distance between emitters and the directionality of radiation, various phenomena may occur, such as radiationless energy transfer [140], radiative energy transfer [141], and even the emergence of collective super- or subradiant states [142] with correspondingly altered emission rates. In the last decades it has been demonstrated that metallic structures are a powerful mean to attain the above-mentioned control [10, 62], thanks to the high confinement of the surface plasmons (SPPs) supported by them. In fact, due to their subwavelength character, SPPs are believed to be one of the best candidates to act as an intermediate between quantum emitters and light. The control of the radiation with SPPs has been also shown to increase the optical interaction of quantum emitters on metallic interfaces [143]. Metallic nanospheres [5, 144], wires [77], and more complex structures [145] have been also considered to reach these goals, and strongly enhanced spontaneous emission decay rates of quantum dots have been demonstrated with a view in future quantum plasmonic applications [41, 43]. One further step consists in exploiting the one-dimensional character of waveguides to provide an intense coupling between two emitters [146].

In this chapter we study the coupling of nano-scale emitters to various plasmonic environments. In section 4.2 we begin studying the problem of single photon emission. Particularly, in subsection 4.2.1, we illustrate the problem of spontaneous emission in homogeneous media. Next, in subsection 4.2.2, we show how surface plasmons can enhance the spontaneous emission and we introduce the most significant magnitudes that characterize such process. In subsection 4.2.3 we analyze the emission-enhancement and the control over single pho-

ton sources using the conventional plasmonic waveguides that were studied in chapter 3. Next, in section 4.3, we study the coupling of two quantum emitters mediated by plasmonic waveguides (PWs). In particular, in subsection 4.3.1, we obtain the coupling parameters mediated by PWs, which arise from the master equation formalism presented in chapter 2. Finally in subsection 4.3.2 we apply the enhanced coupling of emitters mediated by PWs to analyze resonance energy transfer, and in subsection 4.3.3 for super and subradiance phenomena.

4.2 Single photon emission in homogeneous and plasmonic inhomogenous mediums

4.2.1 Single photon emission in homogeneous mediums

One of the most important concepts of quantum mechanics is the spontaneous emission of photons from matter. This physical effect explains a large amount of light emitting sources (atoms, quantum dots, fluorescent molecules [47], LEDs [147], thresholdless lasers [148]) and it is important to understand other light mediated interactions (resonance energy transfer [140], superradiance [142] and Raman signals [10], among others).

In one of the first pioneering works in quantum mechanics, Albert Einstein suggested with very general arguments that a molecule can emit a photon without the presence of an incoming radiation field [149]. The concept is illustrated in Figure 4.1. The atom, starting from a excited energetic state E_2, with wavefunction Ψ_2, can decay to a state Ψ_1 with lower energy E_1 in a short characteristic time τ due to the emission of a single photon. τ can be evaluated from its relation to the spontaneous emission decay rate γ_0 ($\tau = \frac{1}{\gamma_0}$), which can be calculated from quantum electrodynamics using Fermi's Golden rule [47]:

$$\gamma_0 = \frac{\omega^3 |\mathbf{d}|^2}{3\pi\hbar\varepsilon_0 c^3}, \tag{4.1}$$

where, apart from the fundamental constants, ω is the angular frequency of the photon transition and $\mathbf{d} = \langle\Psi_2| \hat{\mathbf{d}} |\Psi_1\rangle$ is the vectorial matrix element containing the average of the electric dipole moment operator $\hat{\mathbf{d}}$. In principle, to calculate this spontaneous emission decay rate, one should solve the atomic hamiltonian and compute the dipole matrix elements $\mathbf{d}$ averaging with the atomic wavefunctions. Nevertheless, a frequent and more practical approach in quantum optics is to obtain the spontaneous emission decay rate from single photon emission experiments with photodetectors [47]. For example, the measured lifetime of the zero phonon line of an NV-center with such approach is 11ns [150]. In the case of weak coupling ($\gamma << \omega$), there is a relation between the total average power P dissipated by a single-photon source, the photon energy ($\hbar\omega$) and the time that it takes to emit the

photon which is $\frac{1}{\gamma_0}$. This relation is given by [47]

$$P_0 = \frac{\hbar\omega}{\frac{1}{\gamma_0}}. \tag{4.2}$$

Basically equation (4.2) expresses the energy conservation, so the average energy flow outside the emitter must come from the statistical emission of single photons with energy $\hbar\omega$ at the characteristic time $\frac{1}{\gamma_0}$. Interestingly, relation 4.2 is convenient to calculate spontaneous emission decay rates ratios from the classical calculation of the power emitted by an infinitesimal electric dipole in an arbitrary dielectric medium. Such relation has been mea-
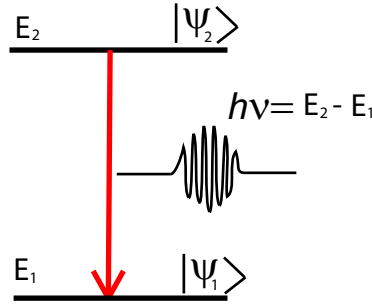
Figure 4.1: (a) Schematic representation of spontaneous emission from a two level system.

sured and tested not only for atoms [151] but also for larger atomic systems like quantum dots [152], NV centers [153] and organic molecules [5]. Only for the case of large emitters the electric point dipole approximation [154, 155] may fail.

The decay of such single emitters in the presence of macroscopic absorbing materials can be calculated as explained in chapter 2. Such approach is very convenient in order to calculate spontaneous emission decay rates in large atomic systems, which would be cumbersome to do from *ab-initio* calculations, though important steps in this path are being taken [156, 157]. In the macroscopic approach the spontaneous emission decay rate for both homogeneous and inhomogeneous environments is calculated by the formula (as seen in chapter 2)

$$\gamma = \frac{2\omega^2}{\hbar\varepsilon_0 c^2}\mathbf{d}^*\,\mathrm{Im}\mathbf{G}(\mathbf{r},\mathbf{r},\omega)\,\mathbf{d}, \tag{4.3}$$

where $\mathrm{Im}\mathbf{G}(\mathbf{r},\mathbf{r},\omega)$ refers to the imaginary part of the classical Green's tensor and is $\mathbf{r}$ the position of the quantum emitter. Notice that the spontaneous emission decay rate depends on the electric dipole orientation and this expression is general for any surrounding dielectric absorbing media. In fact, if we introduce the quantity $\mathrm{Im}\mathbf{G}(\mathbf{r},\mathbf{r},\omega)$ for vacuum $\frac{\omega}{6\pi c}\mathbf{I}$ [64] in formula (4.3), where $\mathbf{I}$ is the unit operator, we recover the spontaneous emission decay rate in vacuum from microscopic QED, *i.e.*, equation (4.1).

It is also illustrative to calculate the spontaneous emission decay rate γ when the emitter is embedded in a inhomogeneous dielectric medium, and compare it with the vacuum one γ_0. The ratio $\frac{\gamma}{\gamma_0}$ is called the Purcell factor, in honor to Edward Mills Purcell [138], who first pointed out that the decay rate is a magnitude intrinsically dependent on the environment of the emitter. The Purcell factor is an important magnitude because it measures the enhancement or suppression of the emitter decay rate in that particular environment. In the weak coupling regime ($\gamma << \omega$), and making use of equation (4.2), we can evaluate $\frac{\gamma}{\gamma_0}$ as [47]

$$\frac{\gamma}{\gamma_0} = \frac{P}{P_0},\tag{4.4}$$

where P refers to the average power emitted in the presence of the inhomogeneous environment. For example, in the particular case of an emitter placed in a homogeneous dielectric with relative dielectric permittivity ε, $\mathrm{Im}\mathbf{G}(\mathbf{r}, \mathbf{r}, \omega)$ equals to $\frac{\omega\sqrt{\varepsilon}}{6\pi c}\mathbf{I}$ [64] and then $\frac{\gamma}{\gamma_0} = \sqrt{\varepsilon}$. It can be observed that $\frac{\gamma}{\gamma_0}$ has increased, so the dielectric environment has an enhancing effect on the emitter emission. This increase is due to the higher number of states available due the presence of the surrounding atoms which form the dielectric.

The spontaneous emission in homogeneous mediums can be also modified by the presence of inhomogeneous environments like photonic crystals [158], dielectric waveguides [159] or metallic surfaces [10]. In the next subsection we introduce the enhancing effects of SPPs in the decay of quantum emitters on flat metallic interfaces, which will permit us to introduce very useful quantities to characterize the spontaneous emission in SPPs.

4.2.2 Single plasmon emission on a metallic surface

Surface plasmon polaritons (SPPs) in flat metallic surfaces have shown a tremendous capability to enhance the photon-emission and interaction of quantum emitters [62, 143, 160]. The advantage of SPPs in a flat surface comes from their subwavelength modal confinement on the metal surface. Such confinement enhances the electric fields at optical wavelengths close to the SPP resonance, as we saw in chapter 3. Those enhanced electric fields rise the photonic density of the states available to the emitter and consequently its decay rate is increased [47]. Physically, the emission enhancement can be understood as a consequence of the EM fields reflected back to the emitter at the metallic interface [10]. The collective response of the surrounding metallic atoms strongly modifies the photon emission rate and the spatial probability of finding the emitted photons. Mathematically, that modification can be extracted from formula (4.3). Now the electric field in the homogeneous medium, which is directly proportional to the homogeneous Green's tensor $\mathbf{G}_{\mathrm{homo}}$, must be replaced by the total electric field, which is a summation of the electric field due to the homoge-

neous medium and the back-scattering coming from the metallic surface [47]. Such total summation is directly proportional to the total Green's tensor ($\mathbf{G}_{\text{total}} = \mathbf{G}_{\text{homo}} + \mathbf{G}_{\text{scatter}}$) and inserting it in equation (4.3), it allows to calculate the emitter decay rate modified by the metallic interface.

The back-scattered field has different contributions which modify with different weights the enhancement of the emitter emission [10]. Basically, we can split the different decay contributions in three main terms, thus the total Green's tensor can be written as

$$\mathbf{G}_{\text{total}} = \mathbf{G}_{\text{free-radiative}} + \mathbf{G}_{\text{spp}} + \mathbf{G}_{\text{non-radiative}}, \tag{4.5}$$

where $\mathbf{G}_{\text{free-radiative}}$ corresponds to the free-radiative term, $\mathbf{G}_{\text{spp}}$ is the SPP contribution and $\mathbf{G}_{\text{non-radiative}}$ is the non-radiative term. Those different contributions in the optical regime depend strongly on the spatial position of the emitter respect to the metallic surface. The $\mathbf{G}_{\text{free-radiative}}$ term accounts for the generation of photons to free-space and it is dominant approximately at emitter-to-surface distances longer than the emission wavelength λ. At intermediate distances ($\sim \lambda/20 - \lambda/2$) and optical frequencies, the generation of single plasmons is important and so the $\mathbf{G}_{\text{spp}}$ term plays a relevant role. For distances smaller than approximately $\lambda/20$, the non-radiative term starts to increase significantly due to the non-radiative energy transfer at the available states in the surrounding metallic atoms. Such available states are reflected in the imaginary part of the metal dielectric function and they generate extremely short ($\ll \lambda$) propagating waves [10]. Importantly, formula (4.5) is valid in general for one dimensional PWs [77] and we will make use of it in the next subsections.

We can illustrate the different decay contributions with the representation of $\frac{\gamma}{\gamma_0}$ as a function of the emitter-surface distance for a quantum emitter. Using formula (4.5), in combination with formulas (4.3) and (4.4), we find that

$$\frac{\gamma}{\gamma_0} = \frac{\gamma_{\text{radiative}}}{\gamma_0} + \frac{\gamma_{\text{spp}}}{\gamma_0} + \frac{\gamma_{\text{non-radiative}}}{\gamma_0}. \tag{4.6}$$

Equation (4.6) shows the different decay contributions originating from equation (4.5) and it can be calculated using the classical EM methods described in chapter 2. Figure 4.2(a) shows $\frac{\gamma}{\gamma_0}$ (black line) as a function of the emitter-surface distance Z (see the illustration in the inset), for an emitter with its dipole moment aligned perpendicularly to a flat silver-air surface, and emitting at an optical wavelength $\lambda = 600\,\text{nm}$. In order to perform the calculations, we have used the values of silver dielectric constants taken from optical measurements [72]. In the same figure it is represented the guided SPP contribution to $\frac{\gamma}{\gamma_0}$, $\frac{\gamma_{\text{spp}}}{\gamma_0}$, in red line, calculated analytically according to reference [10], *i.e.*,

$$\frac{\gamma_{\text{spp}}}{\gamma_0} = \frac{3\pi \text{Re}\left\{ \frac{\sqrt{-\varepsilon_{\text{metal}}}}{1-\varepsilon_{\text{metal}}} k_{\text{zSPP}}^5 \exp\left(-2\sqrt{\frac{-Z}{\varepsilon_{\text{metal}}}} k_{\text{zSPP}} \right) \right\}}{k_0^5}, \tag{4.7}$$

where k_{zSPP} is the SPP wavevector and ε_{metal} is the metal dielectric constant, both defined as in equation (3.2). We can observe that for distances Z larger than the wavelength, $\frac{\gamma}{\gamma_0}$ slightly oscillates around the unit value. Such oscillations arise from the phase of the electric fields reflected in the metallic interface which propagate in free-space. Accordingly, the factor $\frac{\gamma_{radiative}}{\gamma_0}$ dominates and $\frac{\gamma_{SPP}}{\gamma_0}$ is well below $\frac{\gamma}{\gamma_0}$ due to the small value of the SPP electric field in a flat surface. Once we approach the emitter closer and closer to the surface, the SPP electric field enhances the emitter emission exponentially, as shown in equation (4.7), and it is manifested in the linear behaviour of $\frac{\gamma_{SPP}}{\gamma_0}$ in Figure 4.2(a). That growth is superposed to the radiative contribution, and the presence of both is reflected in the small departure of $\frac{\gamma_{SPP}}{\gamma_0}$ from $\frac{\gamma}{\gamma_0}$. Nevertheless we can appreciate that $\frac{\gamma_{SPP}}{\gamma_0}$ is dominant for distances smaller than $\lambda/2$. Finally, at very small distances ($Z \approx 20$nm), there is an abrupt increase of $\frac{\gamma}{\gamma_0}$ that departs even further from $\frac{\gamma_{SPP}}{\gamma_0}$. Such sudden increase is a signature of the predominant contribution of the non-radiative decay $\frac{\gamma_{non-radiative}}{\gamma_0}$ due to the presence of available states in the surrounding atoms that constitute the metallic surface.
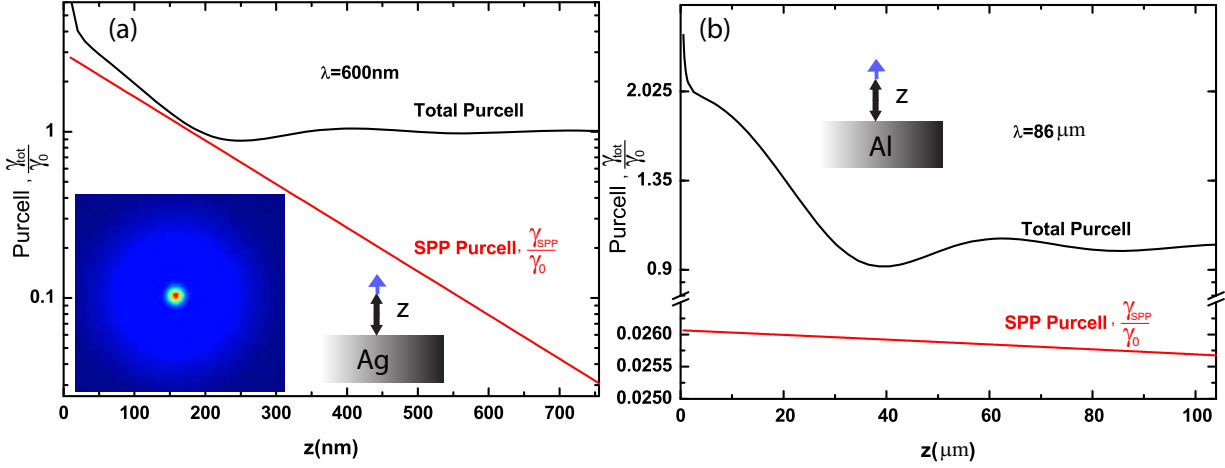
Figure 4.2: (a) $\frac{\gamma}{\gamma_0}$ (black line) in logarithmic scale as a function of the emitter-surface distance Z in the optical regime ($\lambda = 600$nm). The cladding is air and the metal is silver, whose dielectric constant is taken from reference [72]. Depicted with red line, the SPP analytical contribution to $\frac{\gamma}{\gamma_0}$, $\frac{\gamma_{SPP}}{\gamma_0}$. In the inset: schematic view of the system and electric field norm contour plot (arbitrary units) at a plane parallel to the surface $Z = 50$nm. (b) $\frac{\gamma}{\gamma_0}$ (black line) in linear scale $Z = 50$nm.(b) $\frac{\gamma}{\gamma_0}$ (black line) in linear scale as a function of the emitter-surface distance Z in the terahertz regime for an aluminum interface whose value of the dielectric constant is taken from reference [73]. Depicted in a linear scale with red line, $\frac{\gamma_{SPP}}{\gamma_0}$, for this regime. The vertical scale has been broken in order to see the small SPP contribution. In the inset, schematic view of the system.

Let us clarify the contribution to $\frac{\gamma}{\gamma_0}$ from the SPP confinement in the optical regime.

For such purpose, we analyze the emission of SPPs in a flat surface in the THz regime in which the SPPs are highly delocalized as we saw in chapter 3. In Figure 4.2(b) we show $\frac{\gamma}{\gamma_0}$ and $\frac{\gamma_{\text{spp}}}{\gamma_0}$ as a function of the distance, at $\lambda = 86\mu$m (frequency = 3THz) and for an aluminum-air interface. The values of the aluminum dielectric constants have been taken from optical measurements [73] and the dipole moment is oriented orthogonally to the interface. For distances approximately below $Z = 30\mu$m, there is an enhancement of $\frac{\gamma}{\gamma_0}$ which comes purely from the free-propagating electric fields reflected at the metallic surface. In large contrast to the optical regime, we can see that such enhancement is not due to the SPP in the flat surface, whose $\frac{\gamma_{\text{spp}}}{\gamma_0}$ contribution is negligible for all distances in the terahertz regime. This fact agrees with the characterization of the SPP confinement given in chapter 3, where we saw that the SPP is no longer sub-λ confined in the terahertz regime. Accordingly, the energy is distributed in a large volume and the enhancement of the emission due to the SPP is extremely poor. In consequence, the values of $\frac{\gamma}{\gamma_0}$ at intermediate distances is always less than 2 which is the expected behaviour for an emitter in front of a perfect electric conductor interface [161]. In addition, most of the energy is emitted in the form of free propagating photons spread in all directions around the emitter. Therefore, we can conclude that the subwavelength confinement is vital to increase and further control the emitter emission in SPPs.

We are particularly interested in the decay of the emitter into SPPs due to their enhancing-emission properties and also in the further control achieved in the emission due to the generation of confined SPPs. Therefore, we need an expression to characterize such process over the other possible decay channels, *i.e.*, free-propagating and non-radiative channels. A good magnitude for that purpose is the spontaneous emission β factor, which is defined as the ratio between the decay rate in SPPs, γ_{spp}, and the total decay rate of the emitter, γ,

$$\beta = \frac{\gamma_{\text{spp}}}{\gamma}. \tag{4.8}$$

Notice that, in the light of formula (4.6), equation (4.8) is equivalent to the ratio between $\frac{\gamma_{\text{spp}}}{\gamma_0}$ and $\frac{\gamma}{\gamma_0}$. Interestingly, this quantity gives the probability of emitting SPPs and therefore it characterizes the efficiency of such process. In Figure 4.3 we display β as a function of the wavelength for four representative emitter-surface distances Z, and for a silver-air interface in which the dipole moment orientation of the emitter is perpendicular to the surface. In general, we can observe how for all the distances Z, the curves present a similar qualitative behaviour, showing a maximum of the beta factor within the optical spectrum. However, there are important differences between them as a consequence of the different decay contributions commented previously. For very close distances ($Z = 30$nm) the non-radiative losses are present importantly in the whole spectrum and therefore the maximum is only 74%. For large distances ($Z = 300$nm) the weight of the free-propagating fields is
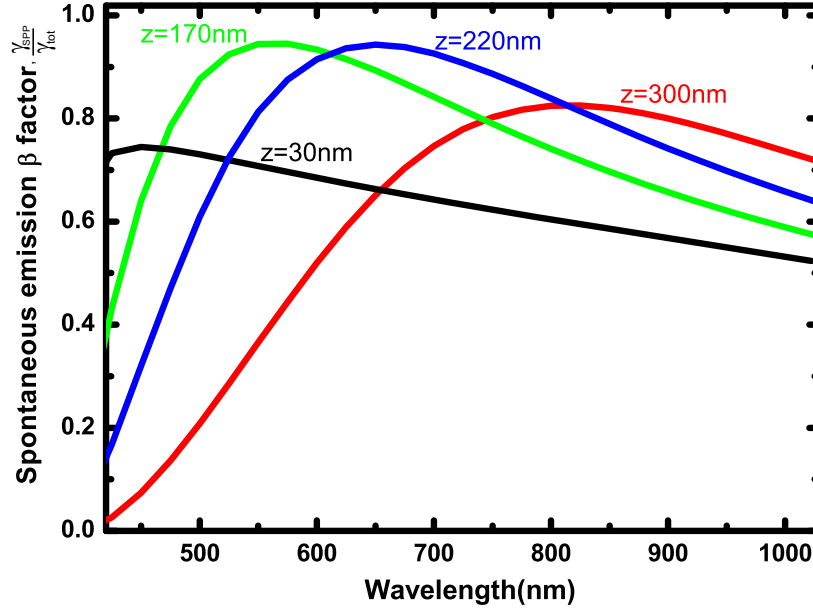
Figure 4.3: (a) β factor as a function of the wavelength for different emitter-surface distances Z. The cladding is air and the metal is silver whose values of the dielectric constants are taken from reference [72]. The electric dipole moment is aligned perpendicularly to the metal surface.

larger, due to the farther distance from the SPP exponential tail, and the maximum is 82%. This is not the case for intermediate distances ($Z = 170$nm, $Z = 220$nm) where we see that the maxima are 94% and therefore the SPP emission can be very efficient. Notice the accordance with the previous results displayed in Figure 4.2 (a), in which we see that both $\frac{\gamma_{\mathrm{spp}}}{\gamma_0}$ and $\frac{\gamma}{\gamma_0}$ curves are very close each other at $Z \approx 200$ nm.

It is important to realize that the generation of the SPPs alters the spatial probability of detecting the emitted photons. For distances Z of high β, the probability of detecting a single plasmon is higher close to the surface than in free space, due to the more intense electric fields. This probability is isotropic around the emitter position due to the symmetry of the planar structure. Such isotropy is reflected in the electric field norm of the SPP in a flat surface as shown in the inset of Figure 4.2(a). Consequently, the fields diminish radially with a factor ($\frac{1}{\sqrt{x}}$) [162] due to the spread of the SPP in all the directions parallel to the flat metallic surface. Such radial redistribution is added to the exponential decay of the SPP due to the electron scattering losses, as commented in chapter 3.

4.2.3 Single plasmon emission on conventional plasmonic waveguides

The additional radial redistribution of SPPs in a flat surface is inconvenient in order to carry the plasmon signal at a particular direction in circuits, *e.g.*, in order to process information. In general, in quantum optical circuits [163], the photon signal is sent to a particular direction where another emitter, optical passive device (like a cavity, beam splitter, etc...) or detector are present. In order to avoid the unnecessary redistribution and to gain more control over the plasmon directionality, it is more reasonable to use one dimensional waveguides. In addition, due to the reduction of the confining dimensions, the SPP modal volumes diminish, as we illustrated in chapter 3, and therefore, in the light of equation (4.3), the emission is further enhanced. This enhancement speeds the dynamics of the emitters through the Purcell effect which can be important for technological applications using quantum plasmonic circuitry [50], *e.g.*, for a faster generation of entanglement between emitters, as it will be shown in chapter 5.

There are important motivations for studying PWs in contrast to excellent low-loss dielectric waveguides. In order to have good coupling with the emitter, some dielectric approaches mainly rely on very limited bandwidths nearby the slow light frequency regime [158]. The operation in this regime implies more restrictive fabrication constraints due to the strong modification of the propagating properties of guided photons with the imperfections of the waveguide. Moreover, broadband dielectric waveguides rely on the coupling of a single emitter at very close emitter-waveguides distances or even on emitters embedded inside the dielectric waveguide [159, 158, 146]. At such small distances spatial variations of the surface, and non-local effects in the dielectric surface, could affect the emitter dynamics and the photon extraction efficiency [64, 84]. Moreover, for the embedded cases, the possibility of using external optical forces for fixing the emitters to the waveguide or manipulating them is restricted. In contrast, the emission in PWs relies on the intrinsic and robust field-enhancement of SPPs which in general is larger in comparison to regular dielectrics [159, 146, 45]. Due to the intrinsic confinement of SPPs, such enhancement can be achieved with air or liquid claddings, whose material allows the use of external forces that can fix the emitters to the PW [164]. A second advantage of PWs compared to dielectric waveguides based on the slow-light regime, is its broadband frequency operation as we saw in subsection 3.2.2. That broadband operation permits to relax the restrictive fabrication conditions needed for dielectrics that exploit the narrow bands associated with the slow-light regime. Another advantage of PWs is the broad spatial positions at which a very good emission into the PW occurs. Such positions are far from the interfaces, which make the PWs an alternative for avoiding the local effects commented above for dielectrics. In addition, PWs have transversal subwavelength confinement and therefore they permit the development of

ultracompact circuitry [1, 18], which can be important for spatial scalability purposes, *i.e.*, the possibility to scale spatially an increasing amount of information. The main limitation of PWs is its reduced propagation distance compared to dielectric waveguides. Those short distances restrict their direct applications in long telecommunications distances. However, a possible solution to such constrain can be achieved through the coupling of both plasmonic and dielectric waveguides [45, 165, 166], thus combining the best of both approaches: higher photon-extraction efficiencies, higher decay rates and low propagation losses. For all these advantages, a study of different PWs for single-plasmon emission seems mandatory in order to identify some of the best plasmonic candidates.

In this subsection, we analyze both namely, the increase in the emission enhancement and further control on single-photon emitters induced by the conventional PWs studied in chapter 3, at optical frequencies. In the calculations for all the metallic PWs we have taken the values of silver dielectric constants extracted from optical measurements [72] and the cladding material is air.

Single plasmon emission on a metallic cylinder

The cylindrical plasmonic waveguide has been one of the chosen candidates for the pioneering works showing the generation of optical single plasmons with one dimensional PWs [45, 41]. In the following, we study the main magnitudes associated with the coupling of single-photon emitters with cylindrical PWs. For such study we use the methods explained in chapter 2 in order to calculate $\frac{\gamma}{\gamma_0}$ and $\frac{\gamma_{\text{spp}}}{\gamma_0}$. In Figure 4.4 we show in three columns: $\frac{\gamma}{\gamma_0}$, $\frac{\gamma_{\text{spp}}}{\gamma_0}$ and the spontaneous emission β factor as a function of the emitter-surface distance Z (see the illustration in the inset of panel (a)). The different rows of panels represent different emitting optical wavelengths and for comparing purposes in each panel we display the behavior for three different radii. In all the panels the dipole moment of the emitter is aligned radially, thus coinciding with the main polarization of the fundamental cylindrical SPP as shown in subsection 3.2.2, chapter 3.

Let us start describing the single-photon emission properties for a certain radius and wavelength, for example, $R = 35$nm and $\lambda = 600$nm (panels (d)-(f)). In panel (d) we can observe how $\frac{\gamma}{\gamma_0}$ is close to one for distances $Z \gtrsim 175$nm and therefore the emission is almost the one in the homogeneous medium. Consequently, the $\frac{\gamma_{\text{radiative}}}{\gamma_0}$ contribution dominates and $\frac{\gamma_{\text{spp}}}{\gamma_0}$ and β are almost zero as we can see in panels (e) and (f), respectively. For distances Z below 175nm, $\frac{\gamma}{\gamma_0}$ starts increasing significantly from 1 due to the contribution of $\frac{\gamma_{\text{spp}}}{\gamma_0}$, which curve is slightly non-exponential due to the radial confinement of the cylindrical SPP [167]. At the distance $Z \approx 20$nm, we can see there is a maximum of β factor ($\beta = 0.62$)
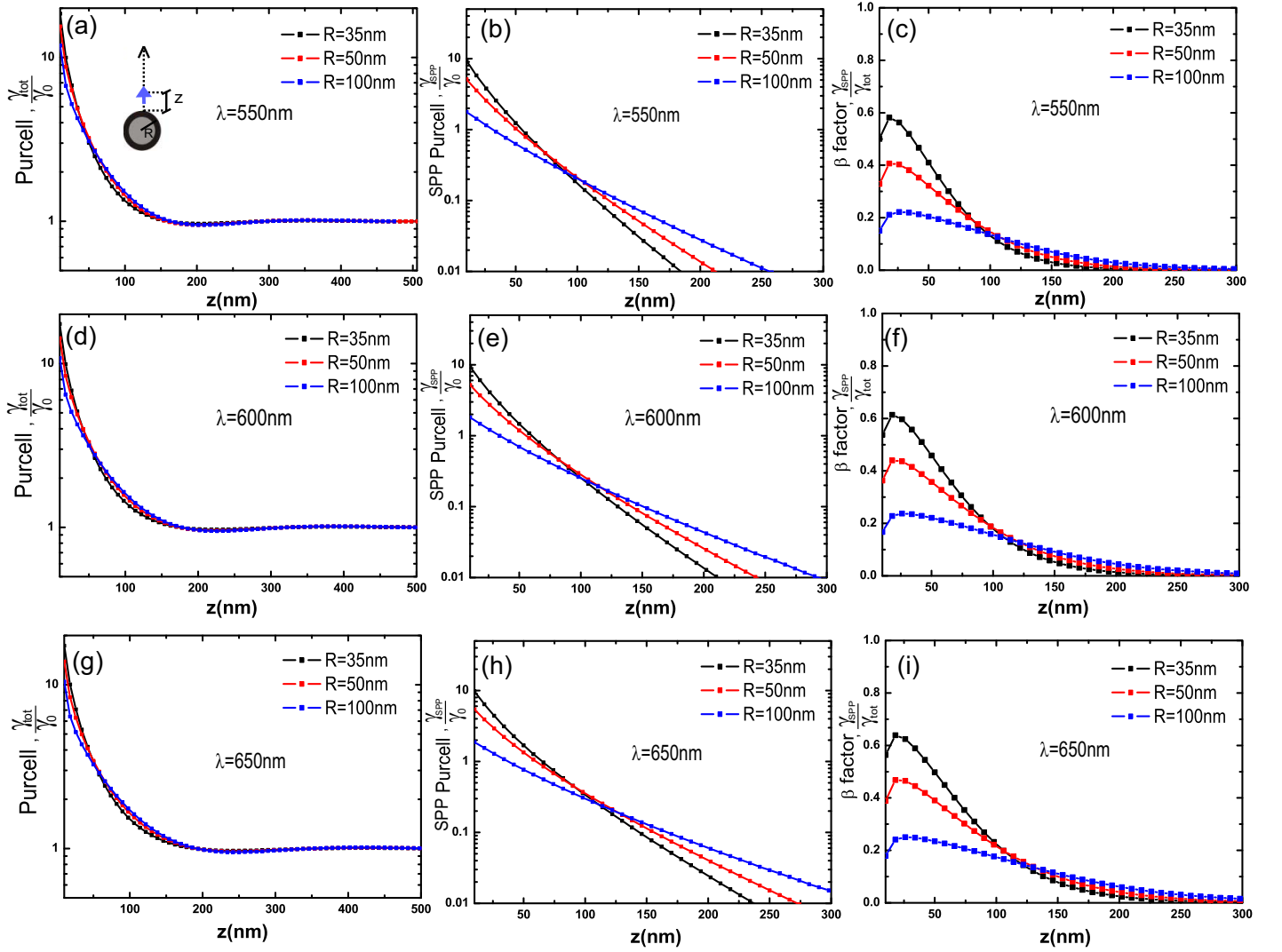
Figure 4.4: Single-photon emission characteristics in the presence of a metallic cylinder for different radius. $\frac{\gamma}{\gamma_0}$ (a), $\frac{\gamma_{\text{spp}}}{\gamma_0}$ (b) and spontaneous emission β (c) as function of the emitter-surface distance Z for an emission wavelength of $\lambda = 550$nm. The different colors represent different radii being $R = 35$nm the black line, $R = 50$nm the red line and $R = 100$nm the blue line. Panels from (d) to (f) and from (g) to (i) corresponds to the same representations for two additional emission wavelengths: $\lambda = 600$nm and $\lambda = 650$nm respectively. Inset of panel (a): Scheme showing the structure parameters, the dipole moment orientation (arrow direction) and the emitter-surface distance Z.

in figure (e), which is due to the trade off between the non-radiative losses and the SPP contribution. This trade-off is reflected in the high values of $\frac{\gamma}{\gamma_0}$ (panel (d)) together with the increasing difference from $\frac{\gamma_{\text{spp}}}{\gamma_0}$ for smaller distances (panel (e)), where non-radiative emission dominates.

Apart from the qualitative similarities, there are remarkable differences between the single-plasmon emission on a metallic cylinder and on the flat surface shown in the previous subsection. For example, at $\lambda = 600$nm, the maximum β factors are 0.62 and 0.94 for the wire and the planar geometry, respectively. In spite of the higher efficiency for plasmon generation shown by the flat surface, the emission in the cylinder is produced in a one dimensional channel instead of a two dimensional one. In addition, for the distances at which the beta factor is maximum, respectively in each structure, $\frac{\gamma_{\text{spp}}}{\gamma_0}$ is an order of magnitude higher in the cylindrical case. This fact reflects the increase of the emission enhancement in the cylinder due to the reduction of the transversal SPP modal size. Both properties, *i.e.*, the one dimensional character and the higher emission rates, show the important advantage of 1D PWs over flat interfaces for controlling and speeding up the dynamics of emitters, for possible applications in quantum plasmonic circuitry.

Additionally, in contrast to the SPP in a flat surface, there is an extra control on the emission properties, which can be tuned by the radius of the wire independently of the single emitter properties. For example, for a single emission wavelength, such variation parameter permits to provide different degrees of modal confinement and propagation lengths. Let us keep focusing on $\lambda = 600$nm for discussing the radius dependence in the emitting magnitudes. Panels (d)-(f) display the behavior of all the previous magnitudes for three different radii. All curves of $\frac{\gamma}{\gamma_0}$ in panel (d) increases with smaller Z due to the different decay rate contributions discussed above. In general, we can observe that the radius behaviour is quite complicated, a fact reflected in the several crossovers between $\frac{\gamma}{\gamma_0}$ curves at different Z, which are due to the different weights of the decay contributions. Nevertheless, we can roughly distinguish in panels (e) and (f) two regions separated by the distance at which there is a crossover between the curves of each radii. For short distances, below the crossover, $\frac{\gamma_{\text{spp}}}{\gamma_0}$ and β are larger for smaller radii, and for distances above the crossover the radius dependence is reversed. Such behaviour is consistent with a larger SPP confinement for the cylinders that have a smaller radius, and that affirmation is in accordance with the dispersion curves described in subsection 3.2.2, in which cylinders with smaller radii imply larger SPP wavevectors.

Finally, we discuss the behavior of the previous magnitudes characterizing the emission for two additional nearby emission wavelengths, $\lambda = 550$nm, and $\lambda = 650$nm (panels (a)-(c) and (g)-(i), respectively). In general we can observe slight changes in $\frac{\gamma}{\gamma_0}$ and $\frac{\gamma_{\text{spp}}}{\gamma_0}$ respect to the case $\lambda = 600$nm. In particular, a small increase in the maximum value of β

can be appreciated for larger wavelengths (panels (c), (f) and (i)). The robustness of those magnitudes against variations in the emission wavelength is a consequence of the broadband properties of the PWs. Therefore, typical variations on the order of 0.001% of the emission wavelength, which can occur due to fluctuations of the atomic systems, does not change the good emission properties into SPPs. Such small modifications on the emission properties for different wavelengths are in agreement with numerical [77] and analytical [45] results of single photon emission on cylinders, and they are in high contrast with dielectric waveguides that rely in the very slow light regime [158].

Single plasmon emission on a metallic wedge

In this subsection we study the main magnitudes associated with the coupling of single-photon emitters with wedge PWs. In contrast to the cylinder, the wedge structure has been barely studied in the context of single plasmon emission at optical wavelengths [58]. Due to the electric field enhancement associated with the tip confinement, an improvement in the emission properties is expected. In addition, the larger number of parameters compared to the cylinder is advantageous to further control the emission of single plasmons.

In order to study those possible controlling capabilities, we start studying the variation of the single-plasmon emission properties due to different wedge angles and wavelengths. We start fixing the height to $L = 200$nm and the tip radius to $R = 5$nm, since they provide a good modal confinement and propagation lengths longer than the free-radiation wavelength, as shown in subsection 3.2.2, in chapter 3. In Figure 4.5 we show in three columns of panels: $\frac{\gamma}{\gamma_0}$, $\frac{\gamma_{\text{spp}}}{\gamma_0}$ and the spontaneous emission β factor as a function of Z as illustrated schematically in the inset of panel (a). Three curves are represented in each panel, that corresponds to different wedge angles: $\theta = 30°$ (black), $\theta = 40°$ (red) and $\theta = 50°$ (blue). The different rows of panels represent different optical emission wavelengths whose values are specified in each panel. In all panels, the dipole moment of the emitter is aligned vertically, thus coinciding with the main polarization of the fundamental wedge SPP as shown in chapter 3. The results have some similarities to those for the cylinder in the previous subsection. For example, it can be observed in figures of the β factor (panels (c),(f) and (i)) three dominating regions of decay: the free-propagating one (large distances), the SPP dominating region (close distances) and the non-radiative region (for very close distances). We can see how the $\frac{\gamma}{\gamma_0}$ curve (panels (a),(d) and (h)) follows in general the increasing tendency of $\frac{\gamma_{\text{spp}}}{\gamma_0}$ (panels (b),(e) and (h)) for smaller Z. The wedge angle plays a similar role to the cylinder radius as reflected in $\frac{\gamma_{\text{spp}}}{\gamma_0}$ (panels (b),(e) and (h)), which presents a Z-crossover between the different curves. For distances Z below the crossover, the values of $\frac{\gamma_{\text{spp}}}{\gamma_0}$ are higher for smaller θ and such trend is reversed for distances above the crossover. That behaviour is consistent with
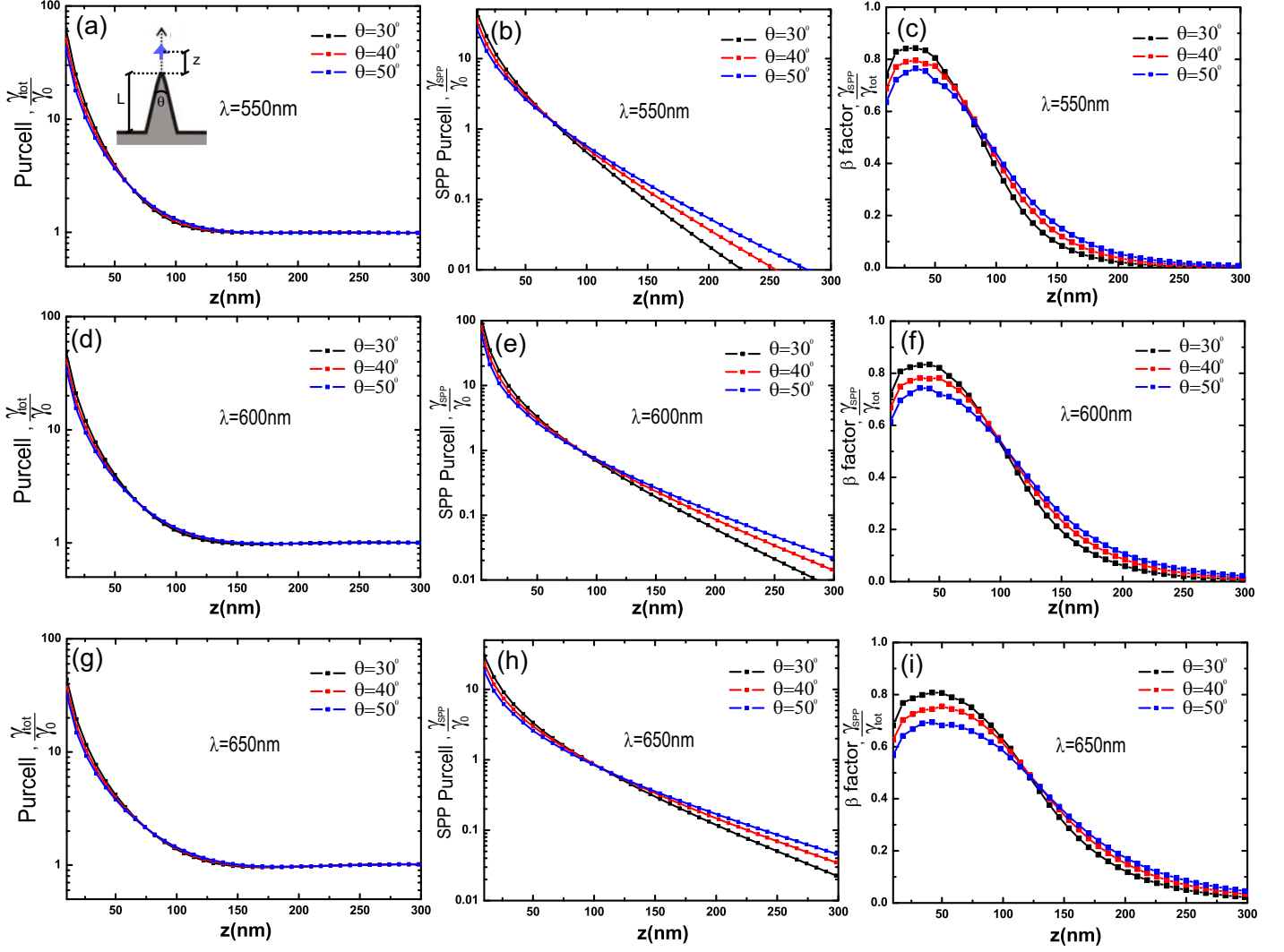
Figure 4.5: Single-photon emission characteristics in the presence of a metallic wedge for tip radius $R = 5$nm, height $L = 200$nm and different wedge angles θ. $\frac{\gamma}{\gamma_0}$ (a), $\frac{\gamma_{spp}}{\gamma_0}$ (b) and spontaneous emission β factor (c) as function of the emitter-tip distance Z for an emission wavelength of $\lambda = 550$nm. The different line colors represent different wedge angles being $\theta = 30°$ black, $\theta = 40°$ red and $\theta = 50°$ blue. Panels from (d) to (f) and from (g) to (i) corresponds to the same representations for two additional emission wavelengths: $\lambda = 600$nm and $\lambda = 650$nm respectively. Inset of panel (a): Scheme showing the structure parameters, the dipole moment orientation (arrow direction) and the emitter-surface distance Z.
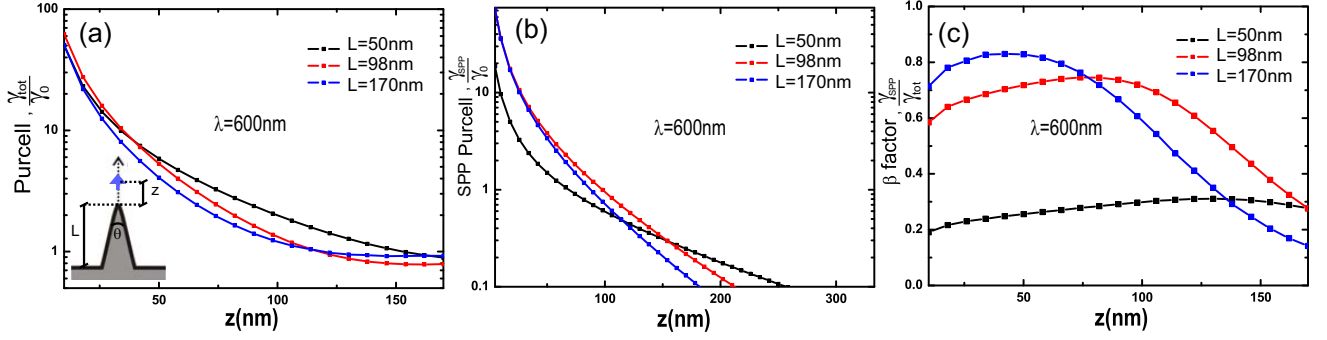
Figure 4.6: Single-photon emission characteristics in the presence of a metallic wedge for tip radius $R = 5$nm, wedge angle $\theta = 30°$ and three different heights L. $\frac{\gamma}{\gamma_0}$ (a), $\frac{\gamma_{spp}}{\gamma_0}$ (b) and spontaneous emission β (c) as function of the emitter-tip distance Z for an emission wavelength of $\lambda = 600$nm. The different line colors represent different heights L [$L = 50$nm (black), $L = 98$nm (red) and $L = 170$nm (blue)]. Inset of panel (a): Scheme showing the structure parameters, the dipole moment orientation (arrow direction) and the emitter-surface distance Z.

the larger degree of confinement of the wedge plasmon with decreasing angles as shown in chapter 3 for the wedge dispersion bands.

Regarding to the variations of the emission wavelength (see panels (a)-(c) and (g)-(i)), we can also observe that in comparison with panels (d)-(f), the differences between the curves with identical angles can hardly be distinguished. Thus the wedge shows single plasmon emission properties that are broadband as in the case of the cylinder, making the wedge emission properties robust for possible variations of the emission wavelength.

Nevertheless, there are important differences between the wedge and the wire. For example, we can compare both PWs with identical propagation lengths, which permit a fair quantitative comparison between both structures. An identical propagation length can be achieved by means of the tuning of the wedge parameters. Let us focus on the curves for wedge angles $\theta = 30°$ and $\lambda = 600$nm, which provides an identical propagation length of 3λ (see subsection 3.2.2). Both $\frac{\gamma}{\gamma_0}$ (panel (d)) and $\frac{\gamma_{spp}}{\gamma_0}$ (panel (e)) are higher in the presence of the wedge than in the best case for the cylinder (see fig 4.4 for $R = 35$ nm, panels (d) and (e)). Such increase is a consequence of the deeper tip confinement compared to the weaker one achieved for the wire, even though their propagation lengths are identical. Accordingly to the higher degree of confinement, now in the wedge SPP contribution (panel(e)), we can clearly see the non-exponential Z dependence, barely observable in the wire (Figure

4.4, panel(e)). Another interesting difference, related to the larger confinement commented above, is the high single plasmon efficiency of the wedge shown in panel (e). In particular, it can be seen that the maximum of β factor in the wedge (at $Z \approx 30$nm, $\beta = 0.83$) is 21% larger than in the cylinder, while $\frac{\gamma_{\text{spp}}}{\gamma_0}$ remains of the same order (≈ 10). Additionally, at the expense of less efficiency, $\frac{\gamma_{\text{spp}}}{\gamma_0}$ can achieve a value of two orders of magnitude for distances $Z < 10$nm in contrast to the wire. These results clearly show the advantage of the wedge in single plasmon emission compared to the wire.

We can further tailor the single plasmon emission properties of the wedge modifying the height L. In order to illustrate such further control, we study the emission properties for variations on the wedge heights L at a particular wavelength, $\lambda = 600$nm. The rest of the wedge parameters are fixed to $R = 5$nm and $\theta = 30°$, which show good $\frac{\gamma}{\gamma_0}$ magnitudes as deduced from the previous analysis. In Figure 4.6, we display the dependence of $\frac{\gamma}{\gamma_0}$, $\frac{\gamma_{\text{spp}}}{\gamma_0}$ and β factor as a function of the emitter-tip distance Z (see the inset) for three wedge heights: $L = 50$nm, $L = 98$nm and $L = 170$nm. Those wedge heights are representative of the different effective index variations of the wedge, as displayed in Figure 3.6, chapter 3. Therefore, considering those wedge heights, we sweep the main confinement regions of the wedge guided modes, which can give rise to different control in the emission of the atomic-system. In all curves, the dipole moment of the emitter is aligned vertically respect to the top part of the tip. We can observe that the trend of $\frac{\gamma}{\gamma_0}$ for different L has a more complex Z dependence than respect to different wedge angles. In fact, the values of $\frac{\gamma_{\text{spp}}}{\gamma_0}$ for different L in panel (b) have a different order compared to those of $\frac{\gamma}{\gamma_0}$ at the same Z (panel (a)). Such complexity arises from the larger influence of the substrate in the wedge plasmon propagation for those representative heights, as commented in chapter 3. The substrate influences the different emission contributions for the same emitter-tip distances, *i.e.*, the radiative, the SPP and the non-radiative emitting channels. In spite of the complex behaviour of the different contributions, we can still glimpse the dependence of $\frac{\gamma_{\text{spp}}}{\gamma_0}$ with L. For very close distances ($Z = 10$ nm) in panel(b), the decreasing trend in $\frac{\gamma_{\text{spp}}}{\gamma_0}$ for smaller wedge heights L is observed, whereas for larger distances $Z > 154$ nm, such tendency is reversed. That behaviour is consistent with the decrease of the confinement for smaller height L, as reflected in the drop of the effective index shown in Figure 3.6, chapter 3. In relation with that effective index drop, we can see how β (panel (c)) also decreases importantly with smaller wedge heights L, which shows the importance of the height election for the efficient generation of wedge single plasmons. Since we are interested in the generation of confined SPP modes, it is convenient to work with large heights. The further control over the emission compared to the wire, the high plasmon efficiencies and decay rates demonstrated above, clearly show the wedge as a robust and promising candidate for single plasmon emission.

Single plasmon emission on a metallic channel

In this subsection, we study the single-plasmon emission in the presence of channel PWs due to the promising confinement provided by the channel gap. Interestingly, the channel has been hardly studied for optical single plasmon generation [58, 168]. Moreover, the large number of parameters permits, as in the case of the wedge, an extra control compared to other structures like the flat surface or the cylindrical wire.

In order to show the controlling properties of the channel for single-plasmon emission, firstly we consider the variation on the emission magnitudes due to different channel angles and wavelengths. For such study, we fix the channel height ($L = 139$nm) and the tip radius ($R = 5$nm), due to the good confinement properties shown in subsection 3.2.2 in chapter 3. In Figure 4.7, we show in three columns of panels: $\frac{\gamma}{\gamma_0}$, $\frac{\gamma_{\text{spp}}}{\gamma_0}$ and the spontaneous emission β factor as a function of the emitter-surface distance Z for three different channel angles. The rows of panels represent different emitting optical wavelengths, whose values are specified in each panel. Additionally for all panels, the dipole moment of the emitter is aligned horizontally at an emitter-surface distance Z (see the the inset of panel (a)), thus coinciding with the predominant polarization of the channel SPP (see Figure 3.7(a)). The three emission magnitudes dependence with Z, with the channel angle, and with the emission wavelength have general similarities with the ones for the previous PWs. Therefore, the channel display the three Z regions of dominant emission in the beta factor (panels (c),(f),(i)). Additionally, we can observe how the values of $\frac{\gamma_{\text{spp}}}{\gamma_0}$ (panels (b),(e),(h)) rise for increasing channel angles at distances Z below the crossover for the different curves, and such tendency is reversed at distances above the crossovers, in agreement with the confinement angle dependence of the channel (see Figure 3.7, chapter 3). Nevertheless, some of the results for all the panels differ from those displayed for the cylinder or the wedge. For example, most of the curves between different rows change for the considered variations of the emission wavelengths. Such differences arise from the channel gap which introduces a propagation cutoff as deduced from Figure 3.7, chapter 3.

In order to provide a fair comparison of the differences between the previous PWs, let us tune the channel angle to $\theta = 20°$, in order to provide an identical propagation length (3λ) at $\lambda = 600$nm. In contrast to the previous PWs, the dependence of $\frac{\gamma}{\gamma_0}$ and $\frac{\gamma_{\text{spp}}}{\gamma_0}$ inside the channel is practically exponential (see panels (g) and (h)) for the distances considered inside the channel aperture, and it diminishes abruptly for regions outside the upper channel aperture at $Z = 139$nm. This behavior in the SPP contribution is due to the channel walls confinement which permits $\frac{\gamma_{\text{spp}}}{\gamma_0}$ to be larger inside the channel than in the cylinder for the small Z (see $R = 35$ nm, Figure 4.4(e)). In comparison to the wedge PW, for wedge regions $Z < 10$nm, $\frac{\gamma_{\text{spp}}}{\gamma_0}$ is larger than in the channel, as it can be observed by comparing
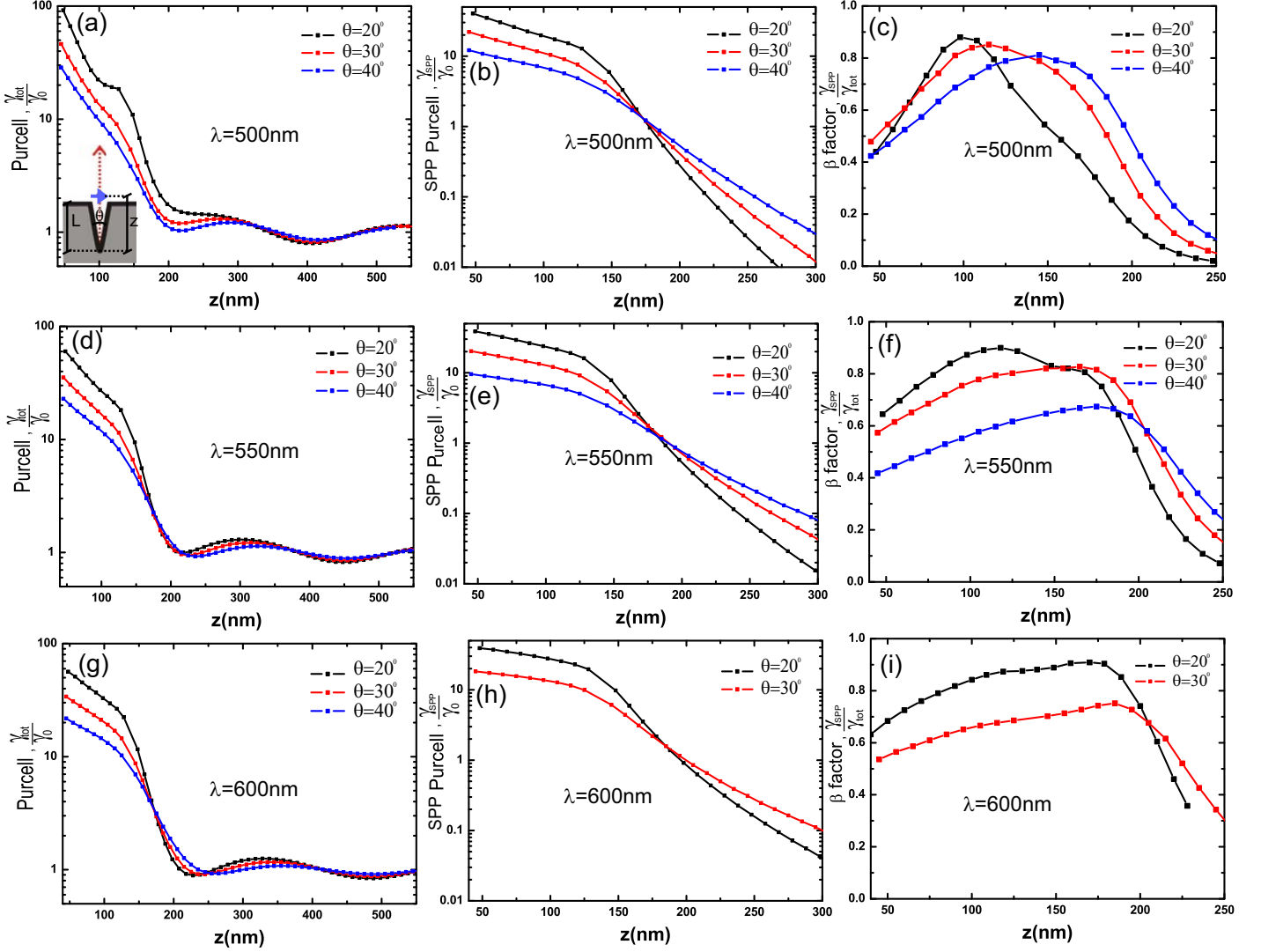
Figure 4.7: Single-photon emission characteristics in the presence of a metallic channel for tip radius $R = 5$nm, height $L = 139$nm and different channel angles θ. $\frac{\gamma}{\gamma_0}$ (a), SPP $\frac{\gamma}{\gamma_0}$ (b) and spontaneous emission β (c), as a function of the emitter-tip distance Z for an emission wavelength of $\lambda = 500$nm. The different line colors represent different channel angles being $\theta = 20°$ black, $\theta = 30°$ red and $\theta = 40°$ blue. Panels from (d) to (f) and from (g) to (i) correspond to the same variations of the channel angles for two additional emission wavelengths: $\lambda = 550$nm and $\lambda = 600$nm respectively. Inset of panel (a): Schematic showing the structure parameters, the dipole moment orientation (arrow direction) and the emitter-surface distance Z.
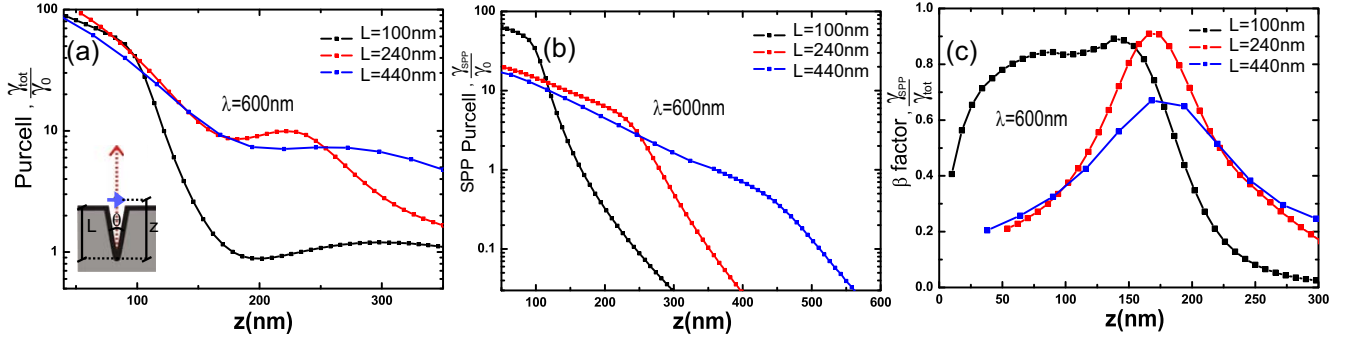
Figure 4.8: Single-photon emission characteristics in the presence of a metallic channel for tip radius $R = 5$nm, channel angle $\theta = 20°$ and three different heights L. $\frac{\gamma}{\gamma_0}$ (a), $\frac{\gamma_{spp}}{\gamma_0}$ (b) and spontaneous emission β (c) as function of the emitter-tip distance Z for an emission wavelength of $\lambda = 600nm$. The different line colors represent different heights L being $L = 100$nm (black), $L = 240$nm (red) and $L = 440$nm (blue). Inset of panel (a): Scheme showing the structure parameters, the dipole moment orientation (arrow direction) and the emitter-surface distance Z.

the values of Figure 4.7(h) ($\theta = 20°$) with those of Figure 4.5(e) ($\theta = 30°$). However, the values of $\frac{\gamma_{spp}}{\gamma_0}$ for the channel structure are higher than the one for the wedge for regions $Z > 10$nm, in which both PWs have their maximum β factor (see $\theta = 20°$, Figures 4.7(h) and (i), compared to Figures 4.5(e) and (f) for $\theta = 30°$). Additionally, as displayed in panel (i), the values of β for the channel PW are higher than the maximum for the wedge ($\beta = 0.83$) for a wide spatial region (from $Z = 100$nm to $Z = 188$nm) with its maximum value at $Z = 170$nm ($\beta = 0.90$). That higher β region is even larger for the cylindrical wire whose maximum β is 0.62. Therefore these properties show the advantages of the channel for single-plasmon generation compared to the wire and the wedge. The broad region of high β in the channel can be interesting for possible experimental realizations due to the challenging positioning of the emitter nearby structures [169, 44]. That is in contrast to broadband dielectric waveguides, in which the emitter has to be placed close to the surface of the dielectric fiber, and in general with smaller β factors [159]. Moreover, PWs with air, or alternatively water, cladding permit in principle the optical manipulation and positioning of the emitter through optical tweezers [164]. Such broad region would permit to do an optical spatial positioning of the emitter with few precision restrictions, and preserving high β factors in contrast to dielectric waveguides.

Finally, we study the control on the single plasmon emission by tuning the height L of the channel. In order to show such control, we focus at a particular wavelength ($\lambda = 600$nm), and we fix the rest of the parameters ($R = 5$nm and $\theta = 20°$), due to the good properties shown above. In Figure 4.8 we display the dependence of $\frac{\gamma}{\gamma_0}$, $\frac{\gamma_{spp}}{\gamma_0}$ and β factor as a function

of the emitter-tip distance (see the inset, panel (a)) for three representative channel heights: $L = 100$nm, $L = 240$nm and $L = 440$nm. Those heights L are representative of the main variations in the effective index (see Figure 3.8 in chapter 3), and therefore they take into account the main regions of control in the emission. In panel (a), we can observe how $\frac{\gamma}{\gamma_0}$ qualitative behaviour is quite different for all the curves due to the very different and complex dependence of the emission contributions with the height L. Moreover, in panel (b), we can see the increase of $\frac{\gamma_{\text{spp}}}{\gamma_0}$ for small distances ($Z < 50nm$), which lead the increasing tendency of $\frac{\gamma}{\gamma_0}$ curves in panel (a).

The confinement dependence with the height L in the SPP emission is not as evident as in the case of the wedge because there is a more complex play between the gap and the edges of the channel. As a consequence, in panel (b), for distances Z inside the channels, $\frac{\gamma_{\text{spp}}}{\gamma_0}$ shows higher values for the smaller heights L considered. Such complex behaviour also can be appreciated in the two qualitative different behaviours of β. In panel (c), the case $L = 100$ nm shows a broader region of high β in contrast to the two remaining heights. In particular, the height $L = 240$nm shows the highest maximum of β ($\beta = 0.91$) compared to $L = 100$nm (2% less) and $L = 440$nm (26% less). Nevertheless, the height $L = 100$nm shows a wide Z region of 80nm, with β factors only 7% less than the maximum for $L = 240$nm. The same corresponding region for $L = 240$nm is only about 30nm. The reason of these two different behaviours comes from the interplay between the modal confinement for the channel and the parameter L (recall the confinement discussion of Figure 3.8 in chapter 3). The transversal confinement changes abruptly the weights of the different emission contributions in the Z direction, depending on the election of L. In particular, for heights $L > 200$ nm, the channel SPP is confined mainly inside the gap, and therefore, the associated curves for $L = 240$ nm and $L = 440$ nm in panel (c), only have one maximum due to the trade off between the non-radiative contribution and $\frac{\gamma_{\text{spp}}}{\gamma_0}$. For heights $L < 200$ nm, the SPP is confined inside the gap and also outside the channel aperture, a fact which is reflected in the large values of $\frac{\gamma_{\text{spp}}}{\gamma_0}$ for $Z > 100$ nm for the $L = 100$ nm curve in panel (b). The high values of the electric field in both regions, associated with the guided SPP, allows for two different trade-offs of $\frac{\gamma_{\text{spp}}}{\gamma_0}$ with the non-radiative contributions, since there is a abrupt reduction of the non-radiative losses for regions outside the gap. Therefore, we find two local maximum of β, one is located inside the channel gap at $Z = 90$ nm, and the other one outside the gap at $Z = 137$ nm. Due to the higher non-radiative losses inside the channel aperture, the largest maximum of β is the one outside the gap. The above-mentioned L behaviour shows the large possible control over the emitter plasmon emission with the parameter L. In practice, it is interesting to have both high beta factors and large $\frac{\gamma}{\gamma_0}$ in broad regions, which makes the emission more robust against possible experimental bad positioning of the emitter. Therefore for practical purposes in single plasmon generation at

$\lambda = 600$ nm, it is convenient to work with heights smaller than $L = 200$nm to have such broad spatial behaviour.

From the high plasmon emission efficiencies, high emission rates and large emission control shown in this section for all the PWs studied, we can conclude that the wedge and the channel are robust and superior candidates for single plasmon emission compared to the wire.

Influence of the dipole orientation on the single emission in conventional plasmonic waveguides

In this subsection we study the modification on the emission properties of single-plasmon sources due to variations on the dipole moment orientation. As opposed to the results studied above for the previous conventional PWs, now the emitter alignment differs from the predominant polarization of the guided mode. This can be important from the experimental point of view since a controlled alignment of the emitters is technically challenging [41, 170, 171, 44]. In general, when the orientation of the emitter is different, the decay rate and the spontaneous emission β factor, induced by the PW, change. The dependence of β with the angular deviation of the dipole from the main electric field polarization is illustrated in Figure 4.9. Panels (a), (b) and (c) correspond to such representations for the cylinder, the channel and the wedge, respectively for an emission wavelength $\lambda = 600$nm. In all cases the emitter position is chosen to have a high β for the predominant SPP polarization: $Z = 20$ nm for the cylinder, $Z = 150$ nm for the channel and $Z = 30$ nm for the wedge. The dipole moment is parallel to the transverse plane, and the definitions of the angular deviation θ are sketched in the diagrams of the corresponding panels. As a general rule, the deviation of the dipole moment from the main electric field polarization has a detrimental effect. In fact β becomes null for $\theta = 90°$ in all cases. Nevertheless, there is a broad angular range where β remains relatively stable and therefore it is not critically affected by relatively large misalignments. Figure 4.9 shows that β deviates less than a 10% of the maximum value within a θ-range of $\Delta\theta = 60°$ for cylinders and $\Delta\theta = 40°$ for channels and wedges. The functional dependence of β with θ is not simple because although $\gamma_{\text{spp}} \propto \cos\theta$ (see equation (2.157) in chapter 2), γ has a more complex dependence on the radiative and non-radiative losses. This behaviour can be observed by comparison of the curves tendencies in the insets of Figure 4.9. Nevertheless we can appreciate how γ_{spp} diminishes for smaller angles and so does γ due to the high β values. After the results shown above we can conclude that the emission properties on PWs are robust against transverse dipole misalignments.
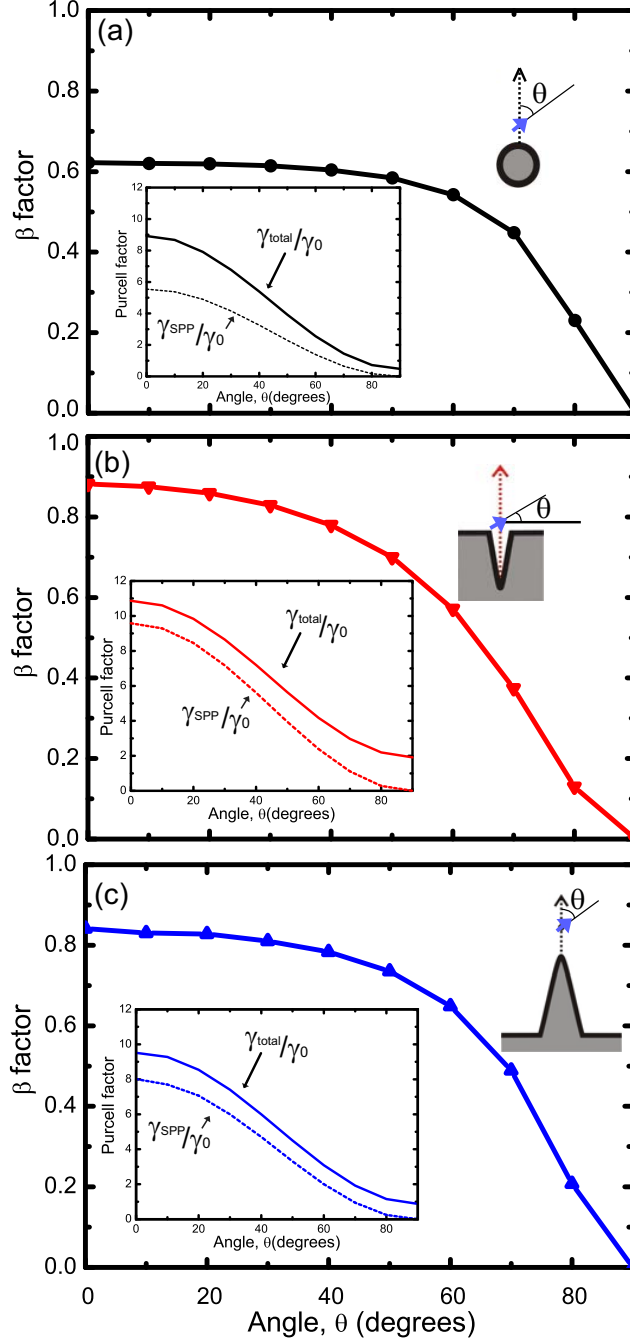
Figure 4.9: Beta factor of one emitter as a function of the angle, θ, formed by the SPP electric field and the dipole moment. (a) Cylinder, (b) channel and (c) wedge. The insets show the total (continuous line) and plasmon (dashed line) decay rates normalized to the vacuum decay rate, $(\gamma/\gamma_0, \gamma_{\text{spp}}/\gamma_0)$, as a function of θ. The positions of the dipoles are detailed in the main text.

4.3 Quantum emitters coupled to plasmonic waveguides

In this section, we first show the calculations of the main coupling parameters governing the dynamics between two spatially separated quantum emitters and PWs. Additionally, we test the model for the interaction that is mediated by single plasmons as developed in chapter 2. Both favorable and unfavorable alignments are considered.

Finally, we study some of the possible applications for the plasmonic mediated coupling between two atomic-systems. In particular, in subsections 4.3.2 and 4.3.2, we test the use of conventional PWs in resonance energy transfer and superradiance phenomena, respectively. We will emphasize on such possible applications for the wedge and channel PWs, due to their good single-plasmon emission properties, as shown in the previous section.

4.3.1 Plasmonic coupling: Coherent and dissipative terms
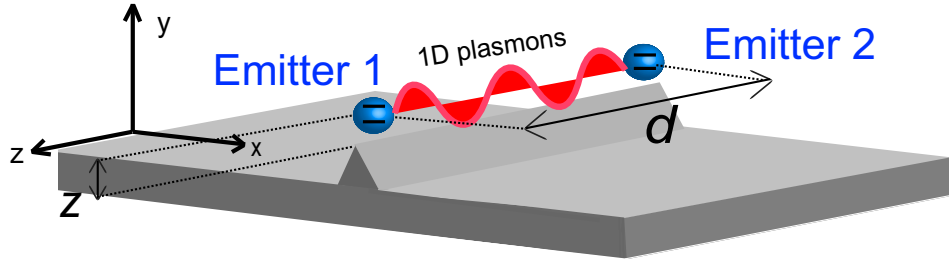
Figure 4.10: (a) Two single-photon emitters interacting with a plasmonic waveguide, in this case a wedge PW.

The coupling parameters for quantum emitters that interact in a macroscopic medium arise from the master equation that governs the system dynamics, as presented in chapter 2. There, we identified two main coupling parameters: the coherent dipole-dipole coupling parameter g_{ij}, and the dissipative terms γ_{ij} which represent the decay rates induced by self (γ_{ii}) and mutual (γ_{ij}) interactions of the emitters. These parameters are computed using the total Green's Tensor $\mathbf{G}_{\text{total}}$ satisfying the classical Maxwell equations. In particular, we are interested in the coupling of two emitters mediated by a PW, as illustrated in Figure 4.10, due to their good properties for single-plasmon generation, and their propagation lengths which can be significantly longer than the wavelength in free-space. Such properties makes the PWs a good platform for the interaction of emitters mediated by 1D plasmons. For

Figure 4.11: Comparison of the exact coupling parameters $(\gamma_{ij}, -2g_{ij})$ with their plasmonic contributions $(\gamma_{ij,\mathrm{pl}}, -2g_{ij,\mathrm{pl}})$, as a function of the emitter-emitter horizontal separation normalized to the plasmon modal wavelength, d/λ_{pl}. All parameters are normalized to the vacuum decay rate γ_0. (a) Cylindrical (b) wedge and (c) channel waveguide. The position and orientations of the dipoles are detailed in the main text.

high β factors, a electric-dipole couples mainly to surface plasmon modes and this, in turn, warrants that the emitter-emitter interaction is predominantly plasmon-assisted at emitters separations d on the order of the propagation length. Under this condition, g_{ij} and γ_{ij} (equations (5.15) and (5.16) in chapter 2) can be evaluated using the plasmonic contribution to the Green's tensor, $\mathbf{G}_{\mathrm{pl}}(\mathbf{r}, \mathbf{r}')$, instead of the total one, $\mathbf{G}_{\mathrm{total}}(\mathbf{r}, \mathbf{r}')$. The resulting approximations for the dipole-dipole shift and decay rates for identical emitters, using equations (2.158),(2.157) and (4.8), read as [57, 56]:

$$g_{ij} \simeq g_{ij,\,\mathrm{pl}} = -\frac{\gamma_{ii}}{2}\beta e^{-d/2\ell}\sin(k_{\mathrm{spp}}d), \tag{4.9}$$

$$\gamma_{ij} \simeq \gamma_{ij,\,\mathrm{pl}} = \gamma_{ii}\beta e^{-d/2\ell}\cos(k_{\mathrm{spp}}d), \tag{4.10}$$

where it has been assumed that the transverse position of both emitters, and their orientations are identical. Importantly, these semi-analytical expressions emphasizes the relevance of the plasmon as a carrier of the electromagnetic interaction. Additionally, as explained in further detail in chapter 2, such analytical approximation facilitates the numerical calculations of g_{ij} and γ_{ij}, since the calculation of the $\mathbf{G}_{\mathrm{pl}}(\mathbf{r}, \mathbf{r}')$ implies a 2D simulation, whereas $\mathbf{G}_{\mathrm{total}}(\mathbf{r}, \mathbf{r}')$ needs to be computed in a 3D one.

In order to check the validity of this approximation, a comparison of the exact parameters $(-2g_{ij},\ \gamma_{ij})$ and the approximate ones $(-2g_{ij,\,\mathrm{pl}},\ \gamma_{ij,\,\mathrm{pl}})$ is presented in Figure 4.11 for the cylinder (panel (a)), the wedge (panel (b)) and the channel (panel (c)). All the coupling parameters are normalized to the vacuum decay rate γ_0 at the emission wavelength $\lambda = 600\,\mathrm{nm}$. The dielectric permittivity of silver at optical frequencies [72] and air claddings are used to calculate the simulations that are described in chapter 2. In all cases, the position and orientation of the emitters are chosen to have high β, *e.g.*, $Z = 20\,\mathrm{nm}$ and vertical orientation for the cylinder, $Z = 30\,\mathrm{nm}$ and vertical orientation for the wedge, and $Z = 150\,\mathrm{nm}$ and horizontal orientation for the channel. In Figure 4.11, the normalized coupling parameters are represented as a function of the emitter-emitter separation, d, normalized to the plasmon modal wavelength, $\lambda_{\mathrm{pl}} = 2\pi/k_{\mathrm{spp}}$ (at the emission wavelength, λ_{pl} is 417 nm for the cylinder, 473 nm for the wedge, and 474 nm for the channel). Let us discuss the results for the normalized coupling parameters calculated with full numerical precision, and the ones calculated approximately. As expected, the approximation is good for the cylinder and excellent for the wedge and the channel, in consonance with the corresponding β factors (0.62, 0.84 and 0.9, respectively). For the cylinder at the chosen Z, the radiative modes play a small but non-negligible role which shows up as a small disagreement between the exact and approximate results. For all the PWs and very small d, the radiative and non-radiative contributions participate in the interaction and the approximation breaks down. A different approach to this issue leading to the same results can be found in reference [83]. The coupling parameters g_{ij} and γ_{ij} are functions of the separation d which oscillate with

a periodicity given by the plasmonic wavelength, λ_{pl}, and they decay exponentially due to the ohmic absorption of the plasmonic mode. Notice that the maxima of γ_{ij} and those of g_{ij} are shifted a distance $\lambda_{\mathrm{pl}}/4$, which implies that the dissipative and coherent terms of the master equation have different weights for different emitter-emitter separations. We will see the relevance of these maxima in the dynamic of the emitters populations, which give rise to the collective decay rates as further explained in subsection 4.3.3.

Let us now consider the effect of misalignment and assume that both dipoles have different fixed orientations respect to the waveguide: one emitter has an orientation θ_1 and the other has an angle θ_2 (see the insets in Figure 4.12). When the orientations of the two dipoles are different, the mutual dipole-dipole coupling and decay rates parameters are obtained similarly than equations (4.9-4.10), which can be expressed as

$$g_{ij,\,\mathrm{pl}} = -\frac{1}{2}\sqrt{\gamma_{ii}\gamma_{jj}}\sqrt{\beta_i\beta_j}e^{-d/2\ell}\sin(k_{\mathrm{spp}}d), \tag{4.11}$$

$$\gamma_{ij,\,\mathrm{pl}} = \sqrt{\gamma_{ii}\gamma_{jj}}\sqrt{\beta_i\beta_j}e^{-d/2\ell}\cos(k_{\mathrm{spp}}d), \tag{4.12}$$

where β_{i} refers to the beta factor of emitter i. Notice that each emitter, in general, will have different values of β_i and different spontaneous emission decay rate γ_{ii} due to their different orientation, as shown in subsection 4.2.3. In Figure 4.12 we consider the behaviour of $-2g_{ij}$ and γ_{ij} and the plasmon contribution $-2g_{ij,\,\mathrm{pl}}$ and $\gamma_{ij,\,\mathrm{pl}}$ for the same heights Z with high β consider above. Those heights are $Z = 20\,\mathrm{nm}$ for the cylinder, $Z = 30\,\mathrm{nm}$ for the wedge and $Z = 150\,\mathrm{nm}$ for the channel. In general, we may observe that different dipole moment alignments have a detrimental behavior in the plasmon coupling parameters. This observation is in agreement with the behaviour of Figure 4.9 in subsection 4.2.3, where it is seen that the β factor diminishes for angles deviated from the predominant electric field polarization. As a consequence, we can observe how the radiative modes play a small but non-negligible role in all panels. In particular for $\theta_2 = 90°$, the coupling to plasmons is zero and the phase of the Green's tensor is modulated by the propagation constant in free space (panels (c), (f) and (i)). Notice how the scale is reduced compared to the other columns of panels. Specially at distances of the free-space wavelength ($d \sim 1.2\lambda_{\mathrm{pl}}$), the free radiative mediated coupling is much smaller than the plasmon mediated one in more favorable alignment conditions. Such situation is also encountered when two emitters interact in a homogeneous environment [91] and it emphasizes the superior properties of plasmon mediated coupling for those distances. In spite of the absence of plasmonic coupling at $\theta_2 = 90°$, we can see that the plasmonic approximation for the coupling parameters is good for the two first columns of panels (*i.e.*, $\theta_1 = 0°, \theta_2 = 60°$ and $\theta_1 = \theta_2 = 60°$) with noticeable differences between the structures. For example, it can be appreciated the worse approximation of the plasmon mediated coupling for the cylinder compared to the wedge and the channel.
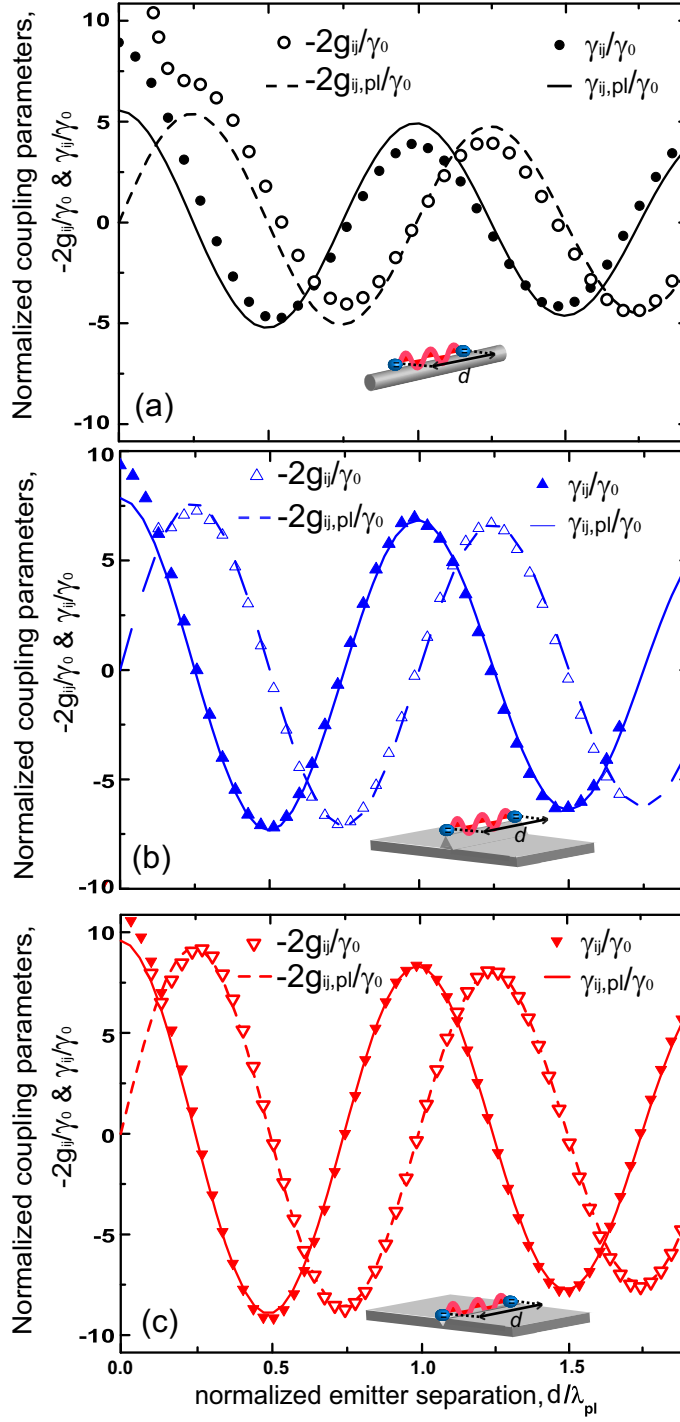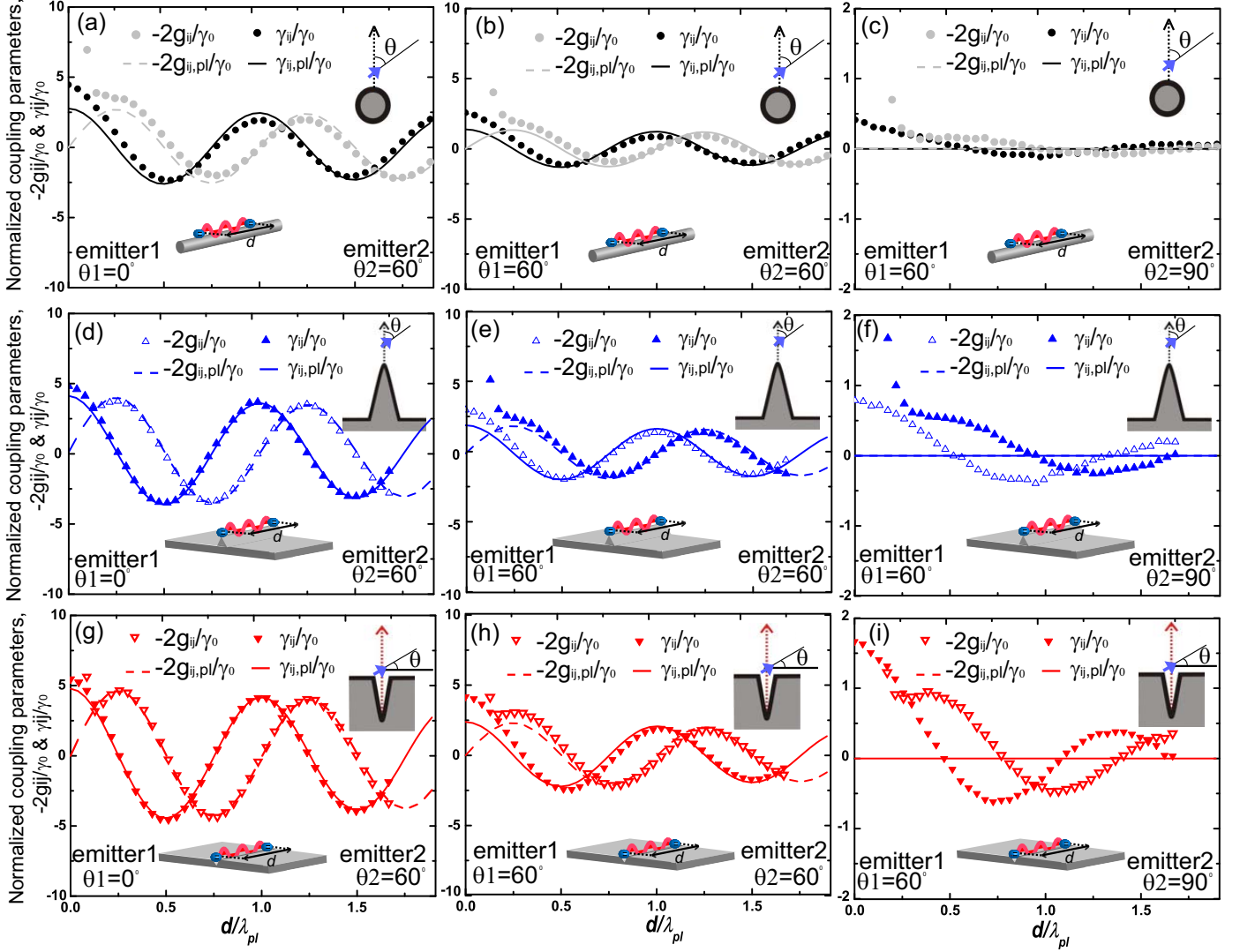
Figure 4.12: Comparison of the exact coupling parameters $(\gamma_{ij}, -2g_{ij})$ with their plasmonic contributions $(\gamma_{ij,\,\mathrm{pl}}, -2g_{ij,\,\mathrm{pl}})$, as a function of the emitter-emitter horizontal separation normalized to the plasmon modal wavelength, d/λ_{pl}. The orientation of the dipoles θ_1, θ_2 are displayed in the lower part of each figure. All parameters are normalized to the vacuum decay rate γ_0. (a)-(c) Cylindrical, (d)-(f) wedge and (g)-(i) channel waveguide. The position of the dipoles are identical to those in Figure 4.11.

This worse behavior can be inferred from the beta factors of the emitters for $\theta = 60°$, which are 0.5, 0.62 and 0.64 for the cylinder, the wedge and the channel respectively. Importantly, these results show that the plasmon coupling is still very important and they are interesting from the experimental point of view in case of accidental dipole misalignment. We can also conclude that the wedge and the channel are more robust in case of transverse misalignment.

4.3.2 Resonance energy transfer mediated by plasmonic waveguides

In this subsection we study the unidirectional energy transfer between fluorescent molecules, known as Resonance Energy Transfer (RET). RET can proceed through various mechanisms. Förster (radiationless) energy transfer strongly decays with the distance between the molecules, and in vacuum it is most effective for distances smaller than about 10 nm. For larger distances radiative transfer takes over, but the transfer rate in vacuum is nevertheless very small [47]. It has been shown that the SPPs arising in an environment consisting of a planar metallic film can enhance the transfer rate [62]. One of the goals of this subsection is to find out the extent to which coupling to PWs can increase the radiative transfer. Given both the one-dimensional character of the waveguides and the plasmonic field enhancement, an important improvement is expected. Similar ideas have been considered for dielectric [146] and very wide metallic waveguides [63]. Here, manufacturable PWs [6] with realistic properties and sub-λ confinement are studied.

The setup is displayed in Figure 4.13: an emitter (the donor) is positioned in the neighborhood of a metallic waveguide running along the Z-axis, and energy is transferred to a second molecule (the acceptor) without back-scattering to the emitter, *i.e.*, unidirectional. Both molecules are located in the vertical symmetry YZ-plane at identical vertical heights h, and separated a distance d along the waveguide. For this study we make use of the PWs studied in the previous subsection: cylinders, wedges, and channels. To simplify the study, we consider emitters with the sharp emission spectrums, which it can be closely achieved for low temperatures for some single-photon emitters [172], *e.g.*, a two-level emitter. This study can account for other emitters with broader emission spectrums [80] due to the broadband properties of the PWs shown in the previous section. In particular, the donor emission wavelength chosen below in this subsection is $\lambda_0 = 600$ nm, which is motivated by the large number of fluorescent emitters available close to this wavelength [61, 150].

In order to quantify the unidirectional RET, we make use of the normalized energy transfer rate (nETR), *i.e.*, the energy transfer rate in the presence of the PW normalized to that in vacuum, keeping the remaining factors (distances and dipole orientations) unchanged. The unidirectional nETR can be written as [47]
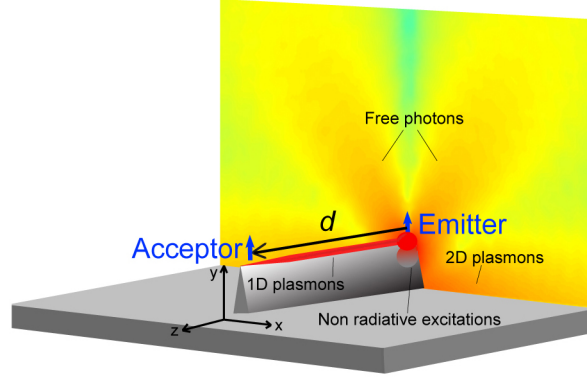
Figure 4.13: Diagram of the considered setup including the donor (emitter), acceptor, and plasmonic waveguide (a metallic wedge in this scheme). The various interaction channels are also schematically shown, including radiated photons, 'radiated plasmons' (1D plasmons guided by the wedge and 2D plasmons supported by the horizontal metallic substrate), and non-radiative excitations in the metal in the neighborhood of the emitter.

$$\text{nETR} = \frac{\text{Im}[\mu_A^* \cdot \mathbf{G}(\mathbf{r}_A, \mathbf{r}_D) \cdot \mu_D]}{\text{Im}[\mu_A^* \cdot \mathbf{G}_0(\mathbf{r}_A, \mathbf{r}_D) \cdot \mu_D]}, \tag{4.13}$$

where μ_D is the donor dipole moment vector positioned at $\mathbf{r}_D$ (with analogous definitions for the acceptor), * stands for complex conjugate, $\mathbf{G}(\mathbf{r}, \mathbf{r}')$ is the Green's tensor in the presence of the PW (with similar definition for the case when both dipoles are in vacuum) and Im stands for the imaginary part. Importantly, the acceptor has an induced dipole moment which, within the linear approximation, can be written as

$$\mu_A = \alpha \mathbf{E}_A, \tag{4.14}$$

that is the contraction of the polarizability tensor α and the electric field in the acceptor position $\mathbf{E}_A$. This polarizability tensor is in general complex-valued and it can be calculated solving the Schrödinger equation from ab-initio calculations for structurally complex emitters [173–175]. In some cases it is possible to simplify α for some emitters [47], assuming that mainly two energy levels are involved in the photon absorption. In addition, if we assume that it can only be polarized in a certain direction then

$$\alpha = \frac{|\mu|^2}{\hbar} \frac{\mathbf{n}_A \otimes \mathbf{n}_A}{\omega_0 - \omega - i\gamma}, \tag{4.15}$$

where ω is the photon incoming energy, ω_0 is the two-level's energy difference, γ is the acceptor decay rate, $|\mu|$ is the acceptor transition dipole matrix modulus and n_A is the orientation of the acceptor dipole moment. The presence of γ in the polarizability makes the

acceptor properties dependent on the environment. Such dependence adds additional complexity and, for a fair characterization of the RET, we would need to identify a particular molecule. In addition, we need to avoid the collective interaction between the acceptor and the donor to define properly an unidirectional RET. In order to avoid both complexities, we consider acceptors that both have large internal decay channels (e-e scattering, e-phonon scattering, etc...) compared to the radiative decay channel. For such emitters the polarizability is, in good approximation, independent of the environment and there is no possible back-interaction between the acceptor and the emitter. Within this supposition, the power transfer is $\frac{\omega \mathrm{Im}\{\alpha\}}{2}|\mathbf{n}_A \cdot \mathbf{E}_D(\mathbf{r}_A)|^2$ [47] and therefore expression (4.13), using equations (4.14) and (4.15), read as

$$\mathrm{nETR} = \frac{\mathrm{Im}\{\alpha\}}{\mathrm{Im}\{\alpha_0\}} \frac{|\mathbf{n}_A \cdot \mathbf{E}_D(\mathbf{r}_A)|^2}{|\mathbf{n}_A \cdot \mathbf{E}_{D,\,\mathrm{vac}}(\mathbf{r}_A)|^2} = \frac{|\mathbf{n}_A \cdot \mathbf{E}_D(\mathbf{r}_A)|^2}{|\mathbf{n}_A \cdot \mathbf{E}_{D,\,\mathrm{vac}}(\mathbf{r}_A)|^2}, \qquad (4.16)$$

where $\mathbf{E}_D(\mathbf{r}_A)$ is the electric field of the donor at the acceptor position in the presence of the PW (with a similar definition when the dipoles are in vacuum). The electric fields involved in equation (4.16) are obtained modeling the donor as a very short (2 nm) oscillating current as explained in further detail in chapter 2. The upper panels of 4.14 display the nETR as a function of d and h for a circular cylinder (a), triangular wedge (b), and triangular channel (c). In order to have a meaningful comparison, the geometric parameters are such that the fundamental mode in all three waveguides has the same propagation length $\ell = [2\mathrm{Im}(k)]^{-1} = 1.7\,\mu\mathrm{m}$, k being the complex modal wavevector. The geometry of the waveguides is summarized in the lower panels of Figure 4.14. Donor and acceptor are set with identical orientation, which is chosen so that it matches the dominant polarization of the plasmonic modes supported by the structures, *i.e.*, vertical (Y-axis) for the wire and wedge, and horizontal (X-axis) for the channel. For the range of distances d displayed in the figure, the nETR essentially grows with increasing donor-acceptor separations. This is due to the fact that in vacuum the energy is spread in all three dimensions, whereas the presence of a waveguide provides a link between the locations of donor and acceptor. The dependence with the vertical coordinate, h, of the molecules is directly related to the corresponding plasmonic modal shapes. These mode profiles are rendered in the lower panels of Figure 4.14, as quantified by the amplitude of the transverse electric field normalized to the carried power, which is proportional to $\frac{\gamma_{\mathrm{spp}}}{\gamma_0}$. Thus, within the present framework, the nETR reaches its maximum at the metallic surface ($h = 0$) for circular wires and wedges, whereas the optimal height is $h = 35\,\mathrm{nm}$ for channels. In absolute terms, the circular cylinder displays the lowest nETR, which is reasonable given its smaller field enhancement as compared with wedges and channels. In the range of d and h shown in Figure 4.14, wedges and channels feature nETRs up to 3×10^4, which is 20 times larger than the one corresponding to cylinders. Let us stress that when the separation d is fixed at, *e.g.*, half a wavelength,
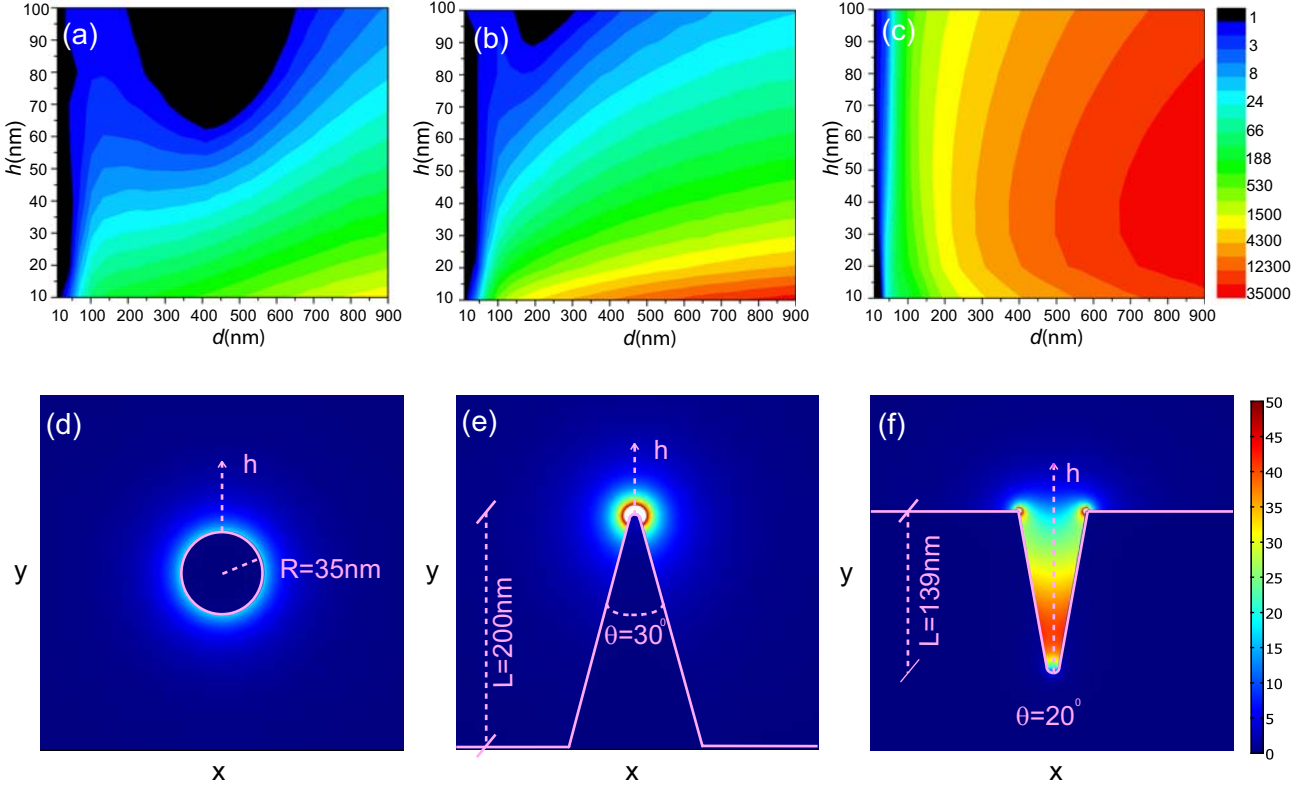
Figure 4.14: Normalized energy transfer rate (a, b, c) and modal shapes (d, e, f) for various plasmonic waveguides: circular wire (a, d), wedge (b, e), and channel (c, f). In the upper panels, the longitudinal separation between both dipoles is d (for its definition see Figure 4.13), and their vertical height is h (for their definitions see the lower panels). The lower panels display the geometry and the transverse electric field amplitude in the XY-plane, normalized to the guided power. The radius of curvature of the wedge tip is 5 nm.

the nETR in the wedge can be strongly enhanced by letting h become smaller than 10 nm, reaching values higher than several tens of thousands. This enhancement is not possible for channels whose maximum achievable nETR is about 5000 for the above-mentioned d. The general conclusion is that the wedge is the most promising structure in terms of resonance energy transfer.

We can estimate the efficiency of the RET process applied to PWs by means of the Förster radius *i.e.*, the efficiency of the transfer compared to the decay rate γ_0 in vacuum of the donor. Assuming that donor and acceptor molecules are characterized by a typical Förster radius, which is on the order of $R_0 = 10$nm [47], and assuming that both acceptor an donor have parallel dipole moments, the efficiency in vacuum predicts that the energy transfer rate of these two molecules separated by a distance $d = 600$nm in vacuum is [47] $\frac{2\pi R_0^6}{\lambda^6} \approx 10^{-8}$

times the donor's decay rate. Typically, the nERT is on the order of 10^4 when donor and acceptor molecules are appropriately placed along a channel or a wedge plasmonic waveguide (see Figure 4.14 at $d = 600nm$). Therefore, multiplying the vacuum efficiency to that typical cases, the resonance energy transfer ratio can be increased up to 10^{-4} due to the presence of the plasmonic waveguide.

The values of the nETR can be quantitatively explained with the following simplified model. The Green's tensor appearing in formula (4.13) can be understood as the sum of several processes involving the excitation of waveguide modes, free space radiation and non-radiative absorption losses as explained in the previous section in detail. An illustration of the various channels in the case of a metallic wedge is suggested in Figure 4.13. If the waveguide is to play a major role, we can expect that the contribution to the Green's function stemming from the plasmonic guided mode is the most important one and neglect the remaining channels. Using equation (4.16), with the guided Green's tensor [equation (2.43) in chapter 2], with the well known expression for the Green's function in vacuum, one arrives to the following approximation for the nETR

$$\text{nETR} = \Big(\frac{4\pi}{3}\Big)^2\Big(\frac{\gamma_{\text{spp}}}{\gamma_0}\Big)^2\exp\Big(-\frac{d}{\ell}\Big)\Big(\frac{d}{\lambda}\Big)^2\Big[1 - \Big(\frac{\lambda}{2\pi d}\Big)^2 + \Big(\frac{\lambda}{2\pi d}\Big)^4\Big]^{-1}, \tag{4.17}$$

where λ is the vacuum wavelength, ℓ is the mode propagation length, and where we have $\mathbf{n}_A = \mathbf{n}_D$. In equation (4.17) γ_{spp} is the spontaneous emission rate into guided plasmons by one single emitter in the presence of the PW, and γ_0 is the spontaneous emission rate of photons by one single emitter in vacuum. When losses are not too high, γ_{spp} can be computed (see chapter 2) as

$$\gamma_{\text{spp}} = \gamma_0 \frac{6\pi c\epsilon_0}{2k_0^2} \frac{|\mathbf{n}_D \cdot \mathbf{e}(\mathbf{r}_D)|^2}{\text{Re}\Big[\int dA\; \mathbf{z} \cdot (\mathbf{e}(\mathbf{r}) \times \mathbf{h}^*(\mathbf{r}))\Big]}, \tag{4.18}$$

where the meaning of the various symbols is the following: c, ϵ_0, k_0 are the speed of light, permittivity, and wavevector in vacuum; $\mathbf{e}(\mathbf{r})$, $\mathbf{h}(\mathbf{r})$ are the electric and magnetic fields corresponding to the guided mode; the normalization integral in the denominator is extended to the transverse XY-plane; and $\mathbf{z}$ is a longitudinal unit vector. Let us remark that γ_{spp} is an h-dependent magnitude as it can be extracted from Figure 4.14. It is interesting to analyze the origin of the various factors in equation (4.17). Besides the geometric constant prefactor, the factor $(\gamma_{\text{spp}}/\gamma_0)^2$, which is independent of the donor-acceptor separation d, accounts for the typical decay rate enhancement in both the donor and the acceptor due to the neighboring metallic structure. The exponential decay with d comes directly from the contribution of the plasmonic mode to the Green's function in the numerator of equation (4.13), and the remaining factors depending algebraically on d/λ stem from the Green's
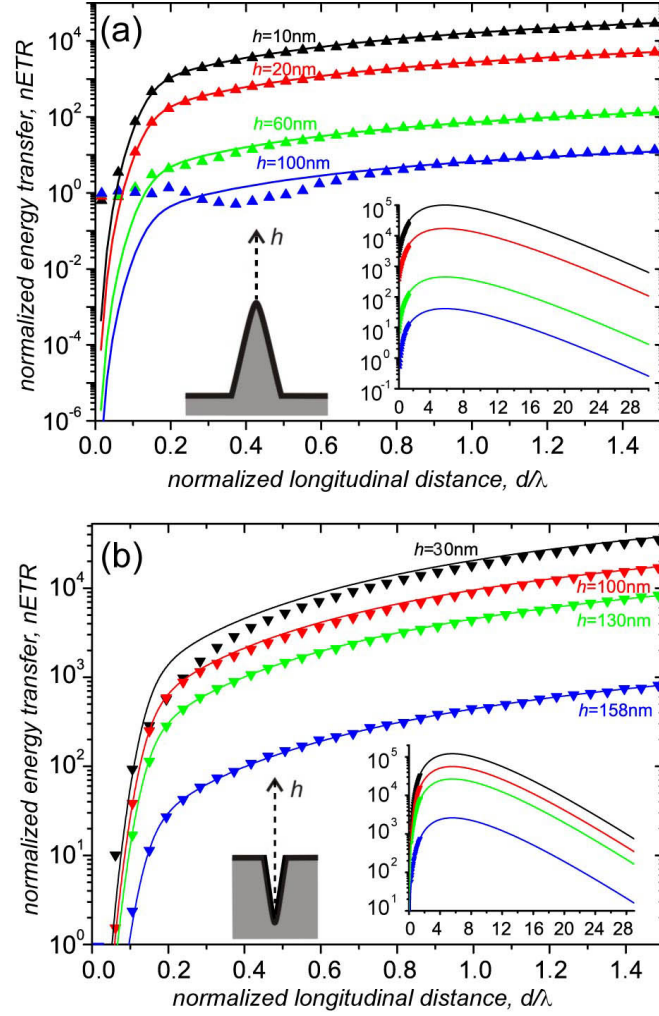
Figure 4.15: Normalized energy transfer rate between a donor and an acceptor as a function of their separation d, for various heights h. (a) Wedge waveguide and (b) channel waveguide. The symbols corresponds to numerical simulations, and the solid lines correspond to the simplified model described in the main text. The insets display the same magnitude for extended values of the abscissa.

function in vacuum, *i.e.*, the denominator of equation (4.13). Notice that the power coupled to the guided mode would keep propagating without decay for an ideal loss-free metal ($\ell = \infty$), whereas the power emitted by the donor spreads in vacuum in the absence of the waveguide link. Thus, although an ideal plasmonic guide would provide a monotonic growth of the nETR with d due to the vacuum normalization, realistic waveguides should display a maximum nETR with donor-acceptor separation. Figure 4.15 renders the nETR as a function of the donor-acceptor separation d normalized to λ, for both full-numerical (symbols) and simplified plasmon model (solid lines), for various heights h. Panels (a) and

(b) correspond to the wedge and the channel, respectively. Notice that all magnitudes in equation (4.17) are numerically computed so that there are no fitting parameters. The good concord between the numerical results and our simple model justifies the validity of our approximation. For wedges (panel (a)) the agreement only breaks down for small separations, $d/\lambda < 0.6$. This is most likely due to two reasons: (i) in this regime the contribution of radiative modes is not negligible and is superimposed to the guided mode contribution, and (ii) in the neighborhood of the donor location the fields present a spatial transient along the longitudinal coordinate Z and our simplified model, which includes only one single propagating mode, can obviously not reproduce this behavior. It is important to notice that our model allows one to explore energy transfer rates at donor-emitter separations which are too large to be numerically modeled. The inset of Figure 4.15(a) displays the nETR for larger separations. The nETRs present maxima at $d \approx 2\ell$, as can be easily obtained from equation (4.17), clearly showing that nETR grows only up to the point where absorption of the SPP mode starts to dominate the picture. The interpretation is analogous for the channel waveguides. The proposed control of the radiative properties of nanosources and enhanced resonance energy transfer may find important applications such as sensing or single-atom spectroscopy.

4.3.3 Superradiance and subradiance phenomena mediated by plasmonic waveguides

In the previous subsection we have demonstrated the enhancement of unidirectional energy transfer via PWs modes, and therefore, it is natural to consider how the collective interaction of two identical emitters can be mediated by 1D plasmons. The cooperative emission rates of several coupled oscillating systems has been considered many times since the paper by Dicke [142], including the recent all-optical analogue of two cavities connected by a photonic crystal waveguide [176], and the effect of a metallic nanoparticle in the emission of an ensemble of dipoles [177]. In this subsection, we show the collective decay rates arising from the coupling between two two-level emitters mediated by a PW. The evolution of the two emitters in interaction with the EM field supported by a PW can be represented using the Green's tensor approach, as explained with further details in chapter 2. In the results shown in the previous subsection, the acceptor dipole moment was induced by the donor's field, but no interaction was coming back to the donor due to the very high internal non-radiative decay rate of the acceptor. Now both emitters have ideally zero internal non-radiative decay rate, they interact through the guided plasmon and, as a consequence, the single emitter decay rate is modified by the presence of the other emitter. Although this is a new situation as compared with the previous section, the above discussed results suggest
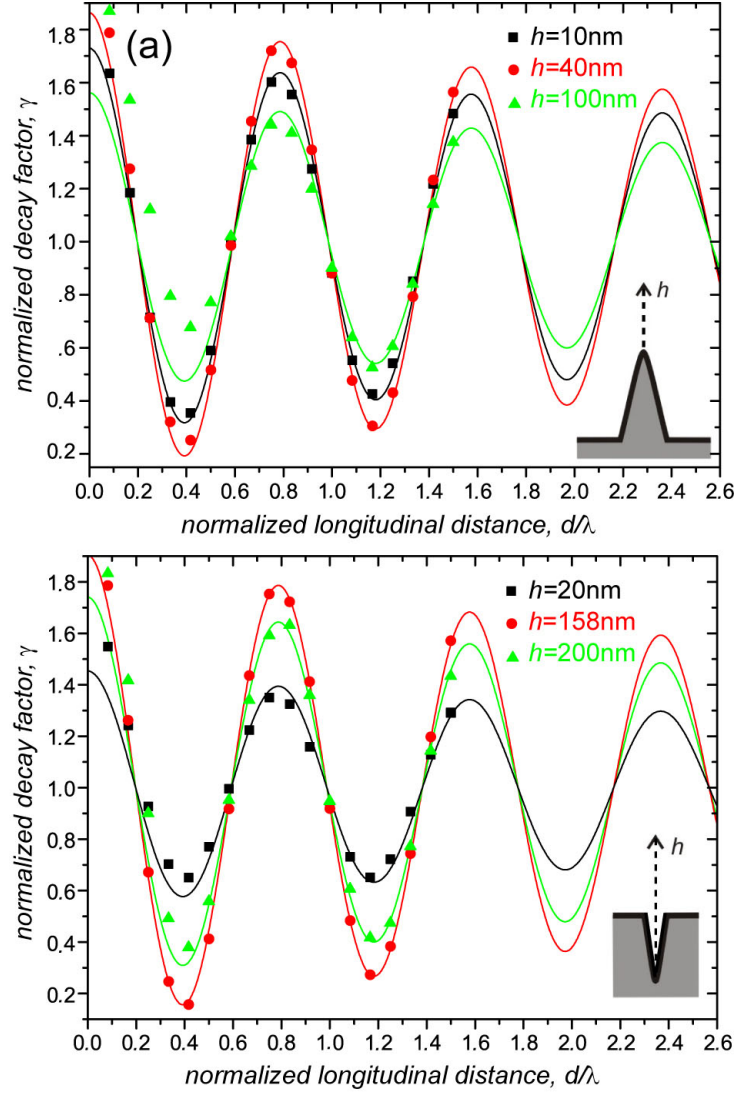
Figure 4.16: Normalized decay factor of two emitters coupled by a PW as a function of their separation d, for various heights h. (a) Wedge waveguide and (b) channel waveguide. The symbols correspond to numerical simulations, and the solid lines correspond to the simplified model described in the main text.

that a PW should provide a very efficient coupling between the two emitters. Since the wedge and the channel waveguides feature a higher nETR, we focus now only on them. We consider that both emitters are identical, with identical dipoles moments **d** separated by a distance d, and identical dipole orientations. The heights h from the emitters to the PW are chosen in order to have a high β factor, and they are identical. In general, in the dynamics of both quantum emitters coupled to the PW, the induced dipole phases of the emitters are not well fixed since they depend on the quantum state of both emitters which depends

on time. For illustration purposes, let assume that we start with a collective symmetric state, $|+\rangle = \frac{1}{\sqrt{2}}(|g_1e_2\rangle + |e_1g_2\rangle)$, in which $|g_ie_j\rangle$ represent the product state of each emitter quantum state, where the subindexes refer to the emitter labeling, whereas e or g refer to the excited and unexcited state of the emitter quantum state, respectively. Such collective state has associated a decay rate $\gamma_{11} + \gamma_{12}$ due to the coupling to the environment, which appears directly in the master equations describing the dynamics of two quantum emitters, as it is explained in further detail in chapter 5. That collective state will be superradiant or subradiant depending on the phase induced by the plasmon. Making use of the spontaneous emission coefficient [equation (5.16), chapter 2], and focusing on the results for identical emitters and identical dipole orientations ($\gamma_{11} = \gamma_{22}, \gamma_{12} = \gamma_{21}$), such collective decay rate of the symmetric state can be characterized by a normalized collective decay rate as

$$\mathrm{n}\gamma = \frac{\gamma_{11} + \gamma_{12}}{\gamma_{11}} = \frac{\mathrm{Im}[\mathbf{d}^* \cdot \mathbf{G}(\mathbf{r}_1, \mathbf{r}_1) \cdot \mathbf{d}] + \mathrm{Im}[\mathbf{d}^* \cdot \mathbf{G}(\mathbf{r}_1, \mathbf{r}_2) \cdot \mathbf{d}]}{\mathrm{Im}[\mathbf{d}^* \cdot \mathbf{G}(\mathbf{r}_1, \mathbf{r}_1) \cdot \mathbf{d}]}. \tag{4.19}$$

This normalized decay factor coincides with the ratio of the total energy rate dissipated by two classical dipoles in the presence of the PW (oscillating in-phase), and the power dissipated in the single dipole case, which it has been numerically computed and it is rendered in 4.16 for a wedge (a) and a channel (b). The symbols are the results of the full-numerical calculations of Maxwell equations for two separated dipoles. Whenever the normalized decay factor is larger (smaller) than 1 the system is in a superradiant (subradiant) state, which means that it has an enhanced (suppressed) collective decay rate respect to the single emitter decay rate γ_{11}. Notice that such superradiant and subradiant character is reversed for a system starting in an antisymmetric state, $|-\rangle = \frac{1}{\sqrt{2}}(|g_1e_2\rangle - |e_1g_2\rangle)$, since its associated collective decay rate is $\gamma_{11} - \gamma_{12}$. The oscillations in the normalized decay rate as a function of the normalized separation, d/λ, observed in both panels are due to the plasmonic coupling that arises from the dissipative coefficient [equation (4.10)], in which the periodicity is given by the plasmon wavelength ($\lambda_{\mathrm{pl}} = 474\mathrm{nm}$). The amplitude of the oscillations is damped due to the lossy character of the plasmonic modes. It is known in the literature that superradiance and subradiant phenomena are intimately related with the dynamical generation of entanglement between two quantum emitters [93], and therefore, PWs are good candidates for such purpose, as it is explained in more detail in chapter 5.

It is important to realize that the normalized decay factor, $\mathrm{n}\gamma$, depends in a non-monotonic fashion with the vertical height of the emitters, h. Let us focus our attention on the maxima in Figure 4.16(a) occurring at $d/\lambda = 0.8$. It is observed that superradiance grows when the height increases from $h = 10\,\mathrm{nm}$ to $h = 40\,\mathrm{nm}$, and then diminishes again when the height increases from $h = 40\,\mathrm{nm}$ to $h = 100\,\mathrm{nm}$. Initially this seems to be at odds with the monotonic decrease of nETR as h is increased, displayed in Figure 4.15(a). However, what is important in the present context is not the nETR but the fraction of photons that are
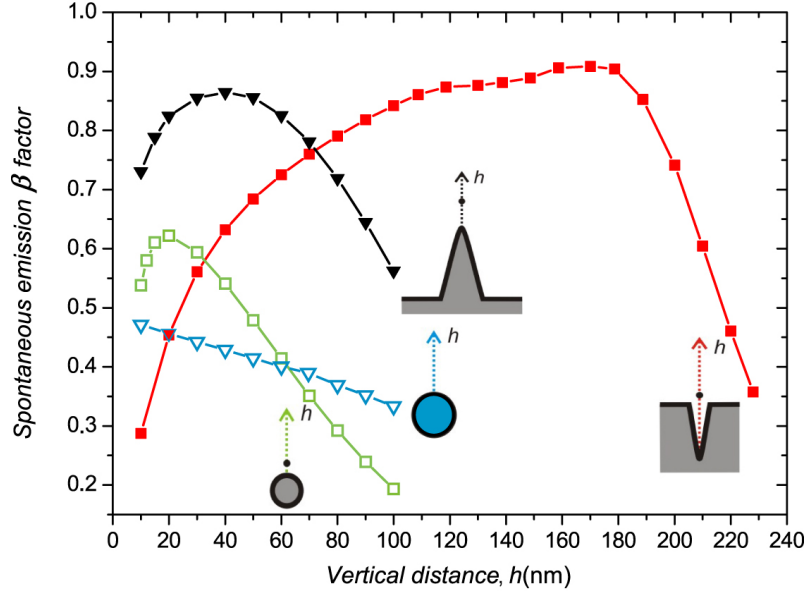
Figure 4.17: Spontaneous emission β factor of one emitter in the neighborhood of a plasmonic waveguide as a function of its height h. Black triangles (wedge waveguide), red solid squares (channel waveguide), green open squares (circular metallic wire), blue open triangles (dielectric circular wire). The metallic waveguides have the same parameters as described in 4.14. The small black dots in the insets correspond to the locations where β is maximum. The dielectric wire has radius $50\,\mathrm{nm}$ and relative permittivity $\epsilon = 15$, which is a typical value for GaAs.

coupled to guided plasmons. Indeed, for wedges the nETR grows when h is decreased, but at the same time the non-radiative losses in the neighborhood of the emitter dominate when h is smaller than about $5\,\mathrm{nm}$, and this quenching reduces the plasmonic coupling between emitters. Therefore, the variation of γ with h should be controlled by the spontaneous emission β factor of one single emitter in the presence of the waveguide, $\beta = \gamma_{\mathrm{spp}}/\gamma_{11}$. Our simplified plasmonic model of the Green's tensor described in equation (4.10) supports this view, since it predicts that the normalized decay factor of both emitters is given by

$$n\gamma = 1 + \beta\cos(k_{\mathrm{spp}}d)\exp\left(-\frac{d}{2\ell}\right), \qquad (4.20)$$

where $k_{\mathrm{spp}} = \mathrm{Re}(k)$ is the real part of the complex wavevector of the plasmonic guided mode. Equation (4.20) is rendered with solid lines in 4.16 for the chosen heights. Again the agreement between the simplified model and the simulations is very good, except for small separations, due to the presence of other radiative and non-radiative modes other than the guided plasmon. In order to illustrate our explanation, the β factor has been computed and plotted as a function of the vertical height h in 4.17 for several waveguides. The black line (triangles) corresponds to a wedge waveguide, and a maximum is indeed observed for

$h = 40\,\mathrm{nm}$, in accordance with the above-mentioned non-monotonic behavior observed in Figure 4.16(a). In a similar way, the β factor for the channel waveguide (4.17, red squares) is maximum when the emitter is slightly outside the channel ($h = 170\,\mathrm{nm}$), fitting the behavior observed in Figure 4.16(b). It is important to emphasize that it is our simplified model what demonstrates the relevance of the plasmonic guided modes and allows us to estimate that the coupling may be large even for separations, d, larger than a few wavelengths. The channel waveguide stands out as the best of the structures considered here, both because it has the largest maximum β factor ($\beta \approx 0.9$), and because it features a broader h-range where β remains high. Therefore it would be better for cases when the vertical position of the dipole are not well controlled or even the dipole alignment as pointed out in subsection 4.3.1 and subsection 4.2.3. Notice that Figure 4.17 also renders the β factors for metallic and dielectric circular wires, showing that even for the most favorable h they are less apt for the present purpose, reaching at most $\beta \approx 0.6$. Therefore, we can conclude that the achieved super and subradiance can be employed to couple quantum emitters at separations much larger than the involved optical wavelength, and such large-separation coupling seems less apt for vacuum, and for emitters coupled outside of the dielectric fiber core.

4.4 Conclusions

In this chapter it has been shown the main magnitudes quantifying the spontaneous emission of two-level emitters on inhomogeneous plasmonic waveguides environments, for one and two quantum emitters.

Regarding to the case of a single emitter, we have illustrated the emission magnitudes for the case of unidimensional plasmonic waveguides in which the strong modal confinement of the guided plasmons enhances the single-plasmon emission. In particular, we have quantified the modification of the Purcell factor, the contributions of guided SPPs to the Purcell factor and the beta factors for cylinders, wedges and channels. A large variation of their geometrical parameters, emission wavelengths and positions of the emitters has been considered. From such study in the above-mentioned plasmonic waveguides, we have identified the regions and favorable parameters for efficient single-plasmon emission. Those results point out that the wedges and channels are two promising candidates for the generation of single-plasmons, with higher efficiencies and higher rates compared to a cylindrical wire. Interestingly, those single-plasmon emission properties change slightly by small modifications of the emission wavelength due to the broadband dispersion characteristics of plasmonic waveguides. In particular, for all the cases considered, we conclude that wedges permit to achieve the highest $\frac{\gamma_{\mathrm{spp}}}{\gamma_0}$ values, whereas the channels allow to achieve the highest β factors. In addition for the channel, we have identified broad regions of high beta factor which are

wider compared to the wedge or the cylinder. Such wide regions of high beta factor can be very interesting for the experimental realization, in case of less accurate positioning of the quantum emitter. Finally, we have studied the detrimental effect of unfavorable emitter orientations. The results show a robust emission, with large beta factors and high single plasmon generation rates, in case of reasonable transversal misalignments.

For two interacting quantum emitters, we have studied the dissipative and coherent parameters involved in the formalism of two quantum emitters interacting by plasmonic waveguides. The robustness for single plasmon emission in plasmonic waveguides has allowed us to identify and check a simpler plasmon model where the plasmon is the main carrier of the interaction between emitters. Such study includes the variation of those coupling parameters, as a function of favorable and unfavorable emitters alignments. We have checked that the plasmon mediated approximation in such both coefficients differs slightly from the full-numerical one. Such result shows the relevance of the plasmon in the interaction, which is manifested in the phase and damping behaviour of both coefficients due to the characteristics of the guided plasmon. The results also show that the wedge and the channel are more robust in case of transversal misalignments, and , for distances of the order of the wavelength, they also permit higher coupling than free-space mediated one. Finally, as an application of the plasmon mediated coupling, we have studied the main features of resonance energy transfer and superradiance assisted by plasmonic waveguides. We have shown that a resonant energy transfer assisted by a plasmonic waveguide is enhanced four-orders of magnitudes higher than the vacuum mediated one and for interaction distances larger than the vacuum emission wavelength. In addition, we have shown how it appears strong superradiant and subradiant oscillations with the emitters separations due to the high plasmonic coupling, and therefore, plasmonic waveguides are good candidates for generation of entanglement between two quantum emitters. Moreover, we have identified with the plasmonic coupling model that the key magnitude for resonance energy transfer is the contribution of the decay rate from guided surface plasmons, whereas in super and subradiance phenomena, the main magnitude is the beta factor. We conclude that a metallic wedge is better for donor-acceptor energy transfer due to the higher field enhancement, whereas a metallic channel is more appropriate for the mutual coupling of two emitters. Finally, we have shown that the wedge and the channel can display much better coupling properties than a metallic cylinder and a typical dielectric waveguide.

5 Entanglement mediated by plasmonic waveguides

5.1 Introduction

Quantum mechanics has experienced a huge progress due to the advantages of their counterintuitive results. One of the branches of quantum mechanics that has reflected these large advances is quantum optics. This progress has been mainly motivated by the possible applications in quantum computation and quantum information [178], which process the information in non-classical manners. In such disciplines, the minimal quantity for processing information is encoded within a *qubit*, which is represented by two possible quantum states. The abstract concept of a qubit can be materialized through photons, atomic systems, solid-state devices and nuclear spins among others [179]. Most of the applications, such as quantum teleportation, quantum cryptography, and other two-qubit operations, are based on the availability of entangled two-qubit systems.

Within those applications, the EM field constitutes one of the most successful mode reservoirs to prepare a system in a targeted entangled state or to couple two preexisting entangled systems. In a number of proposed schemes, qubit-qubit interactions have been suggested either by coupling to a common EM cavity mode [180–182] or, when large separations between the qubits are desired, to a fiber-guided mode [146, 183]. With independence of the chosen environment, the dominant paradigm in quantum-state engineering relies almost exclusively on exploiting the coherent dynamics, or in other words, on using the wavefunction interferences in order to implement the operations needed for quantum information processing [184, 185, 179]. In those approaches, the coherent interactions or equivalently unitary operations, are crucial to exploit the quantum operations needed for quantum information theory. This initial approach was taken by cavity quantum electrodynamics in order to perform universal quantum operations [180]. The traditional view holds that dissipation, being responsible for decoherence (or equivalently, the destruction of the interference phenomena), spoils the desired coherent operations therefore playing only a negative role.

Nevertheless realistic systems are open in nature, which limits the applications of coherent

approaches. An open system necessarily implies a coupling of the system (*e.g.* two qubits) to an external environment reservoir (the background) for which the system gets entangled with. These environmental couplings, or dissipative processes within the quantum optical jargon, limit the time survival of the maximally entangled states of the system by the process called decoherence. Therefore, the decoherence presented in dissipative systems restricts the application of coherent approaches in quantum information. However, some theoretical ideas have changed the negative role of dissipation, converting it into a positive property that leads the system to a desired entangled state [42, 186, 187]. Those ideas are based on the natural entanglement formation in systems that are coupled to a common dissipative environment. When this dissipative environment is engineered, the systems can be fully used for universal operations in quantum computation [42]. The experimental steps through this quantum computational approach have already shown its potential applications with remarkable theoretical [188, 189] and experimental [190, 191] results.

Among different proposals as possible key elements for dissipative quantum computation, some pioneer ones have come from the field of quantum plasmonics [45, 50, 192, 51]. The main practical advantage of SPPs in quantum optics is its deep spatial-confinement which permits to largely control quantum emitters that act as qubits. This control is achieved by means of the small photonic areas associated with SPPs which strongly modify the emitter's decay rate, as commented in chapter 4. Different plasmonic proposals have shown the control of single-photon emitters by SPPs [41, 169, 58] and the detection of generated single SPPs [46, 49]. Those experimental and theoretical steps pave the path to on-chip quantum operations between single emitters mediated by SPPs [50, 51]. Towards the full implementation of quantum operations mediated by plasmons, we have explored [57, 56] the entangling capabilities of deep sub-wavelength plasmonic waveguides (PWs).

In this chapter we present a comprehensive study of the generation of two-qubit entanglement mediated by PWs. First, in section 5.2, we study the generation of transitory entanglement between two-qubits mediated by a homogeneous environment, which permits us to illustrate the most significant magnitudes and physical processes that characterize such phenomena. Next, in section 5.3, we study the creation of transitory entanglement shared by two distant qubits coupled to a common PW, taking advantage of the enhanced-emission capabilities and the large coupling control of the PWs shown in chapter 4. In particular, we characterize quantitatively the entanglement of the system and explain the main mechanisms that generate it. The variation in the entangling properties by changing the main initial conditions in the system (populations, emitters separation and the emitters orientations) are considered. In section 5.4, we go a step further introducing coherent pumping that represents the effect of a laser impinging resonantly on the emitters. Such addition allows the achievement of a stationary entangled state. In subsection 5.4.1, we per-

form a comprehensive study of the time evolution of entanglement for weak pumping and analyze the main mechanisms that generate it by varying the qubit-qubit separation and the pumping configuration. Next in subsection 5.4.2, we consider several issues related to the experimental study: the behaviour of the laser intensity, its relation with the waveguide efficiency, and the decoherent effect of laser-induced pure dephasing. Finally, we analyze the second order correlation at zero delay that is strongly modulated by the two qubits separation and pumping schemes.

5.2 Transitory entanglement mediated by a homogeneous medium
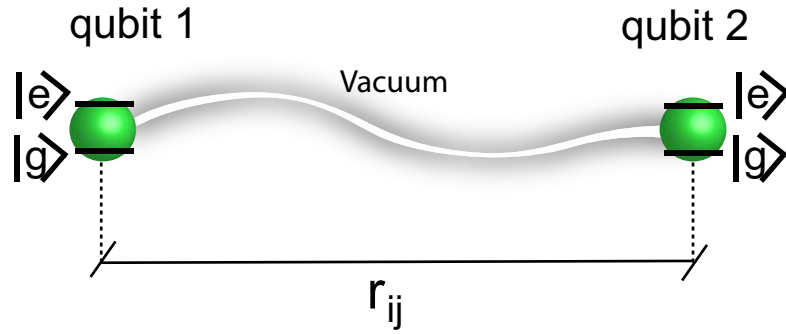
Figure 5.1: (a) Schematic representation of two identical qubits interacting at a separation distance $\mathbf{r}_{ij}$ through vacuum electromagnetic modes.

In 1954, Dicke [142] discussed one of the pioneering systems where qubits were entangled by a common bath of electromagnetic modes. In particular, he considered that two neutrons, with two possible spin states and separated closely in vacuum, do not in general behave like independent emitting objects but they interact collectively. A more abstract but equivalent system is illustrated in Figure 5.1, where the emitters are substituted by identical qubits separated by a distance $\mathbf{r}_{ij}$ and the common bath is regular vacuum in its fundamental mode. The qubits represent any two-level emitter with a peak emission wavelength λ_0. The interaction of two-level systems mediated by vacuum has been extensively revisited afterwards by many authors [193, 87, 91], including the possibility of initializing the vacuum environment in some squeezed state [91, 194] (or equivalently, vacuum modes that have non-zero correlations). In the following we focus on the generation of entangled states by regular non-squeezed vacuum in order to illustrate its entangling capabilities.

The dynamics of the reduced density matrix operator $\hat{\rho}$, associated to such system (see Figure 5.1), can be described by the following master equation (for a formal derivation, see

chapter 2):

$$\frac{\partial \hat{\rho}}{\partial t} = -\frac{i}{\hbar}[\hat{H}_\mathrm{s}, \hat{\rho}] - \frac{1}{2}\sum_{i,j}\gamma_{ij}(\hat{\rho}\hat{\sigma}_i^\dagger\hat{\sigma}_j + \hat{\sigma}_i^\dagger\hat{\sigma}_j\hat{\rho} - 2\hat{\sigma}_j\hat{\rho}\hat{\sigma}_i^\dagger), \tag{5.1}$$

where $\hat{\sigma}_i^\dagger$ and $\hat{\sigma}_i$ are the i-qubit raising and lowering operator respectively, and the hamiltonian $\hat{H}_\mathrm{s}$ included in the coherent part of the dynamics is given by the expression

$$\hat{H}_\mathrm{s} = \sum_i \hbar(\omega_0 - \delta_i)\,\hat{\sigma}_i^\dagger\hat{\sigma}_i - \sum_{i\neq j}\hbar g_{ij}\,\hat{\sigma}_i^\dagger\hat{\sigma}_j. \tag{5.2}$$

The interpretation of the various constants appearing in equations (5.1) and (5.2) is the following. The Lamb shift, δ_i, is due to the qubit EM self-interaction which for optical emitters is in general of the order of a few GHz [47, 194] and therefore its role in the dynamics is small at optical frequencies. The term g_{ij} represents the level shift induced by the dipole-dipole coupling, and γ_{ij} represents the self (γ_{ii}) and collective ($\gamma_{ij}, i \neq j$) dissipative terms associated with the spontaneous emission from the qubits. In the case of emitters with mutually-parallel dipole moments, such coefficients are specifically given by [91]:

$$\begin{aligned}
\gamma_{ij} =&\frac{3\sqrt{\gamma_{ii}\gamma_{jj}}}{2}\left\{\left[1 - \left(\frac{\mathbf{d}}{|\mathbf{d}|}\cdot\frac{\mathbf{r}_{ij}}{|\mathbf{r}_{ij}|}\right)^2\right]\frac{\sin(k_0 r_{ij})}{k_0 r_{ij}}\right.\\
&\left.+ \left[1 - 3\left(\frac{\mathbf{d}}{|\mathbf{d}|}\cdot\frac{\mathbf{r}_{ij}}{|\mathbf{r}_{ij}|}\right)^2\right]\left[\frac{\cos(k_0 r_{ij})}{(k_0 r_{ij})^2} - \frac{\sin(k_0 r_{ij})}{(k_0 r_{ij})^3}\right]\right\},
\end{aligned} \tag{5.3}$$

$$\begin{aligned}
g_{ij,i\neq j} =&\frac{3\sqrt{\gamma_{ii}\gamma_{jj}}}{4}\left\{\left[1 - \left(\frac{\mathbf{d}}{|\mathbf{d}|}\cdot\mathbf{r}_{ij}\right)^2\right]\frac{\cos(k_0 r_{ij})}{k_0 r_{ij}}\right.\\
&\left.- \left[1 - 3\left(\frac{\mathbf{d}}{|\mathbf{d}|}\cdot\mathbf{r}_{ij}\right)^2\right]\left[\frac{\sin(k_0 r_{ij})}{(k_0 r_{ij})^2} + \frac{\cos(k_0 r_{ij})}{(k_0 r_{ij})^3}\right]\right\},
\end{aligned} \tag{5.4}$$

where $\gamma_{ii} = \frac{\omega_0^3|\mathbf{d}_i|^2}{3\pi\varepsilon_0\hbar c^3}$ and $\mathbf{d}_i$ are the i-qubit decay rate and dipole moment, respectively. It is worth mentioning that under Dicke's argument of the small sample of atoms in reference [142], the term γ_{ij} was $\mathbf{r}_{ij}$ independent and the dipole-dipole interaction was negligible ($g_{ij} = 0$). However, in the small sample limit ($\mathbf{r}_{ij} \ll \lambda$), we can easily check from equations (5.3-5.4) that both suppositions are a simplification and in fact g_{ij} diverges for $\mathbf{r}_{ij} \to 0$. In order to illustrate the differences introduced by equations (5.3) and (5.4) and Dicke's assumptions, we are going to solve equation (5.1) for two representative cases: the small sample limit ($\mathbf{r}_{ij} \ll \frac{\lambda}{2}$) and the intermediate-distance limit, *i.e.* $\mathbf{r}_{ij} \sim \frac{\lambda}{2}$.

In order to solve the master equation (5.1), we need to choose an appropriate wavefunction basis for the two qubit to expand the different terms of the system's density operator. A
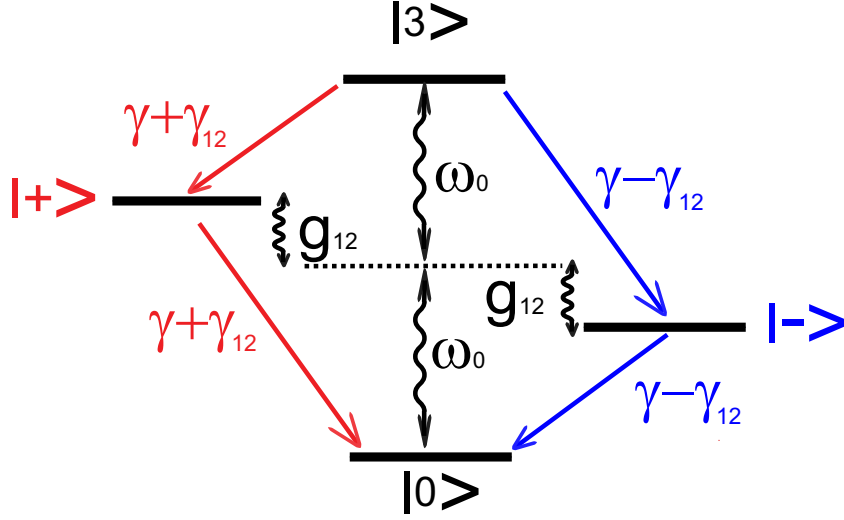
Figure 5.2: Scheme of levels for two identical qubits located at equivalent positions in vacuum or a waveguide and with identical orientations ($\gamma_{11} = \gamma_{22} = \gamma$ and $\gamma_{12} = \gamma_{21}$).

convenient complete basis that makes $\hat{H}_\mathrm{s}$ diagonal is formed by the following collective state basis, firstly introduced by Dicke [142]: $|3\rangle = |e_1 e_2\rangle$, $|\pm\rangle = \frac{1}{\sqrt{2}}(|g_1 e_2\rangle \pm |e_1 g_2\rangle)$ and $|0\rangle = |g_1 g_2\rangle$, where $|g_i\rangle$ and $|e_i\rangle$ label the ground and excited state of the i-qubit, respectively. The diagonal character of the $\hat{H}_\mathrm{s}$ matrix operator in the above-mentioned basis is depicted in the level scheme shown in Figure 5.2, representing the eigenenergies. In addition, using the same basis, and assuming that the reduced density matrix at the initial time is in a crossed X-form (*i.e.* with their matrix elements being zero, except its diagonal and anti-diagonal), the evolution of the non-trivial density matrix elements from equation (5.1) is given by [93]:

$$\dot{\rho}_{33}(t) = -2\gamma\rho_{33}(t), \tag{5.5}$$

$$\dot{\rho}_{++}(t) = (\gamma + \gamma_{12})\rho_{33}(t) - (\gamma + \gamma_{12})\rho_{++}(t), \tag{5.6}$$

$$\dot{\rho}_{--}(t) = (\gamma - \gamma_{12})\rho_{33}(t) - (\gamma - \gamma_{12})\rho_{--}(t), \tag{5.7}$$

$$\dot{\rho}_{00}(t) = (\gamma + \gamma_{12})\rho_{++}(t) + (\gamma - \gamma_{12})\rho_{--}(t), \tag{5.8}$$

$$\dot{\rho}_{+-}(t) = -(\gamma - 2ig_{12})\rho_{+-}(t), \tag{5.9}$$

$$\dot{\rho}_{30}(t) = -(\gamma + 2i\omega_0)\rho_{30}(t), \tag{5.10}$$

where, as a consequence of the identical character of the qubits, we have used $\gamma_{11} = \gamma_{22} = \gamma$ and $\gamma_{12} = \gamma_{21}$. Notice that due to the properties of the reduced density matrix operator and the type of master equation (5.1), the relations $1 = \rho_{++} + \rho_{--} + \rho_{33} + \rho_{00}$ and $\rho_{ij} = \rho_{ji}^*$ hold

in time. Equations (5.5)-(5.10) explain the possible decay and coherent mechanisms of the system as illustrated in Figure 5.2. The equations with equal indexes, or diagonal elements in the density matrix, represent the evolution of the populations, *i.e.*, the probability of finding an excitation in a certain state of the system. The non-diagonal terms represent the coherences between different states or in other words the terms resulting from quantum interference. Therefore, the terms containing $2\omega_0$ and $2g_{12}$ coefficients mediate the coherent, oscillatory dynamics between levels $|3\rangle \leftrightarrow |0\rangle$ and $|+\rangle \leftrightarrow |-\rangle$ respectively, as seen from the presence of the imaginary number i in equation (5.5). On the other hand, the terms γ and γ_{12} governs the dissipative dynamics which is associated with the damping of the populations and the coherences of the system.

We are specially interested in studying the generation of entangled states and consequently, we need a systematic way to identify them. Regarding the quantification of entanglement, there are several alternatives [195] but all of them are related to each other for a bipartite system, *i.e.*,two-qubits. We will make use of the *concurrence C* defined by Wooters [196], due to its computation easiness and intuitive characterization. The concurrence is defined as follows: $C \equiv [\max\{0, \sqrt{\lambda_1} - \sqrt{\lambda_2} - \sqrt{\lambda_3} - \sqrt{\lambda_4}\}]$, where $\{\lambda_1, \lambda_2, \lambda_3, \lambda_4\}$ are the eigenvalues of the matrix $\rho T \rho^* T$ in decreasing order (the operator T is $\sigma_y \otimes \sigma_y$, σ_y being the Pauli matrix). The interpretation of the concurrence is quite simple: it takes a value 0 for completely unentangled states and 1 for maximally entangled states. Any intermediate value results from a mixed entangled state and therefore it cannot be represented as a mixture of factorizable pure states [196]. For the particular case of an initial density matrix in a crossed X-form, such shape of the density matrix is kept at time t and the concurrence has two non-trivial solutions that are easily derived [93, 197]:

$$C = max\{0, C_1, C_2\}, \tag{5.11}$$

where

$$C_1(t) = 2\sqrt{(\text{Re}[\rho_{03}(t)])^2 + (\text{Im}[\rho_{03}(t)])^2} - \sqrt{[\rho_{++}(t) + \rho_{--}(t)]^2 - 4\text{Re}[\rho_{+-}(t)]^2}, \tag{5.12}$$

and

$$C_2(t) = \sqrt{[\rho_{++}(t) - \rho_{--}(t)]^2 + 4\text{Im}[\rho_{+-}(t)]^2} - 2\sqrt{\rho_{00}(t)\rho_{33}(t)}. \tag{5.13}$$

Now that we have all the tools, let us characterize the generation of entanglement for two qubits with mutually-parallel dipole moments in the small sample and the intermediate-distance limits. In figures 5.3 (a) and (b), we represent the numerical results for the concurrence versus the normalized time for both cases $|\mathbf{r}_{ij}| = \frac{\lambda}{12}$ and $|\mathbf{r}_{ij}| = \frac{\lambda}{2}$, respectively. Both cases starts in the initial state with one of the qubits excited, *e.g.* $\rho_{++} = \rho_{--} = \rho_{+-} = \rho_{-+} = \frac{1}{2}$, which can be realized assuming that one of the qubits has been excited with a π-pulse [198].

Let us describe first the behaviour of the small sample limit. In panel (a) we can observe that the concurrence (black line) starts from zero, due to the initial unentangled state condition, and it raises fast until it starts developing rapid oscillations which decrease in time. Such behaviour continues until the oscillations stop being observable after approximately $\gamma t = 3$, and then the concurrence decays exponentially in time. The generated entanglement can be understood from the analytical solution of the concurrence (5.11) in which only equation (5.13) has a non-negative value for the considered initial density matrix. In particular we can easily obtain from the solutions of equations (5.5) the following expression [93]:

$$C(t) = \frac{1}{2}\sqrt{[e^{-(\gamma-\gamma_{12})t} - e^{-(\gamma+\gamma_{12})t}]^2 + e^{-2\gamma t}4(\sin(2g_{12}t))^2}. \tag{5.14}$$

All the terms inside the square root contribute to the fast increase of the concurrence in time and therefore to the generation of entanglement. We can clearly see that the concurrence oscillations come from the sinusoidal term which arises from the coherence between the states $|+\rangle$ and $|-\rangle$, $\rho_{+-}(t)$, which is induced by the dipole-dipole interaction g_{12}. Additionally, we can easily observe that the first term inside the square root, arising from the difference between the $|+\rangle$ and the $|-\rangle$ populations, is responsible for the dominance of the concurrence at longer times. This fact is due to the faster, exponential decay of the 'coherent' term respect to the purely dissipative term as it is explained next. The population $\rho_{--}(t)$ decays with a reduced decay $\gamma - \gamma_{12} = 0.05\gamma$ compared to the fast decay times of $\rho_{+-}(t)$ and $\rho_{++}(t)$, which are two orders of magnitude larger (γ and $\gamma + \gamma_{12} = 1.95\gamma$ respectively). Therefore the reduced lifetime of the antisymmetric state is responsible for the later stage of the concurrence as it can be seen from the asymptotic approach of C to $\rho_{--}(t)$ (dashed blue line), which slowly decays to zero in an infinite time.

In the intermediate-distance case (Figure 5.3(b)) we can observe that the general behaviour of the concurrence is very different from the small sample limit. The oscillations are overdamped by the factor $e^{-2\gamma t}$, which is a result from the small values of the mutual coherent parameter ($g_{12} = 0.21\gamma$). It can be appreciated that still the coherent term dominates for times approximately smaller than $\gamma t = 3$ and the dissipative terms for longer times, as it can be deduced visually from the difference between $\rho_{--}(t)$ and $\rho_{++}(t)$ in Figure 5.3(b). In addition, in contrast to the small sample, the maximum values of the concurrence have been reduced considerably which is due to the small values of g_{12} and γ_{12} ($\gamma_{12} = 0.15\gamma$), and the decay is faster due to the reduced lifetime of the antisymmetric population $\rho_{--}(t)$. The main conclusion we can take from figures 5.3(a) and (b) is that for intermediate-distances larger than $\frac{\lambda}{2}$, the entanglement generation starts to be relatively poor in contrast to the relatively large and long-lasting degree of entanglement in the small-sample regime. Additionally, it can be inferred that such situation gets drastically worse for

far-distances $|\mathbf{r}_{ij}| > \lambda$ as it is deduced from the decreasing behaviour of γ_{12} and g_{12} with $\frac{|\mathbf{r}_{ij}|}{\lambda}$.
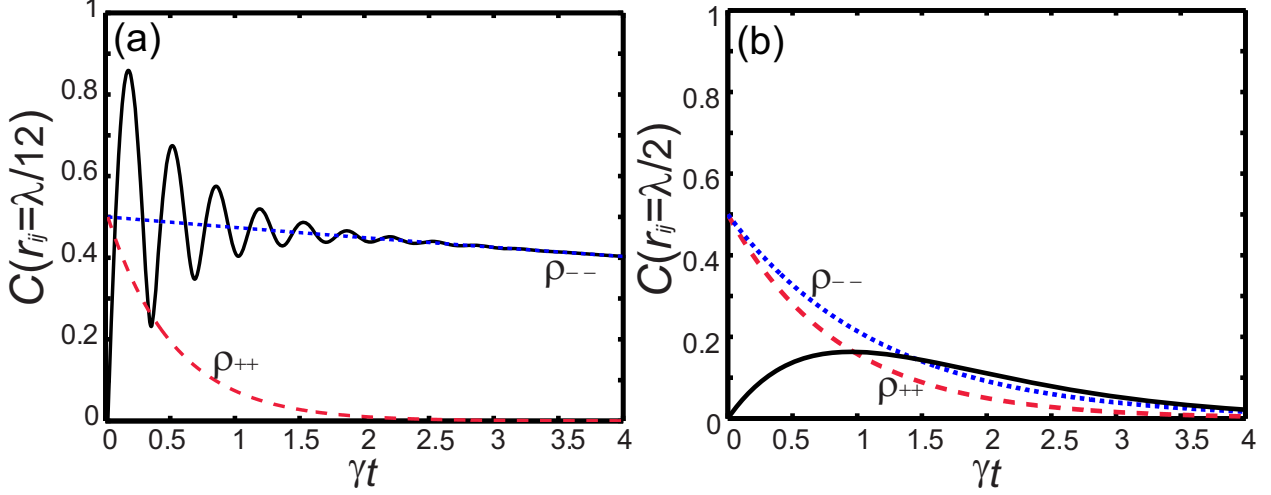
Figure 5.3: Concurrence C versus the time t, in normalized decay-rate γ units, for two fixed distances: $|\mathbf{r}_{ij}| = \frac{\lambda}{12}$ (a) ($\gamma_{12} = 0.95\gamma$ and $g_{12} = 4.65\gamma$, extracted from (5.3) and (5.4), respectively) and $|\mathbf{r}_{ij}| = \frac{\lambda}{2}$ (b) ($\gamma_{12} = 0.15\gamma$ and $g_{12} = 0.21\gamma$). In both cases the two dipoles moments are parallel-oriented and perpendicularly aligned to the connecting distance $\mathbf{r}_{ij}$, *i.e.*, $\mathbf{dr}_{ij} = 0$. For illustrative purposes, they are also displayed the time dependencies of the antisymmetric $\rho_{--}(t)$ (dashed blue line) and symmetric populations $\rho_{++}(t)$ (dashed red line).

5.3 Transitory entanglement mediated by plasmonic waveguides

5.3.1 Far-distance entanglement

The poor two-qubit entanglement generation mediated by vacuum at far distances, has motivated the search of different coupling schemes for improving it. Some of these improvements have come from the coupling of emitters to single-mode cavities [180, 181] and dielectric waveguides [146, 183] taking advantage of the small photonic losses in those mediums. Very different attempts have come from the field of plasmonics, where the higher presence of propagation losses is compensated by the stronger control (*i.e.* higher β factor) of the emitters, due to the sub-wavelength modal sizes of plasmons as shown in chapter 4. Motivated in addition by the experimental evidence that single [41, 49] and two-plasmon correlations [53, 199] are preserved in lossy plasmonic environments, some theoretical proposals have explored the advantage of plasmonic environments to generate entanglement [57, 56, 200]. In

this section we study the generation of entanglement between two identical qubits mediated by one dimensional plasmons that are supported by the conventional metallic waveguides studied in chapter 4. The problem is illustrated in Figure 5.4, where two identical optical
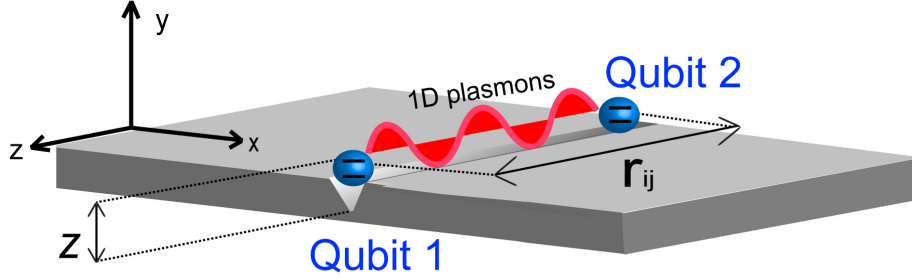
Figure 5.4: (a) Two qubits interacting with a plasmonic waveguide, in this case a channel waveguide

emitters separated by a distance $d = |\mathbf{r}_{ij}|$, are placed close to a plasmonic waveguide (in particular in this case for a channel plasmonic waveguide). Both atomic systems are modelled as two-level emitters or qubits and they have associated a transition dipole moment $\mathbf{d}$ with a fixed orientation. The master equation describing the dynamics of such system is identical to equation (5.1) where the dipole-dipole coupling g_{ij} and the dissipative term γ_{ij} are given in general by (see chapter 2):

$$g_{ij,i\neq j} = \frac{\omega_0^2}{\hbar\varepsilon_0 c^2}\mathbf{d}_i^* \operatorname{Re}\mathbf{G}(\mathbf{r}_i, \mathbf{r}_j, \omega_0 - \delta_j)\,\mathbf{d}_j, \tag{5.15}$$

$$\gamma_{ij} = \frac{2\omega_0^2}{\hbar\varepsilon_0 c^2}\mathbf{d}_i^* \operatorname{Im}\mathbf{G}(\mathbf{r}_i, \mathbf{r}_j, \omega_0 - \delta_j)\,\mathbf{d}_j. \tag{5.16}$$

Expressions (5.15) and (5.16) are obtained from the calculation of the EM field Green's tensor in the frequency domain [81, 181] and it is general for any lossy assisting medium. In the case of mutually-parallel emitters in vacuum, the substitution of the vacuum Green's tensor in those expressions leads to equations (5.3) and (5.4). In the particular case of emitters coupled to plasmonic waveguides, those equations for $i \neq j$ can be very well approximated by the guided plasmonic Green's tensor resulting in the coefficients $g_{ij,pl}$ and $\gamma_{ij,pl}$ calculated in chapter 4 (see equations (4.9), (4.10) and (4.11), (4.12)). Additionally, the Lamb shift, δ_j, appearing in (5.15) and (5.16), is due to the qubit EM self-interaction in the presence of the PW. In the case of structurally complex PWs like wedges or channels, it is difficult to calculate it numerically due to the frequency integral involved for the calculation

of δ_j (see chapter 2). Nevertheless it is known that such frequency shifts are relevant at distances from the emitter to the metallic surface much smaller than the wavelength ($\frac{Z}{\lambda} \ll$ 1), in which the emission is mainly non-radiative [47, 201, 202]. For such short distances, the shift can be estimated from the reflected fields at a flat metallic surface or a spherical particle, which are of the same order [201]. In particular, at optical frequencies, for a dipole-surface distance of 10 nm in a silver metal surface [201], we estimate that shift of the order of $100\gamma_0$. For the typical optical emitters in vacuum, $\gamma_0 \sim 1$GHz, and consequently the percentage of change in the emission wavelength is smaller than 0.001%. Therefore for emitter-surface distances larger than 10 nm, we expect δ_j to be very small [47, 202] compared to the emission wavelength, as considered in the coefficients calculated in chapter 4. Moreover, we are going to consider mostly symmetrical orientations and positioning, in which these shifts are equal for both emitters and therefore they do not play a relevant role in the dynamics.

Let us show the advantages arising from the use of PWs in comparison with the vacuum, considering when both emitters have mutually-parallel dipole moments, and the emitters are separated by a far distance $d > \lambda$. The alignment and positions of the emitters are chosen to have high plasmon coupling, *i.e.*, β factor, and only one of the emitters starts in its excited state. Figure 5.5 shows the time evolution of the concurrence C for two emitters placed in different conventional PWs or vacuum at a separation distance $d = 1.6\lambda$, being $\lambda = 600$ nm the optical emission wavelength. We can clearly see that the concurrence maxima displayed by the PWs are more than a factor of three larger than the vacuum one (even six for the channel), so the plasmon largely enhances the generated degree of entanglement at far distances. Such significant values are kept by times intervals of the order of $1/\gamma$. Also be noticed from the decay-rate factor in the time dependence, that the entanglement is achieved at shorter times due to the higher values of γ for the PWs (see the different values in the caption), and therefore making the dynamics faster. In addition, we can observe the increasing values of the concurrence maxima for the cylinder, wedge and channel respectively. This behaviour can be understood from the plasmon coupling efficiencies which are 0.62, 0.84, and 0.9, respectively, therefore increasing the coupling parameters as deduced from formulas (4.9) and (4.10) (see the caption). Consequently, it is very important the design and efficiency of the plasmonic waveguide in order to achieve higher degrees of entanglement between the qubits.
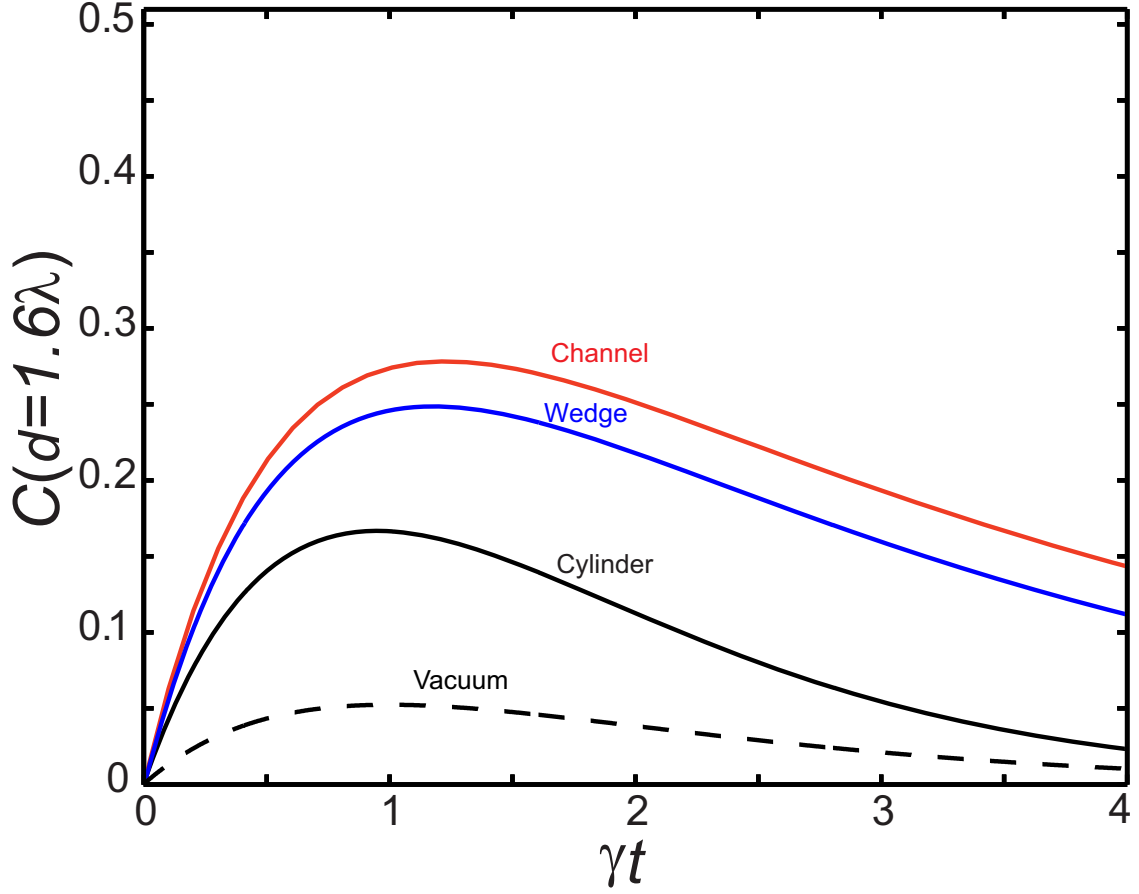
Figure 5.5: (a) Concurrence C versus the time t, in their normalized decay-rate units, for a qubit-qubit distance $d = 1.6\lambda$ in vacuum (dashed black line), a cylinder (black line), a wedge (blue line) and a channel (red line). The coupling parameters are extracted from the calculations shown in Figure 4.11, chapter 4 and formulas (5.3) and (5.4). The corresponding values are respectively; $(\gamma = \gamma_0$, $\gamma_{12} = 0.09\gamma_0$ and $g_{12} = -0.06\gamma_0)$ for the vacuum, $(\gamma = 9\gamma_0$, $\gamma_{12} = -0.07\gamma$ and $g_{12} = 0.22\gamma)$ for the cylinder, $(\gamma = 9.6\gamma_0$, $\gamma_{12} = 0.63\gamma$ and $g_{12} = 0.00\gamma)$ for a wedge and $(\gamma = 10.4\gamma_0$, $\gamma_{12} = 0.68\gamma$ and $g_{12} = 0.00\gamma)$ for the channel.

5.3.2 Influence of qubit separation on the dissipative and coherent dynamics

Let us acquire a deeper physical insight into the dynamics and its dependence with the emitters separation distance d in the presence of PWs. From the plasmon coupling coefficients g_{ij} and γ_{ij} (formulas (4.9) and (4.10)), we can observe how the values of the different coupling parameters are controlled by the qubit-qubit separation respect to the plasmon wavelength. Due to their sine and cosine dependence, there are two relevant sets of dis-

tances: the one where the mutual coherent terms g_{ij} cancel (from now on, we name it the dissipative set), and the second one where the mutual dissipative terms γ_{ij} vanish (coherent set). We firstly analyze the dissipative set for a distance $d = \lambda_{pl}$ where γ_{ij} attains its maximum value as shown in Figure 4.11(b) and then for distances corresponding to the coherent set. In both situations we consider that the qubits dipoles are mutually-parallel and horizontally-y aligned coinciding with the predominant polarization of a channel plasmon at a distance $Z = 150$ nm.

The system is initialized in the (unentangled) state $|1\rangle = |e_1 g_2\rangle = \frac{1}{\sqrt{2}}(|+\rangle + |-\rangle)$ for a qubit-qubit distance $d = \lambda_{pl}$. In this case the evolution is confined to the subspace spanned by $\{|0\rangle, |+\rangle, |-\rangle\}$ and the non-trivial elements of the master equation (5.5) are reduced to:

$$\dot{\rho}_{++}(t) = -(\gamma + \gamma_{12})\rho_{++}(t), \tag{5.17}$$

$$\dot{\rho}_{--}(t) = -(\gamma - \gamma_{12})\rho_{--}(t), \tag{5.18}$$

$$\dot{\rho}_{00}(t) = (\gamma + \gamma_{12})\rho_{++}(t) + (\gamma - \gamma_{12})\rho_{--}(t), \tag{5.19}$$

$$\dot{\rho}_{+-}(t) = -\gamma\rho_{+-}(t). \tag{5.20}$$

These non-zero entries in $\hat{\rho}(t)$ make the expression for the concurrence from equation (5.11) very simple:

$$C(t) = |\rho_{++}(t) - \rho_{--}(t)|, \tag{5.21}$$

where we see that an imbalance of the populations ρ_{++} and ρ_{--} results in a non-zero concurrence ($\mathrm{Im}\rho_{+-}(t)$ is zero for the chosen conditions). Solving equations (5.17)-5.20), and using the plasmon coupling formulas (4.9) and (4.10), the concurrence becomes

$$C(t) = e^{-\gamma t} \sinh[\gamma\beta e^{-\lambda_{\mathrm{pl}}/(2\ell)}t]. \tag{5.22}$$

This concurrence and the relevant populations are plotted in Figure 5.6 as a function of time (C is the black thick line, and ρ_{++}, ρ_{--} are the red dashed and blue dotted lines, respectively). Panel (a) corresponds to the idealized case where $\beta = 1$ and the plasmon propagation length is $\ell = \infty$, which is shown for illustration purposes due to the resemblance of the conditions described by Dicke [142] where $g_{ij} = 0$ and $\gamma_{ij} = \gamma$. The concurrence grows with time monotonically up to a value of $C = 0.5$ where it remains constant. This process can be easily understood using equation (5.21) and observing the mentioned population imbalance. Since $\gamma_{12} = \gamma$, the population ρ_{++} decays at an enhanced rate 2γ, whereas ρ_{--} stays constant due to its zero decay rate. Consequently, there is a half probability of generating the antisymmetric maximally entangled state $|-\rangle$ which agrees with the result discussed by Dicke. Dicke's case corresponds to an idealized situation hard to realize experimentally, and its results differ very much for lossy plasmonic waveguides. Panel (b) corresponds to a realistic channel PW with $\beta = 0.9$ and $\ell = 1.7\,\mu$m. In this case the concurrence reaches

Figure 5.6: Concurrence (black thick line) and populations ρ_{++} (red dashed line), ρ_{--} (blue dotted line), versus time. (a) Ideal PW satisfying $\beta = 1$ and $\ell = \infty$. (b) Realistic channel PW. The time is scaled with the emitter lifetime $(1/\gamma)$. The coupling parameters are extracted from the calculations shown in Figure 4.11, chapter 4) which are $(\gamma = 10.4\gamma_0$, $\gamma_{12} = 0.78\gamma$ and $g_{12} = 0.00\gamma_0)$ for the channel.

a maximum value of $C = 0.33$ for $t \simeq 1/\gamma$ and then decays exponentially to zero. For this realistic structure both populations have finite decay rates and the concurrence eventually vanishes at long times. In both panels, $|+\rangle$ and $|-\rangle$ are examples of superradiant and subradiant states, respectively, as commented in further detail in chapter 4. We can now present a qualitative picture of more general entanglement generation processes by referring to Figure 5.2. The upper levels depopulate along two routes: through the state $|+\rangle$, with decay rate $\gamma + \gamma_{12}$, and through the state $|-\rangle$ with decay rate $\gamma - \gamma_{12}$. It is the difference in the decay rates along both routes what results in the transient build up of the concurrence. Therefore it seems crucial to have the decay rate $\gamma_{12} - \gamma$ as low as possible, which is achieved by increasing β factor, in accordance with the results commented previously in Figure 5.5. From the magnitude and sign spatial dependence of γ_{12}, which is proportional to $\cos(2\pi \frac{d}{\lambda_{pl}})$ (formula (4.10)), is that the qualitative dynamics just commented above is repeated for distances which are integer numbers of $\lambda_{pl}/2$. In addition, it can be easily seen that, due to the changes in sign of γ_{12}, the roles of the states $|+\rangle$ and $|-\rangle$ are exchanged at odd-integer numbers of the distance $d = \lambda_{\text{pl}}/2$, being $|+\rangle$ subradiant and $|-\rangle$ superradiant. Nevertheless, it is important to notice the reduction of the coupling coefficients at longer distances due to the exponential factor $e^{(-\frac{d}{2\ell})}$ coming from the propagation losses of the plasmons, therefore limiting the lengths for generating entanglement in the system.

The other significantly different set of distances are those when d equals odd-integer numbers of $\lambda_{\text{pl}}/4$ and consequently γ_{12} vanishes, *i.e.* the coherent set. In this case the interaction is mediated by a pure coherent dynamics, reflected in the dipole-dipole interaction term g_{12}. As considered before, we treat the initial condition where the system starts in the unentangled state $|1\rangle = |e_1 g_2\rangle = \frac{1}{\sqrt{2}}(|+\rangle + |-\rangle)$. In this case the master equation (5.5) is reduced to

$$\dot{\rho}_{++}(t) = -\gamma \rho_{++}(t), \tag{5.23}$$

$$\dot{\rho}_{--}(t) = -\gamma \rho_{--}(t), \tag{5.24}$$

$$\dot{\rho}_{00}(t) = \gamma \rho_{++}(t) + \gamma \rho_{--}(t), \tag{5.25}$$

$$\dot{\rho}_{+-}(t) = -(\gamma - 2ig_{12})\rho_{+-}(t). \tag{5.26}$$

For the initial conditions considered ($\rho_{--} = \rho_{++} = \frac{1}{2}$), we can easily deduce from equations (5.23) and (5.24), that both populations are equal on time. Therefore using equation (5.11) and the solutions of equation (5.23), it can be easily derived the following evolution for the concurrence:

$$C(t) = 2|\text{Im}[\rho_{+-}(t)]| = e^{-\gamma t}|\sin(2g_{12}t)|, \tag{5.27}$$

showing that the generation of entanglement is due to the imaginary part of the coherence ρ_{+-}. We display in Figure 5.7 the time dependence of the concurrence, the imaginary part
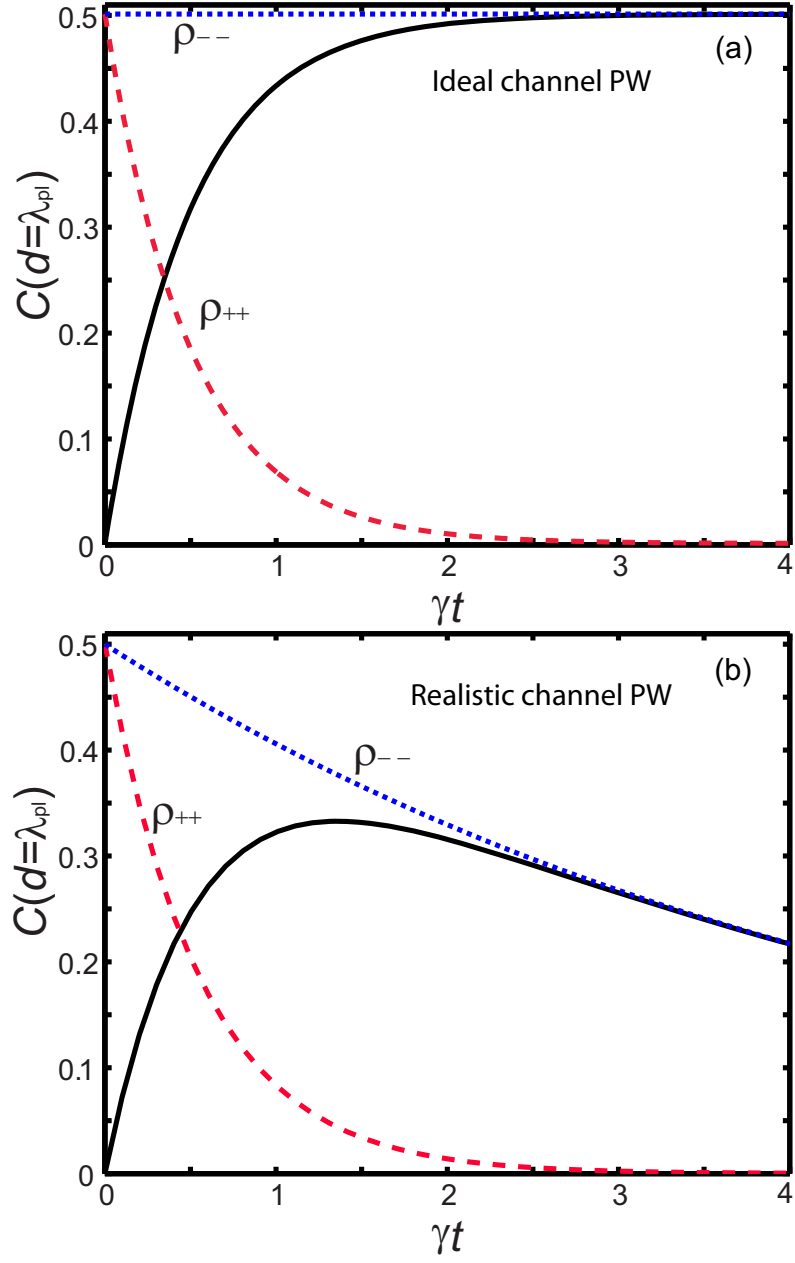
Figure 5.7: Concurrence C (black thick line), populations ρ_{++} (red dashed line), ρ_{--} (blue dotted line), and imaginary part of the coherence ρ_{+-} (dashed green line) versus time. The time is scaled with the emitter lifetime $(1/\gamma)$. The coupling parameters are extracted from the calculations shown in Figure 4.11, chapter 4) which are $(\gamma = 10.4\gamma_0,\ \gamma_{12} = 0.00\gamma_0$ and $g_{12} = 0.40\gamma)$ for the channel. Inset: Zoom of the main panel in the second concurrence oscillation.

of the coherence $\text{Im}\rho_{+-}$ and the populations $\rho_{++}(t)$ and $\rho_{--}(t)$. The concurrence starts from zero due to the initial unentangled state, and then it achieves a maximum, which is related to the population transfer from the state $|+\rangle$ to $|-\rangle$. It can be easily checked from the time derivative of formula (5.27) that the maxima at 0.84γ occurs at the condition $\tan(2g_{ij}t) = \frac{2g_{ij}}{\gamma}$. As time increases, the concurrence diminishes and it achieves a zero at the time $2g_{ij}t = \pi$ as deduced from the sinusoidal dependence of equation (5.27). Then the oscillatory behaviour of equation (5.27) is drastically damped due to the exponential decay induced by the spontaneous emission (see the inset for a zoom of the second oscillation). Interestingly, it can be deduced directly from equation (5.27) that even in the case of an ideal

waveguide, the entanglement will decrease in time due to presence of the exponential decay. Such decay arises from the spontaneous emission reflected in the γ factor that appears in the equation for $\dot{\rho}_{+-}(t)$ in (5.23). Also, it is interesting to point out in Figure 5.7 that the concurrence in the purely coherent case ($C = 0.27$) is smaller than the purely dissipative one considered in Figure 5.6 ($C = 0.33$). Notice that such lower value occurs even though the qubit-qubit separation $d = 0.75\lambda_{\mathrm{pl}}$ is smaller than in the dissipative case, and therefore it implies a smaller spatial decay of the plasmon. In addition, the entanglement in the coherent set decays with a constant γ, whereas in the dissipative one, it decays within a considerably reduced scale $\gamma - \gamma_{12}$. Therefore we can conclude that for entanglement generation, the dissipative set is more robust than the coherent set.

At qubit-qubit distances which are between the two commented sets, the system will display a mix of both coherent and dissipative dynamics. Consequently, the time scale of the survival of the entanglement will be reduced at a slower scale $\gamma - \gamma_{12}$ compared to the nearest pure coherent distance. Nevertheless, γ_{12} is not maximum and it will decay faster than the nearest pure dissipative distance. In addition, in light of equation (5.21), the concurrence in such intermediate distances is averaged between both the pure dissipative and the pure coherent cases. Accordingly, the maximum degree of entanglement is necessarily smaller compared to the nearest purely dissipative distance. Therefore, we can conclude that, in order to generate entanglement, it is more convenient to place the qubits at distances where the dynamics of the system is purely dissipative.

5.3.3 Different dissipative evolutions. Sudden birth, death and revival of entanglement

So far we have considered the evolution from the single qubit excitation $|1\rangle = |e_1 g_2\rangle$ and it is interesting to consider different initial states which can give other possible dynamical evolutions. We are going to restrict to initial states that correspond to density matrixes having a crossed X-shape. Therefore the master equation (5.5) and the analytical concurrence equation (5.11) can be used to help analyzing the system dynamics. In any case, such restriction still will permits us to study interesting cases such as the double excited state $|3\rangle$ and the maximally-entangled Bell state $\frac{1}{\sqrt{2}}(|0\rangle + |3\rangle)$. In both initial cases, we consider qubits at a separation distance in the dissipative set ($d = \lambda_{\mathrm{pl}}$), with their dipole moments aligned, and placed to have a high plasmon-coupling efficiency in a channel, *e.g.* $Z = 150\,\mathrm{nm}$ at $\lambda = 600\,\mathrm{nm}$. The coupling parameters are deduced from Figure 4.7 in chapter 4.

Firstly, we consider the evolution from the double excited state which can be initialized by sending two π-pulses, each one exciting a single qubit respectively. In this case the
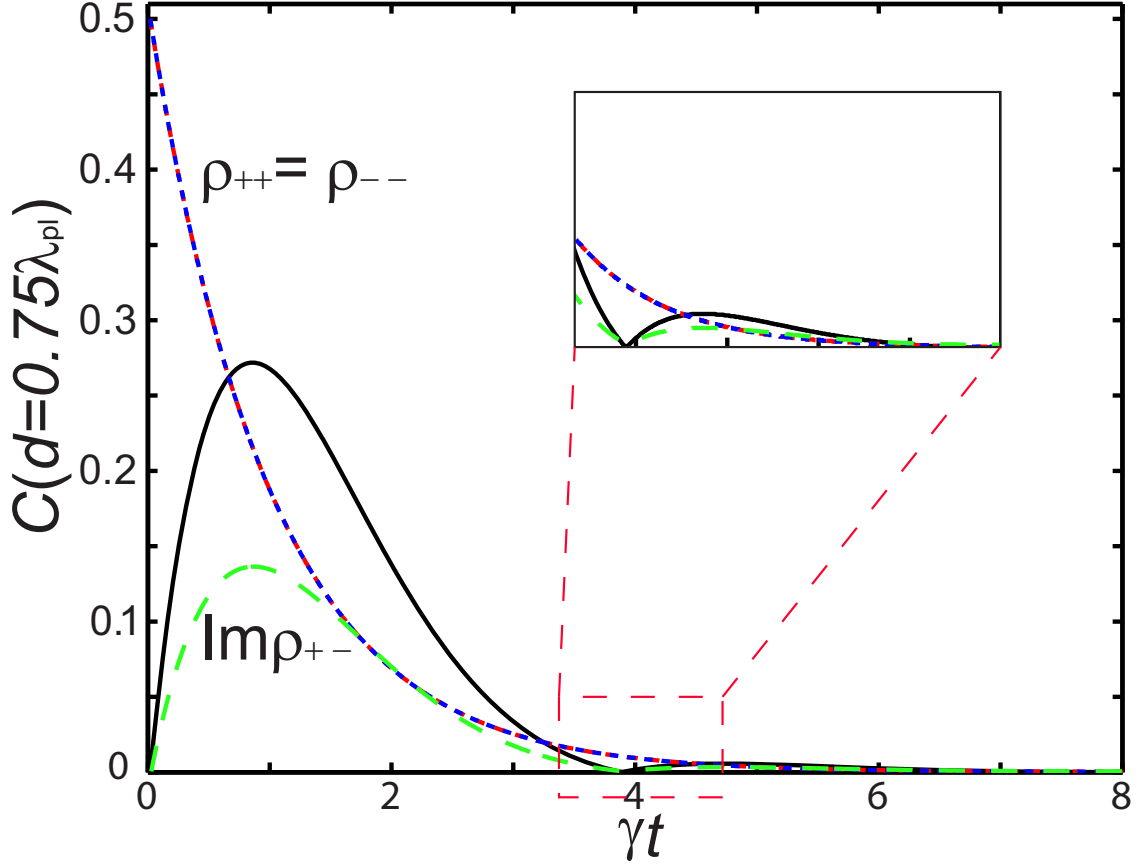
Figure 5.8: Concurrence C (black thick line), populations ρ_{++} (red dashed line), ρ_{--} (blue dotted line), and ρ_{33} (green line) versus time. The time is scaled with the emitter lifetime ($1/\gamma$). The coupling parameters are extracted from the calculations shown in Figure 4.11, chapter 4) which are ($\gamma = 10.4\gamma_0$, $\gamma_{12} = 0.78\gamma$ and $g_{12} = 0.00\gamma_0$) for the channel.

relevant dynamics is given by the equations

$$
\begin{aligned}
\dot{\rho}_{33}(t) &= -2\gamma\rho_{33}(t), \\
\dot{\rho}_{++}(t) &= (\gamma + \gamma_{12})\rho_{33}(t) - (\gamma + \gamma_{12})\rho_{++}(t), \\
\dot{\rho}_{--}(t) &= (\gamma - \gamma_{12})\rho_{33}(t) - (\gamma - \gamma_{12})\rho_{--}(t), \\
\dot{\rho}_{00}(t) &= (\gamma + \gamma_{12})\rho_{++}(t) + (\gamma - \gamma_{12})\rho_{--}(t),
\end{aligned}
\tag{5.28}
$$

due to the fact that the coherences start and remain zero at all times. Therefore it can be easily deduced from equations (5.12) and (5.13) that the concurrence is given by

$$
C(t) = max\{0, |\rho_{++}(t) - \rho_{--}(t)| - 2\sqrt{\rho_{00}(t)\rho_{33}(t)}\}.
\tag{5.29}
$$

Figure 5.8 represents the time evolution of the concurrence for the initial density matrix with $\rho_{33} = 1$ and the remaining terms zero, *i.e.*, both emitters excited. As in the case of a single excitation, the system begins from an initial unentangled state and consequently the concurrence is zero. However instead of raising fast to non-zero values, the concurrence remain zero until $\gamma t = 3.7$ where it starts raising. Such entanglement sudden birth can be understood from equation (5.29) due to the fact that $|\rho_{++}(t) - \rho_{--}(t)| < |2\sqrt{\rho_{00}(t)\rho_{33}(t)}|$, making the second term negative and therefore the concurrence takes the zero value. Consequently we can see in Figure 5.8 that the formation of entanglement starts when the double excited (unentangled state) is drastically depleted. Then, the concurrence grows until it achieves a maximum and it asymptotically approaches the antisymmetric state which, for the considered distance, is the slow decaying subradiant state. Therefore, it is the dissipative dynamics induced by the plasmon the responsible for the formation of entanglement. Accordingly, the entanglement is formed for all distances d, except for odd-integer numbers of $\lambda_{\mathrm{pl}}/4$, *i.e.*, when $\gamma_{12} = 0$. For such distances, we can notice from the above analysis of the coherent set, in subsection 5.3.2, the coherences have zero values and the decay rate of the populations ρ_{++} and ρ_{--} are equal. Consequently that implies that no entanglement can be generated since $|\rho_{++}(t) - \rho_{--}(t)| = 0$.

Next, we analyze the evolution from the Bell state ($|\Phi^+\rangle = \frac{1}{\sqrt{2}}(|0\rangle + |3\rangle)$) which, unlike the previous cases, is a maximally entangled state. In this case the relevant equations governing the dynamics of the system, are

$$\dot{\rho}_{33}(t) = -2\gamma\rho_{33}(t), \tag{5.30}$$

$$\dot{\rho}_{++}(t) = (\gamma + \gamma_{12})\rho_{33}(t) - (\gamma + \gamma_{12})\rho_{++}(t), \tag{5.31}$$

$$\dot{\rho}_{--}(t) = (\gamma - \gamma_{12})\rho_{33}(t) - (\gamma - \gamma_{12})\rho_{--}(t), \tag{5.32}$$

$$\dot{\rho}_{00}(t) = (\gamma + \gamma_{12})\rho_{++}(t) + (\gamma - \gamma_{12})\rho_{--}(t), \tag{5.33}$$

$$\dot{\rho}_{30}(t) = -(\gamma + 2i\omega_0)\rho_{30}(t), \tag{5.34}$$

$$\tag{5.35}$$

and therefore the concurrence analytical formula reduces to

$$C = max\{0, C_1, C_2\}, \tag{5.36}$$

where

$$C_1(t) = 2\sqrt{(\mathrm{Re}[\rho_{03}(t)])^2 + (\mathrm{Im}[\rho_{03}(t)])^2} - |\rho_{++}(t) + \rho_{--}(t)|, \tag{5.37}$$

and

$$C_2(t) = |\rho_{++}(t) - \rho_{--}(t)| - 2\sqrt{\rho_{00}(t)\rho_{33}(t)}. \tag{5.38}$$

It can be seen in Figure 5.9 the time dependence of the concurrence, the populations $\rho_{++}(t)$, $\rho_{--}(t)$ and $\rho_{33}(t)$, and twice the coherence modulus $2|\rho_{03}|$. We can clearly see
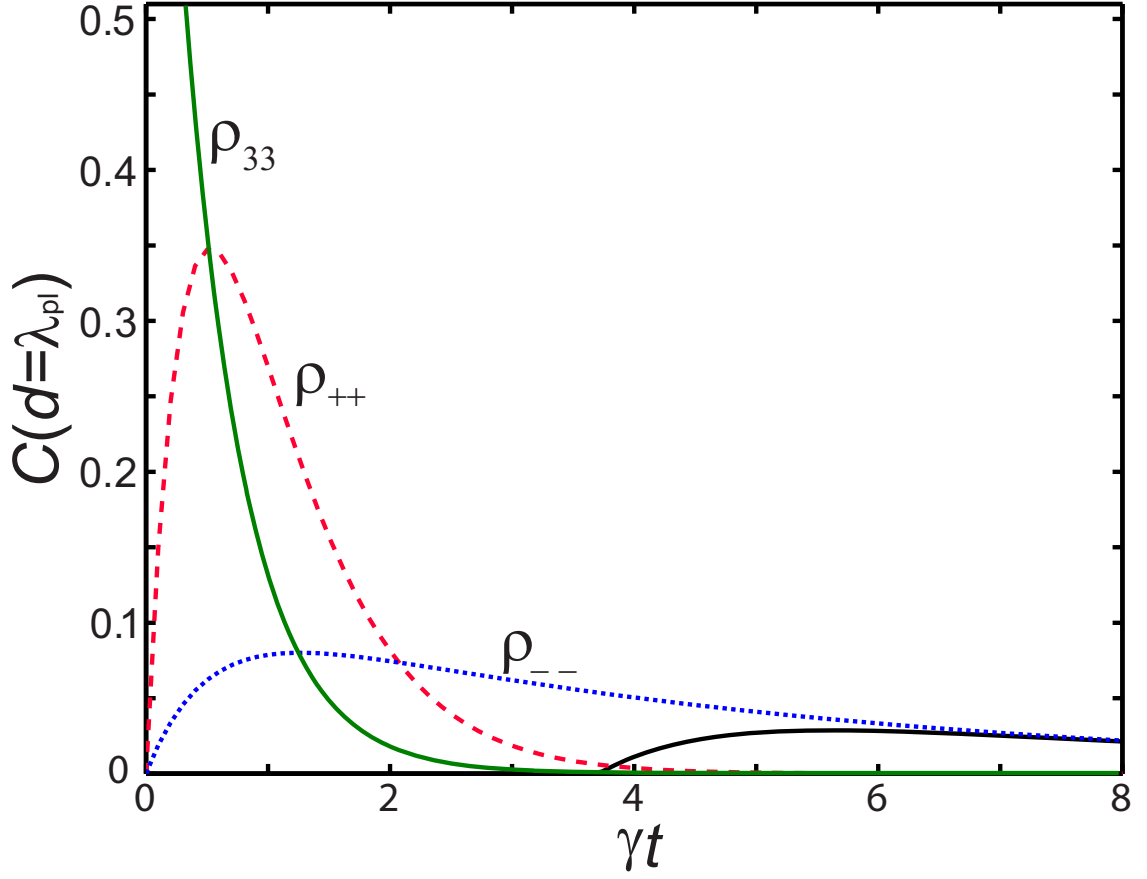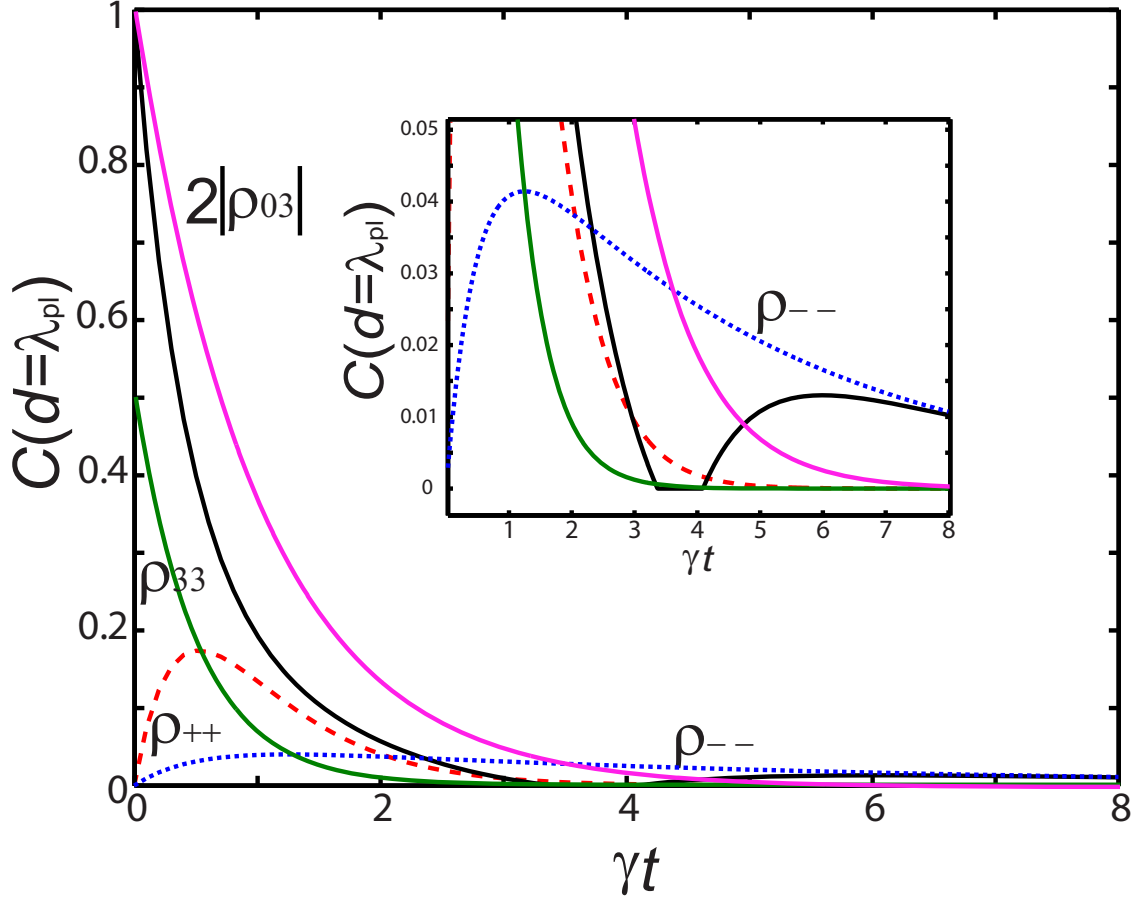
Figure 5.9: Concurrence C (black thick line), populations ρ_{++} (red dashed line), ρ_{--} (blue dotted line), ρ_{33} (green line), and $2|\rho_{03}|$ (magenta line) versus time. The time is scaled with the emitter lifetime $(1/\gamma)$. The coupling parameters are extracted from the calculations shown in Figure 4.11, chapter 4, which are $(\gamma = 10.4\gamma_0, \gamma_{12} = 0.78\gamma_0$ and $g_{12} = 0.00\gamma_0)$ for the channel. Inset: zoom of the main panel showing the abrupt concurrence change.

how the concurrence starts from one due to the maximum degree of entanglement of the initial Bell state. Due to the dissipative dynamics, the concurrence diminishes in time until $\gamma t = 3.4$ where the system becomes completely disentangled, an interesting behaviour known as sudden death in the literature [203]. Then, it remains zero until the normalized time $\gamma t = 4$, where the entanglement rebirth again. Finally, the concurrence increases achieving a maximum and then it decays exponentially at long times. Such complicated behaviour of the concurrence arises from the interplay between the three terms appearing in equation (5.36). The different regions can be easily explained. The first decreasing region of the entanglement comes from formula (5.37) because the second formula (5.38) is negative

due to small value of $|\rho_{++}(t) - \rho_{--}(t)|$ compared to $2\sqrt{\rho_{00}(t)\rho_{33}(t)}$. From the density matrix terms represented in Figure 5.9, we can observe that the term $2|\rho_{03}|$ is the main contribution in (5.37), though it is the $|\rho_{++}(t) + \rho_{--}(t)|$ term which makes the concurrence drop to zero. In the second region both equations (5.37) and (5.38) remain negative until the term (5.38) becomes positive, similar to the sudden birth previously analyzed for the double excited state (Figure 5.8). Consistently with such view, we can observe that the main contribution at longer times in equation (5.38) is the slowly decaying population of the subradiant state which, together with the depletion of $\rho_{33}(t)$, is mainly responsible for the rebirth of the entanglement. It can be easily inferred that for qubit-qubit distances different from integer numbers of $\lambda_{\mathrm{pl}}/2$, the third region is reduced or even completely suppressed. At separations odd-integer numbers of $\lambda_{\mathrm{pl}}/4$, the term $|\rho_{++}(t) - \rho_{--}(t)| =$ remain zero due to the fact that $\gamma_{12} = 0$ and equation (5.38) remains negative at all times. From all the variety of initial cases so far considered, we can mainly conclude that the most interesting evolution of entanglement is generated at integer numbers of $\lambda_{\mathrm{pl}}/2$ where the dissipative dynamics dominates.

5.3.4 Unfavorable emitters orientations

In the previous subsections, we have been considering the generation of two-qubit entanglement mediated by plasmons in highly favorable scenarios, where the emitters dipole moments are mutually-parallel and oriented to have optimum plasmonic coupling. In this subsection we consider the effect of different dipole moments orientations to check the robustness of the entanglement formation against possible alignment imperfections. In Figure 5.10 we represent the concurrence evolution for two qubits placed at $Z = 150\,\mathrm{nm}$ from the bottom of a channel waveguide, with mutual separation of $d = \lambda_{\mathrm{pl}}$ and the system is initialized in the state $|1\rangle = |e_1 g_2\rangle = \frac{1}{\sqrt{2}}(|+\rangle + |-\rangle)$. We represent three sets of different dipole orientations: $(\theta_1 = 0°, \theta_2 = 0°)$, $(\theta_1 = 0°, \theta_2 = 60°)$ and $(\theta_1 = 60°, \theta_2 = 60°)$, represented with blue, green and magenta colors respectively, where the angle θ_i of the i-qubit is defined respect to the maximum horizontal-polarization of the channel plasmon (see the inset for an illustration). It can be observed how the maxima of $(\theta_1 = 0°, \theta_2 = 60°)$ and $(\theta_1 = 60°, \theta_2 = 60°)$ are smaller than for the optimum orientation $(\theta_1 = 0°, \theta_2 = 0°)$ due to the reduction of the coupling coefficients (see their values in the caption). In particular, we can see that the asymmetric case shows a slightly smaller maximum. Although, the faster decrease occurs for the symmetrical case $(\theta_1 = 60°, \theta_2 = 60°)$, which has the lowest effective β_i values, and therefore the larger $\gamma_{ii} - \gamma_{12}$ values. In spite of the degradation of the maximum generated concurrence and its faster temporal decrease, we can see that for such quite large variations of angles, the entanglement formation is not largely affected.
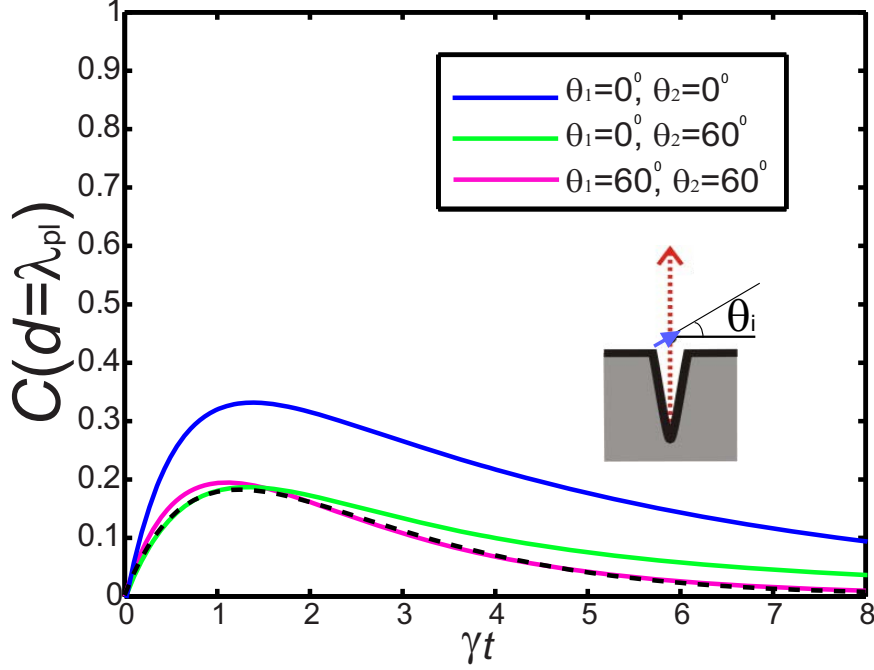
Figure 5.10: Concurrence C (black thick line) versus time for three different sets of dipole orienta-
tions: ($\theta_1 = 0°, \theta_2 = 0°$) blue line, ($\theta_1 = 0°, \theta_2 = 60°$) green line and ($\theta_1 = 60°, \theta_2 = 60°$) magenta line. The time is scaled with the maximum emitter lifetime ($1/\gamma$). The coupling parameters are extracted from the calculations shown in Figure 4.12, chapter 4 which are for the three previous sets: ($\gamma_{11} = 10.4\gamma_0$, $\gamma_{22} = 10.4\gamma_0$, $\gamma_{12} = 0.78\gamma_0$), ($\gamma_{11} = 10.4\gamma_0$, $\gamma_{22} = 4.3\gamma_0$, $\gamma_{12} = 4.54\gamma_0$) and ($\gamma_{11} = 4.3\gamma_0$, $\gamma_{22} = 4.3\gamma_0$, $\gamma_{12} = 2.3\gamma_0$) respectively. For all the sets, $g_{12} = 0.00\gamma_0$ due to the qubit-qubit separation $d = \lambda_{pl}$. Additionally, it is represented the ($\theta_1 = 0°, \theta_2 = 60°$) case for two different emitters differing in frequency by $\delta\omega_2 = 0.58\gamma_{11}$ (dashed black line). Inset: illustration of the definition of the i-qubit angle θ_i.

In the previous results we have approximated that the frequency shifts of the emitters are equal, which is exact for the symmetrical cases, but it differs for the case of mutually-different dipole orientations. In principle, even small Lamb shifts induced by the plasmonic waveguide can play a role in the dynamics because they induce different emitting frequencies in each emitter. However, for the typical considered PWs, the optimal distance from the emitter to the metal surface is larger than ($\approx 25\,\text{nm}$), which is quite large and there-fore the shift difference is expected to be small. An upper rough estimation can be done approximating the metal to that of a metallic plane. For a distance of $25\,\text{nm}$, the difference in the frequency shift between an horizontally and a vertically oriented dipole moment is estimated [201] to be $\delta\omega_2 \approx 6\gamma_0 < 10.4\gamma_0 = \gamma_{11}$. We have included such small difference shift in the concurrence evolution represented in Figure 5.10 with the black dashed line

for the channel PW. Apart from a small reduction of the maxima and a slightly increase of the decay, we can see that such small frequency shifts do not affect importantly the concurrence evolution. Therefore we can conclude from the considered cases that the generated entanglement is robust for quite large emitter misalignments and also for resonably different emitters frequencies.

5.4 Stationary entanglement mediated by plasmonic waveguides

5.4.1 System characterization: Time evolution and distance-pumping probe
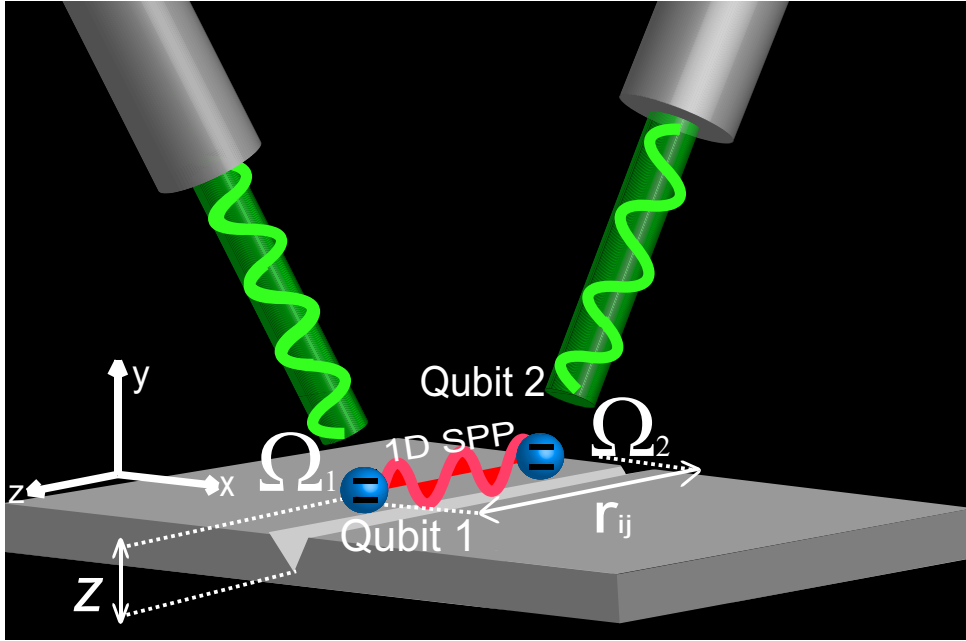
Figure 5.11: (a) Two qubits interacting with a channel plasmonic waveguide and impinging resonant lasers with Rabi frequencies Ω_1 and Ω_2.

In the previous section we have seen the spontaneous generation of entanglement but, as explained above, the process is a transient phenomenon. To compensate the depopulation of the upper levels, the system could be externally pumped by means of a laser in resonance with the frequency of the qubits [57, 56] as sketched in Figure 5.11. Similar treatments have been considered in the study of the resonance fluorescence by the light scattered by a single atom [90] and also for resonant interaction between two emitters in vacuum [91].

In those studies, the laser light is treated to be in a coherent photonic state with a sharp spectrum and it contributes to the coherent hamiltonian (5.2) with an additional term (see the derivation in chapter 2):

$$\hat{H}_\mathrm{L} = -\sum_i [\hbar\Omega_i\,\hat{\sigma}_i^\dagger e^{i\omega_\mathrm{L} t} + \mathrm{h.c.}]. \tag{5.39}$$

Here, the strength and phase of the laser are characterized by the Rabi frequencies $\Omega_i = \mathbf{d}_i\mathbf{E}_\mathrm{L}\,e^{i\mathbf{k}_\mathrm{L}\mathbf{r}_i}/\hbar$, where $\mathbf{E}_\mathrm{L}$ and $\mathbf{k}_\mathrm{L}$ are the amplitude and wave vector of the driving laser field, respectively. We will particularly exploit the cases where the Rabi frequencies are much smaller than the emitters decay rates γ, which permits to probe the system without significantly altering its main properties [88]. First, let us show the temporal characteristics
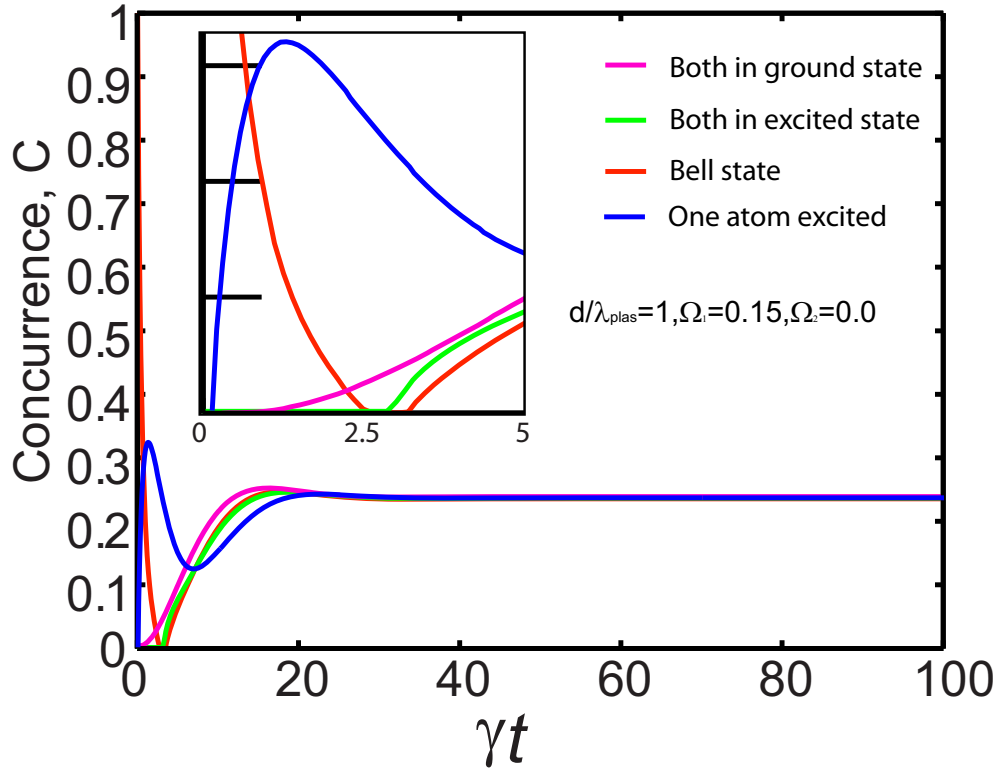
Figure 5.12: Time evolution for the concurrence C in the following initial states: single excited atom (blue line), double unexcited state (magenta line), double excited state (green line) and maximally entangled Bell state ($|\Phi^+\rangle = \frac{1}{\sqrt{2}}(|0\rangle + |3\rangle)$)(red line). The time is scaled with the emitter lifetime ($1/\gamma$). The mutual separation of the qubits is $d = \lambda_{pl}$ and the separation from the bottom of the channel is $Z = 150\,\mathrm{nm}$. The coupling parameters are extracted from the calculations shown in Figure 4.11, chapter 4 for the channel ($\gamma = 10.4\gamma_0$, $\gamma_{12} = 0.78\gamma$ and $g_{12} = 0.00\gamma$). Inset: zoom of the main panel showing the transient concurrence behaviour.

of the concurrence for different initial states in the system displayed in Figure 5.11. In the following we will mainly focus on the use of a channel PW motivated by its good entangling characteristics as shown in the previous subsection (see the system parameters in the caption). Firstly, we consider the illumination of the first emitter resulting in a Rabi frequency of $\Omega_1 = 0.15\gamma$ which value will be justified in the next subsection with the variation of the laser intensity. Additionally, we delay the study of other different laser configurations and qubit-qubit distances below in this subsection. In particular, we consider the evolution from the double unexcited state ($|0\rangle$), which is the typical experimental case. Also for comparison purposes, we consider the same initial states considered previously for the spontaneous formation of entanglement, *i.e.*, the single atom excited state ($|e_1 g_2\rangle = \frac{1}{2}(|+\rangle - |-\rangle)$), the double excited state ($|3\rangle$) and the maximum entangled Bell state ($|\Phi^+\rangle = \frac{1}{\sqrt{2}}(|0\rangle + |3\rangle)$). For those general cases, the determination of the density matrix $\hat{\rho}(t)$ requires the numerical integration of equation (5.1) with the appropriate initial conditions [204, 92]. From the numerical solutions for the above initial states, we show in Figure 5.12 the time evolution of the numerically calculated concurrence, which has the definition considered in the previous section [196]. After a transient behaviour, we can see in Figure 5.12 how the degree of entanglement grows until all the concurrences, independently of the initial state, acquire the same value. Such is a logical consequence of the steady state solution that results from the system of linear equations $\dot{\hat{\rho}} = 0$, which of course does not depend on the initial state. The only differences arises from the transient times ($\gamma t < 20$). The concurrence behaviour is quite complicated because the laser involves in general all the populations and coherences. Therefore, it is more difficult to get an analytical formula for the concurrence like in the previous section. Nevertheless we can notice that at times $0 < \gamma t < 5$, the concurrence evolution is quite similar to the initial states analyzed in section 5.3. Therefore, we can see that for the Bell state, it decreases from one to zero and then rebirths, for the double excited state it remains zero and then suddenly births at longer times and for the single excited state it achieves a maximum which then decays on time. Such similar behaviour is attributed to the small Rabi frequency ($\Omega_1 << \gamma$), which does not significantly alter the evolution of the density matrix elements at short times because the coefficients associated with the laser are small perturbations. Only in the evolution of the double unexcited state, the perturbation is initially important because the density matrix elements other than ρ_{00} are initially zero and the pump only increases them. Within these view we can also observe that the curves at times $\gamma t \gtrsim 5$ display a similar tendency because it corresponds to times slightly longer than $1/(\gamma - \gamma_{12})$, when the transient part of the longest living population $\rho_{--}(t)$ is expected to be negligible compared to the terms induced by the laser. Accordingly, all the curves display a similar increasing tendency which reaches a small bump nearby $\gamma t = 17$. Due to the small transient perturbation at those

times, we can observe that the bump slightly shifts to longer times, depending on the values of the subradiant population ρ_{--} at early times. In particular, for a time $\gamma t = 1$, the ρ_{--} values and therefore the bump is increasingly shifted for the initial states $|0\rangle$, $|\Phi^+\rangle$, $|3\rangle$ and $|e_1 g_2\rangle$, respectively. Additionally, such ordering of the subradiant state at $\gamma t = 1$ is preserved in the absence of a laser, as it is extracted from figures 5.6, 5.8 and 5.9 of section 5.3. That fact is consistent with the view that the laser represents a small perturbation to the system at early times.
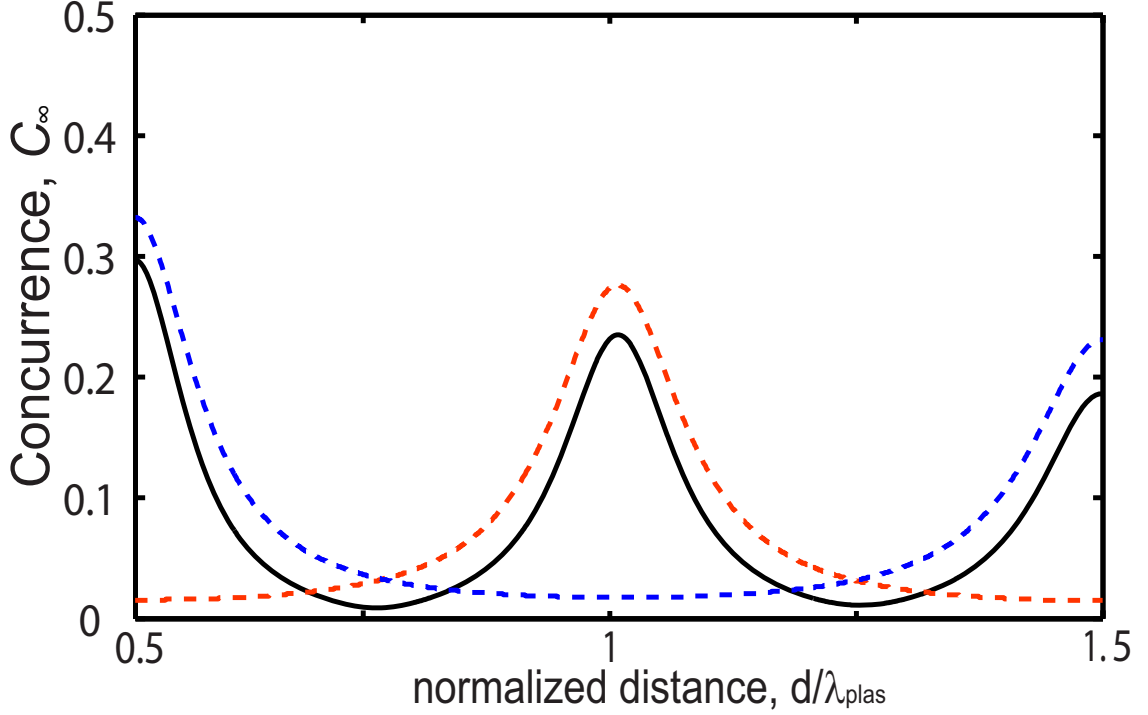
Figure 5.13: Steady state concurrence as a function of the normalized separation d/λ_{pl} for different pumping schemes: Symmetric pumping ($\Omega_1 = \Omega_2 = 0.1\gamma$, dashed blue line) , antisymmetric pumping ($\Omega_1 = -\Omega_2 = 0.1\gamma$, dashed red line), and asymmetric pumping ($\Omega_1 = 0.15\gamma, \Omega_2 = 0$, black line). The qubits are placed in front of a channel PW at $Z = 150\,\text{nm}$ for an emission wavelength of $\lambda = 600\,\text{nm}$ and mutually-horizontal oriented dipoles.

We can get more physical insight about the relevance of the subradiant state in the generation of stationary entanglement, studying its dependence with the qubit-qubit separation and the pumping scheme. The concurrence reached in the corresponding steady state, C_∞, is plotted in Figure 5.13 as a function of the qubits separation normalized to the modal wavelength, d/λ_{pl}, and using the previous considered waveguide configuration (see the relevant system parameters in the caption). Three kinds of coherent driving schemes have

been considered, differing in the relative Rabi values of the laser fields acting on qubit 1 and 2: symmetric pumping means identical Rabi frequencies, $\Omega_1 = \Omega_2$ (dashed blue line), antisymmetric pumping means $\Omega_1 = -\Omega_2$ (dashed red line), and asymmetric pumping corresponds to $\Omega_1 \neq 0$, $\Omega_2 = 0$ (black line). The absolute value of the non-zero Rabi frequencies is 0.15γ for the asymmetric pumping and 0.1γ for the other two situations, *i.e.*, relatively weak. It is very important to realize that we consider now arbitrary separations between the qubits and this implies that both plasmon-mediated coherent and dissipative dynamics are active, its relative weight depending on d/λ_{pl} (see Figure 4.11 in chapter 4). With independence of the pumping scheme, the concurrences C_∞ in Figure 5.13 present an oscillating behavior with the qubits separation, and damped due to the plasmon absorption. Importantly, the concurrence maxima occur for those d/λ_{pl} where the absolute value of γ_{ij} is maximum (see Figure 4.11). This suggests a relationship between the entanglement generation and the dissipative set of separations for the two-qubit dynamics. Let us justify the position of the maxima of C_∞ applying the ideas developed for the undriven case. When the pumping is symmetric (dashed blue line), the laser populates the symmetric state $|+\rangle$. This state is subradiant for $d = \frac{1}{2}\lambda_{\mathrm{pl}}, \frac{3}{2}\lambda_{\mathrm{pl}}, \ldots$ leading to a population imbalance and the corresponding concurrence. For $d = \lambda_{\mathrm{pl}}, 2\lambda_{\mathrm{pl}}, \ldots$, $|+\rangle$ is superradiant and the weak pumping is not able to induce a significant ρ_{++} population. For antisymmetric pumping (dashed red line), it is the state $|-\rangle$ the one that is pumped by the laser. This state is subradiant for $d = \lambda_{\mathrm{pl}}, 2\lambda_{\mathrm{pl}}, \ldots$, again leading to a population imbalance and entanglement. For $d = \frac{1}{2}\lambda_{\mathrm{pl}}, \frac{3}{2}\lambda_{\mathrm{pl}}, \ldots$, the situation is reversed. Finally, for asymmetric pumping (black line) both $|+\rangle$ and $|-\rangle$ are populated and the situation is a mixture of the previous two, showing maxima for $d = \frac{1}{2}\lambda_{\mathrm{pl}}, \lambda_{\mathrm{pl}}, \frac{3}{2}\lambda_{\mathrm{pl}}, \ldots$.

To verify that the previous interpretation is correct, we plot the tomography of the steady state density matrix in Figure 5.14, leading to the concurrence displayed in Figure 5.13. We choose two of the previous considered pumping cases and the most relevant three different qubit separations. Let us start describing the asymmetric pumping. Panel (a) shows the stationary tomography at $d = \lambda_{\mathrm{pl}}/2$. Besides the population of the ground state, we recognize the large ρ_{++} population of the subradiant state $|+\rangle$ driven by the pumping, and the negligible ρ_{--} population of the superradiant state $|-\rangle$. Additionally, we can see reflected as a consequence of the $|+\rangle$ pumping, the relative high values of the coherence $|\rho_{0+}|$. For $d = \lambda_{\mathrm{pl}}$ [panel (b)], we now observe a large ρ_{--} population of the subradiant state $|-\rangle$ driven by the pumping, as it can be seen from the significant value of $|\rho_{0-}|$, and the negligible ρ_{++} population of the superradiant state $|+\rangle$. Let us remark that, strictly speaking, equation (5.21) is not correct when pumping is included, because now further elements of $\hat{\rho}$ are non zero. However, the tomography shows that, beside the $|\rho_{0-}|$ and $|\rho_{0+}|$ coherences, these additional elements are quite small and equation (5.21)
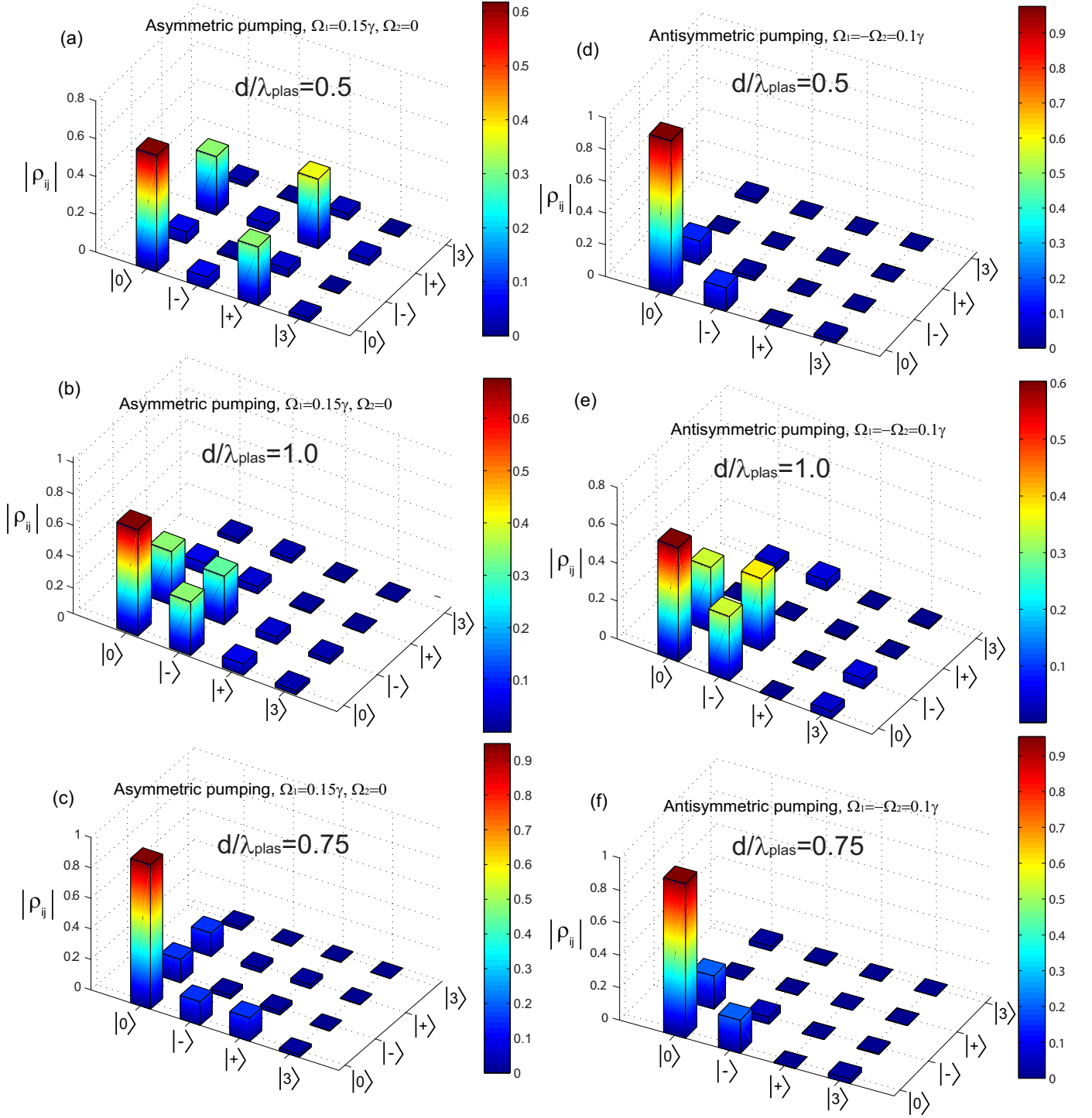
Figure 5.14: 3D bar plot of the absolute value of the elements of the steady state density matrix for asymmetric pumping ($\Omega_1 = 0.15\gamma$, $\Omega_2 = 0$). (a) $d = \lambda_{\text{pl}}/2$, (b) $d = 1.0\lambda_{\text{pl}}$ and (c) $d = 0.75\lambda_{\text{pl}}$, for the most relevant distances shown in Figure 5.13. Analogue 3D bar plot for antisymmetric pumping ($\Omega_1 = 0.1\gamma$, $\Omega_2 = -\Omega_1$) and different distances: (d) $d = \lambda_{\text{pl}}/2$, (e) $d = 1.0\lambda_{\text{pl}}$ and (f) $d = 0.75\lambda_{\text{pl}}$.

should be approximately valid, supporting the argument that population imbalance leads to concurrence. For complementing such argument we also show in [panel (c)] the tomography for $d = 0.75\lambda_{\mathrm{pl}}$ for which the concurrence has very low values ($C_\infty = 6 \times 10^{-3}$, see Figure 5.13). In this case we can observe that both coherences $|\rho_{-0}|$ and $|\rho_{+0}|$ are significant but none of the populations ρ_{--} or ρ_{++} considerably excited. This fact reenforces the previous argument that the entanglement is mainly generated due to the population imbalance mediated by dissipation because in this case both ρ_{++} and ρ_{--} have the same decay rates ($\gamma_{12} = 0$).

In order to see the consistency of such interpretation, we comment the tomography in the antisymmetric pumping case. In panel (d) for $d = \lambda_{\mathrm{pl}}/2$ we can observe, in contrast to panel (a), how the ρ_{+0} coherence is zero due to the opposite phases of both Rabi frequencies ($\Omega_1 = -\Omega_2$). As a consequence, the subradiant state $|+\rangle$ is not populated and the superradiant state $|-\rangle$, in spite of being pumped $\rho_{-0} \neq 0$, is not significantly excited. Such situation is similar to that for the distance $d = 0.75\lambda_{\mathrm{pl}}$ (see panel (f)), for which the decay of ρ_{--} is fast. Therefore in both cases the population imbalance is small and the concurrence is close to zero (see the concurrence values at $d/\lambda_{\mathrm{pl}} = 0.5$ and $d/\lambda_{\mathrm{pl}} = 0.75$ in Figure 5.13, dashed red line). On the contrary, the described situation is completely reversed at a distance $d = \lambda_{\mathrm{pl}}$ as displayed in panel (e), where now the state $|-\rangle$ is subradiant and ρ_{--} is greatly populated, opposite to the superradiant population ρ_{++} which is nearly zero. Accordingly the population imbalance is significant and the concurrence differs importantly from zero (as displayed in Figure 5.13), consistently with the previous argument given in panels [a-c]. Therefore, since this population imbalance is due to the different decay rates of the super- and subradiant states, both of which are produced by dissipation, we want to emphasize that the entanglement generation is driven by the two-qubit dissipative dynamics mediated by the plasmons.

5.4.2 Experimental issues: pumping intensity, pure dephasing, and plasmon mediated correlations

In the previous subsection we have given a comprehensive study of the generation of stationary entanglement and the importance of the dissipation mediated by the guided plasmons. Nevertheless, there are important experimental issues for the generation of stationary entanglement which have not been considered. Up to now we have focused on few weak pumping rate, and on channel plasmonic waveguides. Additionally, we have not considered other decoherent noise sources different from spontaneous emission which can spoil further the generated entanglement, for example due to laser-induced heating in the emitters. Finally it would be interesting to look for possible measurable magnitudes which can reflect signa-
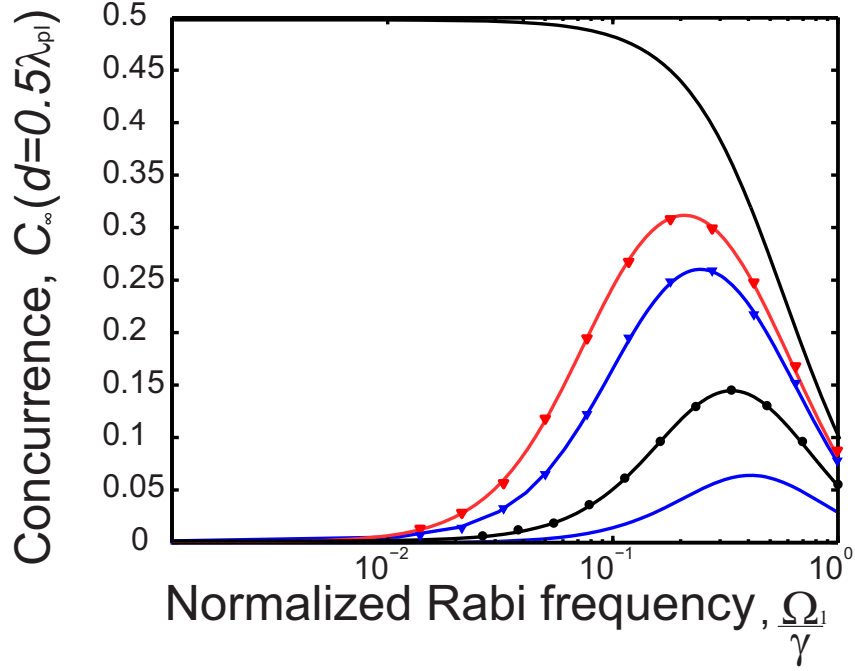
Figure 5.15: Steady state concurrence as a function of the normalized driving laser power for asymmetric pumping ($\Omega_1 \neq 0$, $\Omega_2 = 0$) and qubits separation $d = \lambda_{\mathrm{pl}}/2$ for the PWs. The coupling parameters are extracted from the calculations shown in Figure 4.11, chapter 4). Ideal case $\gamma_{12} = 1.0\gamma$, $g_{12} = 0\gamma$ (black line), for a cylinder $\gamma_{12} = -0.58\gamma$, $g_{12} = 0.00\gamma$ (black circles), wedge $\gamma_{12} = -0.77\gamma$, $g_{12} = 0.00\gamma$ (blue circles), and channel $\gamma_{12} = -0.84\gamma$, $g_{12} = 0.00\gamma$ (red triangles). Also for comparison purposes we display the results for vacuum (blue line) at $d = \lambda/3 \sim \lambda_{\mathrm{pl}}/2$ with coupling parameters $\gamma_{12} = -0.30\gamma$, $g_{12} = -0.29\gamma_0$ calculated with formulas (5.3) and (5.4).

tures of entanglement in external photo-detectors. In this subsection we deal with some of those issues which can be important for an experimental implementation of the stationary generation of entanglement mediated by plasmons.

As illustrated in subsections 5.3.1 and 5.3.4, the coupling efficiency is important to increase the maximum transitory generation of entanglement mediated by plasmons. In the stationary entanglement problem, it is interesting to explore the possible influence of both, the waveguide election and the pumping rate. It is also desirable to find the range for which the described phenomena may happen. Such influence of the pumping intensity and the waveguide choice is analyzed in Figure 5.15, which renders the stationary concurrence, C_∞, versus the normalized Rabi frequency, Ω_1/γ. Here, asymmetric pumping is considered and a qubit separation $d = \lambda_{\mathrm{pl}}/2$. The results are computed for four PWs with different coupling

efficiencies for mutually-parallel dipole orientations: a cylinder ($\beta = 0.6$, black circles), a wedge ($\beta = 0.83$, blue triangles), a channel ($\beta = 0.9$, red triangles), and an ideal waveguide ($\beta = 1$ and no absorption, black line). In addition, for comparison purposes they are also displayed the results for vacuum mediated entanglement at a distance $d = \lambda/3$, *i.e.*, a value close to the qubits separations for the above PWs. Each considered scenario, except the ideal waveguide, presents an optimum pumping power to achieve maximum concurrence. This behaviour can be explained due to the following reasoning. In order to obtain a non-negligible concurrence, the subradiant state has to be populated at a rate faster than its lifetime, which explains why the concurrence is small at low pumping rates for realistic waveguides. For stronger pumping the emitters polarizability start to be saturated [47], suppressing the spontaneous emission and this explains why all the curves diminish for higher Ω_1/γ. Consequently, it can be observed how the structures with lower β require a higher normalized pumping to reach their optimum entanglement. Additionally, we can see that the maximum attainable stationary concurrence improves for higher β factor. Therefore, we can again justify the use of high efficient plasmonic waveguides like channels or wedges for generation of stationary entanglement, instead of low efficient ones, like cylindrical PWs or simply vacuum. Additionally, we can conclude that the tuning of the laser intensity is important to generate significant stationary entanglement, specially for systems with low emitter-to-plasmon couplings.

The intensity of the laser impinging on the emitters can heat them and pump phonon excitations, which would further decrease the emitters lifetimes and coherences due to the additional noise-fluctuations [205]. Such decoherent process is known in the literature as pure dephasing. In particular, it results from the randomization of the emitter-wavefunction phases due to phonon interactions, causing the overlap between the wavefunction of the upper and lower level to decay in time [206, 205]. Such effect has to be added to the spontaneous emission, so far the only considered dephasing process caused by the electromagnetic fluctuations. The increase of the total dephasing due to laser-induced pure dephasing has been experimentally measured for resonantly laser-driven NV-centers [207]. For this reason, we have recomputed the dynamics of the system including now in the master equation (5.1) a phenomenological term representing pure dephasing. That term is given by [206]

$$\mathcal{L}_{\text{deph}}[\hat{\rho}] = \frac{\gamma^\phi}{2} \sum_i \left[[\hat{\sigma}_i^\dagger \hat{\sigma}_i, \hat{\rho}], \hat{\sigma}_i^\dagger \hat{\sigma}_i \right]. \tag{5.40}$$

In general, it is difficult to estimate the value of the dephasing rate γ^ϕ because it is very dependent on the particular realization of the qubit and it can be strongly influenced by the presence of the metallic part of the system. For nitrogen-vacancy centers in vacuum under weak resonant pumping, pure dephasing times up to $100\,\text{ns}$ have been measured [208, 207],
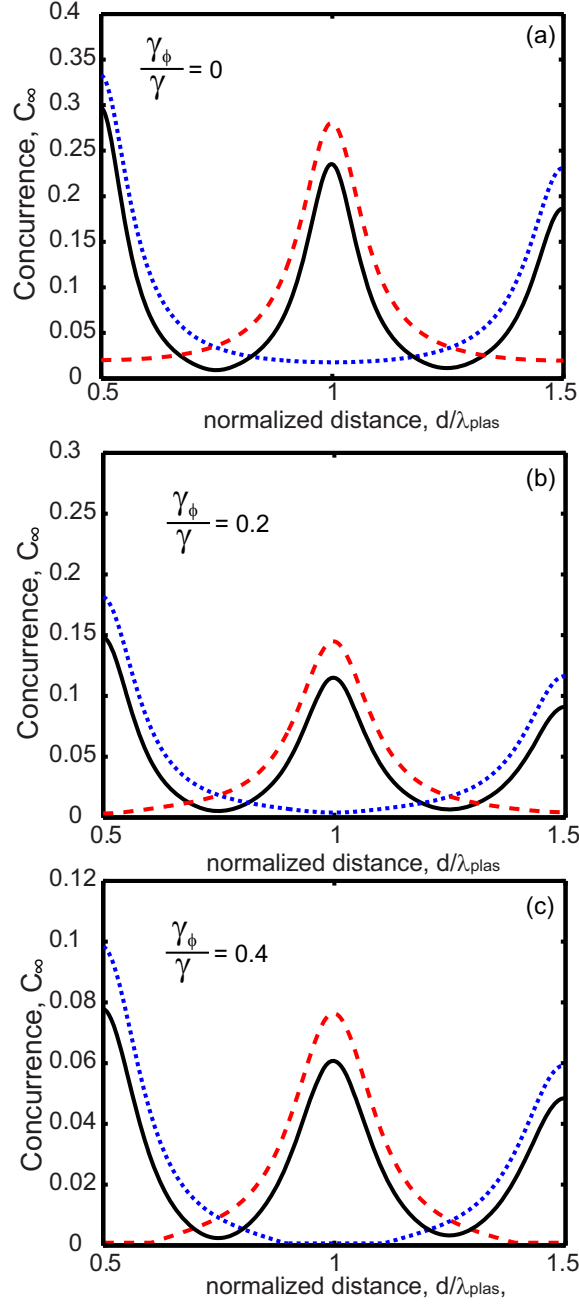
Figure 5.16: Steady state concurrence as a function of the normalized separation d/λ_{pl} for different pumping conditions and pure dephasing rates. (a) $\gamma^\phi/\gamma = 0.0$, (b) $\gamma^\phi/\gamma = 0.2$, and (c) $\gamma^\phi/\gamma = 0.4$. In all panels the blue dotted lines correspond to symmetric pumping ($\Omega_1 = \Omega_2 = 0.1\gamma$), the red dashed lines correspond to antisymmetric pumping ($\Omega_1 = -\Omega_2 = 0.1\gamma$), and the black continuous lines correspond to asymmetric pumping ($\Omega_1 = 0.15\gamma$, $\Omega_2 = 0$). Notice that the vertical scale is not the same in the three panels. The qubits are placed in front of a channel PW at $Z = 150$ nm for an emission wavelength of $\lambda = 600$ nm and mutually-horizontal oriented dipoles.

whereas the homogeneous lifetime, $1/\gamma_0$, is of the order of 10ns. For the typically considered situation in the previous section, where the Purcell factor is about 10, this corresponds to γ^ϕ about one hundredth of the emission rate γ. In our calculations we will consider larger dephasing values, both as a conservative measure and because they may be more relevant for other emitter types. Figure 5.16 shows the steady state concurrence as a function of the qubit-qubit separation d for different values of the pure dephasing rate and various pumping conditions. The emitters are mutually-parallel aligned over a channel plasmonic waveguide, whose relevant parameters are displayed in the caption. Pure dephasing grows from zero in panel (a) to $\gamma^\phi/\gamma = 0.4$ in panel (c). The qualitative behavior is almost the same in all panels, but the value of C_∞ decreases as the dephasing rate grows (notice that the vertical scale is not the same in all panels). The most significant difference appears in panel (c), which shows how the system becomes completely disentangled for certain widths of distances. In particular, there are widths close to the separations $d/\lambda_{\rm pl} = 0.5, 1.5$ in the antisymmetric pumping, and next to $d/\lambda_{\rm pl} = 1$ in the symmetric case. Despite of the general decreasing behaviour of the concurrence for larger pure dephasing rates, the value of the concurrence maxima are non-negligible even in the worst case, *i.e.*, panel (c). Therefore, our results show that pure dephasing reduces qubit-qubit stationary entanglement but not as much as to preclude its formation by strongly confined one dimensional plasmons.

Once the tomography of the system density matrix is measured experimentally, the calculation of concurrence (or any other equivalent entanglement quantifier) is straightforward. However, quantum state tomographic procedures are experimentally cumbersome because they require the determination of a large number of parameters [178]. For this reason, it is of interest to establish connections between entanglement and other more easily measurable magnitudes. In our two-qubit system, entanglement is associated with the probability that the state of the system is $|+\rangle$ or $|-\rangle$. In other words, entanglement is related with having a strong correlation between the states $|1\rangle = |e_1 g_2\rangle$ and $|2\rangle = |g_1 e_2\rangle$. This must manifest in the correlations of single plasmons emitted from qubit 1 and from qubit 2. The correlations of electromagnetic field operators in the far-field, are proportional to product summations of both qubits lowering and raising operators, since the emitted fields arise from the electric-dipolar coupling of both qubits [91]. Hanbury Brown-Twiss-like experiments are able of measuring such plasmon-plasmon second order correlations in the far field [49]. In particular within those correlations, which include the summation of different products of both qubit operators, it is included the cross-term of the second order coherence function. For zero delay, the cross-term takes the form [209, 48, 194]

$$g_{12}^{(2)} = \frac{<\sigma_1^\dagger \sigma_2^\dagger \sigma_2 \sigma_1>}{<\sigma_1^\dagger \sigma_1><\sigma_2^\dagger \sigma_2>}. \tag{5.41}$$
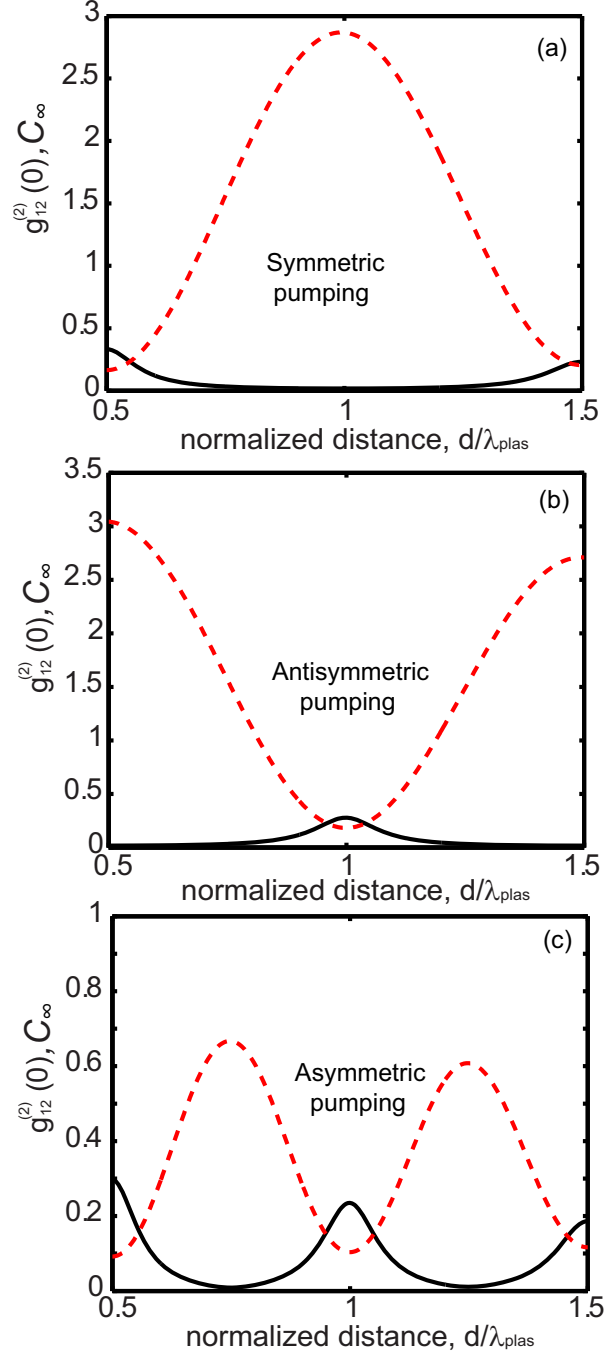
Figure 5.17: Steady state concurrence (black line) and cross second order correlation (red dashed line) as a function of the normalized separation d/λ_{pl}. (a) Symmetric pumping ($\Omega_1 = \Omega_2 = 0.1\gamma$), (b) antisymmetric pumping ($\Omega_1 = -\Omega_2 = 0.1\gamma$), and (c) asymmetric pumping ($\Omega_1 = 0.15\gamma$, $\Omega_2 = 0$). The qubits are placed in front of a channel PW at $Z = 150\,\mathrm{nm}$ for an emission wavelength of $\lambda = 600\,\mathrm{nm}$ and mutually-horizontal oriented dipoles.

Figure 5.17 displays together the concurrence C_∞ (black continuous lines) and the second order correlation function at zero delay $g_{12}^{(2)}$ (red dashed lines). In all three panels it is observed that when C_∞ is large, a clear antibunching ($g_{12}^{(2)} \to 0$) takes place, which is consistent with the system predominantly being in a state $|+\rangle$ or $|-\rangle$. On the other hand, when $C_\infty \to 0$, $g_{12}^{(2)}$ grows and the antibunching is reduced, which is again consistent with a decreased correlation between $|1\rangle$ and $|2\rangle$. The main result to be drawn is the distinct relationship between C_∞ and $g_{12}^{(2)}$. Lacking an analytical expression relating C_∞ and $g_{12}^{(2)}$, our results clearly support the idea of measuring antibunching cross-terms of the second order coherence, at zero delay, as a manifestation of entanglement.

5.5 Conclusions

We have presented a detailed analysis of how plasmonic waveguides can be used to achieve non-negligible degrees of entanglement between two distant qubits mediated by single plasmons.

In particular, we have studied the generation of transitory qubit-qubit entanglement mediated by plasmonic waveguides, in terms of the concurrence. Several plasmonic waveguides with realistic parameters have been compared respect to vacuum at a distance longer than the emission wavelength. We have demonstrated that, at such distance, realistic plasmonic waveguides display larger values of concurrence compared to vacuum. Additionally, we have shown the importance of the design and efficiency of the plasmonic waveguide in order to achieve higher and more stable degrees of entanglement between the qubits.

Additionally, the strong plasmonic modulation of the generated entanglement with the qubit separation has been characterized and studied. Whereas entanglement is found to occur at a continuum of distances, two main qubit separation sets have been identified with different characteristics: the coherent and the dissipative set. We have shown how local maxima of concurrence appear at distances within the dissipative set and how this corresponds to the longest-living entangled-mixtures of both qubits states. In this case, we have identified that the main mechanism that generates entanglement is the difference between the superradiant and subradiant decay rates.

Different dissipative evolutions have been studied which give rise to interesting phenomena like the sudden birth, death and revival of transitory entanglement. From all the variety of initial cases considered, we can conclude that most of these phenomena occurs due to the importance of the subradiant state, induced by the dissipative dynamics.

Additionally, we have considered unfavorable cases where the emitters have mutually-different alignments, differing from the predominant plasmon polarization and slightly distinct emission wavelengths. After analyzing the main results, we have seen the robustness

of the transitory entanglement for quite large emitter misalignments and also for medium induced differences in the qubits emitting frequencies.

Next, we have studied the formation of plasmon-mediated stationary entanglement between two-qubits by introducing a resonant laser impinging in the qubits. By means of the concurrence, we have analyzed the temporal evolution of the entanglement from different initial states. We have noticed how the initial evolution resembles that of the transitory generation of entanglement, without coherent pump, for times smaller than the subradiant lifetime, due to the low-perturbation introduced by a weak pumping. After a transient behaviour, we have seen how the degree of entanglement grows until all concurrences, independently of the initial state, acquire the same stationary value.

We have studied the dependence of the generated stationary concurrence with the qubit-qubit separation and the pumping scheme for small Rabi frequencies compared to the single-emitters decay rates. The relevance of the dissipative part of the qubit-qubit interaction mediated by plasmons has been pointed out, remarking that the local maxima of concurrence occur for qubit-qubit separations in which strong subradiant states appears.

Finally, we have analyzed the sensitivity of the plasmon-mediated stationary entanglement to different parameters which can be important for an experimental implementation. In particular, the relevance of the waveguide choice and its relation with the pumping intensity has been shown. We have shown that, for all the entangling waveguides schemes, the concurrence display a maximum. The results clearly show higher concurrences for higher β plasmonic waveguides, which supports the election of high efficient waveguides compared to lower ones, including vacuum. Additionally, due to the possible heat introduced by the laser, we have studied the detrimental effect of pure dephasing with cautious experimental bounds. In all cases, we have found that the dissipation-driven generation of entanglement is robust enough to survive with the conventional plasmonic waveguides that are currently available. Finally, we have proposed a term in the cross-term second order coherence function to measure the emergence of entanglement in these structures. The proposal is based on establishing a direct link between the concurrence and photon antibunching that can be extracted from photo-detection experiments.

6 General conclusions and outlook

English

In this thesis we have studied different physical phenomena associated with surface electromagnetic modes attached to one-dimensional complex metallic waveguides. For such purpose, we have made use of the finite element method to develop accurate numerical models to calculate the electromagnetic fields bound to the waveguides. In particular, the Green's tensor has been extracted from those numerical models and, importantly, we have obtained an analytical formula that contains the contribution of the guided modes to such tensor. From the quantization of the macroscopic Maxwell's equations, we have presented a master equation governing the dynamics of two qubits in the presence of inhomogeneous absorbing materials, with or without the presence of a resonant coherent laser. The resulting coefficients of interaction in the master equation can be evaluated for realistic plasmonic waveguides from the Green's tensor which is numerically calculated. Specifically, to show the relevance of the guided plasmonic modes, we have made use of the deduced analytical formula in order to evaluate the explicit contribution of this surface electromagnetic waves to those coefficients.

First in our research, we have performed a broad study of one-dimensional metallic waveguides in order to extend the confinement properties of plasmonic waveguides from the optical to the terahertz regime. For such purpose, we have made use of periodical corrugations in conventional plasmonic waveguides to modify the dispersion relation of their associated electromagnetic modes. In particular, we have demonstrated the abilities of corrugations for lowering the cut-off frequencies in corrugated channels, slots and ridges. The use of corrugations gives rise to new transversely confined surface plasmon modes. Among these electromagnetic waves, we have identified the ones associated to a periodic chain of metallic particles standing on top of metallic substrates, and which show good propagation properties. For certain geometrical parameters, the approach based on a particle chain shows a superior confinement and propagation characteristics as compared to metallic wedges and channels in the telecom regime. Additionally, we have extended such periodic waveguide to the terahertz regime for demonstrating a novel guiding scheme that shows planar-fabrication compatibility, full transverse subwavelength confinement, and reasonable

bending and propagation losses. Interestingly, we have found a remarkable insensitivity of the bands to variations in the lateral width of the particles. This property allows to design important passive components for terahertz circuitry, such as tapers, couplers, beam splitters and waveguide-ring resonators, that work at deep subwavelength scales. Moreover, most of the particle-waveguide properties described in this thesis have been confirmed experimentally in different spectral regimes by other research groups.

Based on the previous waveguide study, we have researched the interaction of a single two-level emitter with one-dimensional plasmonic waveguides at optical wavelengths. Specifically, we have identified the favorable system configurations for an efficient single-plasmon emission on metallic cylinders, wedges and channels. We have shown that the emission properties of those systems barely change with relatively large modifications of the emitter orientation or with considerable variations of the emission wavelength. Remarkably, we have found that wedges and channels show higher efficiencies for the generation of single plasmons compared to a cylindrical wire, and they also induce a higher decay rate of the emitter excited state.

The good single-photon emission properties associated to one-dimensional plasmonic waveguides have allowed us to successfully study the plasmon-mediated coupling of a pair of separated two-level emitters with such waveguides. We have calculated the parameters involved in the master equation for two quantum emitters interacting by means of metallic waveguides (cylinders, wedges and channels) and we have considered several orientational configurations of the emitters. Remarkably, a simpler plasmon mediated model of the interaction has been identified, which is in excellent agreement with full-numerical calculations for favorable emitters alignments, and is qualitatively good for unfavorable orientations. As an application of the plasmon mediated coupling, we have study the resonant energy transfer between an emitter and an acceptor that is assisted by one-dimensional plasmonic waveguides. In particular, we have demonstrated how plasmonic waveguides allow to enhance largely the resonance energy transfer rate in comparison with vacuum at distances longer than the emission wavelength. Moreover, we have studied the coupling of two separated emitters mediated by plasmonic waveguides, and we have demonstrated the appearance of strong superradiant and subradiant collective decay rates that depend on the emitters separation. We have identified that metallic channels perform better for the mutual coupling of two emitters whereas the wedge is more appropriate for resonance energy transfer purposes.

Finally, we have studied the possibility to generate transitory qubit-qubit entanglement mediated by plasmonic waveguides. We have shown the superior performance of plasmonic waveguides respect to vacuum for generating entanglement at distances longer than the emission wavelength. Importantly, we have demonstrated that structures presenting higher

single-plasmon emission efficiency can help to obtain higher degrees of entanglement. We have also shown that a transitory generation of entanglement is achieved for quite large emitter orientations, and for reasonable variations in the qubits emission frequencies. The evolution of different initial states has been studied, showing interesting phenomena like the sudden birth, death and revival of transitory entanglement. Moreover, we have demonstrated that a weak resonant laser impinging on the qubits allows the formation of plasmon-mediated stationary entanglement. The dependence of the generated entanglement with the qubit-qubit separation, initial state configuration, and the pumping scheme, has been analyzed. We can conclude that the most favorable entangling cases occurs at qubits separations for which significantly different superradiant and subradiant decay rates are present. The detrimental effect of pure dephasing in the presence of laser excitation has also been considered and we have found that the entanglement generation is robust against it. Finally, we have proposed to measure antibunching in a particular term of the second order cross-correlation function as a possible witness of the formation of entanglement in those systems.

The waveguide schemes presented in this thesis, which extend the subwavelength transverse properties of plasmonic waveguides from the optical to the terahertz regime, allow to study similar optical quantum plasmonic phenomena at longer wavelengths. The existing single photon sources in the telecom regime can benefit from the abilities of subwavelength corrugated metallic waveguides for enhancing their emission and the interaction of several emitters. Further progress is necessary in order to extend such interaction processes to the terahertz, due to the large internal decoherence rates of the emitters that must be carefully considered. Both extensions can give rise to new interesting quantum processes based on plasmonic waveguides in unexplored wavelength regimes.

Español

En esta tesis se han estudiado fenómenos de interacción que involucran modos electromagnéticos de superficie ligados a guías de ondas metálicas complejas. Con tal propósito, se ha hecho uso del método de elementos finitos para desarrollar modelos numéricos que calculen, de manera precisa, los campos electromagnéticos soportados por tales guías de ondas. En particular, se ha extraído el tensor de Green de los modelos numéricos, y obtenido una fórmula analítica que contiene explícitamente la contribución de los modos guiados a dicho tensor. A partir de la cuantización de las ecuaciones de Maxwell macroscópicas, hemos hallado una ecuación maestra que rige la dinámica de un par de emisores de dos niveles en presencia de materiales inhomogéneos con absorción. Dentro de esa evolución, se han considerado los casos tanto en presencia de un láser en resonancia con los emisores como en ausencia de este último. Los coeficientes resultantes en la ecuación maestra han sido evaluados para guías de onda plasmónicas mediante el cálculo numérico del tensor de Green. A fin de mostrar la relevancia de los plasmones de superficie en dichas interacciones, hemos hecho uso de la fórmula analítica mencionada anteriormente para evaluar la contribución explícita de los modos de las guías plasmónicas en esos coeficientes.

En primer lugar en nuestra investigación, hemos realizado un amplio estudio de guías de ondas metálicas unidimensionales con el objetivo de extender las propiedades de confinamiento de las guías plasmónicas desde el régimen óptico hasta el régimen de terahercios. Con tal propósito, se ha hecho uso de ondulaciones periódicas en guías de ondas plasmónicas convencionales para modificar fuertemente las relaciones de dispersión de los modos electromagnéticos que soportan. En particular, hemos visto la capacidad de las corrugaciones para reducir las frecuencias de corte de tales modos en guías de canal, de ranura y de cuña rectangular. Adicionalmente, se ha demostrado cómo una cadena periódica de partículas metálicas, fijadas en la parte superior de un substrato metálico, da lugar a nuevos modos plasmónicos transversalmente confinados. Para ciertos parámetros geométricos y distintas longitudes de onda en el infrarrojo cercano, en particular aquellas usadas en telecomunicaciones, esta guía de ondas basada en partículas presenta un confinamiento y características de propagación superiores a las de cuñas y canales metálicos. Hemos extendido el uso de esta guía de ondas al régimen de terahercio, demostrando así un nuevo sistema de guiado que muestra compatibilidad para su fabricación con geometrías planas. Los modos electromagnéticos soportados por esta guía presentan confinamiento transversal sublongitud de onda y unas pérdidas de propagación razonables, tanto en guías rectas como curvadas. Además, se ha encontrado una notable insensibilidad de las bandas a variaciones de la anchura lateral de las partículas. Tal característica permite diseñar importantes componentes pasivos para circuitos ultra compactos en el régimen del terahercio, tales como concentradores, acopladores,

divisores de haz y resonadores de anillo. Dichas propiedades y algunos dispositivos de las guías de ondas basadas en cadenas de partículas han sido confirmados experimentalmente por otros grupos de investigación, en particular, en frecuencias cercanas a los terahercios.

Usando como base la investigación anterior, se ha estudiado la interacción de un único emisor cuántico con distintas guías plasmónicas unidimensionales en longitudes de onda ópticas. Concretamente, hemos identificado las configuraciones favorables para la emisión eficiente de plasmones guiados individuales en cilindros, cuñas y canales metálicos. Se ha mostrado cómo las propiedades de emisión, en tales sistemas, cambian ligeramente para pequeñas variaciones de la longitud de onda de emisión, así como para grandes modificaciones de las orientaciones de los emisores. De manera destacable, se ha encontrado que las cuñas y los canales muestran mayores eficiencias para la generación de plasmones individuales, en comparación con un nanohilo cilíndrico, e inducen mayores tasas de decaimiento de los estados excitados del emisor.

Las buenas propiedades de emisión, encontradas en guías plasmónicas unidimensionales con un único emisor, nos han permitido estudiar con éxito el acoplamiento de un par de emisores de dos niveles mediado por los plasmones soportados en tales guías de ondas. En particular, hemos calculado los parámetros que intervienen en la ecuación maestra de dos emisores cuánticos con guías de ondas plasmónicas (cilindros, cuñas y canales), para distintas orientaciones de los emisores. Es importante destacar que se ha identificado un modelo de interacción por plasmones guiados, el cual está en excelente acuerdo con los cálculos numéricos completos en el caso de emisores alineados favorablemente, y que es cualitativamente bueno para casos desfavorables. Como una aplicación del acoplamiento mediado por plasmones guiados, hemos demostrado la transferencia de energía resonante asistida por una guía de onda plasmónica entre un emisor y un aceptor. Concretamente, hemos mostrado que las guías de onda plasmónicas, en comparación con el caso de vacío, permiten aumentar considerablemente la tasa de transferencia de energía en resonancia para distancias mayores que la longitud de onda de emisión. Por otro lado, se ha analizado el acoplo, mediado por plasmones guiados, entre dos emisores idénticos en presencia de guías plasmonicas y su magnitud a dicho orden de distancias. Se ha demostrado la aparición de estados colectivos fuertemente superradiantes y subradiantes como consecuencia de dichos acoplos, los cuales dependen de las distintas separaciones entre los emisores. De manera adicional, se ha mostrado que los canales metálicos pueden funcionar mejor para el acoplamiento mutuo entre dos emisores idénticos mientras que las cuñas metálicas son más adecuadas para propósitos de transferencia unidireccional de energía resonante.

Por último, se ha estudiado la formación de entrelazamiento transitorio entre bits cuánticos separados mediada por guías de ondas plasmónicas. Hemos demostrado el rendimiento superior de las guías de onda plasmónicas respecto al vacío para generar entrelazamiento

a distancias mayores que la longitud de onda de emisión. Destacan los resultados de las estructuras que presentan mayor eficiencia en la generación de plasmones individuales, las cuales permiten alcanzar mayores grados de entrelazamiento. Tal capacidad de generar enredo cuántico se mantiene para desviaciones grandes de la orientación de los emisores, y para variaciones razonables en las frecuencias de emisión de los bits cuánticos. La evolución de distintos estados iniciales ha sido estudiada y se han observado fenómenos interesantes, tales como el nacimiento repentino, la muerte súbita, y el renacimiento de enredo cuántico transitorio. Por otro lado, hemos mostrado la influencia de un láser resonante de intensidad débil con los bits cuánticos, la cual permite la formación estacionaria de entrelazamiento entre dos emisores mediada por modos plasmónicos. Se ha analizado la dependencia del entrelazamiento con la separación entre los emisores, con la configuración del estado inicial y con el esquema de bombeo. Podemos concluir que los casos más favorables de formación de enredo ocurren a separaciones entre bits cuánticos en las que las tasas de los estados simétrico y antisimétrico difieren significativamente. El efecto perjudicial del desfase puro (o 'pure dephasing' en inglés), el cual puede surgir por la presencia de excitación láser, ha sido también considerado, y se ha encontrado que la generación de entrelazamiento es robusta frente a tal efecto. Finalmente, para distinguir la creación de enredo cuántico en el sistema, se ha propuesto medir una disminución de las correlaciones de los fotones emitidos por debajo del régimen de fotones individuales, también llamado antiagrupamiento (o 'anti-bunching' en inglés). En concreto, hemos analizado tal decrecimiento en un término determinado de la función de correlación de segundo orden cruzada como posible testigo de dicho entrelazamiento cuántico.

Las guías de ondas corrugadas presentadas en esta tesis permiten extender el estudio de fenómenos cuánticos, similares a los considerados en longitudes de onda ópticas, a frecuencias de emisión menores. Los actuales emisores de fotones individuales, en el régimen de frecuencias de las telecomunicaciones, pueden beneficiarse del confinamiento sublongitud de onda de las guías plasmónicas corrugadas para mejorar su emisión e interacción entre varios emisores. Mayores avances son necesarios para extender tales procesos de interacción al régimen del terahercio, debido a las grandes tasas de decoherencia de los emisores existentes que deben ser cuidadosamente consideradas. Ambas extensiones del estudio a menores frecuencias de emisión en guías plasmónicas pueden dan lugar a nuevos fenómenos de interacción basados en regímenes espectrales aún no explorados.

Bibliography

[1] W. L. Barnes, Alain Dereux, and T. W. Ebbesen. Surface plasmon subwavelength optics. *Nature*, 424:824, 2003.

[2] H. Raether. *Surface plasmons*. Springer-Verlag, 1988.

[3] S. Nie and S.R. Emory. Probing single molecules and single nanoparticles by surface-enhanced raman scattering. *Science*, 275:1102, 1997.

[4] M. Lin, L. He, J. Awika, L. Yang, D.R. Ledoux, H. Li, and A. Mustapha. Detection of melamine in gluten, chicken feed, and processed foods using surface enhanced raman spectroscopy and hplc. *Journal of food science*, 73:T129, 2008.

[5] P. Anger, P. Bharadwaj, and L. Novotny. Enhancement and quenching of single-molecule fluorescence. *Phys. Rev. Lett.*, 96:113002, 2006.

[6] D.K. Gramotnev and S.I. Bozhevolnyi. Plasmonics beyond the diffraction limit. *Nature Photonics*, 4:83, 2010.

[7] A. W. Snyder and J. Love. *Optical Waveguide Theory*. Springer,New York, 1983.

[8] T.A. Birks, J.C. Knight, and P.S.J. Russell. Endlessly single-mode photonic crystal fiber. *Opt. letters*, 22:961, 1997.

[9] D.F.P. Pile, T. Ogawa, D.K. Gramotnev, T. Okamoto, M. Haraguchi, M. Fukui, and S. Matsuo. Theoretical and experimental investigation of strongly localized plasmons on triangular metal wedges for subwavelength waveguiding. *Appl. Phys. Lett.*, 87:061106, 2005.

[10] G.W. Ford and W.H. Weber. Electromagnetic interactions of molecules with metal surfaces. *Phys. Rep*, 113:195, 1984.

[11] H. Ditlbacher, A. Hohenau, D. Wagner, U. Kreibig, M. Rogers, F. Hofer, F.R. Aussenegg, and J.R. Krenn. Silver nanowires as surface plasmon resonators. *Phys. Rev. Lett.*, 95:257403, 2005.

Bibliography

[12] S.I. Bozhevolnyi, V.S. Volkov, E. Devaux, J.Y. Laluet, and T.W. Ebbesen. Channel plasmon subwavelength waveguide components including interferometers and ring resonators. *Nature*, 440:508, 2006.

[13] R. Ramaswami. Optical fiber communication: From transmission to networking. *Communications Magazine, IEEE*, 40:138, 2002.

[14] V.S. Volkov, S.I. Bozhevolnyi, S.G. Rodrigo, L. Martin-Moreno, F.J. Garcia-Vidal, E. Devaux, and T.W. Ebbesen. Nanofocusing with channel plasmon polaritons. *Nano letters*, 9:1278, 2009.

[15] V.S. Volkov, S.I. Bozhevolnyi, E. Devaux, J.Y. Laluet, and T.W. Ebbesen. Wavelength selective nanophotonic components utilizing channel plasmon polaritons. *Nano letters*, 7:880, 2007.

[16] S.I. Bozhevolnyi, V.S. Volkov, E. Devaux, J.Y. Laluet, and T.W. Ebbesen. Channelling surface plasmons. *Applied Physics A: Materials Science & Processing*, 89:225, 2007.

[17] S.I. Bozhevolnyi, V.S. Volkov, E. Devaux, and T.W. Ebbesen. Channel plasmon-polariton guiding by subwavelength metal grooves. *Phys. Rev. Lett.*, 95:46802, 2005.

[18] S. I. Bozhevolnyi, V. S. Volkov, E. Devaux, J.-Y. Laluet, and T. W. Ebbesen. Channel plasmon subwavelength waveguide components including interferometers and ring resonators. *Nature*, 440:508, 2006.

[19] E. Moreno, F. J. Garcia-Vidal, Sergio G. Rodrigo, L. Martin-Moreno, and Sergey I. Bozhevolnyi. Channel plasmon-polaritons: modal shape, dispersion, and losses. *Opt. Lett.*, 31:3447, 2006.

[20] S. Maier, S. R. Andrews, L. Martin-Moreno, and F. J. Garcia-Vidal. Terahertz surface plasmon-polariton propagation and focusing on periodically corrugated metal wires. *Phys. Rev. Lett.*, 97:176805, 2006.

[21] A.I. Fernández-Domínguez. *Electromagnetic phenomena based on surface modes and their transfer to quantum optics.* PhD thesis, 2009. UAM.

[22] A.I. Fernández-Domínguez, CR Williams, FJ García-Vidal, L. Martín-Moreno, SR Andrews, and SA Maier. Terahertz surface plasmon polaritons on a helically grooved wire. *Appl. Phys. Lett.*, 93:141109, 2008.

[23] M. Tonouchi. Cutting-edge terahertz technology. *Nature Photonics*, 1:97, 2007.

[24] B. Ferguson and X.C. Zhang. Materials for terahertz science and technology. *Nature Mater.*, 1:26, 2002.

[25] P. H. Siegel. Terahertz technology. *IEEE Trans. Microwave Theory and Tech.*, 50:910, 2002.

[26] P. H. Siegel. Terahertz technology in biology and medicine. *IEEE Trans. Microwave Theory and Tech.*, 52:2438, 2004.

[27] A.J.L. Adam. Review of near-field terahertz measurement methods and their applications. *Journal of Infrared, Millimeter and Terahertz Waves*, 32:976, 2011.

[28] A.A. Gowen, C. O'Sullivan, and C.P. O'Donnell. Terahertz time domain spectroscopy and imaging: Emerging techniques for food process monitoring and quality control. *Trends in Food Science & Technology*, 2012.

[29] S. Withington. Terahertz astronomical telescopes and instrumentation. *Phil. Trans. R. Soc. Lond. A*, 362:395, 2004.

[30] J. Federici and L. Moeller. Review of terahertz and subterahertz wireless communications. *Journal of Applied Physics*, 107:111101, 2010.

[31] J. B. Pendry, L. Martin-Moreno, and F. J. Garcia-Vidal. Mimicking surface plasmons with structured surfaces. *Science*, 305:847, 2004.

[32] S. A. Maier A. I. Fernández-Dominguez L. Martin-Moreno C. R. Williams, S. R. Andrews and Nature Photonics **2** 175 F. J. Garcia-Vidal, Highly confined guiding of terahertz surface plasmon polaritons on structured metal surfaces. 2008. 2008.

[33] A. I. Fernandez-Dominguez, E. Moreno, L. Martin-Moreno, and F. J. Garcia-Vidal. Terahertz wedge plasmon polaritons. *Opt. Lett*, 34:2063, 2009.

[34] A. I. Fernandez-Dominguez, E. Moreno, L. Martin-Moreno, and F. J. Garcia-Vidal. Guiding terahertz waves along subwavelength channels. *Phys. Rev. B*, 79:233104, 2009.

[35] A. Rusina, M. Durach, K. A. Nelson, and M. I. Stockman. Nanoconcentration of terahertz radiation in plasmonic waveguides. *Opt. Express*, 16:18576, 2008.

[36] J. Cunningham, M. Byrne, P. Upadhya, M. Lachab, E. H. Linfield, and A. G. Davies. Terahertz evanescent field microscopy of dielectric materials using on-chip waveguides. *Appl. Phys. Lett.*, 92:032903, 2008.

[37] W. Huang, Y. Zhang, and B. Li. Ultracompact wavelength and polarization splitters in periodic dielectric waveguides. *Opt. Express*, 16:1600, 2008.

[38] D. Martin-Cano, M.L. Nesterov, A.I. Fernandez-Dominguez, F.J. Garcia-Vidal, L. Martin-Moreno, and E. Moreno. Domino plasmons for subwavelength terahertz circuitry. *Opt. Express*, 18:754, 2010.

[39] D. Martin-Cano, O. Quevedo-Teruel, E. Moreno, L. Martin-Moreno, and F.J. Garcia-Vidal. Waveguided spoof surface plasmons with deep-subwavelength lateral confinement. *Opt. Lett.*, 36:4635, 2011.

[40] M.L. Nesterov, D. Martin-Cano, A.I. Fernandez-Dominguez, E. Moreno, L. Martin-Moreno, and F.J. Garcia-Vidal. Geometrically induced modification of surface plasmons in the optical and telecom regimes. *Opt. Lett.*, 35:423, 2010.

[41] A. V. Akimov, A. Mukherjee, C. L. Yu, D. E. Chang, A. S. Zibrov, P. R. Hemmer, H. Park, and M. D. Lukin. Generation of single optical plasmons in metallic nanowires coupled to quantum dots. *Nature*, 450, 2007.

[42] F. Verstraete, M.M. Wolf, and J.I. Cirac. Quantum computation and quantum-state engineering driven by dissipation. *Nature Physics*, 5:633, 2009.

[43] R. Kolesov, B. Grotz, G. Balasubramanian, R.J. Stöhr, A.A.L. Nicolet, P.R. Hemmer, F. Jelezko, and J. Wrachtrup. Wave-particle duality of single surface plasmon polaritons. *Nature Physics*, 5:470, 2009.

[44] A. Huck, S. Kumar, A. Shakoor, and U.L. Andersen. Controlled coupling of a single nitrogen-vacancy center to a silver nanowire. *Phys. Rev. Lett.*, 106:096801, 2011.

[45] D. E. Chang, A. S. Sørensen, P. R. Hemmer, and M. D. Lukin. Quantum optics with surface plasmons. *Phys. Rev. Lett.*, 97:053002, 2006.

[46] A.L. Falk, F.H.L. Koppens, C.L. Yu, K. Kang, N. L. Snapp, A.V. Akimov, M.H. Jo, M.D. Lukin, and H. Park. Near-field electrical detection of optical plasmons and single-plasmon sources. *Nature Physics*, 5:475, 2009.

[47] L. Novotny and B.Hecht. *Principles of Nano-Optics*. Cambridge University Press, Cambridge UK, 2006.

[48] D.F. Walls and G.J. Milburn. *Quantum optics*. Springer Verlag, 1994.

[49] R. W. Heeres, S.N. Dorenbos, B. Koene, G.S. Solomon, L. P. Kouwenhoven, and V. Zwiller. On-chip single plasmon detection. *Nano Letters*, 10:661, 2010. PMID: 20041700.

[50] D. E. Chang, A. S. Sørensen, Demler. E. A., and M. D. Lukin. A single-photon transistor using nanoscale surface plasmons. *Nature Physics*, 3:807, 2007.

[51] D. Dzsotjan, A.S. Sørensen, and M. Fleischhauer. Quantum emitters coupled to surface plasmons of a nanowire: A Green's function approach. *Phys. Rev. B*, 82:075427, 2010.

[52] M.J. Bremner, C.M. Dawson, J.L. Dodd, A. Gilchrist, A.W. Harrow, D. Mortimer, M.A. Nielsen, and T.J. Osborne. Practical scheme for quantum computation with any two-qubit entangling gate. *Phys. Rev. Lett.*, 89:247902, 2002.

[53] E. Altewischer, M.P. Van Exter, J.P. Woerdman, et al. Plasmon-assisted transmission of entangled photons. *Nature*, 418:304, 2002.

[54] E. Moreno, F. J. García-Vidal, D. Erni, J. Ignacio Cirac, and L. Martín-Moreno. Theory of plasmon-assisted transmission of entangled photons. *Phys. Rev. Lett.*, 92:236801, 2004.

[55] S. Fasel, F. Robin, E. Moreno, D. Erni, N. Gisin, and H. Zbinden. Energy-Time Entanglement Preservation in Plasmon-Assisted Light Transmission. *Phys. Rev. Lett.*, 94:1, 2005.

[56] D. Martín-Cano, A. González-Tudela, L. Martín-Moreno, F.J. García-Vidal, C. Tejedor, and E. Moreno. Dissipation-driven generation of two-qubit entanglement mediated by plasmonic waveguides. *Phys. Rev. B*, 84:235306, 2011.

[57] A. Gonzalez-Tudela, D. Martin-Cano, E. Moreno, L. Martin-Moreno, C. Tejedor, and F. J. Garcia-Vidal. Entanglement of two qubits mediated by one-dimensional plasmonic waveguides. *Phys. Rev. Lett.*, 106:020501, 2011.

[58] D. Martin-Cano, L. Martin-Moreno, F. J. Garcia-Vidal, and E. Moreno. Resonance energy transfer and superradiance mediated by plasmonic nanowaveguides. *Nano Letters*, 10:3129, 2010.

[59] G.S. Engel, T.R. Calhoun, E.L. Read, T.K. Ahn, T. Mančal, Y.C. Cheng, R.E. Blankenship, and G.R. Fleming. Evidence for wavelike energy transfer through quantum coherence in photosynthetic systems. *Nature*, 446:782, 2007.

[60] E. Collini, C.Y. Wong, K.E. Wilk, P.M.G. Curmi, P. Brumer, and G.D. Scholes. Coherently wired light-harvesting in photosynthetic marine algae at ambient temperature. *Nature*, 463:644, 2010.

[61] P.R. Selvin et al. The renaissance of fluorescence resonance energy transfer. *nature structural biology*, 7:730, 2000.

[62] P. Andrew and WL Barnes. Energy transfer across a metal film mediated by surface plasmon polaritons. *Science*, 306:1002, 2004.

[63] A. Kuzyk, M. Pettersson, J.J. Toppari, T.K. Hakala, H. Tikkanen, H. Kunttu, and P. Törmä. Molecular coupling of light with plasmonic waveguides. *Opt. Express*, 15:9908, 2007.

[64] S. Scheel L. Knöll and D.-G. Welsch. *Coherence and Statistics of Photons and Atoms*. Wiley, New York, 2001.

[65] R. E. Collin. *Field theory of guided waves, 2nd ed.* Wiley-IEEE Press Series on Electromagnetic Wave Theory, 1990.

[66] Jianming Jin. *The finite element method in electromagnetics,2nd edition*. John Wiley & Sons.Inc, New York, 2002.

[67] J. D. Jackson. *Classical Electrodynamics*. Wiley, 1999.

[68] Y. Zhang, J. von Hagen, M. Younis, C. Fischer, and W. Wiesbeck. Planar artificial magnetic conductors and patch antennas. *Antennas and Propagation, IEEE Transactions on*, 51:2704, 2003.

[69] J.P. Berenger. A perfectly matched layer for the absorption of electromagnetic waves. *Journal of computational physics*, 114:185, 1994.

[70] A. Taflove and S.C. Hagness. *Computational electrodynamics*, volume 160. Artech house BostonLondon, 2000.

[71] COMSOL Multiphysics. User's guide, version 3.5 a. *www.comsol.com*, 2008.

[72] E. Palik. *Handbook of Optical Constants of Solids*. Academic Press, 1998.

[73] M. A. Ordal, L. L. Long, R. J. Bell, S. E. Bell, R. R. Bell, R. W. Alexander, and C. A. Ward. Optical properties of the metals Al, Co, Cu, Au, Fe, Pb, Ni, Pd, Pt, Ag, Ti, and W in the infrared and far infrared. *Appl. Opt.*, 22:1099, 1983.

[74] A. Vial, A.S. Grimault, D. Macías, D. Barchiesi, and M.L. de La Chapelle. Improved analytical fit of gold dispersion: Application to the modeling of extinction spectra with a finite-difference time-domain method. *Phys. Rev. B*, 71:85416, 2005.

[75] E. Moreno Soriano. *MMP modeling and optimization of photonic crystals, optical devices, and nanostructures.* PhD thesis, ETH, 2002.

[76] F. J. Garcia-Vidal, L. Martin-Moreno, and J. B. Pendry. Surfaces with holes in them: New plasmonic metamaterials. *J. Opt. A: Pure Appl. Opt.*, 7:S97, 2005.

[77] Y. Chen, T.R. Nielsen, N. Gregersen, P. Lodahl, and J. Mørk. Finite-element modeling of spontaneous emission of a quantum emitter at nanoscale proximity to plasmonic waveguides. *Phys. Rev. B*, 81:125431, 2010.

[78] P.A. Huidobro, A.Y. Nikitin, C. González-Ballestero, L. Martín-Moreno, and F.J. García-Vidal. Superradiance mediated by graphene surface plasmons. *Phys. Rev. B*, 85:155438, 2012.

[79] P.A.M. Dirac. The quantum theory of dispersion. *Proceedings of the Royal Society of London. Series A*, 114:710, 1927.

[80] H.T. Dung, L. Knöll, and D.G. Welsch. Intermolecular energy transfer in the presence of dispersing and absorbing media. *Phys. Rev. A*, 65:043813, 2002.

[81] H. Dung, L. Knöll, and D. Welsch. Resonant dipole-dipole interaction in the presence of dispersing and absorbing surroundings. *Phys. Rev. A*, 66:063810, 2002.

[82] A. Gonzalez-Tudela, F. J. Rodríguez, L. Quiroga, and C. Tejedor. Dissipative dynamics of a solid-state qubit coupled to surface plasmons: From non-markov to markov regimes. *Phys. Rev. B*, 82:115334, 2010.

[83] D. Dzsotjan, J. Kästel, and M. Fleischhauer. Dipole-dipole shift of quantum emitters coupled to surface plasmons of a nanowire. *Phys. Rev. B*, 84:075419, 2011.

[84] S. Scheel and S. Y. Buhmann. Macroscopic quantum electrodynamics-concepts and applications. *Acta Physica Slovaca*, 58:675, 2008.

[85] P.W. Milonni and C. Eberlein. *The quantum vacuum: an introduction to quantum electrodynamics*, volume 1. Academic press New York, 1994.

[86] D.P. Craig and T. Thirunamachandran. *Molecular quantum electrodynamics.* Dover Publications, 1998.

[87] G. Agarwal. Quantum statistical theories of spontaneous emission and their relation to other approaches. *Quantum Optics*, page 1, 1974.

[88] E. Del Valle. *Quantum Electrodynamics with Quantum Dots in Microcavities*. PhD thesis, 2009. UAM.

[89] A. Gonzalez-Tudela, D. Martin-Cano, E. Moreno, L. Martin-Moreno, F.J. Garcia-Vidal, and C. Tejedor. Exploring qubit-qubit entanglement mediated by one-dimensional plasmonic nanowaveguides. *Physica status solidi (c)*.

[90] B.R. Mollow. Power spectrum of light scattered by two-level systems. *Physical Review*, 188, 1969.

[91] Z. Ficek and R. Tanas. Entangled states and collective nonclassical effects in two-atom systems. *Physics Reports*, 372:369, 2002.

[92] S.M. Tan. A computational toolbox for quantum and atomic optics. *Journal of Optics B: Quantum and Semiclassical Optics*, 1:424, 1999.

[93] R. Tanas and Z. Ficek. Entangling two atoms via spontaneous emission. *Journal of Optics B: Quantum and Semiclassical Optics*, 6:S90, 2004.

[94] S.I. Bozhevolnyi. Plasmonic nano-guides and circuits. 2008.

[95] R. Hanson, L. P. Kouwenhoven, J. R. Petta, S. Tarucha, and L. M. K. Vandersypen. Spin in few-electron quantum dots. *Rev. Mod. Phys.*, 79:4, 2007.

[96] H. Ditlbacher, JR Krenn, G. Schider, A. Leitner, and FR Aussenegg. Two-dimensional optics with surface plasmon polaritons. *Appl. Phys. Lett.*, 81:1762, 2002.

[97] T. W. Ebbesen, C. Genet, and S. I. Bozhevolnyi. Surface-plasmon circuitry. *Physics Today*, 5:44, 2008.

[98] K. Wang and D. M. Mittleman. Metal wires for terahertz wave guiding. *Nature*, 432:376, 2004.

[99] C. Kittle. *Introduction to solid state physics*. Wiley, 1996.

[100] P. Johnson and R. Christy. Optical constants of the nobel metals. *Phys. Rev. B*, 6:4370, 1972.

[101] C.A. Pfeiffer, E.N. Economou, and K.L. Ngai. Surface polaritons in a circularly cylindrical interface: surface plasmons. *Phys. Rev. B*, 10:3038, 1974.

[102] A. Manjavacas and F.J. Garcia de Abajo. Robust plasmon waveguides in strongly interacting nanowire arrays. *Nano letters*, 9:1285, 2008.

[103] Y. Fang, Z. Li, Y. Huang, S. Zhang, P. Nordlander, N.J. Halas, and H. Xu. Branched silver nanowires as controllable plasmon routers. *Nano letters*, 10:1950, 2010.

[104] N. P. de Leon, B. J. Shields, C. L. Yu, D. E. Englund, A. V. Akimov, M.D. Lukin, and H. Park. Tailoring light-matter interaction with a nanoscale plasmon resonator. *Phys. Rev. Lett.*, 108:226803, 2012.

[105] A. Boltasseva, V.S. Volkov, R.B. Nielsen, E. Moreno, S.G. Rodrigo, and S.I. Bozhevolnyi. Triangular metal wedges for subwavelength plasmon-polariton guiding at telecom wavelengths. *Opt. Express*, 16:5252, 2008.

[106] E. Moreno, S.G. Rodrigo, S.I. Bozhevolnyi, L. Martin-Moreno, and F. J. Garcia-Vidal. Guiding and focusing of electromagnetic fields with wedge plasmon-polaritons. *Phys. Rev. Lett.*, 100:023901, 2008.

[107] Z. Pan, J. Guo, R. Soref, W. Buchwald, and G. Sun. Mode properties of flat-top silver nanoridge surface plasmon waveguides. *JOSA B*, 29:340, 2012.

[108] R.B. Nielsen, I. Fernandez-Cuesta, A. Boltasseva, V.S. Volkov, S.I. Bozhevolnyi, A. Klukowska, and A. Kristensen. Channel plasmon polariton propagation in nanoimprinted v-groove waveguides. *Opt. Lett.*, 33:2800, 2008.

[109] E.J.R. Vesseur, F.J. Garcia de Abajo, and A. Polman. Modal decomposition of surface- plasmon whispering gallery resonators. *Nano letters*, 9:3147, 2009.

[110] M.T. Hill, M. Marell, E.S.P. Leong, B. Smalbrugge, Y. Zhu, M. Sun, P.J. Van Veldhoven, E.J. Geluk, F. Karouta, Y.S. Oei, et al. Lasing in metal-insulator-metal sub-wavelength plasmonic waveguides. *Opt. Express*, 17:11107, 2009.

[111] S.I. Bozhevolnyi and J. Jung. Scaling for gap plasmon based waveguides. *Opt. Express*, 16:2676, 2008.

[112] A.P. Hibbins, B.R. Evans, and J.R. Sambles. Experimental verification of designer surface plasmons. *Science*, 308:670, 2005.

[113] F.J. Garcia de Abajo and J.J. Sáenz. Electromagnetic surface modes in structured perfect-conductor surfaces. *Phys. Rev. Lett.*, 95:233901, 2005.

Bibliography

[114] J. R. Krenn, A. Dereux, J. C. Weeber, E. Bourillot, Y. Lacroute, J. P. Goudonnet, G. Schider, W. Gotschy, A. Leitner, F. R. Aussenegg, and C. Girard. Squeezing the optical near-field zone by plasmon coupling of metallic nanoparticles. *Phys. Rev. Lett.*, 82:2590, 1999.

[115] H. A. Atwater S. Meltzer E. Harel B. E. Koel S. A. Maier, P. G. Kik and A. A. G. Requicha. Local detection of electromagnetic energy transport below the diffraction limit in metal nanoparticle plasmon waveguides. *Nature Mat.*, **2**:229, 2003.

[116] D. F. P. Pile R. F. Oulton, G. Bartal and X. Zhang. *New J. Phys.*, **10**:105018, 2008.

[117] A.J. Huber, F. Keilmann, J. Wittborn, J. Aizpurua, and R. Hillenbrand. Terahertz near-field nanoscopy of mobile carriers in single semiconductor nanodevices. *Nano letters*, 8:3766, 2008.

[118] H.W. Hübers. Terahertz technology: Towards thz integrated photonics. *Nature Photonics*, 4:503, 2010.

[119] T.-I. Jeon and D. Grischkowsky. Thz zenneck surface wave (thz surface plasmon) propagation on a metal sheet. *Appl. Phys. Lett.*, 88:061113, 2006.

[120] Z. Gao, X. Zhang, and L. Shen. Wedge mode of spoof surface plasmon polaritons at terahertz frequencies. *Journal of Applied Physics*, 108:113104, 2010.

[121] W. Zhao, O.M. Eldaiki, R. Yang, and Z. Lu. Deep subwavelength waveguiding and focusing based on designer surface plasmons. *Opt. Express*, 18:21498, 2010.

[122] E.M.G. Brock, E. Hendry, and A.P. Hibbins. Subwavelength lateral confinement of microwave surface waves. *Appl. Phys. Lett.*, 99:051108, 2011.

[123] D. L. Sengupta. On the phase velocity of wave propagation along an infinite yagi structure. *IRE Trans. Antennas Propag.*, 7:234, 1959.

[124] A. Pors, E. Moreno, L. Martin-Moreno, JB Pendry, and F.J. Garcia-Vidal. Localized spoof plasmons arise while texturing closed surfaces. *Phys. Rev. Lett.*, 108:223905, 2012.

[125] S. A. Maier, M. L. Brongersma, and H. A. Atwater. Electromagnetic energy transport along arrays of closely spaced metal rods as an analogue to plasmonic devices. *Appl. Phys. Lett.*, 78:16, 2001.

[126] E. Verhagen, M. Spasenovic, A. Polman, and L. K. Kuipers. Nanowire plasmon excitation by adiabatic mode transformation. *Phys. Rev. Lett.*, 102:203904, 2009.

[127] M.A. Seo, H.R. Park, S.M. Koo, D.J. Park, J.H. Kang, O.K. Suwal, S.S. Choi, P.C.M. Planken, G.S. Park, N.K. Park, et al. Terahertz field enhancement by a metallic nano slit operating beyond the skin-depth limit. *Nature Photonics*, 3:152, 2009.

[128] H. Liang, S. Ruan, and M. Zhang. Terahertz surface wave propagation and focusing on conical metal wires. *Opt. Express*, 16:18241, 2008.

[129] S. Kawata, Y. Inouye, and P. Verma. Plasmonics for near-field nano-imaging and superlensing. *Nature Photonics*, 3:388, 2009.

[130] K. Ishihara, K. Ohashi, T. Ikari, H. Minamide, and H. Yokoyama. Terahertz-wave near-field imaging with subwavelength resolution using surface-wave-assisted bow-tie aperture. *Appl. Phys. Lett.*, 89:201120, 2006.

[131] A. Ishikawa, S. Zhang, D. A. Genov, G. Bartal, and X. Zhang. Deep subwavelength terahertz waveguides using gap magnetic plasmon. *Phys. Rev. Lett.*, 102:043904, 2009.

[132] M. L. Nesterov, A. V. Kats, and S. K. Turitsyn. Extremely short-length surface plasmon resonance devices. *Opt. Express*, 16:20227, 2008.

[133] Y.G. Ma, L. Lan, S.M. Zhong, and C.K. Ong. Experimental demonstration of subwavelength domino plasmon devices for compact high-frequency circuit. *Opt. Express*, 19:21189, 2011.

[134] A. Bousseksou, A. Babuty, J.P. Tetienne, I. Moldovan-Doyen, R. Braive, G. Beaudoin, I. Sagnes, Y. De Wilde, and R. Colombelli. Sub-wavelength energy concentration with electrically generated mid-infrared surface plasmons. *Opt. Express*, 20:13738, 2012.

[135] D. Sievenpiper. *Review of Theory, Fabrication, and Applications of High-Impedance Ground Planes*, page 285. Wiley, 2006.

[136] M.J. Lockyear, A.P. Hibbins, and J.R. Sambles. Microwave surface-plasmon-like modes on thin metamaterials. *Phys. Rev. Lett.*, 102:73901, 2009.

[137] E. Rajo-Iglesias, Ó. Quevedo-Teruel, and L. Inclan-Sanchez. Planar soft surfaces and their application to mutual coupling reduction. *Antennas and Propagation, IEEE Transactions on*, 57:3852, 2009.

[138] E.M. Purcell. Spontaneous emission probabilities at radio frequencies. *Physical Review*, 69:681, 1946.

[139] P. Bharadwaj, B. Deutsch, and L. Novotny. Optical antennas. *Advances in Optics and Photonics*, 1:438, 2009.

[140] T. Förster. Zwischenmolekulare energiewanderung und fluoreszenz. *Annalen der Physik*, 437:55, 1948.

[141] C.A. Marocico and J. Knoester. Intermolecular resonance energy transfer in the presence of a dielectric cylinder. *Phys. Rev. A*, 79:053816, 2009.

[142] R.H. Dicke. Coherence in spontaneous radiation processes. *Physical Review*, 93:99, 1954.

[143] J. Bellessa, C. Bonnand, J. C. Plenet, and J. Mugnier. Strong coupling between surface plasmons and excitons in an organic semiconductor. *Phys. Rev. Lett.*, 93:036404, 2004.

[144] S. Kühn, U. Håkanson, L. Rogobete, and V. Sandoghdar. Enhancement of single-molecule fluorescence using a gold nanoparticle as an optical nanoantenna. *Phys. Rev. Lett.*, 97:17402, 2006.

[145] T.H. Taminiau, F.D. Stefani, and N.F. van Hulst. Enhanced directional excitation and emission of single emitters by a nano-optical yagi-uda antenna. *Opt. Express*, 16:10858, 2008.

[146] F. Le Kien, S.D. Gupta, KP Nayak, and K. Hakuta. Nanofiber-mediated radiative transfer between two distant atoms. *Phys. Rev. A*, 72:063815, 2005.

[147] L.A. Coldren, S.W. Corzine, and M.L. Mashanovitch. *Diode lasers and photonic integrated circuits*. Wiley, 2012.

[148] M. Khajavikhan, A. Simic, M. Katz, JH Lee, B. Slutsky, A. Mizrahi, V. Lomakin, and Y. Fainman. Thresholdless nanoscale coaxial lasers. *Nature*, 482:204, 2012.

[149] A. Einstein. On the quantum theory of radiation. *Phys. Z*, 18:121, 1917.

[150] C. Kurtsiefer, S. Mayer, P. Zarda, and H. Weinfurter. Stable solid-state source of single photons. *Phys. Rev. Lett.*, 85:290, 2000.

[151] B. Darquié, MPA Jones, J. Dingjan, J. Beugnon, S. Bergamini, Y. Sortais, G. Messin, A. Browaeys, and P. Grangier. Controlled single-photon emission from a single trapped two-level atom. *Science*, 309:454, 2005.

[152] T. Lund-Hansen, S. Stobbe, B. Julsgaard, H. Thyrrestrup, T. Sünner, M. Kamp, A. Forchel, and P. Lodahl. Experimental realization of highly efficient broadband coupling of single quantum dots to a photonic crystal waveguide. *Phys. Rev. Lett.*, 101:113903, 2008.

[153] D. Englund, B. Shields, K. Rivoire, F. Hatami, J. Vuckovic, H. Park, and M.D. Lukin. Deterministic coupling of a single nitrogen vacancy center to a photonic crystal cavity. *Nano Letters*, 10:3922, 2010.

[154] I.D. Rukhlenko, D. Handapangoda, M. Premaratne, A.V. Fedorov, A.V. Baranov, and C. Jagadish. Spontaneous emission of guided polaritons by quantum dot coupled to metallic nanowire: Beyond the dipole approximation. *Opt. Express*, 17:17570, 2009.

[155] M.L. Andersen, S. Stobbe, A.S. Sørensen, and P. Lodahl. Strongly modified plasmon-matter interaction with mesoscopic quantum emitters. *Nature Physics*, 7:215, 2010.

[156] S. Thongrattanasiri, A. Manjavacas, and F.J. Garcia de Abajo. Quantum finite-size effects in graphene plasmons. *ACS nano*, 6:1766, 2012.

[157] J. Zuloaga, E. Prodan, and P. Nordlander. Quantum description of the plasmon resonances of a nanoparticle dimer. *Nano letters*, 9:887, 2009.

[158] G. Lecamp, P. Lalanne, and J. P. Hugonin. Very large spontaneous-emission β factors in photonic-crystal waveguides. *Phys. Rev. Lett.*, 99:023902, 2007.

[159] V. V. Klimov and M. Ducloy. Spontaneous emission rate of an excited atom placed near a nanofiber. *Phys. Rev. A*, 69:013812, 2004.

[160] C. M. Galloway, P. G. Etchegoin, and E. C. Le Ru. Ultrafast nonradiative decay rates on metallic surfaces by comparing surface-enhanced raman and fluorescence signals of single molecules. *Phys. Rev. Lett.*, 103:063003, 2009.

[161] H. Morawitz. Self-coupling of a two-level system by a mirror. *Physical Review*, 187:1792, 1969.

[162] T. Søndergaard and S. I. Bozhevolnyi. Surface plasmon polariton scattering by a small particle placed near a metal surface: An analytical study. *Phys. Rev. B*, 69:045422, 2004.

Bibliography

[163] P.J. Shadbolt, M.R. Verde, A. Peruzzo, A. Politi, A. Laing, M. Lobino, J.C.F. Matthews, M.G. Thompson, and J.L. O'Brien. Generating, manipulating and measuring entanglement and mixture with a reconfigurable photonic circuit. *Nature Photonics*, 6:45, 2011.

[164] M. Righini, G. Volpe, C. Girard, D. Petrov, and R. Quidant. Surface plasmon optical tweezers: Tunable optical manipulation in the femtonewton range. *Phys. Rev. Lett.*, 100:186804, 2008.

[165] R. F. Oulton, Volker J. Sorger, T. Zentgraf, R.M. Ma, L. Dai, G. Bartal, and X. Zhang. Plasmon lasers at deep subwavelength scale. *Nature*, 461, 2009.

[166] X.W. Chen, V. Sandoghdar, and M. Agio. Highly efficient interfacing of guided plasmons and photons in nanowires. *Nano letters*, 9:3756, 2009.

[167] D. E. Chang, A. S. Sørensen, P. R. Hemmer, and M. D. Lukin. Strong coupling of single emitters to surface plasmons. *Phys. Rev. B*, 76:035420, 2007.

[168] K.C. Vernon, N. Tischler, and M.L. Kurth. Coupling of energy from quantum emitters to the plasmonic mode of v groove waveguides: A numerical study. *Journal of Applied Physics*, 111:64323, 2012.

[169] A. G. Curto, G. Volpe, T. H. Taminiau, M. P. Kreuzer, R. Quidant, and N.F. van Hulst. Unidirectional emission of a quantum dot coupled to a nanoantenna. *Science*, 329:930, 2010.

[170] D. Englund, A. Majumdar, A. Faraon, M. Toishi, N. Stoltz, P. Petroff, and J. Vuckovic. Resonant excitation of a quantum dot strongly coupled to a photonic crystal nanocavity. *Phys. Rev. Lett.*, 104:073904, 2010.

[171] R.K. Kramer, N. Pholchai, V.J. Sorger, T.J. Yim, R. Oulton, and X. Zhang. Positioning of quantum dots on metallic nanostructures. *Nanotechnology*, 21:145307, 2010.

[172] C. Santori, M. Pelton, G. Solomon, Y. Dale, and Y. Yamamoto. Triggered single photons from a quantum dot. *Phys. Rev. Lett.*, 86:1502, 2001.

[173] J.P. Goss, R. Jones, S.J. Breuer, P.R. Briddon, and S. Öberg. The twelve-line 1.682 ev luminescence center in diamond and the vacancy-silicon complex. *Phys. Rev. Lett.*, 77:3041, 1996.

[174] AM Saitta, F. Buda, G. Fiumara, and PV Giaquinta. Ab initio molecular-dynamics study of electronic and optical properties of silicon quantum wires: Orientational effects. *Phys. Rev. B*, 53:1446, 1996.

[175] R.A.G. Cinelli, V. Tozzini, V. Pellegrini, F. Beltram, G. Cerullo, M. Zavelani-Rossi, S. De Silvestri, M. Tyagi, and M. Giacca. Coherent dynamics of photoexcited green fluorescent proteins. *Phys. Rev. Lett.*, 86:3439, 2001.

[176] J. Pan, S. Sandhu, Y. Huo, N. Stuhrmann, M.L. Povinelli, J.S. Harris, MM Fejer, and S. Fan. Experimental demonstration of an all-optical analogue to the superradiance effect in an on-chip photonic crystal resonator system. *Phys. Rev. B*, 81:041101, 2010.

[177] V.N. Pustovit and T.V. Shahbazyan. Cooperative emission of light by an ensemble of dipoles near a metal nanoparticle: The plasmonic dicke effect. *Phys. Rev. Lett.*, 102:77401, 2009.

[178] M. A. Nielsen and I. A. Chuang. *Quantum computing and quantum information.* Cambridge, 2000.

[179] T.D. Ladd, F. Jelezko, R. Laflamme, Y. Nakamura, C. Monroe, and J.L. O'Brien. Quantum computers. *Nature*, 464:45, 2010.

[180] A. Imamoglu, D. D. Awschalom, G. Burkard, D. P. DiVincenzo, D. Loss, M. Sherwin, and A. Small. Quantum information processing using quantum dot spins and cavity qed. *Phys. Rev. Lett.*, 83:4204, 1999.

[181] H.T. Dung, S. Scheel, D.G. Welsch, and L. Knöll. Atomic entanglement near a realistic microsphere. *Journal of Optics B: Quantum and Semiclassical Optics*, 4:S169, 2002.

[182] A. Laucht, J. M. Villas-Bôas, S. Stobbe, N. Hauke, F. Hofbauer, G. Böhm, P. Lodahl, M.-C. Amann, M. Kaniber, and J. J. Finley. Mutual coupling of two semiconductor quantum dots via an optical nanocavity. *Phys. Rev. B*, 82:075305, 2010.

[183] P. Yao and S. Hughes. Macroscopic entanglement and violation of bell's inequalities between two spatially separated quantum dots in a planar photonic crystal system. *Opt. express*, 17:11505, 2009.

[184] Y. Makhlin, G. Schön, and A. Shnirman. Quantum-state engineering with josephson-junction devices. *Rev. Mod. Phys.*, 73:357, 2001.

[185] M. V. G. Dutt, L. Childress, L. Jiang, E. Togan, J. Maze, F. Jelezko, A. S. Zibrov, P. R. Hemmer, and M. D. Lukin. Quantum register based on individual electronic and nuclear spin qubits in diamond. *Science*, 316:1312, 2007.

[186] S. Diehl, A. Micheli, A. Kantian, B. Kraus, HP Büchler, and P. Zoller. Quantum states and phases in driven open quantum systems with cold atoms. *Nature Physics*, 4:878, 2008.

[187] B. Kraus, H.P. Büchler, S. Diehl, A. Kantian, A. Micheli, and P. Zoller. Preparation of entangled states by quantum markov processes. *Phys. Rev. A*, 78:042307, 2008.

[188] A. F. Alharbi and Z. Ficek. Deterministic creation of stationary entangled states by dissipation. *Phys. Rev. A*, 82:054103, 2010.

[189] M. J. Kastoryano, F. Reiter, and A. S. Sørensen. Dissipative preparation of entanglement in optical cavities. *Phys. Rev. Lett.*, 106:090502, 2011.

[190] H. Krauter, C.A. Muschik, K. Jensen, W. Wasilewski, J.M. Petersen, J.I. Cirac, and E.S. Polzik. Entanglement generated by dissipation and steady state entanglement of two macroscopic objects. *Phys. Rev. Lett.*, 107:80503, 2011.

[191] J.T. Barreiro, M. Müller, P. Schindler, D. Nigg, T. Monz, M. Chwalla, M. Hennrich, C.F. Roos, P. Zoller, and R. Blatt. An open-system quantum simulator with trapped ions. *Nature*, 470:486, 2011.

[192] S. Savasta, R. Saija, A. Ridolfo, O. Di Stefano, P. Denti, and F. Borghese. Nanopolaritons: Vacuum rabi splitting with a single quantum dot in the center of a dimer nanoantenna. *ACS Nano*, 4:6369, 2010.

[193] R.H. Lehmberg. Radiation from an n-atom system. i. general formalism. *Phys. Rev. A*, 2:883, 1970.

[194] M.O. Scully and M.S. Zubairy. *Quantum optics*. Cambridge Univ Pr, 1997.

[195] R. Horodecki, P. Horodecki, M. Horodecki, and K. Horodecki. Quantum entanglement. *Rev. Mod. Phys.*, 81:865, 2009.

[196] W.K. Wootters. Entanglement of formation of an arbitrary state of two qubits. *Phys. Rev. Lett.*, 80:2245, 1998.

[197] T. Yu and J.H. Eberly. Evolution from entanglement to decoherence of bipartite mixed. *Arxiv preprint quant-ph/0503089*, 2005.

[198] L. Mandel and E. Wolf. *Optical coherence and quantum optics*. Cambridge Univ Press, 1995.

[199] E. Moreno, F.J. García-Vidal, D. Erni, J.I. Cirac, and L. Martín-Moreno. Theory of plasmon-assisted transmission of entangled photons. *Phys. Rev. Lett.*, 92:236801, 2004.

[200] G.Y. Chen, Y.N. Chen, and D.S. Chuu. Spontaneous emission of quantum dot excitons into surface plasmons in a nanowire. *Opt. Lett.*, 33:2212, 2008.

[201] H.T. Dung, L. Knöll, and D.G. Welsch. Decay of an excited atom near an absorbing microsphere. *Phys. Rev. A*, 64:013804, 2001.

[202] A. Trügler and U. Hohenester. Strong coupling between a metallic nanoparticle and a single molecule. *Phys. Rev. B*, 77:115403, 2008.

[203] T. Yu and JH Eberly. Sudden death of entanglement. *Science*, 323:598, 2009.

[204] Z. Ficek and B. C. Sanders. Quantum beats in two-atom resonance fluorescence. *Phys. Rev. A*, 41:359, 1990.

[205] H. Carmichael. *An open systems approach to Quantum Optics: lectures presented at the Université Libre de Bruxelles, October 28 to November 4, 1991*, volume 18. Springer, 1993.

[206] E. Del Valle. Steady-state entanglement of two coupled qubits. *JOSA B*, 28:228, 2011.

[207] A. Batalov, C. Zierl, T. Gaebel, P. Neumann, I.Y. Chan, G. Balasubramanian, PR Hemmer, F. Jelezko, and J. Wrachtrup. Temporal coherence of photons emitted by single nitrogen-vacancy defect centers in diamond using optical rabi-oscillations. *Phys. Rev. Lett.*, 100:77401, 2008.

[208] F. Jelezko and J. Wrachtrup. Single defect centres in diamond: A review. *Physica status solidi (a)*, 203:3207, 2006.

[209] E. Del Valle. Strong and weak coupling of two coupled qubits. *Phys. Rev. A*, 81:053811, 2010.